Abstract

Title of dissertation:	NEW METHODOLOGY FOR PREDICTING ULTIMATE CAPACITY OF ONE-SIDED COMPOSITE PATCH REPAIRED CRACKED ALUMINUM PLATE
	Daniel C. Hart, Doctor of Philosophy, 2020
Dissertation directed by:	Professor Hugh A. Bruck Department of Mechanical Engineering

Composite patch repairs are an alternative to traditional weld repair methods to address cracking in aluminum plates. Analytical and numerical design methods use linear elastic fracture mechanics (LEFM) that do not account for elastic-plastic crack tip behavior demonstrated in static tests of one-sided patch repaired ductile panels. This research used digital image correlation (DIC) and three-dimensional finite element analysis (FEA) with first order elements to study crack tip effects due to the one-sided composite patch applied to center crack tension (CCT) specimens loaded monotonically to failure. The measurable effects on crack tip behavior due to the composite patch were ultimate tensile load increase of more than 100% and a total achieved crack opening displacement (COD) increase of 20% over the unpatched behavior. Crack tip fracture behavior was found to be an intrinsic property of the aluminum and directly related to the COD independent of the one-sided

composite patch. Increased capacity was related to accumulation of large-strain free surface area and through thickness volume ahead of the crack tip. Test data and numerical predictions correlated with measured load, strain, displacement fields, and J-integral behavior. Correlation of displacement fields with HRR and K fields established a state of small scale yielding prior to failure. Data and predictions indicated critical COD occurs when unpatched and patched large strain area is equivalent, which occurs before crack tip behavior transitions from small scale to large scale yielding and crack growth. Identifying a critical COD for both small and large scale one-sided patch repaired cracked ductile panels results in a predicted failure closer to the ultimate tensile load and 80% greater than predicted with LEFM methods.

Observations and predictions demonstrated in this research resulted in three scientific contributions: (1) development of criteria to determine crack growth in cracked ductile panels repaired with a one-sided composite patch using a critical COD, (2) development of a three-dimensional FEA to study development of the plastic zone and evolution of the large-strain region ahead of the crack tip, and (3) development of a numerical methodology to predict ultimate tensile load capacity of cracked ductile panels repaired with a one-sided composite patch.

NEW METHODOLOGY FOR PREDICTING ULTIMATE CAPACITY OF ONE-SIDED COMPOSITE PATCH REPAIRED CRACKED ALUMINUM PLATE

by

Daniel Constantine Hart

Dissertation submitted to the Faculty of the Graduate School of the
University of Maryland, College Park in partial fulfillment
of the requirements for the degree of
Doctor of Philosophy
2020

Advisory Committee:

Professor Hugh Bruck (Chair)
Professor Peter Chung
Professor Abhijit Dasgupta
Professor Teng Li
Professor Sung Lee (Dean's Representative, Aerospace Department)

Dedication

To my family and friends, this effort would not have been possible without your dedication and support.

To my Dad, I would not have started nor completed this journey without your encouragement.

And to my Mom, whose encouragement, support, editing skills, and financial assistance helped me reach my goal.

Acknowledgements

Work described was performed by the Naval Surface Warfare Center Carderock Division's Survivability, Structures, Materials Department, and University of Maryland College Park's Mechanical and Reliability Engineering department. Financial and technical support was provided by an Office of Naval Research In-house Laboratory Independent Research (ILIR) program element 97X4930N under Dr. Jack Price, and a grant provided to UMD by program officer Dr. Paul Hess of the Office of Naval Research Code 331 under grant number N000141612351. Opinions expressed are those of the authors and do not necessarily reflect opinions of the sponsors.

This research was supported by so many people. First, I'd like to thank Dr. Paul Hess for the funding and guidance that supported research of the composite patch repair. His support helped start the composite patch repair effort and his continued encouragement motivated me complete my PhD. Small scale testing and specimen manufacturing was performed at the University of Maryland with support of research assistants Raphael Kraeling, Felix Filafer, and Christoph Sailer along with fellow graduate students Nelson Quispe-Benavides and Huisung Yun. Large scale testing performed at NSWCCD could not have been successful without the dedicated work of Ed Udinski and our lab technicians Tim Dapp and John Kim, who assisted in setting up test frames, the manufacture of specimens, measureing and gauging specimens, and running tests. Support from my department and division from training approvals to proposal ideas was critical in my efforts and I thank all of those involved. A special thanks to Shannon, for without her help I would not have contacted the right people or filled out the right forms in the right order.

Table of Contents

Table of Figures

Table of Tables

1 Introduction

Composite patch repair method development for marine structures lags behind that of the aerospace industry, even though a lot of similarities exist. For both industries, key assumptions used to design and analyze bonded repairs of cracked aluminum do not adequately capture either through thickness or ductile behavior due to one-sided repairs.

Composite patch repairs are used to repair corrosion, cracking, and over stress of metallic damage to metallic plates. The composite patch provides an alternative load path by bridging the crack and reinforcement of the metallic material ahead of the crack tip. Structural fibers bridging the crack carry load and decrease the ability of the crack to open, resulting in reduction of the energy available at the crack tip and retardation of the crack growth. Reinforcement at the crack tip of the plate surface changes the through thickness stress distribution. This effect is more dramatic for one-sided repairs and when the adherends stiffness mismatch, or stiffness ratio, is greater than one. In general, the repair laminate can be designed to replace the in-plane load carrying capability of the plate, match the bending stress capacity of the structure, or reduce fracture energy available at the crack tip.

General bonded joint design was first addressed around 1940 defined by the governing differential equations for an explicit adhesive layer [1, 2]. Later advancements were made when Hart-Smith introduced inelastic behavior of the adhesive layer to the equations [3, 4]. The application of bonded joint design in the development of aircraft patch repairs continued to evolve through a combination of and improvement of mechanical characterization protocols, development of appropriate design methods based on adhesive

and adherend governing equations, and enhancement of analytical prediction efforts [5, 6, 7]. This was accomplished by incorporating linear elastic fracture mechanics (LEFM) to calculate either strain energy release rate (SERR) or stress intensity (K) at the metallic crack tip. Wang and Rose extended the design approach for 2D joints to include the crack tip of composite patched aluminum repairs by using a distribution of springs across the crack to represent the adhesive and patch. Plate theory incorporates a linear elastic energy balance, coupled normal and bending stress components to predict crack tip stress intensity [8, 9]. Advancements in computational algorithms, particularly Finite Element Analysis (FEA) techniques such as Virtual Crack Closure (VCCT), simplified the development of numerical analysis approaches [10, 11, 12]. As the thickness and loading of the repaired plate increases, inelastic failure mechanisms play significant roles in the ultimate load capacity of the repaired plate that are not accounted for by either the analytical or the numerical methods account for.

Recent testing of low modulus one-sided composite patched center crack tension (CCT) and large scale ductile tearing specimens [13, 14, 15] have demonstrated increased monotonic load and displacement capacity compared with unpatched specimens. Plastic deformation of the aluminum ahead of the crack tip was observed as a common failure mechanism. Large scale testing of one-sided patched aluminum specimens, shown in Figure 1-1, have demonstrated that the elastic-plastic crack tip behavior occurs before ultimate failure [13, 16].

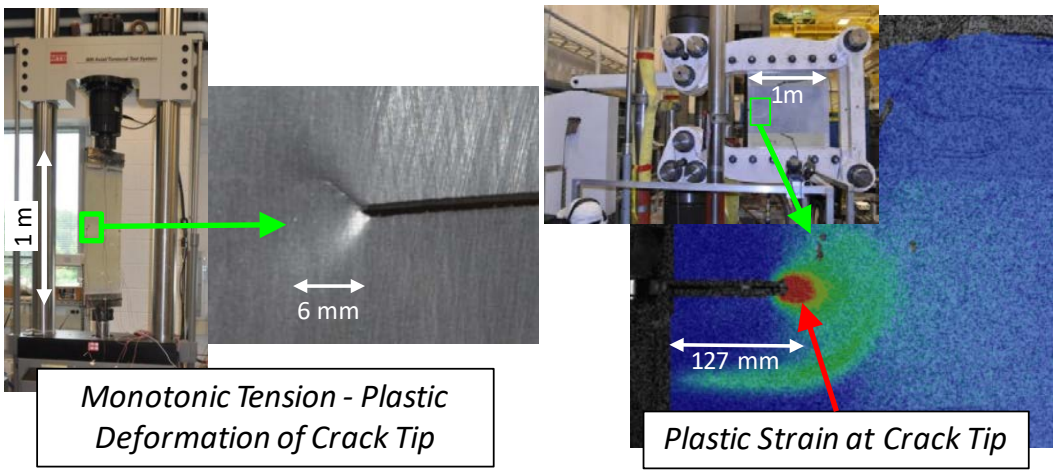

Figure 1-1 Plastic zone developed on the free surface of 28 x 92 cm large scale patched CCT (L) and 1 m^2 ductile tearing (R) specimens.

Plastic behavior observed in large scale testing was confirmed in preliminary small scale CCT testing using digital image correlation (DIC) and full field free surface strain data ahead of the crack tip [17, 18]. Typical strain fields in the crack blunting stage shown in Figure 1-2 highlight the concentration of large strains ahead of the crack tip that correlate with residual plastic zones observed at full scale.

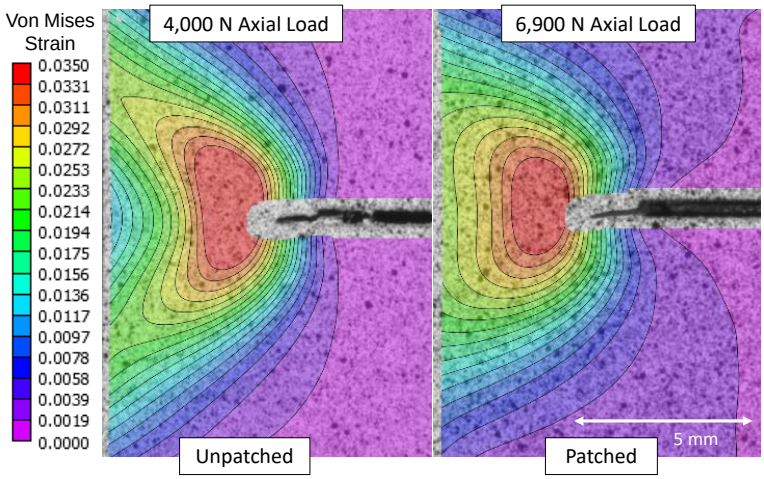

Figure 1-2 Small scale strain fields in the crack blunting stage showing large strains concentrated at the crack tip of both unpatched and patched specimens.

The goal of this research was to build on current university, marine industry, and defense industry work to improve design and analysis methods for one-sided composite patch

repaired cracked aluminum plate during extreme one-time load scenarios. Composite patch repair design methods used by the U.S. Navy assumed elastic-plastic adhesive behavior, linear elastic adherends, and used closed form equations to size the composite patch overlap length [4, 16, 19]. Once the joint length was determined, Rose's model based on linear elastic fracture mechanics (LEFM) was used to determine the minimum patch stiffness and thickness required to reduce the fracture energy available at the crack tip [8]. A simplified Rose's model assumes plane stress with no out of plane bending, even though Rose's model was extended to include small out of plane displacements for one-sided repairs [9]. The simplified Rose's model did produce a conservative design. However under in-plane loads one-sided composite patches create asymmetry and bending that results in through thickness behavior in the adherends and at the crack tip which violates the plane stress assumption. Current design methods are not adequate to predict ultimate strength during a one-time worst case load scenario such as blast or shock. Under extreme loading the methodology must account for material behavior beyond yield as well as out of plane bending at the crack tip.

The focus of this research was to study the effects a one-sided adhesively bonded low modulus E-Glass/Epoxy composite patch has on the development of the crack tip plastic zone for small scale cracked aluminum CCT specimens loaded monotonically in tension until failure. To improve our understanding of the one-sided surface reinforcement effects on crack tip material behavior, three-dimensional FEA and full field 2D DIC data from the free aluminum surface for both unpatched and patched specimens were compared from initial linear elastic loading response through the plastic zone development, crack

blunting stage, and ultimate failure. The ultimate goal was to develop an improved design methodology for one-sided composite patch repairs using numerical prediction methods.

2 Literature Review

Discussion of adhesive joining and composite patch repairs requires the use of standard composite materials industry terms to describe the constituents, material directions, and failure modes. Definitions of terms used will be provided or match those in ASTM 3878 [20].

2.1 Military and Marine Industry Use of Composite Patches

Composite patch repairs of metallic aircraft structures were pioneered in the 70's and 80's with work in both Australia and the U.S. by Dr. Baker and Dr. Hart-Smith. Christian et. al. outlined the design studies and repair locations selected for U.S. Air Force (USAF) transport C-141B [21]. Detailed FEA was used to select structural locations for repair and previous technology developed by the Royal Australian Air Force (RAAF) and Army Research Lab (ARL) to simplify development. The USAF feasibility study applied composite patch repairs to several in-service aircraft locations and several static structural components. The study selected a low temperature film adhesive, the surface bonding agent, and both boron and carbon fibers for reinforcement.

In the 1960's aluminum became a common material for use in ship structures for the destroyers and frigates of the Netherlands Navy and British Royal Navy. With 1/3rd the stiffness of steel, the resulting stress from sea way loading in the aluminum deckhouse structure would be lower than that of the steel hull. Stress concentrations and low fatigue resistance of aluminum left structures susceptible to fatigue cracking. Allan and Clark examined the strength of steel and carbon patches applied to the fatigued and over-stressed areas of the aluminum superstructure on British Royal Navy Type 21 Frigates [22]. Designer of the patch repairs assumed the patch was long enough, the adhesive

layer thin enough, sections remain plane, and enough local structure supported plating to negate bending and make standard beam equations valid. Since most of the early composite patch work was performed by the aerospace industry, the base and patch material were thin and assumed to be in a state of plane stress. With these assumptions the stress in the plate is simply governed by the material stiffness and thickness ratio of the repaired system.

$$\sigma_1 = \frac{\sigma_o}{1 + \left(\frac{E_{2t_2}}{E_{1t_1}}\right)} \qquad \text{Equation 1}$$

Allan and Clark performed fatigue testing of butt-joints and welded aluminum joints with and without double sided composite patches [22]. Butt joint fatigue life was significantly lower than the welded and patched specimens. End clamps were used to reduce the peel stresses at the composite patch tips to improve the fatigue life of patched butt joints. Tapering the patch edges and increasing the amount of adhesive at the patch edges were both shown to improve the joint strength and fatigue life.

The Royal Australian Navy experimented with carbon fiber vinyl ester composite patches on FFG-7 class frigates to address an overstressed region of the deckhouse [23, 24]. Composite patches were large, 5 m x 1 m x 1.25 cm thick, and carried longitudinal seaway loads at the top level of the deckhouse along the midship dog-bone section. Fiber, resin, and, surface preparation procedure selections were made according to material characterization, environmentally conditioned Boeing wedge testing, and lap shear testing efforts. Lamination procedures and resulting laminate quality were compared by fiber volume fraction (FVF), porosity content, interlaminar shear strength (ILSS), flexural strength, and flexural modulus of both high and low quality sections of the test

panels. Design of the thick carbon fiber patches were performed using combined stress failure criteria for matrix dominated failure. Analysis used 2D iso-parametric elements to model a machine tapered aluminum specimen with a two-sided composite patch over the machined taper [25]. Results of the effort demonstrate that this method produced quality lamination and adhesion that significantly reduced strain levels in the aluminum with high fatigue stress tolerance. The composite patches were designed to reduce the peak stress in the region by up to 20%. After 15-years of service, coatings maintenance, and repairs the composite patches were considered a success. Structural and non-structural repairs were fully documented along with metal structural modifications and welding in close proximity to the patches [24].

QinetiQ used stiffness matching defined in Equation 2 in the design of carbon fiber patches for UK's Royal Navy Type 21 Frigates, Type 42 Destroyers, and also commercial off-shore oil platforms. However, starting in 1982, Type 21 frigates had cracking in their aluminum deckhouse structures. Weld repairs of the cracks resulted in re-cracking of the repair in relatively short amount of time. Re-cracking occurred where deck plate thickness changed from 1.9 to 0.76 cm. A 0.5 cm thick unidirectional carbon patch repair was applied across the weld repaired crack. Repair of the first ship was followed by repair or reinforcement of the remaining six ships in the class.

$$\frac{E_{Patch}}{t_{Patch}} = \frac{E_{substrate}}{t_{substrate}} \qquad \text{Equation 2}$$

In 1998 the repair of food tray lift shafts onboard the Type 42 destroyers were performed on the steel plate, by cropping out and welding replacement steel back in. Composite patches offered a cost and time efficient repair method to address the cracking. Seven

ships and 35 patches were applied using hand layup, infusion, and pre-preg installation methods, all of which were performed successfully in restricted spaces. Following these successes, QinetiQ installed composite patch repairs on floating production storage and offloading (FSPO) oil platforms. Because these FSPOs are tethered to the ocean floor and operate on station, meaning they do not move, these platforms are subject to higher fatigue stresses than would occur in a typical free floating ship and see experience instances of fatigue cracking. Weld repair, or “hot-work”, is dangerous and restricted onboard FSPO’s. Performing weld repair requires gas free environment and oil free tanks for a minimum of 2 bulkheads in any direction, which is a costly endeavor for an oil production environment. Consequently, in 2002, QinetiQ repaired the steel structure of an FSPO ballast tank with a film adhesive bonded carbon pre-preg repair to address a 60 mm crack between cargo and ballast tanks, since composite patch repairs do not require welding. Hydrostatic pressure acting on the bond side of the patch was addressed with an aluminum plate bonded and sealed to the opposite side of the steel plate inside the ballast tank. Research by Turton and Livingstone demonstrated patch repairs increased fatigue life of the plate by a minimum of 3 times. Also, a one-sided repair does not stop crack growth, but does significantly decreases the growth rate. To monitor crack growth rate, the researched used an alternating current potential difference (ACPD) non-destructive evaluation (NDE) inspection methods, which requires imbedding spot-welded electrodes at equidistant positions ahead of the crack tip. This allows periodic checking of the potential difference (PD) between the electrodes, change indicates crack growth [26].

2.2 U.S. Navy Design and Testing Experience

U.S. Navy experience with composite patches to address aluminum sensitization and stress corrosion began in December of 2010 with LEFM based design, lap-shear testing, and process development [16]. Design of the composite patch repair used linear elastic fracture mechanics (LEFM), adhesively bonded joint equations [4], and simplified Rose's Model [8] closed-form solutions. The well characterized LEFM center crack tension (CCT) specimen was chosen as the design load case. Detailed FEA assumed a perfect rigid bond between the aluminum surface and the composite patch. Initial unpatched CCT specimen FEA results correlated with plane-stress closed form solutions. The analysis was refined to investigate the out of plane contributions of the one-sided composite patch on the out of plane displacements and the through thickness stress intensity distribution at the crack tip. Although the composite patch repair did not eliminate crack growth at the stress levels applied for this test series, the growth rate was significantly decreased and the static tensile load capacity of the repaired cracked aluminum plate increased more than 80% [27], as shown in Figure 2-1. Static test results for the aluminum and patched aluminum specimens demonstrated a 43% increase in stiffness of the initial linear crack opening displacement (COD) versus load response and a 33% increase of the load at which nonlinear behavior initiates.

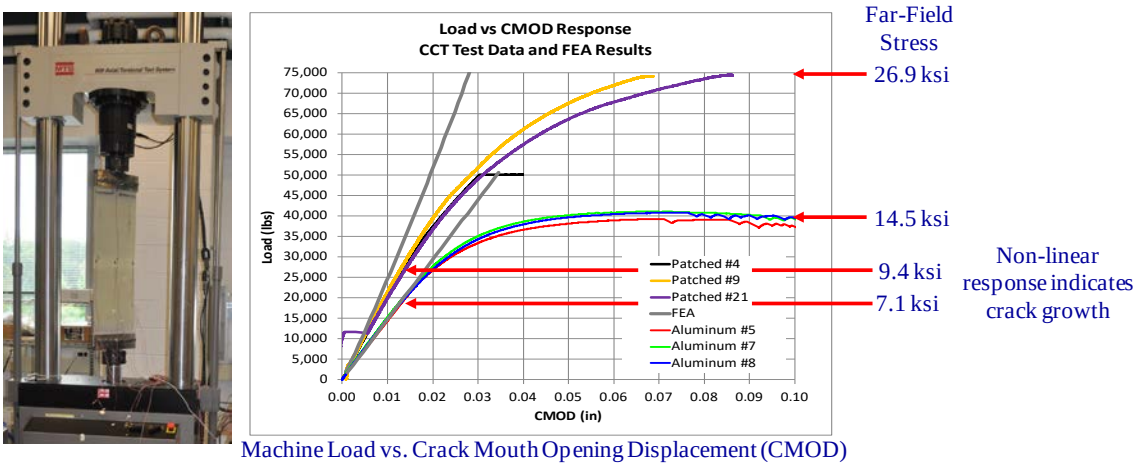

Figure 2-1: CCT test configuration and static load results [27].

Numerical predictions for strain and displacement for the aluminum panels were within l% in the linear response region. Approximating the laminates contribution with shell elements decreased the accuracy of the predictions. The predicted load versus COD response was 16.9% stiffer. Low modulus one-sided composite patches of a cracked aluminum plate are capable of reducing the stress intensity at crack tips such that crack growth rates are reduced by a factor between 4 and 10 [13, 28, 29]. Testing of the composite patch repaired CCT specimens provided proof of concept and the performance of the repair statically and at three far-field stress states [15].

2.3 Adhesive Bonded Design

The foundation of composite patch repair design are the fundamental relationships and differential equations that describe load carried by the adherends and the load transferred across the adhesive between the adherends. Simplifying assumptions are common to all methods presented with strong recommendations to rely on 3D FEA to account for elastic-plastic and through thickness behavior associated with one-sided patch repairs.

2.3.1 Failure Modes

Proper identification of the failure modes and common failure mode drivers for adhesive bonded components and repair in the aviation industry should drive the selection process and methods [30]. Kinloch identifies four basic theories to determine bond strength; surface profile, diffusion of adhesive on surface, molecular attraction, chemical bonds between adhesive and adherends. Poor-long term performance, or durability, can be attributed to process selection based on simple static testing for bond strength when bond durability through fatigue and environmental testing drives the durability. Bonding surface contamination, hydration resistance of the surface, and hydration resistance of the chemical bonds are important aspects of bond application process that can lead to premature failure. Proper selection of adhesive, bonding agent, and surface preparation are independent of load level. Poor quality bonds fail at any load when moisture corrupts the bond strength. The Boeing wedge test is recommended to address long-term durability. Even environmentally conditioned specimens do not fully represent the gradual degradation of the bond strength during moisture ingress and cyclic loading [31].

Adhesive failure modes include cohesive, adhesive, and adherend failure. Cohesive failure being failure of the adhesive layer. Adhesive failure is failure between the adhesive and adherend. Adherend failure occurs outside of the bond area within one of the substrates. Adhesives are fatigue resistant, typical cohesive failure does not occur due to fatigue, but rather to poor joint design or overload. Adhesive failures are generally caused by long term load and moisture effects and surface preparation quality [31].

Mixed mode failure of adhesive bonded joints are discussed by Davis and Tomblin in the Federal Aviation Administration (FAA) best practices document that references Hart-

Smith equations and talks about hydration of the chemical bonds. Davis and Tomblin also provide reference pictures and discussions concerning design of the bond for hydration, since coatings only slow the moisture diffusion into the composite patch and do not stop diffusion [32] eventually leading to the bond line being affected by moisture, as reported by Davis and McGregor [33].

2.3.2 Bonded Joint Design

Initial formulations of bonded joint mechanics were developed by de Bruyne, Goland and Reissner, and Volkersen for bonded single and double lap joints [2, 1]. These models assumed linear elastic material behavior and described the shear deformation of the adhesive layer. Volkersen developed formulations for both bonded double and single lap joints, but they did not include inelastic shear behavior of the adhesive.

Hart-Smith work focused on stress-based approach to determine failure by calculating the peel and normal stresses within the adhesive accounting for the elastic-plastic behavior of the adhesive to determine the joint strength and performance [3, 4].

Tsai added a linear adherend shear stress distribution to the classical solutions developed by de Bruyne, Goland and Reissner. The derivation by Tsai was limited to short overlaps and small loads because higher loads and longer overlaps resulted in overly conservative results due to the assumed shear stress distribution through the joint sections. Moiré interferometry measurements of the cross section showed that shear stress extended into the composite adherends, where the adherend shear was assumed to be negligible in previous formulations. For composite adherends with low interlaminar shear stiffness and strength this additional stress is important [34].

Duong expanded the Goland-Reissner solution method to include a tapered adherened with geometric nonlinearity [35], that was later expanded to include stress predictions at the crack tip and strain energy release rates to predict adhesive fracture [36]. The approach presented a generalized solution to solve the fracture mechanics of adhesively bonded adherends, represented by beams, with the crack plane at the center of the adhesive layer. The updated model included a disbond and first order shear deformation theory with a shear correction factor in the beam formulation. A differential equation relating the deflection and curvature of a beam relates the tensile force, moment, and composite plate flexural rigidity for each segment of the tapered plate. Solving the differential equation gives displacement as a function of location for each segment of the tapered joint. Equilibrium and constitutive relationships between the adhesive and adherends are used to solve the differential equations. In the two-step method, the adherends are first assumed to be rigidly joined and the nonlinear moment distribution along the entire joint can be represented with simple closed form equations. In the second step of the process the stresses in the overlap portion of the joint are determined by setting up and solving a set of differential equations governing the behavior of the composite cross section for each taper step. The nonlinear bending moment, boundary conditions and constitutive behavior of the adherends are used to solve for the stresses. Once the shear and peel stresses are known the strain energy release rate (SERR) can be calculated by modifying the geometry of the taper tip to include an assumed disbond length, then the stress can be calculated at this point. In the isotropic adhesive the SERRs are related to the stress by Equation 3 and Equation 4, with the total SERR being the sum of G_I and G_{II}. The closed form solutions presented were then verified against FEA results.

In the FEA results the element formulation was critical. FEA SERRs were predicted using a modified virtual crack closure technique (VCCT) that used nodal displacements and forces from the FEA results to manually calculate the SERRs. For thin 1.6 mm aluminum isotropic adherends both ABAQUS CPS4 and CPS4R plane stress elements produced essentially equivalent results. Hourglass deformation was a problem with the CPS4R elements along the crack surface. When orthotropic adherends were analyzed the CPS4 elements produced better results. The adhesive layer was represented by four elements through the thickness. Wang and Zhang offer a comparison of the different modeling techniques for bonded joints [37]. Using the beam/adhesive layering method results in stress that is independent of location through the thickness with closed form solutions as compared to plane stress results. No explicit assumptions were made that limit the formulation to thin adherends. However, adherends are assumed to behave linear elastically, which is required to determine the first order shear deformation of a laminated beam.

$$G_I = \frac{\sigma_a^2 t_a}{2E_a}$$ Equation 3

$$G_{II} = \frac{\tau_a^2 t_a}{2G_a}$$ Equation 4

2.3.3 Rose's Model

Contributions from Baker et. al. document Rose's models from simplified calculations assuming double-sided or one-sided repairs supported against bending along with solving logarithmic singularities to design one-sided including bending [8]. Plane stress

conditions are assumed such that there is no through thickness stress gradient (thin plates, in-plane loading), the adherends do not deform in shear, and there is no out of plane bending. In the load transfer mechanisms between the repair and the cracked plate assume plane strain conditions for the cross section and the plates are wide enough that along the crack plane (x-dir) strain is zero. Adherends are assumed to be elastic solids. The adhesive behaves as a shear spring with the assumed solution taking the form in Equation 7 below, with x running along the crack, y being the location along the length of the joint, z going through the thickness in the direction of the patch, and constants C to be determined by the boundary conditions. Adherends, the composite patch repair and base plate, are assumed to stretch according to the following relationships:

$$\sigma_{plate} = \frac{E_{plate}}{1-\nu_{plate}^2}\epsilon_{plate} = \frac{E_{plate}}{1-\nu_{plate}^2}\frac{du_p}{dy} \quad \text{Equation 5}$$

$$\sigma_{patch} = \frac{E_{patch}}{1-\nu_{patch}^2}\epsilon_{patch} = \frac{E_R}{1-\nu_R^2}\frac{du_R}{dy} \quad \text{Equation 6}$$

The adhesive transfers the load between the patch repair and the plate through shear only and behaves as a shear spring. Therefore, the shear stress can be related to the difference in the local adherend stretch, adhesive thickness, and the shear modulus (G_A) of the adhesive.

$$\tau_A = G_A\frac{u_R - u_P}{t_A} \quad \text{Equation 7}$$

Assuming that the adhesive applies a constant body force to the interface of the infinitesimal adherend and adhesive that is equivalent to the shear stress divided by the adherend thickness, the equilibrium equation simplifies to Equation 8 where the assumed shear solution is Equation 9 and the coefficient β is defined by Equation 10:

$$\frac{d^2\tau_A}{dy^2} - \beta^2\tau_A = 0 \qquad \text{Equation 8}$$

$$\tau_A = C_1 \sinh \beta y + C_2 \cosh \beta y \qquad \text{Equation 9}$$

$$\beta^2 = \frac{G_A}{t_A}\left[\frac{1-\nu_P^2}{E_P t_P} + \frac{1-\nu_R^2}{E_R t_R}\right] \qquad \text{Equation 10}$$

Solving Equation 8 with the following plate stress at the end of the patch equal the far field stress (y=±B) and in-plane stress at the end of the patch resolved to 0 (y=±B) yields the adhesive shear stress with B being the half-length of the patch repair along the y axis.

$$\tau_A = -\sigma^\infty \frac{(1-\nu_P^2)G_A}{\beta t_A E_P \cosh \beta B} \sinh \beta y \qquad \text{Equation 11}$$

Here the adhesive shear stress is asymptotic at the repair ends and decays exponentially toward the center of the patch. This means that the load transfer happens near the ends of the repair over a length the order of 1/ β. The stress in the plate directly beneath the repair at y=0, mid length of the repair is defined by Equation 12 with the term S defined by Equation 13. This formulation of stress ignores the load attraction effect due to the localized increased stiffness of the repaired region. Therefore this local stress under the repair underestimates the actual stress.

$$\sigma_0 = \frac{\sigma^\infty}{1+S}\left[1 + \frac{S}{\cosh \beta B}\right] \qquad \text{Equation 12}$$

$$S = \frac{(1-\nu_P^2)}{(1-\nu_R^2)}\frac{E_R t_R}{E_P t_P} \qquad \text{Equation 13}$$

The two stage process of Rose's Model uses an inclusion analogy followed by calculating the stress intensity factor. The inclusion analogy treats the repaired region as a

homogenous section with a representative or equivalent stiffness inside an infinite plate. In this configuration the stress in the inclusion is determined first, then the stress sharing between the repair and plate of the inclusion using classical lamination theory is determined second. Knowing the stress in the plate under the repair allows determination of the stress intensity factor at the crack tips. To determine the stress intensity factor a cut is made along the crack length with an internal pressure applied such that the crack faces are stress free. Knowing the stress in the repair patch, Equation 5 and Equation 6 can be used to determine the crack opening displacement at the center of the crack for a symmetric double-sided repair or one that is supported against out of plane displacement. Using Equation 11 and the governing differential equation one can solve for the crack opening displacement u_y. With the crack opening, $\delta = 2u_y$, consider the change in potential energy (Equation 15), which contains the strain energy release rate and work performed by the external load (Equation 16).

$$u_y = \frac{\beta t_P t_A}{G_A}\sigma_0 \qquad \text{Equation 14}$$

$$\Pi = U_E - W = \frac{1}{2}\sigma_0 t_P \delta - \sigma_0 t_P \delta = -\frac{1}{2}\sigma_0 t_P \delta \qquad \text{Equation 15}$$

$$G_\infty t_P = -\frac{\partial \Pi}{\partial a} = \frac{1}{2}\sigma_0 t_P \delta \qquad \text{Equation 16}$$

$$\sigma_0 = \frac{1}{2}kE_P\delta \;\rightarrow\; \delta = \frac{2\sigma_0}{kE_P} \qquad \text{Equation 17}$$

$$k = \frac{S\beta}{(1+S)(1-\upsilon_P^2)} \qquad \text{Equation 18}$$

The strain energy release rate for crack growth of *da*, is calculated with the following equation:

$$G_\infty = \frac{1}{2}\sigma_0\left(\frac{2\sigma_0}{kE_P}\right) = \frac{\sigma_0^2}{kE_P} \qquad \text{Equation 19}$$

The equations listed above assume linear elastic solids and a symmetric repair or one in which the out of plane displacements are constrained. For plane stress conditions the stress intensity, *K*, can be calculated using the following relationships:

$$G = \frac{K^2}{E} \qquad \text{Equation 20}$$

$$K_\infty = \frac{\sigma_0}{\sqrt{k}} \qquad \text{Equation 21}$$

If the adhesive can deform plastically, the stress versus crack opening displacement curve is no longer linear and the rate at which strain energy accumulates with crack opening decreases. This change occurs with the stress is greater than the yield stress of the adhesive. When this occurs the crack opening displacement can be defined by Equation 22.

$$\delta = \frac{\sigma_{0Y}}{kE_P}\left[1 + \left(\frac{\sigma_0}{\sigma_{0Y}}\right)^2\right] \qquad \text{Equation 22}$$

Then by calculating the change in potential energy and relating the change in potential energy with respect to the crack length, the SERR in the plastic region is defined by Equation 23 and the stress intensity by Equation 24.

$$G_\infty = \frac{\sigma_0^2}{kE_P}\left[\frac{\left(\frac{\sigma_0}{\sigma_{0Y}}\right)^3 + 3\left(\frac{\sigma_0}{\sigma_{0Y}}\right) - 1}{3\left(\frac{\sigma_0}{\sigma_{0Y}}\right)^2}\right] \quad \text{Equation 23}$$

$$K_\infty = K_{\infty,elastic} = \frac{\sigma_0}{\sqrt{k}}\left[\frac{\left(\frac{\sigma_0}{\sigma_{0Y}}\right)^3 + 3\left(\frac{\sigma_0}{\sigma_{0Y}}\right) - 1}{3\left(\frac{\sigma_0}{\sigma_{0Y}}\right)^2}\right]^{1/2} \quad \text{Equation 24}$$

The above stress intensity calculation does not account for the through thickness gradient when bending is present. Wang and Rose presented a simplified approach to account for bending caused by one-sided repairs by using a stress concentration factor and the root means square (RMS) stress intensity. By assuming geometrically linear behavior, this approach is less rigorous then the later crack bridging method [38, 8, 9] and predicts the stress intensity limit at much shorter crack lengths.

For single sided repairs Wang and Rose expanded the symmetric derivation above to include cylindrical bending of plates and out of plane displacements. With stress varying through the thickness, the plates are assumed to be in plane strain. For the repaired section the neutral axis and the moments of inertia are:

$$\bar{z} = \frac{S\left(t_p + t_R + 2t_a\right)}{2(1+S)} \quad \text{Equation 25}$$

$$I_t = I_p + I_R\frac{E_R}{E_P}\frac{(1-\upsilon_P^2)}{(1-\upsilon_R^2)} \quad \text{Equation 26}$$

$$I_P = \frac{1}{12}t_p^3 + t_p\bar{z}^2 \quad \text{Equation 27}$$

$$I_R = \frac{1}{12}t_R^3 + \frac{1}{4}t_R\left(t_p + t_R - 2\bar{z}\right)^2 \quad \text{Equation 28}$$

The stress through the thickness that are assumed to be defined by the section forces, moments, and stress intensity distribution are therefore linear.

$$N_0 = \frac{\sigma_\infty t_p}{1+S} + \frac{\sigma_\infty t_p^2 \bar{z}^2}{I_t} \quad \text{Equation 29}$$

$$M_0 = \frac{\sigma_\infty t_p^4 \bar{z}}{12 I_t} \quad \text{Equation 30}$$

$$K(z) = K_m - K_b \frac{2z}{t_p} \quad \text{Equation 31}$$

The above equation now reflects the strain energy contributions from the membrane and bending, therefore, the single sided SERR can be related to the crack mouth opening and the rotation of the crack front.

$$G_\infty^* t_P = N_0 u_0 + M_0 \theta_0 \quad \text{Equation 32}$$

SERR is comprised of both membrane and bending components related to the in-plane crack mouth opening displacement and the rotation angle of the crack face governed by the crack opening displacement and crack face rotation angle. The displacement and rotation can be related to the membrane force and moment, both at the center of the crack (x=0) and at the mid-plane of the repaired plate (z=0), with the following relationship:

$$\begin{Bmatrix} u_0 \\ \theta_0 \end{Bmatrix} = \begin{bmatrix} c_{11} & c_{12} \\ c_{21} & c_{22} \end{bmatrix} \begin{Bmatrix} N_0 \\ M_0 \end{Bmatrix} \quad \text{Equation 33}$$

Expanding Equation 33 and inserting the results into Equation 32 yields the following:

$$G_\infty^* t_P = c_{11} N_0^2 + (c_{12} + c_{21}) N_0 M_0 + c_{22} M_0^2 \quad \text{Equation 34}$$

Coefficients c_{ij} are derived using the governing differential equations for the adhesive, both shear and peel strains, and assuming that adhesive strains are constant through the thickness of the adhesive. Wang and Rose derived the following coefficients:

$$c_{11} = \frac{t_p(t_p + t_R)}{4\kappa D_R} + \left[\frac{(1-\upsilon_P^2)}{E_P t_p} + \frac{(1-\upsilon_R^2)}{E_R t_R} + \frac{t_r(t_p + t_R)}{4D_R}\right]\left[\frac{1}{2\beta} - \frac{G_a t_p}{16\kappa^2 \beta t_a}\left(\frac{t_R}{D_R} - \frac{t_p}{D_p}\right)\right] \quad \text{Equation 35}$$

$$c_{12} = \frac{t_p}{2\kappa D_R}\left(1 + \frac{D_R}{D_p}\right) + \left(\frac{t_R}{2D_R} - \frac{t_p}{2D_p}\right)\left[\frac{1}{2\beta} - \frac{G_a t_p}{16\kappa^2 \beta t_a}\left(\frac{t_R}{D_R} - \frac{t_p}{D_p}\right)\right] \quad \text{Equation 36}$$

$$c_{21} = \frac{t_R + t_p}{2\kappa D_R} - \frac{G_a}{8\kappa^2 \beta t_a}\left(\frac{t_R}{D_R} - \frac{t_p}{D_p}\right)\left[\frac{(1-\upsilon_P^2)}{E_P t_p} + \frac{(1-\upsilon_R^2)}{E_R t_R} + \frac{t_r(t_p + t_R)}{4D_R}\right] \quad \text{Equation 37}$$

$$c_{22} = \frac{1}{\kappa D_R}\left(1 + \frac{D_R}{D_p}\right) - \frac{G_a}{16\kappa^2 \beta t_a}\left(\frac{t_R}{D_R} - \frac{t_p}{D_p}\right)^2 \quad \text{Equation 38}$$

Here the stiffness (D), for either the plate (p) or repair (R), and the stiffness coefficient (κ) are from classical plate theory.

$$D_{\_} = \frac{t_{\_}^3}{12}\frac{E_{\_}}{(1-\upsilon_{\_}^2)} \quad \text{Equation 39}$$

$$\kappa^4 = \frac{E_{adh}}{4t_{adh}(1-\upsilon_{adh}^2)}\left[\frac{1}{D_R} + \frac{1}{D_P}\right] \quad \text{Equation 40}$$

Equilibrium equations require first derivatives of normal and shear stresses to balance. Compatibility requires the second derivatives of the normal stresses to balance. From beam theory and total energy balance the 4th derivative of the through thickness strain and peeling force must balance to simplify the relationship in Equation 34 [38].

$$G_{\infty}^{*} = \frac{(\sigma_{\infty})^2}{(1+S)} \frac{\omega^2 (1-\upsilon_P^2)}{k E_p} \qquad \text{Equation 41}$$

Here the bending factor (ω) can be approximated by the following relationship:

$$\omega^2 \approx 2 + \frac{3t_p}{2t_R} + \frac{3\beta t_p}{\kappa t_R}\left(1 + \frac{t_p}{t_R}\right) + (1+S)\left(2 + \frac{3t_p}{2t_R}\right)\frac{\bar{z}^2 t_p}{I_t} + \frac{\beta}{\kappa}(1+S)\left(1 + \frac{t_p}{t_R}\right)\frac{\bar{z} t_p^3}{t_R I_t}\left(\frac{3\bar{z}}{t_p} + \frac{1}{2}\right) \qquad \text{Equation 42}$$

$$K_{\infty,rms}^{*} = \frac{\sigma_{\infty}}{1+S}\frac{\omega}{\sqrt{k}} \qquad \text{Equation 43}$$

$$K_{rms}(a) = \frac{\sigma_{\infty}}{1+S}\sqrt{\pi a} F\left(\frac{k}{\omega^2} a\right) \qquad \text{Equation 44}$$

Here the K_{rms} and the energy method used to determine it do not distinguish between membrane and bending contributions, but use a stress intensity reduction factor (F) to determine a maximum stress intensity due to bending, as defined in Equation 45. Here the typical k from Equation 18 is replaced with a one-sided repair spring constant k/ω^2.

$$F(ka) = \sqrt{\frac{1}{\pi \frac{k}{\omega^2} a} TANH\left[\frac{\pi \frac{k}{\omega^2} a}{1 + 0.3\pi \frac{k}{\omega^2} a}\right]} \qquad \text{Equation 45}$$

The above relationships do not separate the membrane and bending terms of the stress intensity. This can be done using the crack bridging model [9] by first taking the inverse

of the c matrix in Equation 33, then replacing the section forces with stress components to get the relationship in Equation 46.

$$\begin{Bmatrix}\sigma_m\\ \sigma_b\end{Bmatrix} = \begin{bmatrix}k_{tt} & k_{tb}\\ k_{bt} & k_{bb}\end{bmatrix}\begin{Bmatrix}u_0\\ \frac{1}{6}\theta_0 t_p\end{Bmatrix} \quad \text{Equation 46}$$

Correcting the relationships for the spring constants presented in [8] and [9] require starting with Equation 33 and performing the inversion operations switches c_{12} and c_{21} that yields the following constants:

$$k_{tt} = \frac{c_{22}}{E_p t_p (c_{11}c_{22} - c_{12}c_{21})} \quad \text{Equation 47}$$

$$k_{tb} = \frac{6c_{12}}{E_p t_p^2 (c_{11}c_{22} - c_{12}c_{21})} \quad \text{Equation 48}$$

$$k_{bt} = \frac{6c_{21}}{E_p t_p^2 (c_{11}c_{22} - c_{12}c_{21})} \quad \text{Equation 49}$$

$$k_{bb} = \frac{36c_{11}}{E_p t_p^3 (c_{11}c_{22} - c_{12}c_{21})} \quad \text{Equation 50}$$

Crack face displacement at the mid thickness of the plate at the center of the crack is expressed as:

$$\frac{E_p t_p}{2\pi}\int_{-a}^{a}\frac{u(\xi)}{(x-\xi)^2}d\xi = N_{yy}(x,0^+) \quad \text{Equation 51}$$

Crack face rotation varies depending on the plate bending theory. Below are the definitions based on Kirchhoff-Poisson and Reissner theories, respectively:

$$\frac{(3+\nu_p)}{(1+\nu_p)}\frac{E_p t_p^3}{24\pi}\int_{-a}^{a}\frac{\theta(t)}{(x-\xi)^2}d\xi = M_{xx}(x,0^+) \quad \text{Equation 52}$$

$$\frac{E_p t_p^3}{24\pi}\int_{-a}^{a}\frac{\theta(t)}{(x-\xi)^2}d\xi+\frac{5}{(1+\nu_p)}\frac{E_p t_p^3}{24\pi}\int_{-a}^{a}L(s)\theta(\xi)d\xi=M_{xx}(x,0^+) \quad \text{Equation 53}$$

Above the function L(s) is a Fredholm kernel with a logarithmic singularity that occurs at s=0 or where the variable s is replaced by a function of r and η that are the normalized locations of x and ξ such that $r=\frac{x}{a}$ and $\eta=\frac{\xi}{a}$. Normalizing locations by the crack length allows integrals to be evaluated between -1 and 1.

$$s=\sqrt{10}(r-\eta)\frac{a}{t_p} \quad \text{Equation 54}$$

The Fredholm kernel, defined below, uses modified Bessel functions of the second kind.

$$L(s)=-\frac{48}{s^4}+\frac{4}{s^2}+4\big(K_2(s)-K_0(s)\big)+\frac{24}{s^2}K_2(s) \quad \text{Equation 55}$$

The modified Bessel functions of the second kind are defined as:

$$K_0(s)=-ln\left(\frac{s}{2}\right)-\gamma_e-\left(\frac{s}{2}\right)^2 ln\left(\frac{s}{2}\right) \quad \text{Equation 56}$$

$$K_2(s)=\frac{2}{s^2}-\frac{1}{2}+\left(ln(2)-\ln(s)-\gamma_e+\frac{3}{4}\right)\frac{s^2}{8}+\left(ln(2)-\ln(s)-\gamma_e+\frac{17}{12}\right)\frac{s^4}{96} \quad \text{Equation 57}$$

First, the Kirchhoff-Poisson method uses the Galerkin method to solve for the unknown function by replacing that function with a series of Chebyshev polynomials of the second kind to get a set of coupled equations that can be solved for the unknown coefficients. Kirchhoff-Poisson does not satisfy the stress free boundary conditions along the crack face. This results in an incorrect stress state near the crack tip and incorrect stress

intensity factors. Reissner's plate theory captures the crack face stress conditions and the bending behavior.

Equation 51 and Equation 53 can be normalized such that they can be expressed in terms of the approximate function h(x) with variables that are normalized over the crack length –a to a.

$$-\frac{1}{2\pi}\int_{-1}^{1}\frac{h_1(\eta)}{(r-\eta)^2}d\eta + k_{tt}ah_1(r) + k_{tb}ah_2(r) = \frac{\sigma_m}{E_p} \qquad \text{Equation 58}$$

$$-\frac{(3+\nu_p)}{(1+\nu_p)}\frac{3}{2\pi}\int_{-1}^{1}\frac{h_2(\eta)}{(r-\eta)^2}d\eta + k_{bt}ah_1(r) + k_{bb}ah_2(r) = \frac{\sigma_b}{E_p} \qquad \text{Equation 59}$$

$$-\frac{3}{2\pi}\int_{-1}^{1}\frac{h_2(\eta)}{(r-\eta)^2}d\eta - \frac{15}{(1+\nu_p)2\pi}\left(\frac{a}{t_p}\right)^2\int_{-1}^{1}L(s)h_2(\eta)d\eta + k_{bt}ah_1(r) + k_{bb}ah_2(r) = \frac{\sigma_b}{E_p} \qquad \text{Equation 60}$$

The above equations must be solved numerically using the Galerkin method by expanding the unknown functions, $h_1(\eta)$ and $h_2(\eta)$, using Chebyshev polynomials of the second kind, and the weighting function $W(x) = \sqrt{1-x^2}$. By normalizing the problem, any function bounded within the range (-1 to 1) can be used to approximate the unknown functions. In this case the functions $h_1(\eta)$ and $h_2(\eta)$ are used to form the bounded function below, which is hyper-singular as $x \rightarrow 1$.

$$\bar{h_i}(x) = \frac{h_i(x)}{W(x)} = \frac{h_i(x)}{\sqrt{1-x^2}} \rightarrow i = 1,2 \qquad \text{Equation 61}$$

Solving these equations numerically requires replacing $h_1(x)$ and $h_2(x)$ with the Chebyshev polynomials, U_i, and the equations are replaced with weighted summations.

$$h_1(x) = W(x)\bar{h}_1(x) \cong W(x)\sum_{i=0}^{n} f_i U_i\,(x) \qquad \text{Equation 62}$$

$$h_2(x) = W(x)\bar{h}_2(x) \cong W(x)\sum_{i=0}^{n} g_i U_i(x) \qquad \text{Equation 63}$$

Using the expansions above, the integrals in Equation 58 through Equation 59 can be simplified to a series of summations relating displacements to membrane and bending stress shown below. The membrane relationship is consistent between Kirchhoff-Poisson and Reissner's plate theory.

$$\sum_{i=0}^{n} \frac{(i+1)}{2} f_i U_i(r) + W(r)k_{tt}a\sum_{i=0}^{n} f_i U_i(r) + W(r)k_{tb}a\sum_{i=0}^{n} g_i U_i(r) = \frac{\sigma_m}{E_p} \qquad \text{Equation 64}$$

The bending relationships for Kirchhoff-Poisson's and Reissner's theory are shown below respectively.

$$\frac{3(3+\nu_p)}{(1+\nu_p)}\sum_{i=0}^{n} \frac{(i+1)}{2} g_i U_i(r) + W(r)k_{bt}a\sum_{i=0}^{n} f_i U_i(r) + W(r)k_{bb}a\sum_{i=0}^{n} g_i U_i(r) = \frac{\sigma_b}{E_p} \qquad \text{Equation 65}$$

$$\frac{3}{2}\sum_{i=0}^{n}(i+1)g_i U_i(r) - \frac{15}{(1+\nu_p)2\pi}\left(\frac{a}{t_p}\right)^2 \sum_{i=0}^{n} g_i \int_{-1}^{1} L(s)W(\eta)U_i(\eta)d\eta + W(r)k_{bt}a\sum_{i=0}^{n} f_i U_i(r + W(r)k_{bb}a\sum_{i=0}^{n} g_i U_i(r) = \frac{\sigma_b}{E_p} \qquad \text{Equation 66}$$

For Equation 64 through Equation 66 convergence was demonstrated with n=32 for small cracks, a≈18mm, and n=64 for larger cracks, a≈180mm, for the Kirchhoff-Poisson's equations with similar behavior noted for Reissner's theory [9]. Because Chebyshev polynomials of the second kind are orthogonal, the above equations can be rewritten as integrals to eliminate the location variable such that a set of coupled equations can be developed to determine the unknown coefficients as a function of only the crack length. First, because the equation is consistent between plate theories, the membrane relationship can be written as:

$$\int_{-1}^{1} W(r)U_j(r)\left(\sum_{i=0}^{n}\frac{(i+1)}{2}f_iU_i(r) + W(r)k_{tt}a\sum_{i=0}^{n}f_iU_i(r) + W(r)k_{tb}a\sum_{i=0}^{n}g_iU_i(r)\right)dr = \int_{-1}^{1} W(r)U(r)\frac{\sigma_m}{E_p}dr \quad \text{Equation 67}$$

The bending relationship for Kirchhoff-Poisson's theory can be rewritten as:

$$\int_{-1}^{1} W(r)U_j(r)\left(\frac{3(3+\nu_p)}{(1+\nu_p)}\sum_{i=0}^{n}\frac{(i+1)}{2}g_iU_i(r) + W(r)k_{bt}a\sum_{i=0}^{n}f_iU_i(r) + W(r)k_{bb}a\sum_{i=0}^{n}g_iU_i(r)\right)dr = \int_{-1}^{1} W(r)U_j(r)\frac{\sigma_b}{E_p}\mathrm{dr} \quad \text{Equation 68}$$

The above integral relationships derived for Kirchhoff-Poisson's theory can be reduced to a set of indexed coefficients and summations [9]. The above equations setup 2n coupled equations that are used to solve for the 2n unknown coefficients. The coefficients, f_i and

g_i, are put back into Equation 62 and Equation 63 with x=1, at the crack tip, to determine the normalized functions h_1 and h_2.

After expanding and simplifying Equation 67 and Equation 68, the following relationships can be combined to form coupled equations.

$$\sum_{i=0}^{n} A_{ij} f_i + B_{ij} g_i = \frac{\pi}{2} \frac{\sigma_m}{E_p} \delta_{0j} \rightarrow i, j = 0,1,2, \dots, n \qquad \text{Equation 69}$$

$$\sum_{i=0}^{n} C_{ij} f_i + D_{ij} g_i = \frac{\pi}{2} \frac{\sigma_b}{E_p} \delta_{0j} \rightarrow i, j = 0,1,2, \dots, n \qquad \text{Equation 70}$$

The coefficients are defined as follows:

$$A_{ij} = \frac{1}{4} \pi (i+1) \delta_{ij} + k_{tt} a \gamma_{ij} \qquad \text{Equation 71}$$

$$B_{ij} = k_{tb} a \gamma_{ij} \qquad \text{Equation 72}$$

$$C_{ij} = k_{bt} a \gamma_{ij} \qquad \text{Equation 73}$$

$$D_{ij} = \frac{3(3+\upsilon_p)\pi}{4(1+\upsilon_p)} (i+1) \delta_{ij} + k_{bb} a \gamma_{ij} \qquad \text{Equation 74}$$

$$\gamma_{ij} = \begin{cases} 0 & \text{i + j = odd} \\ \dfrac{4(i+1)(j+1)}{(\text{i + j + 3})(\text{i + j + 1})(\text{i − j + 1})(\text{j − i + 1})} & \text{i + j = even} \end{cases} \qquad \text{Equation 75}$$

The stress intensity contributions from membrane and bending are directly related to h_1 and h_2, respectively. With x=1 the Chebyshev polynomials, U_i, reduce to a summation of (i+1) for i=0, 1, ...n. The membrane stress intensity at the crack tip can be solved as shown below.

$$K_m(a) = \frac{E_p\sqrt{\pi a}}{2}\bar{h}_1(1) \qquad \text{Equation 76}$$

The Kirchhoff-Poisson's theory bending contribution to the stress intensity in Equation 77 does not result in an appropriate relationship between normal and membrane stress intensity contributions and the location through the plate thickness.

$$K_b(a) = \frac{(3+\nu_p)}{(1+\nu_p)}\frac{3E_p\sqrt{\pi a}}{2}\bar{h}_2(1) \qquad \text{Equation 77}$$

Reissner's plate theory results in a stress distribution similar to that predicted by simple elasticity theory. The Reissner's plate theory bending contribution described in Equation 66 presents a numerical integration challenge with the hyper singular function. The Gauss-Legendre numerical integration scheme was used to perform simple numerical integration.

Wang and Rose followed the work of Joseph and Erdogan [39] to expand and simplify the Fredholm kernel to facilitate numerical integration about the singularity.

$$\sum_{i=0}^{n} C_{ij}f_i + F_{ij}g_i = \frac{\pi}{2}\frac{\sigma_b}{E_p}\delta_{0j} \rightarrow i,j = 0,1,2,\dots,n \qquad \text{Equation 78}$$

The coefficients are defined as follows:

$$C_{ij} = k_{bt}a\gamma_{ij} \qquad \text{Equation 79}$$

$$F_{ij} = \frac{3}{4}\pi(i+1)\delta_{ij} + k_{bb}a\gamma_{ij} - \frac{15}{2\pi(1+\upsilon_p)}\left(\frac{a}{t_p}\right)^2 L_{ij} \qquad \text{Equation 80}$$

Using the method of Joseph and Erdogan, Rose and Wang simplified the expression for L_{ij} by separating the logarithmic singularity out of the equation.

$$L_{ij} = \int_{-1}^{1}\int_{-1}^{1}\left[\mathrm{L}\left(\frac{\mathrm{a}\sqrt{10}}{\mathrm{t_p}}|\mathrm{r}-\eta|\right) - \ln|\mathrm{r}-\eta|\right]\mathrm{W(r)W}(\eta)U_i(\eta)U_j(\mathrm{r})\mathrm{d}\eta\mathrm{d}\mathrm{r} + \alpha_{\mathrm{ij}} \quad \text{Equation 81}$$

$$\alpha_{ij} = \begin{cases} -\frac{\pi^2}{16}(1+4\ln 2) & \mathrm{i=j=1} \\ -\frac{\pi^2}{8}\left(\frac{1}{\mathrm{j}-1}+\frac{1}{\mathrm{j}+1}\right) & \mathrm{i=j>1} \\ \frac{\pi^2}{8(\mathrm{j}-1)} & \mathrm{j=i+2} \\ \frac{\pi^2}{8(\mathrm{j}+1)} & \mathrm{j=i-2} \\ 0 & \text{otherwise} \end{cases} \quad \text{Equation 82}$$

The membrane stress intensity at the crack tip can be solved using Equation 69. For Reissner's theory the bending contribution to stress intensity is shown below

$$K_b(a) = \frac{3E_p\sqrt{\pi a}}{2}\bar{h}_2(1) \quad \text{Equation 83}$$

Numerical integration using Gauss-Legendre quadrature approximates the integration as a summation of the function at specific Gauss points (N) multiplied by weighting functions (w_i) for those Gauss points. Because the location variables, ξ and η, are normalized to the half crack length, the true function space goes from -1 to 1 and there is no need to include the Jacobian relationship.

$$\int_{-1}^{1}\int_{-1}^{1} G(r,\eta)drd\eta = \sum_{i=1}^{N}\sum_{j=1}^{N} G(r_i,\eta_j)w_i w_j \quad \text{Equation 84}$$

This is convenient to setup up using the Matlab Meshgrid function. This sets up a list of all the variable combinations for the double summation, however solution of the

logarithmic singularities was not successfully replicated for this work. The Kirchhoff-Poisson plate theory will be used for comparison purposes later.

Guyt developed an analytical design tool called CalcuRep for aircraft bonded patch repairs based on Rose's model to calculate the stress intensity at the crack tip, stress in the adherend, stress in the skins at the patch tip, characteristic overlap length, shear strain in the adhesive layer, and adherend stresses at the patch edge (i.e. peel stresses). Operating temperature was an important factor in material selection. In this case a pressurized aircraft fuselage, which sees the highest stresses at cruising altitude where the temperature is the lowest, was repaired. This temperature factor is important when selecting materials and their corresponding coefficient of thermal expansion (CTE) [40].

Duong expanded Rose's two stage approach to calculating the patch and skin stresses and strains to include thermo-mechanical loads [7]. This method uses superposition of two sub problems, one with fictitious simple strain fields and one with opposing strain fields and the desired strain. The same response for both mechanical and thermal loads was seen. This allowed the method to combine mechanical, thermal, and post-cure residual stresses to calculate the stresses under the patch at the patch tip and stresses in the patch. For one-sided patches the stress intensity varies through the thickness of the repaired plate. For the analytical approach uses the RMS stress intensity as the maximum value of the through thickness distribution. A modified equation for stress intensity that uses the membrane and bending components of stress intensity was proposed.

$$K_{mod} = K_{max} + (1 - \sqrt{3}) \frac{K_b}{K_{max}} K_{rms} \qquad \text{Equation 85}$$

Here K_{max} and K_{rms} are defined by:

$$K_{max} = K_{mem} + K_b \quad \text{Equation 86}$$

$$K_{rms} = \sqrt{K_{mem}^2 + \frac{K_b^2}{3}} \quad \text{Equation 87}$$

The methods described were implemented in the design code for composite repair of aircraft (CRAS) developed by Boeing and funded by the US Air Force [41].

Governing differential equations common amongst researchers use similar assumptions and classical plate bending theory. Classical plate bending theory differential equation with "w" being the out of plane displacement, "M" being the moment applied to an infinitesimal section, and D being the bending stiffness is defined by Equation 39, although Hart-Smith added a coefficient k_b to decouple the extensional and bending stiffness [4].

$$\frac{d^2w}{dx^2} = -\frac{M}{D} \quad \text{Equation 88}$$

Adhesive shear differential equation [8]:

$$\frac{d^2\tau_A}{dy^2} - \beta^2\tau_A = 0 \quad \text{Equation 89}$$

Higher derivatives for adhesive shear stress [9]:

$$\frac{d^3\tau_A}{dy^3} - \beta^2\frac{d\tau_A}{dy} = 0 \quad \text{Equation 90}$$

The peel stress in the adhesive layer is governed by the following relationship:

$$\frac{d^4\varepsilon_A}{dy^4} - 4\kappa^2\varepsilon_A = 0 \quad \text{Equation 91}$$

Here, κ is defined in Equation 40.

2.3.4 Adhesive Fracture

Yan studied the effect of substrate and adhesive thickness using double cantilever beam (DCB) measured Mode-I fracture toughness with aluminum and steel adherends. The stiffness of the adherends and the thickness of the bond line can change the crack-tip stress fields and the resulting strain energy for ASTM D3433 and E399 methods. Research found that the measured strain energy release rate (Gc) was lower for the steel substrate compared with the aluminum substrate and that the J-integral calculation was less sensitive to substrate material. Two types of test specimens were tested. The first set was made of 7075 aluminum and FM73 adhesive with a bondline thickness of 1 mm and the second set used 2024 aluminum and rubber toughened epoxy with bondline thickness of 0.4, 0.8, 1.0, 1.5, and 1.8 mm [42].

Spinks et. al. reviewed the use of fracture mechanics associated with adhesive joints and the derivation of methods to calculate the stress intensity factors for fracture of adhesive joints. The equations account for the variation in modulus between the adhesive and substrate and distinguishes plane stress versus plane strain. The test specimens and geometry factors presented were for double torsion, tapered double cantilever beam, and single edge notch.

$$G = \frac{P^2}{2B}\frac{dC}{da} \qquad \text{Equation 92}$$

For plane stress homogeneous materials:

$$\frac{dC}{da} = \frac{2B}{P^2}\frac{K_1^2}{E} \qquad \text{Equation 93}$$

For plane strain homogeneous materials:

$$\frac{dC}{da} = \frac{2B}{P^2}\frac{K_1^2}{E}(1-\upsilon^2)$$ Equation 94

Modified for thin adhesives in plane stress, the modulus is for the substrate (E_s):

$$\frac{dC}{da} = \frac{2B}{P^2}\frac{K_1^2}{E_s}$$ Equation 95

Slightly modified for thin adhesives in plane strain:

$$\frac{dC}{da} = \frac{2B}{P^2}\frac{K_1^2}{E_s}(1-\upsilon^2)$$ Equation 96

Johnson et. al. reported testing and analysis efforts studying the fracture mechanics of bonded joints and established effects of long-term exposure to humidity and temperature. The study found that the tensile stress at the bondline tips governs lap joint strength with significant degradation in performance rather than the shear stress when exposed to moisture. A modified Hart-Smith approach was used to calculate shear strain energy per unit bonded area and establish a joint strength limit in addition to looking at SERR and K. Johnson et. al. noted that developing a relationship between K and crack growth rate results in the full development of a plastic zone where K is not valid. However, the thick adherends do not develop a full plastic zone, so comparing the energy, or SERR, resulted in valid crack growth rate under cyclic loading. The other finding from this work was that environmental conditioning can significantly affect long-term bond durability with different adhesive-adherend combinations responding differently to conditioning and processing conditions [43].

2.3.5 Det Norske Veritas (DNV) Efforts

From the early 2000's Det Norske Veritas (DNV) researched cold bonded solutions for repair of Floating Production Storage and Offloading (FPSO) ships for the oil industry because the cost of stopping production of oil, emptying storage tanks, and degassing compartments to perform welded repairs onboard is extremely expensive. During that time DNV developed a recommended practice document for design, fabrication, operation, and qualification of bonded composite repair of steel structure. For the FPSO repair adhesively bonded composite to steel lap joints were tested and analyzed in a symmetric double-lap configuration and on a deep steel I-beam flange in four point bending [44]. Testing showed that the strength of bonded joints does not typically agree with experimental results. This led to the investigation of fracture mechanics based approaches to predict the failure of adhesively bonded joints.

Osnes and McGeorge extended the Tsai, Oplinger et. al. and Hart-Smith bonded double-lap joint equations to an over-laminated double–lap joint, which does not have an explicit adhesive layer, to include shear behavior of the adherend and the interfacial normal-stress distribution through the thickness of the joint. The extension included coupling the normal and shear stresses through the thickness of the adhesive and adherends, where Hart-Smith assumed shear stress to be constant through the thickness in order to decouple the governing differential equations [45].

Osnes and McGeorge further extended theoretical predicitons for bonded double-lap joints to include both the shear behavior of the adherend and the inelastic shear behavior of the adhesive. In this situation the linear shear stress in the adherend from Tsai, Oplinger et. al. was combined with the nonlinear behavior of the adhesive in Hart-Smith.

Several key assumptions were made. First, the adherends behave linear elastically with a linear distribution of the shear and normal stress through the thickness of the adherend. Second, for a double-lap shear joint the shear stress in the adhesive deforms plastically only on the free end of the single adherend. Force equilibrium on infinitesimal elements formed the basis for the governing differential equations, one for the linear elastic regions and a second for the plastically deforming adhesive section. Resulting differential equations form a boundary value problem that has seven nonlinear equations with nine coefficients that must be solved for. Two of the coefficients can be determined experimentally, while a nonlinear numerical solver is required to determine the remaining coefficients. Linear joint design theory and the current inelastic theory were compared against experimental data showing the importance of the inelastic behavior of the adhesive when adhesive joints are loaded close to ultimate capacity [46].

McGeorge presented an appraisal of analytical approaches to calculating fracture of adhesive bonded joints. Testing and analysis efforts focused on steel substrate with adhesively bonded composite patches with both design and testing performed with under-matched stiffness patches. This meant the stiffness of the patch was lower than that of the repaired material; E-Glass, High Modulus Carbon, and Ultra High Modulus Carbon epoxy patches [47]. McGeorge then identified a gap between the total capacity of bonded joints and the failure predictions. The failure predictions produced conservative estimates of the joint capacity because the region of inelastic behavior was limited and only used the materials plastic strain value at failure, which under predicted the ultimate strength of the joint. Theoretical models based on strength of materials indicate bondline thickness drives the joint strength. However, this was not observed in test data reviewed.

Calculating the joint capacity relies on critical plastic strains, that are not entirely material dependent, but are influenced by the design parameters of the joint itself. The overlap length and the stiffness of the adherends and adhesive influence the plastic failure strain. Joints develop plastic strains over a large area of the adhesive, which provides much of the joint capacity. In a long overlap as load increases shear stress reaches a plateau and shear strain increases until fracture. Test data for two bondline thicknesses and three materials indicated a constant apparent adhesive shear yield strength derived from the test data for short overlap lengths. Tension per unit width at the point of overlap fracture was plotted as a function of the joint overlap length. The slope of the line for the “short” overlaps is where the entire bondline is under shear stress and the joint strength is governed by the adhesive yield strength. This slope appeared constant for the three material combinations tested. Based on a limited collection of data, only a weak link was made between the bond line thickness and the total capacity of the joint. Results of the study also indicated that the joint overlap length should be sufficiently greater than the length needed to reach the strength plateau. The simplification for this research was to only look at single-lap shear joints with no out of plane bending. Testing was performed on deep web steel I beams subjected to four point bending such that the cracked and repaired flange were in tension with the cut extending across the flange and into the web, meaning there was not an explicit crack tip. The composite patch extended across the width of the flange and formed an overly long overlap so that the middle region of adhesive was unstressed. The overly long overlap also ensures that plastic stress region at the notch, or crack tip, remains the same during crack growth. Overlap lengths tested ranged from 50 to 200 mm, although the E-Glass on steel configuration was only tested

for 50 and 200 mm overlaps, therefore a true plateau or transition to a plateau was not determined but assumed.

The theory was developed using a method that balances energy and work from elastic deformation, plastic deformation, and fracture energy for crack growth. Derivation of the energy method ignored the shear deformations of the adherends, which were included in the previous work and disconnects the joint capacity from the shear strength of the adhesive. This model is restricted to joints with long overlaps and repair performed on I-beams in four point bending and assumes shear strain through the thickness of the adhesive is constant. One significant simplification to the formulation of the energy balance was to ignore the elastic shear contributions to the energy since plastic shear terms dominate the behavior. The resulting model has no dependency on the bondline thickness because the shear strain was assumed constant. The model does not account for peel stresses, and does not account for out-of-plane loads due to asymmetric joint configuration and loading. The model is also limited to the specific configuration tested, which was for a repaired four point bend beam, with fracture resistance being related to the total energy in the system at time of failure not necessarily the behavior at the crack.

Analytical efforts used updated inelastic fracture mechanics approach for bonded joints as well as use of cohesive zone model to represent the bondline. Short overlap joint strength is proportional to the length and is governed by the adhesive yield stress in shear, while the longer joints achieve a shear stress plateau and develop plastic zones at the ends. Stiffness of the adherends is also important because the critical plastic strain is governed by the joint configuration. An observation from this study was that for minor variations in bondline thickness overall joint strength did not vary significantly. In these

studies the joints were designed such that the strength of the adherends exceeds the fracture load level of the joint. Critical plastic strain criteria depend on adhesive thickness which is not typically supported by experimental results, although only limited bondline thickness, 1 and 2 mm, were tested. Review, application, and comparison of the previous inelastic theory and the fracture energy based approach were performed. Previous experimental work was analyzed, specimens had double sided patch repairs or a cracked beam flange with single sided bonded composite patch in four point bending with the cracked flange in tension. Bondline fracture toughness was represented using cohesive zone modeling that assumes a critical SERR and only Mode II fracture with only 2-D plane strain FEA performed. Fracture load was not affected by a change in the yield shear stress and critical failure criteria were determined by analyzing available lap shear test data for a joint with long overlap. The critical fracture toughness was tuned so that the FEA results correlated with the test data which under predicted results for the E-Glass laminate, but was in good agreement with the carbon patches [44].

Luo and Tong derived equilibrium equations for a symmetric single strap bonded repair using symmetry boundary conditions to butt two single-lap shear joints together. Referencing previous work, Luo and Tong setup the differential equations to solve for the adherend displacements, edge moment factors, and the adhesive stresses that accounted for large deflections and geometric nonlinearity. The adhesive material behavior remained linear and did not account for the nonlinear response or yielding of ductile adhesives. Closed form solutions for the full case were simplified using trigonometric approximations for sinh and cosh functions found for the solution to the differential equations and the resulting constants. The closed form solutions performed very well

when compared with geometric nonlinear FEA of isotropic adherends. With composite adherends the difference between FEA and closed form solution increased. This is likely due to the fact that the composite adherends have a lower transverse, or through thickness, stiffness that was not accounted for in the close form solution but was included in the nonlinear FEA. Including the higher order terms for the adhesive layer is also important and excluded from the formulation using approximations. In addition, classical beam theory used to formulate the equilibrium predicts through thickness stresses poorly. However, the Euler Bernouli theory employed accurately captures the large beam deflections, edge moments, and the shear stress [48].

In the aerospace industry plating is considered thick at 6.35-12.7 mm. Jones and Chiu looked at 2.29 mm aluminum plate and used purely elastic closed form solutions to design composite patched specimens for specimens that did not include any bending by assuming half the solution for a double shear joint, meaning the double shear joint is made up of two single sided patches with half the load applied [6]. Shear energy in the adhesive was calculated using Equation 97 and the SERR in the repaired plate was calculated using Equation 98. Previously derived LEFM solutions provided the stress intensity for a semi-infinite plate with a stress intensity reduction factor based on load sharing between the patch and base plate. The closed form relationships require joint geometry and the normal and shear moduli of both the patch material, repaired plate, and the adhesive.

$$W = \frac{P^2}{16 * E t_r t_a} \qquad \text{Equation 97}$$

$$G = \frac{K_{\infty}^2}{E} + \frac{\sigma^2 L(\frac{t_p}{t_r})}{2E_r(1 + \frac{E_r t_r}{E_p t_p})}$$ Equation 98

For cases with an initial disbond, the strain energy release rate (SERR) was estimated using the stress intensity for the case without a disbond as well as in a case where the disbond is perpendicular to the crack plane with a length of 2L. Stress intensity was predicted using 3D FEA with higher order bricks and wedges at the crack tip, that allowed through the thickness crack tip behavior for a one-sided patch. Jones and Chiu also looked at interaction of cracks under the same patch, and found that at a distance of 5 mm or more the interaction at the surface was less than 10% and interaction at the mid thickness was negligible, although the results may have been due to the mesh being different between the two models. They used Tsai-Hill composite failure for uni-directional plies to predict composite failure, but did not use the nonlinear response of adhesive and designed joints such that the stress in the adhesive was less than that required to cause damage based on linear elastic properties. On important conclusion was that full 3D stress FEA should be performed to design composite patches for structural applications with thicker plate dimensions.

Ouinas et. al. studied the effects of a disbond on the stress intensity at a semicircular edge notch repaired with a composite patch. Failure was predicted using stress intensity factors at the crack tip using the FEA based FRANC2D/L software [49]. Analyses performed used 8-noded serendipity elements with quadratic shape functions applied only on the boundary of the elements. The disbond was found to amplify the stress intensity at the root of the notch. Along with the disbond, fiber orientations for the high stiffness

unidirectional patch were found to influence the stress intensity values at the crack tip and that the thickness of the patch helps attenuate the effect of a disbond.

Muller and Fredell discussed the localized stress concentrations and bending stress associated with multiple composite patches in close proximity to each other on thin plane stress aircraft skin [12]. Analytical studies were done for elliptical and rectangular patch geometries using the 2D axisymmetric plane elastic structures (APES) code to predict the stresses at the patch tip. The total stress concentration factor had contributions from a load attraction, out of plane bending, and thermal coefficient mismatch coefficients in the following relationship:

$$\sigma_{tip} = \sigma_{applied} \cdot K_{t(load\ attraction)} \cdot K_{t(bending)} \cdot K_{t(thermal)} \qquad \text{Equation 99}$$

Each coefficient, K_t, was studied separately. First, patch shape and separation were studied for individual, transversely spaced, and longitudinally spaced repairs with respect to the load direction. APES assumes plane stress with no out of plane displacement, the patch region is a homogenous isotropic material with thickness and stiffness equivalent to the composite section, and the crack has negligible effect on stress concentration magnitude, and is therefore not explicitly modeled. Typical test specimen geometries were analyzed with the specimen width three times that of the repair. The resulting stress concentrations were adjacent to the repair and occurred at the patch tip in the unreinforced substrate. Single patch analytical results compared well with Lekhnitskii closed form solutions for elliptical patches. When analyzing rectangular repairs, high corner stresses were absent due to the lack of through thickness effects from load transfer across the adhesive bondline that cannot be represented in APES. Analytical results indicate that stress concentration magnitude increases with the length to width aspect

ratio and that elliptical patch tips should be clipped to form octagonal shaped repairs. When the row of repairs is transverse to the load line, stress concentrations on the outside edges were unaffected by the repair separation if the absolute separation was greater than one tenth of the width. Stress concentration between patches decreases as separation decreases analogous to transitioning to one large patch. When arranged in a column, or longitudinal to the load, there was little interaction between patches for separation over length ratios greater than 0.5. The stress concentration coefficient increases significantly as s_p/a ratio was less than 0.025. The authors recommended minimizing the patch aspect ratio and maintaining an s_p/a ratio greater than 0.5 to minimize substrate stresses. The neutral line model (NLM) was used to assess secondary bending because APES does not allow out of plane displacements or through thickness stresses. The 2D cross section in the NLM does not account for the bondline, maintains a constant eccentricity, uses classical beam theory without transverse shear stress, and assumes constant stress through the thickness. Secondary bending magnitude was influenced by the patch stiffness and thickness, patch and structure eccentricity relative to the load line, taper architecture, thermally or mechanical residual stresses, and severity or length of the crack. When compared with a FEA solution neither the absolute size of the patch nor the absolute patch separation was important when studying interaction effects. Based on strain compatibility, the load attraction was divided along the patch width and therefore limiting the peak stress.

Baker et. al. presented the results of a comprehensive repair substantiation program for a safety critical repair to an F111 lower wing skin. The repairs were designed and implemented by the Royal Australian Air Force (RAAF). Applications and demonstrator

programs that used composite patches included two instances of stress corrosion cracking in 7075 aluminum used to construct C130 wing stiffeners and weapon longeron flanges of the F111. Patch constituents included unidirectional boron/epoxy prepreg, 0.4mm thick, for the C130 repair and wet lay-up graphite cloth patch with EA9394 epoxy resin and epoxy paste adhesive used to repair the F111. Repairs used glass cloth as the outer ply to protect the highly stressed boron/epoxy plies from UV light and light abrasion, while an aluminum foil secured with PR-1470 sealant was used as a moisture barrier. Repair substantiation required that the analytical formulae used for the repair design were validated by an independent method, resulting material properties were verified through representative article testing, and that structural integrity of the repaired section was restored to a specified level. Validation consisted of an integrated test and stress analysis program followed by full 3D analysis of the cracked wing skin and component level bonded joints. The results of the 3D FE model correlated well with results of a static strain survey of the repaired structure.

The component level test specimens were stiffened wing skin panels that included typical geometrical features. Specimens were wide enough such that crack growth would not be influenced by edge effects yet narrow enough to fit within the purpose-built environmental chamber. The group also tested box specimens representative of the actual wing structure. This allowed full compressive loads of the load spectrum to be applied.

Static strength validation compared the initial unrepaired structure to the design load limit, post-repair performance, and performance at cold and hot temperatures. The initial residual strength of the structure with a 40 mm crack was below the design load limit.

When a bonded patch is applied, the residual strength exceeded the design ultimate load capability [11].

2.4 Analytical and Numerical Fracture Prediction Methods

Although material behavior has been the primary focus of bonded joint design, extending analysis to the crack tip requires fracture mechanics. At higher stress states plastic behavior at the crack tip requires elastic-plastic fracture mechanics (EPFM).

2.4.1 Crack Tip Plastic Zone Estimation

Irwin's approach can be used to estimate the plastic zone radius ahead of the crack tip [50]. Assuming plane stress conditions, the point at which elastic material yields is when the normal stress is equal to the yield stress from the uniaxial tension test. Under plane stress conditions this yields a second order estimate of the plastic zone diameter, r_p, in Equation 100 that is derived by performing a force balance near the crack tip that includes elastic and plastic stresses shown in Figure 2-2. The plane stress first order Irwin plastic zone correction is one half of r_p and the estimated plane strain plastic zone is smaller by a factor of 3.

$$r_p = \frac{1}{\pi}\left(\frac{K_I}{\sigma_{ys}}\right)^2 \qquad \text{Equation 100}$$

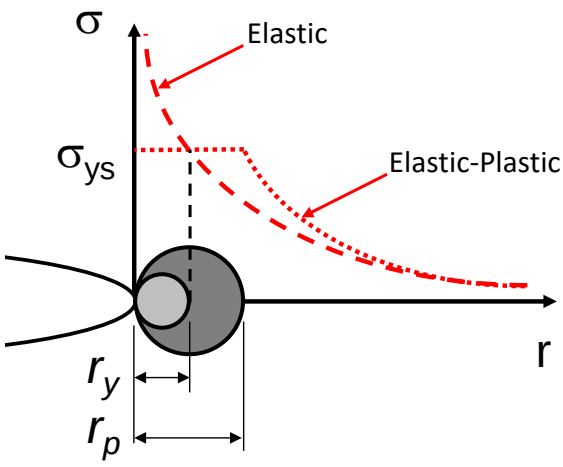

Figure 2-2 First and second order plane stress plastic zone estimates and generalized stress behavior approaching the crack tip singularity along the crack plane.

The above equation provides a 1-D estimate of the plastic zone size on the plane of the crack. For elastic isotropic material the plastic zone shape can be estimated relative to the crack tip by setting the von Mises equivalent stress equal to the uniaxial tensile yield stress. The equivalent stress is a function of the principle stresses, that for Mode I loading can be approximated with singular stress fields based on the Mode I stress intensity. Setting the equivalent stress equal to the yield stress results in an expression for the plastic zone as a function of the angle from the crack plane. For plane stress the cylindrical coordinates of the plastic zone boundary at a prescribed level of mode-I stress intensity, K_I, are related using Equation 101 and under plane strain conditions are related using Equation 102.

$$r(\theta) = \frac{1}{4\pi}\left(\frac{K_I}{\sigma_{ys}}\right)^2\left[1 + \cos\theta + \frac{3}{2}\sin^2\theta\right] \qquad \text{Equation 101}$$

$$r(\theta) = \frac{1}{4\pi}\left(\frac{K_I}{\sigma_{ys}}\right)^2\left[(1-2\nu)^2(1 + \cos\theta) + \frac{3}{2}\sin^2\theta\right] \qquad \text{Equation 102}$$

Mode I fracture testing of 5052-H32 aluminum was not performed and test data for the 2.29 mm thick plate was not readily available in published research. According to ASTM plane strain fracture testing requirements, Equation 103 can be used to estimate the minimum plate thickness (B) required to measure critical K_{Ic}. The minimum thickness ranges from 86 to 155 mm. This places the 2.29 mm CCT specimen outside linear elastic fracture mechanics behavior. This indicates that the test data produced will not produce a valid linear elastic K_{Ic} for these specimens. For valid elastic-plastic conditions the dimensions need to be larger than 25 times the crack opening displacement, which can be modified to relate crack tip opening displacement (δ_t) to K_I, E, and σ_{ys} by assuming linear elastic material behavior and small deformations in Equation 104. Critical sizes can be estimated by converting J to K, where E^* is simply E for plane stress and $E/(1-\upsilon^2)$ for plane strain resulting in a critical thickness (B), ligament (L), or crack length (a) between 1.2 and 1.4 mm.

$$a, B, (W-a) \geq 2.5\left(\frac{K_I}{\sigma_{ys}}\right)^2 \qquad \text{Equation 103}$$

$$a, B, L \geq 25\delta_t \cong 25\frac{J}{\sigma_{ys}} \cong 25\frac{K_I^2}{E^*\sigma_{ys}} \qquad \text{Equation 104}$$

Accurately locating the crack tip when studying DIC data is critical for studying displacement and strain fields. The technique used assumes a parabolic shape to the vertical displacements (V) approaching the crack tip, as shown in Figure 2-3. Displacements are extracted along parallel paths as close to the crack plane as possible. The crack tip can be located by fitting the V-displacement data to a parabola using a least squares fit [51]. The apex of the parabola fit is a good approximation of the crack tip

location. Care must be taken when selecting the largest X-location to include when approaching the crack tip. Although theoretical displacements close to the crack tip are assumed to approach zero, errors due to speckle pattern and local material behavior can be difficult to fit. One must visually study the data points and determine where they no longer fit a parabolic shape. Bruck included a more complex fit of the data, but concluded that the simple parabolic fit was sufficient to locate the crack tip.

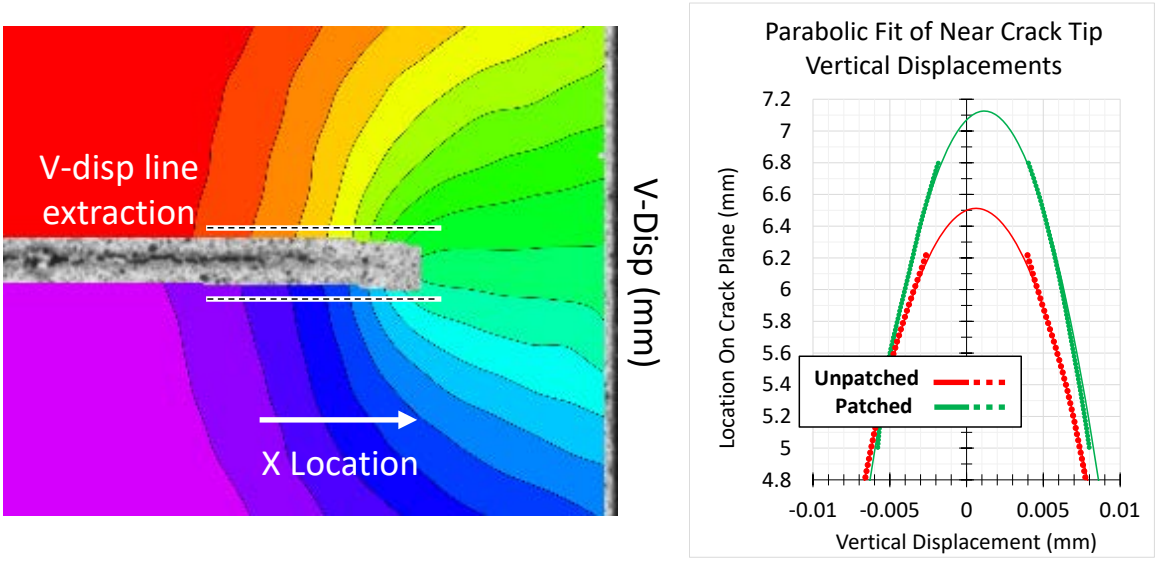

Figure 2-3 Parabolic fit of vertical displacements to locate the crack tip.

2.4.2 Linear Elastic Fracture Mechanics

Finite dimensions of standard fracture mechanics test specimens require further refinement from the infinite and semi-infinite plate assumptions used to develop analytical expressions for the crack tip stress intensity. Assuming a stress concentration at the crack tip with axial stress lines diverting around a crack, the actual stress concentration changes as the relationship between the crack length and specimen width change. To develop an approximation for this relationship polynomial fits of FEA results were developed for common test specimen geometries. The basic Mode I stress intensity

relationship between load, specimen width, and thickness combined with a stress concentration factor in Equation 105 replaces the infinite plate form using far-field stress and crack length. For unpatched CCT specimens Equation 106 is the stress concentration factor [50].

$$K_I = \frac{P}{B\sqrt{W}} f\left({}^{a}/_{W}\right) \qquad \text{Equation 105}$$

$$f\left({}^{a}/_{W}\right) = \sqrt{\frac{\pi a}{4W} sec\left(\frac{\pi a}{2W}\right)}\left[1 - 0.025\left(\frac{a}{W}\right)^2 + 0.06\left(\frac{a}{W}\right)^4\right] \qquad \text{Equation 106}$$

Assuming linear elastic materials the J-integral simplifies to the Mode I SERR (G) and can both be related to the stress intensity using the equations and relationships below.

$$J = G_I = \frac{{K_I}^2}{E'} \qquad \text{Equation 107}$$

$$E' = \begin{cases} E & Plane\ Stress \\ {}^{E}/_{(1-\upsilon^2)} & Plane\ Strain \end{cases} \qquad \text{Equation 108}$$

2.4.3 Extended Finite Element Method Fracture

Fracture prediction methods, such as cohesive zone and virtual crack closure methods, do not arbitrarily predict crack growth or growth direction and are dependent on the FEM geometry and mesh configuration. Development of the extended finite element method (XFEM) provides a foundation for predicting the volumetric response of materials using an adaptive grid work of virtual nodes that can be disconnected to create a 3D crack front within the element during the analysis [52]. The 3D stress state is used within the XFEM element to calculate stress state and SERR mode mix at points along the crack front. The

virtual crack closure technique (VCCT) is used to predict the stress intensity factor at the crack tip and the stress state is used to determine the direction of crack growth.

2.4.4 Stress Intensity Approach

Generalized stress singularity approach was used to predict failure of adhesively bonded joints [53]. Van Tooren argues for a combined stress intensity approach for adhesive joints because the singularity caused at the bimaterial interface geometry and material stiffness ratio drive design decisions and cannot be determined by the stress based approach. Rather than using a stress based failure criterion for singularities one should look at the severity of the stress field at a singularity by relating the stress intensity factor, number of stress singularity terms, geometric stress concentration function, the distance from the singularity, and the order of the singularity because the critical stress intensity was found to not govern failure alone.

A common definition of the stress field at the crack tip where the $Hf_{ij}(\theta)$ term is similar to HRR terms that include J, dimensionless stress function, and an integration constant. Here the singularity order (λ), when compared to HRR fields, must be a function of the material hardening coefficient (n).

$$\sigma_{i,j} = H\frac{1}{r^{\lambda}} f_{i,j}(\theta) \qquad \text{Equation 109}$$

The criticality of the stress state depends on the stress intensity factor, the stress gradient, and the order of the stress singularity. Typical stress intensities are a material and geometry related property and are defined at a singularity order of zero with only normal stress, or perfectly plastic according to HRR description of the stress state. As the stress gradient increases near the crack tip the allowable stress intensity decreases. Failure then

occurs when the singularity order and the stress intensity value intersect the curve connecting material failure stress limit (plastic $\lambda = 0$) to the critical linear elastic stress intensity ($\lambda = 0.5$). Van Tooren et. al. used detailed FEA of a single lap bonded joint to predict the stress gradient at three angles radiating from the singularity. A least squares approximation of the calculated stress points is used to determine the order of the singularity. Plasticity, when included, reduces the order of the singularity. FEA results relate the stress gradients in critical areas to the stress singularity function and singularity order to material test data plotted on a failure curve. The approach was performed as a post-processing step of FEA results.

2.5 HRR Fields and the J-Integral

Hutchinson, Rice, and Rosengren (HRR) [54, 55, 50] established the J-integral method and the stress, strain, and displacements fields to describe inelastic crack tip behavior for ductile metals. Crack tip behavior of the unpatched CCT can be predicted using LEFM and EPFM where the singular stress behavior at the crack tip is governed by $1/\sqrt{r}$ and $(1/r)^{1/n+1}$, respectively. Generalized near tip plastic zone stress states for increasing load, left to right, are shown in Figure 2-4 with assumed true stress behavior as a function of radius. Ductile materials exhibit small scale yielding (SSY) at the crack tip singularity, where LEFM and EPFM solutions exist, to elastic-plastic behavior where only EPFM solutions are valid at higher loads. Moving from the far-field in to the crack tip, material behavior is initially governed by LEFM, K dominated region. As the plastic zone develops, the stress field transitions from K dominated to a J-dominated region where elastic-plastic behavior can be described by HRR fields. Validity of the HRR fields are limited to semi-infinite crack, small deformations, no unloading, and loading that is

proportional in all direction and does not account for crack tip blunting (large displacements). Continuing to approach the crack tip, large strains develop. Here true behavior deviates from HRR fields and must be described by more advanced two parameter crack tip fields or material failure models that incorporate crack tip blunting and material plasticity [56, 57, 58, 59].

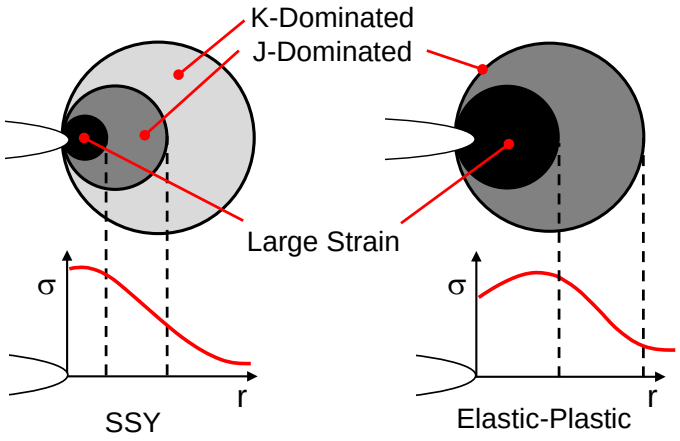

Figure 2-4 Generalized crack tip stress behavior from SSY to elastic-plastic

For linear elastic behavior inside the K dominated region the stress and displacement fields are governed by $1/\sqrt{r}$ and $\sqrt{r}$, respectively. The fields are generally described by equations Equation 110 and Equation 111 below, where r and θ are defined in and the functions *A* and *B* are sine/cosine relationships with *B* including the material shear modulus. True calculations of these values will be replaced by a generic fit to the DIC measured field data as a simplified means to compare measured fields with fracture mechanics theory. This paper focuses on the measured displacement fields and the logarithmic displacement as a function of *r*.

$$\sigma_i(\theta) = A(\theta) \left. K_I \right/ \sqrt{r} \qquad \text{Equation 110}$$

$$u_i(\theta) = B(\theta)K_I\sqrt{r} \qquad \text{Equation 111}$$

Inside the J-dominated region elastic-plastic material behavior is included in the formulations. The resulting stress and displacement fields are governed by $(1/r)^{1/n+1}$ and $(r)^{1/n+1}$, respectively where *n* is the Ramberg-Osgood hardening coefficient of the material. Comparing the equations, when *n*=1 the material behavior is linear-elastic and reduces to $1/\sqrt{r}$ and $\sqrt{r}$ singularities seen in Equation 110 and Equation 111. When perfectly plastic, *n* approaches ∞ where the stress-strain behavior has a slope of zero. The functions *C* and *D* in the below equation include elastic-plastic material parameters along with the HRR integration constant (I_n) and dimensionless functions of stress ($\tilde{\sigma}_{ij}(\theta, n)$) and displacement ($\tilde{u}_{ij}(\theta, n)$) that are combined into one variable and visually fit to measured data. Once fit, the values of the constant and functions can be compared with known values [50]. Using *n*=9.9 and taking the natural log of the HRR displacements as a function of *r* yields a slope of 0.09 for HRR fields and with *n*=1 the slope is 0.5 for K fields.

$$\sigma_{ij}(\theta, n) = C(\theta, n)\left(\frac{J}{r}\right)^{1/n+1} \qquad \text{Equation 112}$$

$$u_{ij}(\theta, n) = D(\theta, n)(J)^{n/n+1}(r)^{1/n+1} \qquad \text{Equation 113}$$

Although not explicitly used in this work, the functions *C* and *D* are listed below:

$$C(\theta, n) = \sigma_0\left(\frac{E}{\alpha\sigma_0^2 I_n}\right)^{1/n+1}\tilde{\sigma}_{ij}(n, \theta) \qquad \text{Equation 114}$$

$$D(\theta, n) = \frac{\alpha\sigma_0}{E}\left(\frac{E}{\alpha\sigma_0^2 I_n}\right)^{n/n+1}\tilde{u}_{ij}(n, \theta) \qquad \text{Equation 115}$$

To characterize the full-field crack tip behavior, DIC [60] can be used to measure surface displacements ahead of the crack tip. Initially used for local linear elastic material behavior [61, 62], inelastic material behavior can be included in the J-integral calculation [63, 64, 65]. Research in the plastic zone development under monotonic loading appears to be limited to typical single material fracture mechanics specimens [66, 67]. Dadkhah and Kobyashi reported displacements and J-integral data with comparison to the HRR displacement fields under static and fatigue crack growth conditions on thin 5052-H32 sheet [68, 69]. Additional work with 6061-T6 and various tempers of 2024 aluminum have also been reported [57, 70].

The J-integral is a path independent contour integral that describes the change in potential energy as the crack area increases, or crack growth occurs [50]. Formulation of the J-integral requires either a plane strain or plane stress assumption for the behavior of the material through the thickness at the crack tip.

$$J = \int_{\Gamma} \left(w dy - T_i \frac{\partial u_i}{\partial x} ds \right) = \int_{\Gamma} \left(\int_0^{\varepsilon_{ij}} \sigma_{ij} d\varepsilon_{ij}\, dy - \sigma_{ij} n_j \frac{\partial u_i}{\partial x} ds \right) \qquad \text{Equation 116}$$

Here w is the strain energy density, T_i is the traction vector normal (n_j) to the path Γ with infinitesimal segments along that path (ds). Displacements (u_i) along the path and displacement data are located in xy space, such that i is associated with the x-direction and j is associated with the y-direction. From the DIC processing U and V are in the x and y-directions respectively. For aluminum, we assume a power-law hardening behavior consistent with the Ramberg-Osgood equation to describe uniaxial material behavior.

$$\frac{\varepsilon}{\varepsilon_0} = \frac{\sigma}{\sigma_0} + \alpha \left(\frac{\sigma}{\sigma_0} \right)^n \qquad \text{Equation 117}$$

Basic review of J-integral measurement methods was performed by Lu et. al., who determined that measuring the hysteresis energy method was comparable to the ASTM E813-81 method and avoided the issue of crack blunting [71]. With the use of DIC to measure full field surface displacements, multiple numerical methods to measure the J-integral value using a single test specimen have been developed. Use of computer vision, or DIC, was developed by Sutton et. al. in the late 80's and used to investigate surface strain behaviors in polymethylemthacrylate (PMMA), or plexiglass, [61, 62]. Sutton et. al. also described practical methods for performing DIC measurements, from selection of optics to techniques and materials to make speckle patterns [60]. Bruck presented a relationship for the path wise displacement gradients and material constants in Equation 118.

$$J = \frac{G}{2}\int_{\Gamma}\left[\left\{k_1\left(\frac{\partial v}{\partial y}-\frac{\partial u}{\partial x}\right)\left(\frac{\partial u}{\partial x}+\frac{\partial v}{\partial y}\right)+\left(\frac{\partial u}{\partial y}+\frac{\partial v}{\partial x}\right)\left(\frac{\partial u}{\partial y}-\frac{\partial v}{\partial x}\right)\right\}dy + \left\{2\left(\frac{\partial u\partial u}{\partial x\partial y}+k_2\frac{\partial u\partial v}{\partial x\partial x}+k_1\frac{\partial v\partial v}{\partial x\partial y}\right)\right\}dx\right] \quad \text{Equation 118}$$

Here the constants are material shear modulus (G) and Poisson's ratio relationships for either plane strain or plane stress conditions (k_i).

$$plane\ strain: k_1 = \frac{2(1-\nu)}{1-2\nu}, k_2 = \frac{1}{1-2\nu} \quad \text{Equation 119}$$

$$plane\ stress: k_1 = \frac{2}{1-\nu}, k_2 = \frac{1+\nu}{1-\nu} \quad \text{Equation 120}$$

For the present work the displacement gradients along the path can be extracted as the displacement gradient tensor (F_{ij}), where the 2D surface i=1,2 and j=1,2 (where 1=x and 2=y directions).

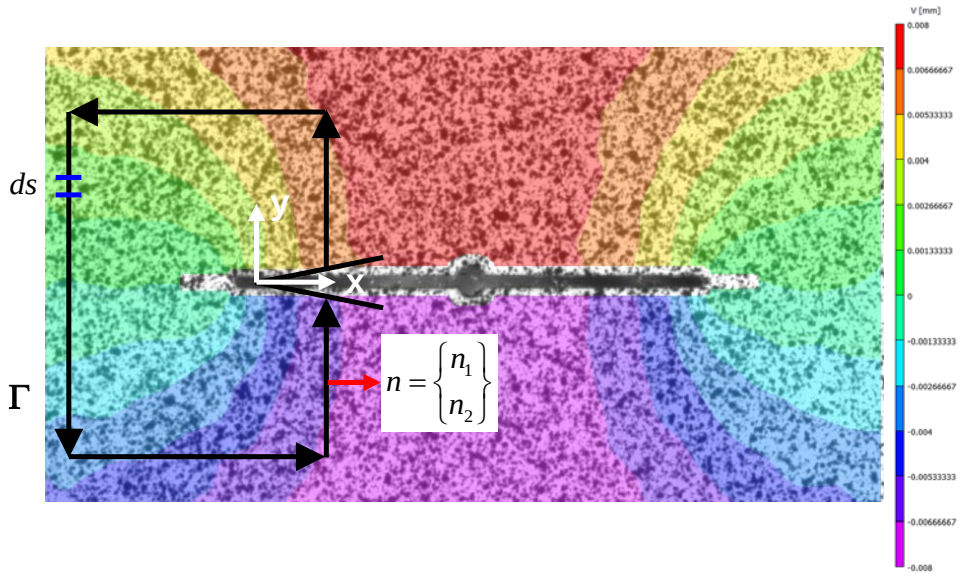

Figure 2-5 Coordinate system, directions, and patch for rectangular J-Integral.

Work by Hamam et. al. and Becker et. al. compared similar methodology as well as a measurement and finite element analysis hybrid method that used the surface displacement fields to inform nodal displacement in a finite element model [67, 65]. The hybrid method is limited to assuming plane strain conditions because measuring the surface strains assumes constant displacement based behavior through the thickness of the material.

Three methods for determining the J-integral were investigated and compared for power-law hardening material; the path integral, domain integral, and least squares fit of HRR fields methods [63]. All methods adequately determined the J-integral for A1050 aluminum, in the pure and annealed state.

2.6 Digital Image Correlation

DIC is a method that measures surface displacements and predicts displacement gradients and strains using shape functions optimized to match the change from one image to the next (Sutton, Orteu et al. 2009). A classic correlation function is the sum of squared

difference (SSD) of individual pixel gray scale values within the subset from the reference image to the deformed image with the addition of 2D displacements. A nominal speckle pattern, subset size, and pixel characterization are shown in Figure 2-6. The correlation function assigns a numerical value to the quality of the subset correlation between images such that a low value indicates good correlation. The image can be searched to minimize the value of the correlation function and locate the subset and determine where the subset moved relative to the reference. The subset shape functions, correlation algorithms that use a continuous spline to represent pixel locations within the subset, can then be compared to the reference subset. A correlation function is used to compare measured and predicted distortions, then the spline function coefficients are optimized to minimize the correlation function. Deformation results are then assigned to data points defined by the step size using a weighting function across the subset, typically a center-weighted Gaussian function. Displacement gradients and strains are then determined from the shape functions and smoothed across a set of data points. Strains are smoothed across the data points using a 90% center-weighted Gaussian decay filter. Smoothing can be accomplished with the filter settings or in a secondary smoothing step, which applies the decay filter to the results. Care must be exercised in selection of subsets, step sizes, filter sizes, and smoothing filters in order to appropriately capture peaks and gradients on the surface.

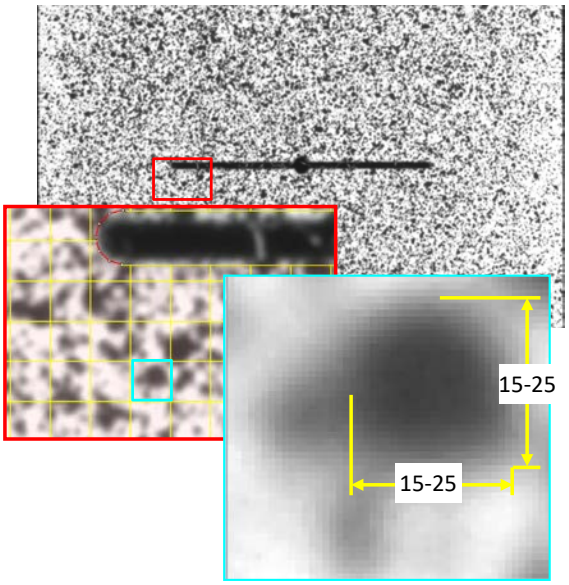

Figure 2-6 Nominal speckle pattern developed with layered spray paint and subset definition with general speckle characteristics used for DIC.

Acciaioli et. al. investigated the practicality of using DIC for small-magnitude strain fields, where strain magnitudes are less than 0.1%, or 100 με with typical DIC applications looking at strain magnitudes greater the 8.0%, or 8,000 με. Minimizing error and achieving practical results use subsets of 60x60 pixels with speckle sizes on the order of 5 pixels and subset overlaps of 50-75%, which confirms Correlated Solutions recommended step size of $1/4^{th}$ the subset size. Even in strain data set sizes of 900 points, noise levels of up to 40 με did exist [72]. Confirming best practices guidance for setup and processing, Balcaen et. al. performed a detailed study of DIC setup and processing parameters using an image simulator. Balancing all the factors associated with DIC measurements is required to determine which method to use. Both 2D and 3D uncertainty quantification were debated with the focus being on the later [73].

For the current research, 2D DIC was selected to simplify data acquisition and processing and with the assumption that speckle pattern movement relative to the depth of field (DoF) was not significant enough to warrant the use of Stereo DIC. Consideration was

also given to the additional sources of uncertainty and error from calibration and camera triangulation.

The International Digital Image Correlation Society published recommendations for DIC setup and processing information reported so that critical aspects of the DIC setup are captured. From the focal distance, aperture size, image sensor type, camera model, lens setup, resulting image size, and the AOI used all contribute to the quality of the DIC data produced [74].

3 Research Plan

To study the interaction of the crack tip plastic zone and increased load and displacement capacity observed in large scale testing, a building block approach was used. From a global response view, small scale CCT specimens were used to study the evolution of the plastic zone with full field DIC data, to develop a prediction methodology based on small scale results. That prediction methodology was then applied to existing large scale global response data as full field data does not exist for the large scale response.

Global response was supported with the measurement of constituents and material systems used in the baseline aluminum and composite patched aluminum specimens. Basic material properties for the 5052-H32 aluminum, pre-fabricated E-glass/epoxy laminate, and the West Systems WestSix10 marine adhesive of the small scale center crack tension specimens, and the Gougeon Brothers Inc. Pro-Set M1002/M2046 resin system and composite patch laminate of the large scale center crack tension specimens was developed.

Crack tip plastic zone development and evolution was investigated at small scale with and without a composite patch. Small scale CCT specimens were tested at approximately $1/3^{rd}$ the large scale specimens with material selection based on availability and ease of specimen manufacturing. The large scale aluminum alloy was not available at the 2.29 mm thickness to maintain scale and was replaced with readily available 5052-H32 alloy. Hand lamination of individual small scale specimens was not feasible, therefore pre-fabricated laminate plates adhesively bonded with a marine grade epoxy from West Systems was selected.

Full field data using 2D DIC was required to measure and compare the displacement and strain fields during evolution of the crack tip plastic zone with LEFM and EPFM theory. Comparison to theory identified regions of valid response prediction and was the basis for identifying specimen behavior during stages of failure. Connecting measured and observed specimen response to failure response resulted in a simplified failure prediction methodology.

Research Outline:

- Developed constituent properties for small and large scale composite patch repaired plates.
- Performed detailed failure mechanism identification from large scale testing.
- Designed and analyzed small scale center crack tension specimens to study evolution of the crack tip plastic zone.
- Characterized local crack tip behavior using DIC for small scale specimens monotonically tested to failure.
- Using small scale DIC and FEA results, developed a numerical analysis based method to predict ultimate tensile capacity of the patch repaired system.
- Validated methodology using small and large scale CCT data.
- Formed conclusions about the use of the proposed methodology.
- Made recommendations for future research and development.

4 Characterization of CCT Specimen Constituents

This section discusses the testing performed to develop mechanical properties and behaviors for the constituents of the small and large scale composite patch repairs. Linear elastic tensile modulus and strength of the laminates and the elastic-plastic properties of the adhesive, resin, and aluminum are documented.

4.1 Materials Selected for Small and Large Scale CCT Testing

Materials selected for CCT specimen manufacturing are detailed in this section. The large scale CCT specimens match materials used for U.S. Navy shipboard repairs. The small scale specimen materials were selected to have similar basic behaviors as the shipboard patch but be 1/3rd the size of shipboard repairs to facilitate simple data acquisition, manufacturing, and testing in readily available test frames.

4.1.1 Small Scale CCT Specimen Materials

Aluminum selected for the small scale CCT specimens was based on readily available plate thickness that allowed a 1/3rd scale from the large scale specimens. A nominally 2.29 mm thick marine grade 5052-H32 aluminum was selected because the typical 5456-H116 was not readily available at that thickness. For ease of manufacturing a commercially available two part marine adhesive, WestSix10, was selected for bonding the prefabricated 1.27 mm thick 0/90 E-Glass epoxy laminate. Origin and manufacturer of the laminate were not available. The laminate, or composite patch, was bonded to the cracked aluminum plate with a nominally 0.6 mm thick bondline, that was controlled using 0.024 inch diameter steel welding wire.

4.1.2 Large Scale CCT Specimens Materials

Marine grade aluminum plate selected for the large scale test specimens was 6.35 mm thick 5456-H116 alloy. A rubber toughed epoxy resin system, M1002, from Pro-Set was selected based on the manufacturer advertised bond strength and toughness. The Pro-Set M1002 was mixed with Pro-Set M2046 slow hardener. Following shipboard installation procedures, the notch and crack were sealed using reinforced epoxy putty consisting of M1002 resin mixed with Pro-Set M2043 fast hardener, fume silica, and 1/32" milled glass fibers. Both resin systems were mixed by volume according to the manufactures recommendations.

The standard large scale composite patch laminate consists of a resin rich 325 g/m^2 Hexcel 7500 style 1:1 plain weave (PW) fabric, a 300 g/m^2 7781 style 8-harness satin (HS) weave fabric, and stitch bonded unidirectional fiber fabric with 410 g/m^2 biaxial ±45 (BX) and 610 g/m^2 0/90 (LT) fiber orientations. The 7500 PW fabric had a warp to fill fiber count of 16:14, while the 7781 had a fiber ratio of 57:54. The higher fiber count of the 8HS weave results in a tighter weave with an aerial weight only 25 g/m^2 lower. The location and orientation of the unidirectional fibers will be designated by T^0 and T_0 for top or bottom of the ply. With eight plies of material, the laminate schedule was [PW/BX^{+45}/LT^0/ BX^{+45}/ BX_{+45}/LT_0/ BX_{+45}/HS].

Large scale laminates were made using a vacuum consolidation process, which consists of wetting out and placing each glass ply manually, a peel ply, perforated film to control resin bleed, two plies of bleeder cloth to provide vacuum paths and absorb excess resin removed during consolidation, a vacuum bag over the part, and a vacuum source to maintain 10 inHg of vacuum over the entire part [75]. Standard room temperature nylon

vacuum bagging material was used, with Airtech Econoply E heat scoured (HS) polyester peel ply, Airtech WL5200 P3 fluoropolymer perforated release film, and Airtech 4 oz Econoweave 44 bleeder fabric.

4.2 Data Acquisition and Standard Material Testing Methods

Material coupons and CCT specimens were tested in both University of Maryland engineering labs and in the Code 65 Composites Lab at the Naval Surface Warfare Center's Carderock Division at one environmental condition; Room Temperature Dry (RTD). RTD is defined as the ambient temperature of a temperature controlled lab with the as-manufactured moisture content. Relative Humidity (RH) was not explicitly controlled, however, typical lab conditions are 20-22°C with approximate RH of 60-65%. Testing methods performed and definitions used were consistent with composite testing guidelines defined by the FAA [76] and Department of Defense (DoD) [77].

4.2.1 Data Acquisition

Full field surface measurements were made on the small scale CCT specimens using DIC. Correlated Solutions Vic2D V6 software was used to process the speckle images and correlate images and machine load [78]. Gray-scale digital images were divided into subsets of pixels which are tracked from a base displacement state to a deformed state. The gray-scale pattern was correlated between images with a direct measurement of global displacement and rotation of the subset. The confidence interval for correlated images provided a measure of how well the software could match the subset gray-scale pattern between images; a sigma value > 1% indicated decreasing confidence in the correlation and an increase in error. Within the subset, shape functions were used to approximate the geometric changes of the subset. The shape function parameters were

determined by minimizing the sum of the squares error between the measured and predicted subset shape. These shape functions were then used to calculate strains and displacement gradients for each subset. The strain value extracted from the DIC software for this project was the 2D Lagrangian formulation shown in Equation 121.

$$\varepsilon_{ab} = \frac{1}{2}\left(\frac{\partial u_j}{\partial U_a}\frac{\partial u_j}{\partial U_b} - \delta_{ab}\right) \quad \text{Equation 121}$$

Full field 2D von Mises strains were calculated by the Vic2D software from directional strains and Equation 122. Von Mises yield criterion is the foundation of Irwin's plastic zone radius approximation as well as the formulation of the plastic zone shape approximations that will be discussed in later sections.

$$\varepsilon_{vm} = \sqrt{\varepsilon_1^2 - \varepsilon_1\varepsilon_2 + \varepsilon_2^2} \quad \text{Equation 122}$$

For small scale CCT testing images of the free aluminum surface were captured using an 8.8MP (4096 x 2160 pixel resolution) Point Grey Flea FL3-U3-88S2C-C digital camera with a Sony IMX121 complimentary metal-oxide-semiconductor (CMOS) sensor and a Tamron 28-80mm f/3.5-22 lens. Typical focal length was close to 80 mm with an f-stop between 8 and 11 depending on the speckle pattern. Lighting was provided by a pair of 250W halogen lights. Care was taken to position lighting equidistant from the specimen as well as the camera with enough space that heat imparted to the specimen or camera was minimal. The camera lens was positioned and set resulting in a nominally 28.2mm x 14.9mm overall field of view (FOV). Initial depth of field (DoF) was set so the free surface remained in focus for the range of out-of-plane deflection experienced minimizing bias error due to movement relative to the camera lens. Estimated out of

plane displacement is the difference in the load line through the aluminum plate and the aluminum/composite centroid and is maximum at the center of the notch on the free surface with a magnitude of 0.36 mm and was assumed to not warrant the use of 3D DIC. The speckle pattern was achieved using a base of flat white spray paint with light passes of flat black spray paint. To achieve the smallest consistent speckles an improvised paint booth was fogged with black spray, then the specimen was placed in the space for the small floating paint particles to settle on the white surface. This process was repeated until sufficient gray scale information was present in the image. The small scale single sided CCT test setup is shown in Figure 4-1 with gripped specimen, free surface FOV, and specimen orientation shown in Figure 4-2. Typical FOVs and speckle patterns are shown in Figure 4-3.

Figure 4-1 2D DIC Setup for the 4-Post 25kN MTS Frame for Round One.

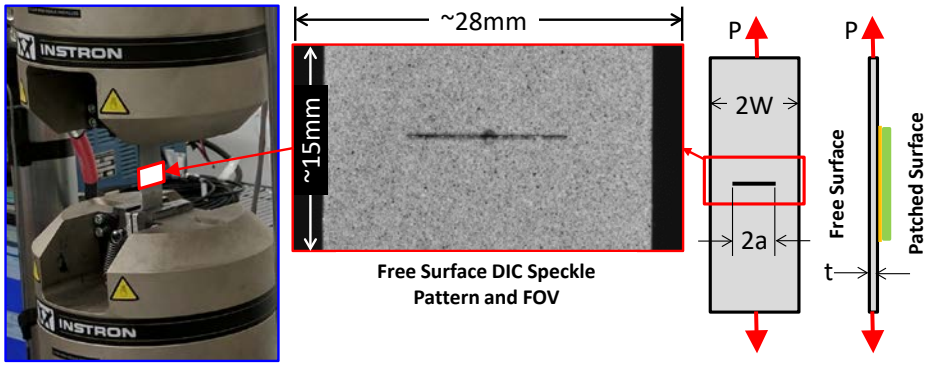

Figure 4-2 Small scale CCT test and DIC configuration (L), FOV (C), and specimen geometry and orientation (R).

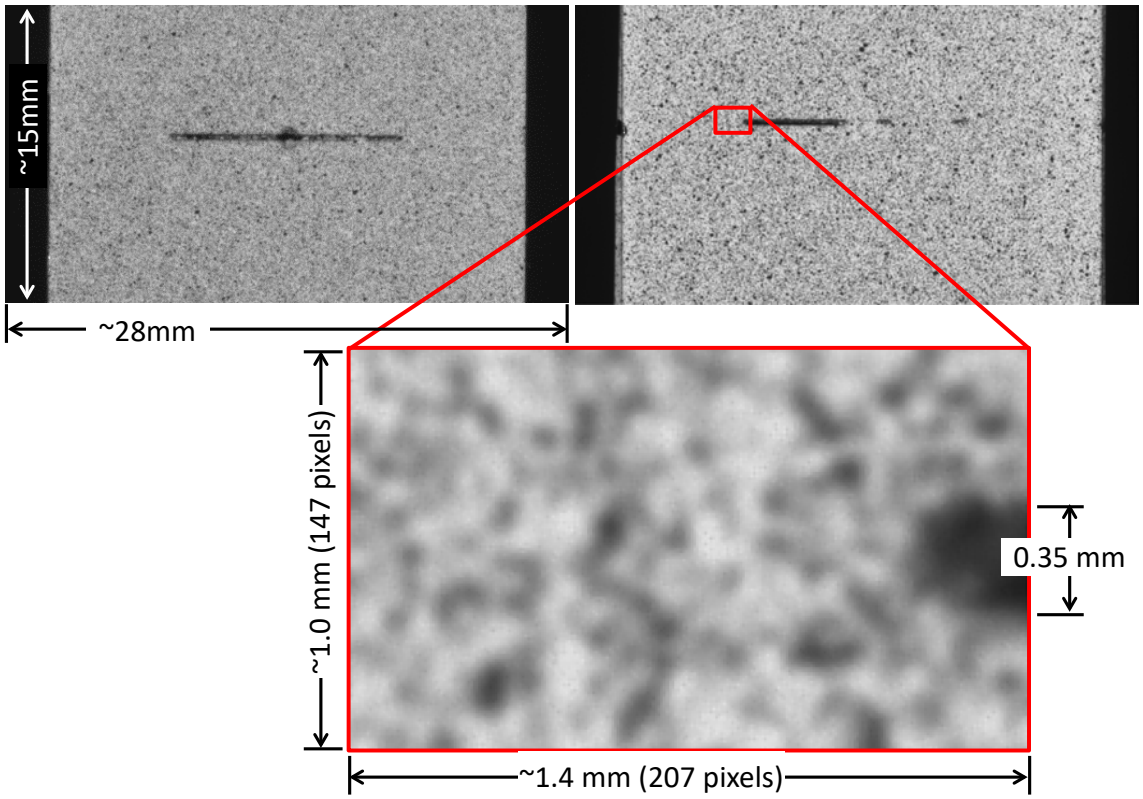

Figure 4-3 Typical DIC Speckle Patterns From Initial CCT Testing.

The second round of CCT testing used the same high resolution setup on the aluminum free surface. The camera lens was positioned and set resulting in a nominally 26.8 x 14.1 mm overall FOV. Available equipment limited data acquisition on the composite patch side to a low resolution setup. Images of the composite patch surface were captured using a 1.3MP (1328 x 1024 pixel resolution) Point Grey Flea FL3-U3-13S2M-CS digital camera with a Sony IMX035 CMOS sensor and a Tamron 28-80mm f/3.5-22 lens. Again, typical focal length was close to 80 mm with an f-stop of between 11 and 16 depending on the speckle pattern. Lighting was provided by a pair of low power Bestlight64 LED camera lights with variable brightness from 5500-6500K. The camera lens was positioned and set resulting in a nominally 23.0 x 18.2 mm overall FOV. Again, both cameras were set such that the surface remained in focus for the range of out of plane deflection

experienced relative to the camera lens. This varied somewhat as lighting, zoom, and focus were adjusted for each specimen. Speckle pattern on the back side was applied in the same manner described above.

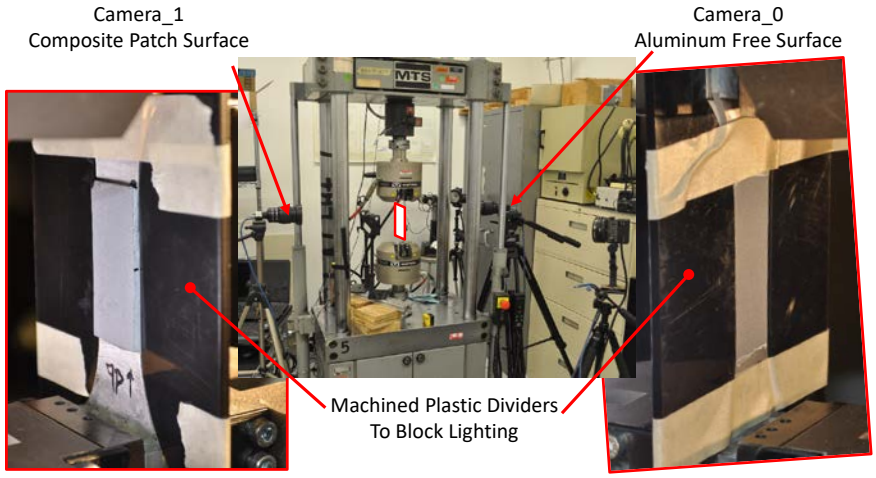

Figure 4-4 Second round of small scale CCT testing with machined plastic dividers taped to the specimen to block light from interfering with the opposite camera.

Small scale laminate testing was performed at both University of Maryland (UMD) and the Composites Lab at NSWCCD. Testing at UMD used an 8.8MP (4096 x 2160 pixel resolution) Point Grey Flea FL3-U3-88S2C-C digital camera with a nominal image size of 63.2 mm x 33.3 mm and an AOI of 45.6 mm x 15.0 mm. At NSWCCD's Composite Lab an Allied Vision Stingray F-504B camera with a 5MP Sony ICXX655 CCD sensor was used to capture static images of the speckle pattern. A 40 mm lens achieved a nominal FOV of 66.0 mm x 55 mm and an AOI of 41 mm x 11.5 mm.

Aluminum dog-bone testing used DIC in the 4-post MTS frame at UMD. Again the 8.8MP (4096 x 2160 pixel resolution) Point Grey Flea FL3-U3-88S2C-C digital camera was used with 65.0 mm x 34.5 mm FOV and a 61.6 mm x 11.0 mm AOI.

Unless otherwise documented standard material coupons used standard 1/4 inch 0/90 stacked strain gauges (CEA-06-125WT-350) to measure engineering strains.

Thick adhesive shear testing used an Epsilon Tech Model 4013-125T-ST KGR type averaging extensometer, shown in Figure 4-5 to measure extension due to shear on both sides of the specimen for an average shear strain across the adhesive test section [79, 77, 80, 81, 82].

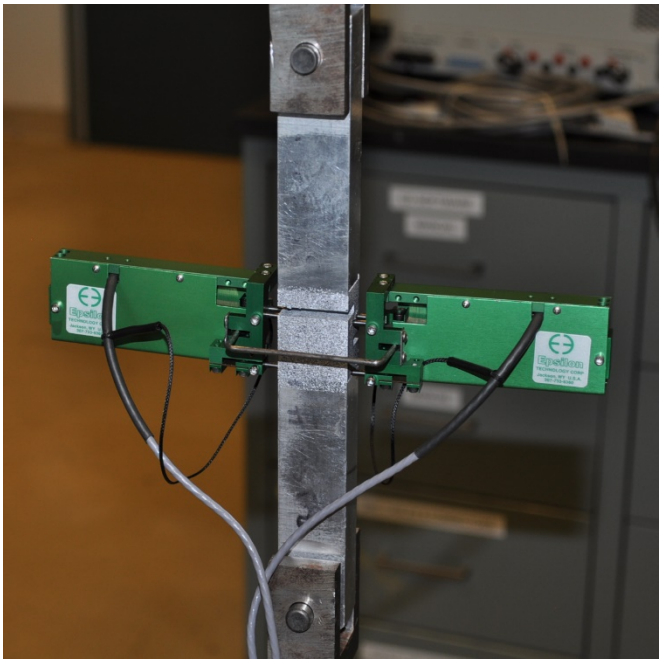

Figure 4-5 Epsilon Tech KGR-1 type extensometer used to measure adhesive shear.

For the large scale CCT testing specimens used an arrangement of 1/4 inch 350 ohm axial strain gauges (CEA-06-250UW-350) along with a John A. Shepic Co. SFDG-30 ring gauge to measure crack opening displacement at the centerline of the specimen.

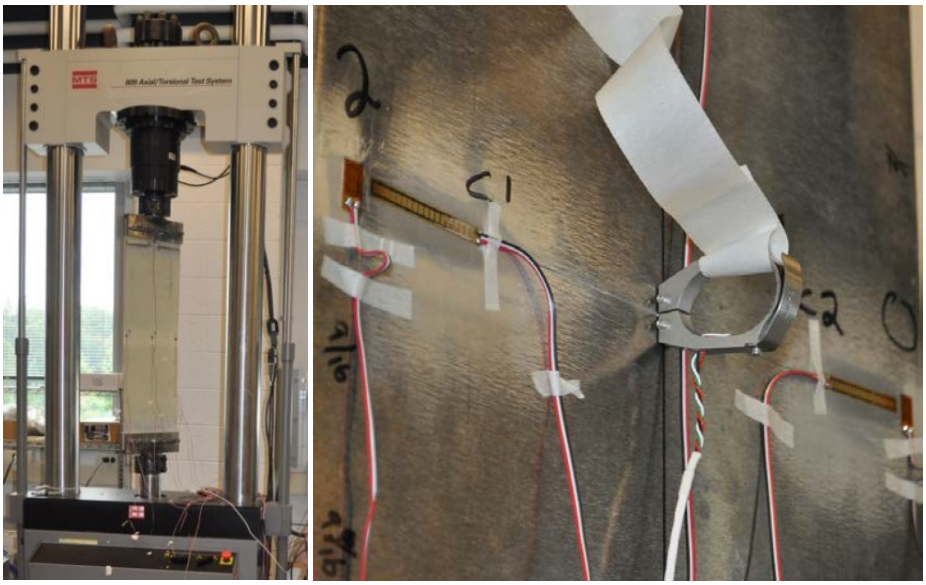

Figure 4-6 Large scale CCT specimen test configuration using 55 kip axial torsion hydraulic test frame and a John A. Shepic ring gauge to measure COD.

4.2.2 Test Data Fitting Method to Develop Ramberg-Osgood Parameters

Fitting of data to determine the best parameters for the Ramberg-Osgood or similar power law material behavior was done using the built-in Matlab function *lsqnonlin*. This function takes the user defined function, in this case the difference between the natural log of the Ramberg-Osgood strain, and the natural log of the true strain at a given tensile stress level. With the elastic stress limit defined by $\sigma_0 = E\varepsilon_0$ the stress-strain relationship from Equation 117 becomes a function of material parameters and stress level.

$$\varepsilon(\sigma) = \frac{\sigma}{E}\left(1 + \alpha\left(\frac{\sigma}{\sigma_y}\right)^{n-1}\right) \qquad \text{Equation 123}$$

Next, the function to be solved is the difference between the natural log of the predicted and measured strains (ε_m) as a function of stress level.

$$f(\sigma) = \log \varepsilon(\sigma) - \log \varepsilon_m \qquad \text{Equation 124}$$

The *lsqnonlin* function uses the Levenberg-Marquardt algorithm [83] to solve for the minimum of the sum of $f(\sigma)^2$ for combinations of α and n. Both the aluminum and adhesive data were assumed describable by the Ramberg-Osgood relationship.

4.2.3 Optical Characterization of Aluminum Grain Structure

Grain structure of the small scale test specimen 5052-H32 aluminum was studied using a light optical microscope (LOM) at magnification levels of 5x and 20x. Images were taken of the long transverse (L-T) surface, as defined in ASTM E399 [84], corresponding to crack plane alignment of the CCT specimens. For grain structure images, samples of the aluminum plate were polished, electrochemically etched following ASTM E407 [85], and imaged using a LOM with a gamma filter and polarized light. Samples were cut and potted with a pure nickel wire protruding from one surface. Each specimen was then mechanically wet sanded and polished in stages from 120 grit to an active oxide polishing OP-U 0.04 μm colloidal silica solution. Directly following the last polishing step specimens were electro-chemically etched using Barker's Reagent (5% HBF solution) and an electric current. With the sample suspended 10-15 mm below the surface of the solution, a 20 VDC was applied between a stainless steel cathode in the beaker and the nickel anode with a current density between 0.5 and 1.5 Amps/in^2 for 2 minutes. Then the sample surface was rinsed with distilled water and alcohol then dried. Microscope images with 20x magnification with known length scale were processed to measure the grain structure. Grain size estimation was performed using two methods. First, the planimetric procedure with non-standard magnification provided a calculation of the grains per square area outlined in ASTM E112 [86]. The second method approximated grains as

ellipses with the major and minor axis points manually selected and measured for randomly selected grains measured from two imaged regions of the sample.

4.2.4 Tension Test Method for Small Scale Specimen Aluminum

Tensile specimens of 5052-H32 aluminum were tested according to ASTM E8-08 [87] with geometry based on the ASTM E466 [88] sheet type specimen. Axial tension was applied to sheet type specimens, shown in Figure 4-7, until rupture of the gauge section occurred. Loading was applied at 1 mm/min on a 4-Post MTS hydraulic axial test frame. One surface of the gauge section was painted with a speckle pattern and images were taken at various rates during the loading. DIC was used to calculate the Lagrangian strain on the surface. Specimens for the 5052-H32 have a nominal thickness of 2.29 mm, grip section width (G) of 45 mm, a gauge section width (W) of 12 mm, a half gauge length(L1) of 12 mm, transition radius (R) of 144.4 mm, transition length (L2) of 68 mm, and an overall specimen length of 250 mm.

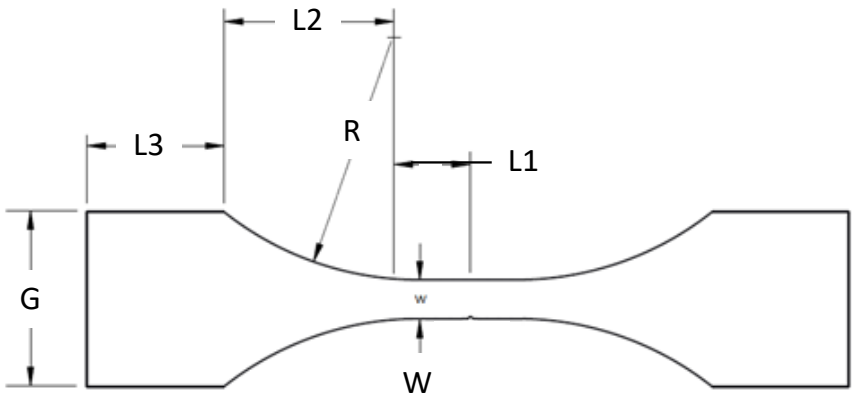

Figure 4-7: ASTM E466 Sheet Type Specimen [87].

4.2.5 Adhesive and Resin Dog Bone Tension Test Method

Tensile specimens of the neat resin system were tested according to ASTM D638 [89]. Axial tension was applied to a type I specimen until failure occurred. The test specimen

had rectangular grip sections that necked down to a narrow test section. Nominal dimensions were 165 mm long (LO), a gauge section width of 12.7 mm (W_C), and a thickness (T) of 3.18 mm as shown in Figure 4-8. The nominal neck radius was 76.2 mm and the gage section length was 57.2 mm (L). A biaxial stacked 0/90 strain gage was applied to each specimen at midspan and along the centerline.

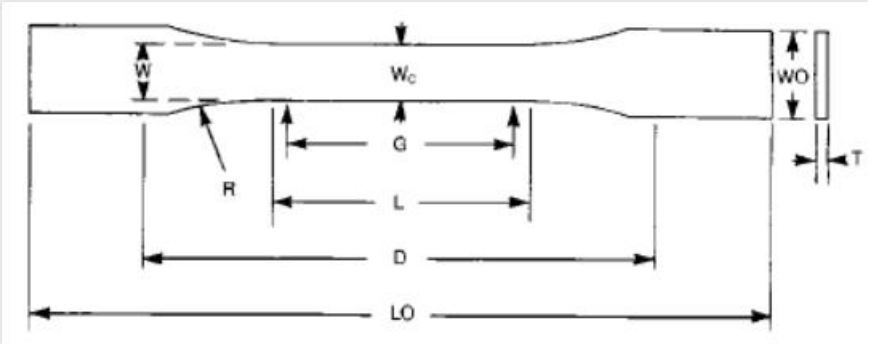

Figure 4-8: ASTM D638 Tabbed tensile specimen.

4.2.6 Tabbed Tension Test Method for Large Scale Specimen Laminate

Tensile specimens, five from each panel, were tested according to ASTM D3039 [90]. Tensile material tests were performed with the principle laminate direction oriented at 0 degrees. The test specimen was straight sided with grip tabs bonded on each end. Nominal dimensions were 250 mm long, a width of 25.4 mm, and 3.8 mm thick as shown in Figure 4-9. An axial strain gage was applied to the bag side of the specimen at midspan and along the centerline.

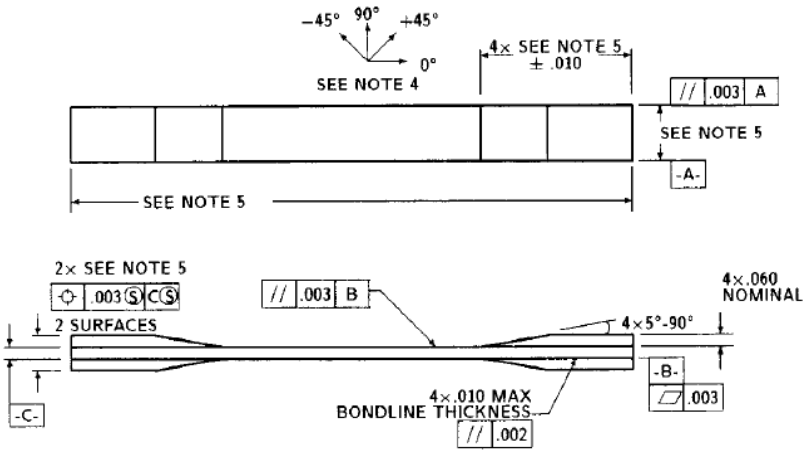

Figure 4-9. Tabbed tensile specimen, ASTM D3039.

4.2.7 Compression Test Method for Large Scale Specimen Laminate

Compression specimens, five from each panel, were tested according to ASTM D6641 [91]. Compression material tests were performed with the principle laminate direction oriented at 0°. The standard compression specimen, shown in Figure 4-10, had nominal dimensions of 12.7 mm wide, 139.7 mm long, and 3.8 mm thick. An axial strain gage was applied to the bag side of the specimen at the midspan.

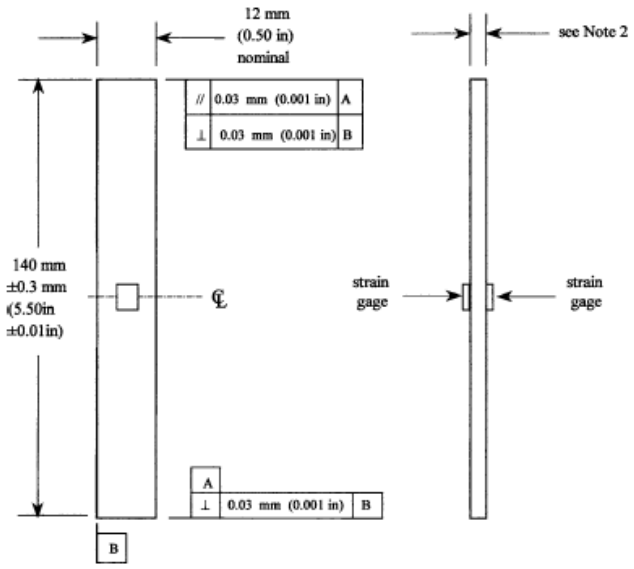

Figure 4-10. Compression specimen, ASTM D6641.

4.2.8 Notched Compression Test Method for Large Scale Specimen Laminate

Notched compression specimens, five from each panel, were tested according to ASTM D3846 [92]. Compression material tests were performed with the principle laminate direction oriented at 0°. The standard compression specimen, shown in Figure 4-11, had nominal dimensions of 19.1 mm wide, 139.7 mm long, and 10.2 mm thick. A notch was machined from each face the depth of each material to form the specimens shown in Figure 4-11 for a test section nominally 6.35 mm long. Specimens were loaded in compression until load dropped below 80% of the measured peak load.

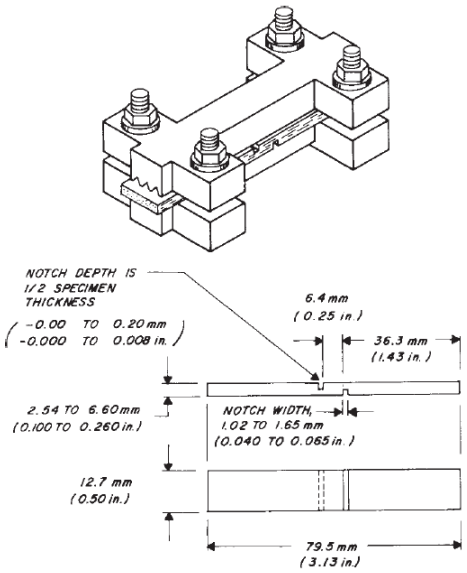

Figure 4-11: ASTM D3846 Compression specimen.

4.2.9 Thick Adhesive Shear Test Method

Thick adhesive shear specimens were manufactured and tested according to ASTM D5656 [82]. Specimens were machined from two bonded 9.5 mm thick 6061 aluminum plates. The adhesive bondline thickness was controlled with a single ply of Hexcel 7500 cut into a hollow rectangle, such that only M1002-237 resin was present in the test section. The standard shear specimen, shown in Figure 4-12, had nominal dimensions of 25.4 mm wide, 228.6 mm long, and 19.3 mm thick with a nominal bond line thickness of 0.76 mm. Specimens were loaded in tension via pin loaded bushings through the specimen. Shear displacement of the adhesive in the test section was measured using an Epsilon Tech KGR type extensometer, which measured extension due to shear on both sides of the specimen for an average across the test section.

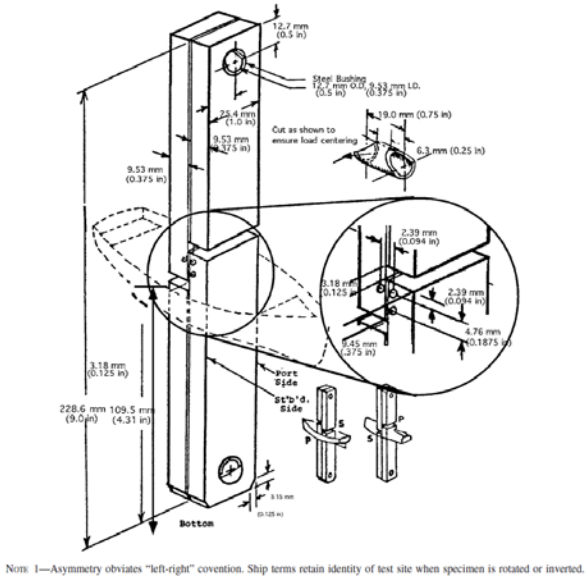

Notes 1—Asymmetry obviates "left-right" covention. Ship terms retain identity of test site when specimen is rotated or inverted.

Figure 4-12: ASTM D5656 thick adhesive shear testing.

4.3 Measured Material Characteristics and Mechanical Properties

Mechanical properties for the materials tested will be reported in this section. Data processed was generated by either conventional axial resistive strain gauges or full field DIC using Correlated Solutions VIC2D version 6 software.

4.3.1 Small Scale CCT Specimen 5052-H32 Aluminum

4.3.1.1 5052-H32 Aluminum Grain Structure

Cold work hardened 5xxx series aluminum alloy contains center face cubic crystals with $(FE,CR)_3SiAl_{12}$, Mg_2Si, and Magnesium as Mg_2Al_3 at concentrations between 2.2% and 2.8% [93, 94]. One characteristic of these alloys are grains that have been elongated and oriented with the rolling direction during cold work. The grain structure of 5052-H32 was characterized using a LOM with gamma filtered polarized light with the small scale specimen orientation and a typical image shown in Figure 4-13. Images were taken of the long transverse (L-T) surface, as defined in ASTM E399 [84], corresponding to crack plane alignment of the CCT specimens. The intermetallics, visible in the microscope

image in Figure 4-13, indicate the rolling direction. Microscope images with 20x magnification with known length scale were used to measure the grain structure.

The planimetric method resulted in an ASTM grain size number of approximately 11.5 (Table 4 in Ref [86]), meaning 39.8 grains per μm^2 and an average grain diameter of 6.3 μm. The planimetric method does not convey the variability in grain structure or the difficulty measuring a 3-dimensional grain from a 2-dimensional plane. From the simplified method of directly measured grain size the average major diameter was 10.8±4.5 μm with the maximum and minimum measurements being 18.1 and 5.4 μm, respectively.

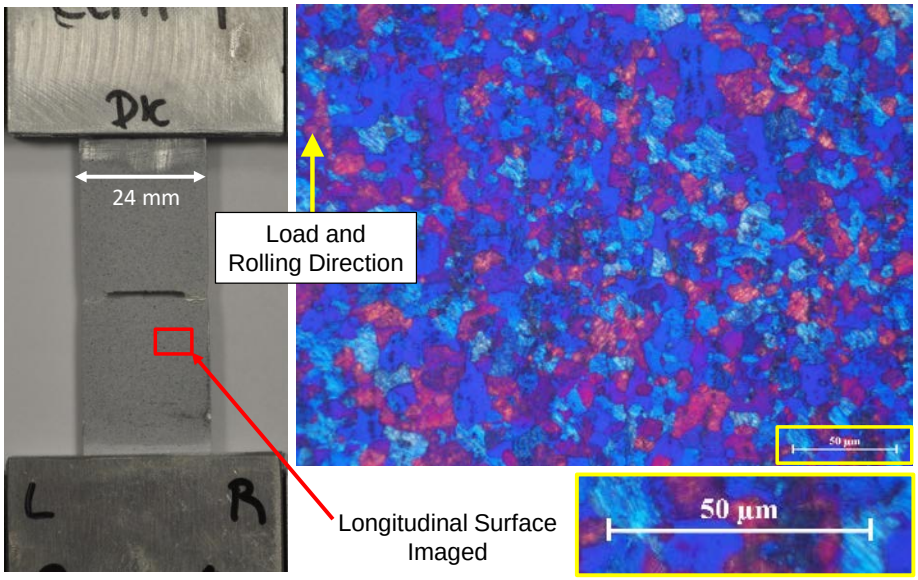

Figure 4-13 Longitudinal Surface Grain Structure of 5052-H32 at 20x in Gamma Filtered Polarized Light Showing Grain Structure Size and Variability in the Specimen Orientation

4.3.1.2 Aluminum Tensile Properties for Small Scale CCT Specimens

Aluminum tensile properties were measured using radius transition sheet type specimens with test results compared against existing data [69, 95]. The stress-strain response and typical Lagrangian axial surface strains measured with DIC are shown in Figure 4-14 and

a summary of mechanical properties measured listed in Table 1 for the four specimens successfully tested. Aluminum properties were averaged for four specimens with resulting modulus of 70.9±0.9 GPa, a Poisson's ratio of 0.34±0.03, a 0.2% offset yield strength of 115.6±0.7 MPa, and Ramberg-Osgood parameters n and α of 9.9±0.9 and 0.22±0.06, respectively.

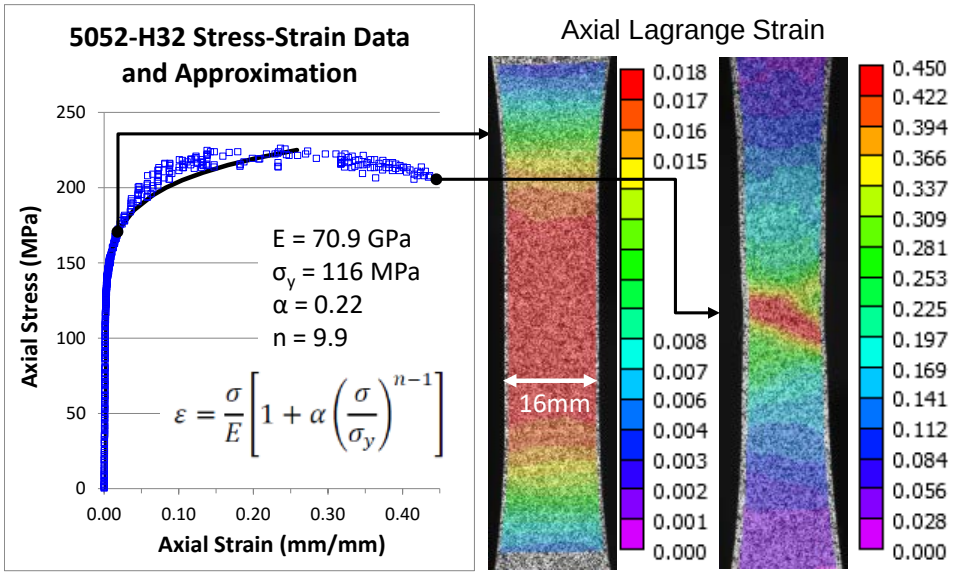

Figure 4-14 Tensile Stress-Strain Behavior of 5052-H32 Aluminum

Table 1 Mechanical Properties of 5052-H32 Aluminum

ASTM E8M Tensile Test Sheet Type Rectangular Cross Section									
Specimen ID	Width (mm)	Thickness (mm)	Modulus (GPa)	Poisson's Ratio	Ultimate Strength (MPa)	0.2% Yield Strength (MPa)	0.2% Yield Strain (με)	Hardening Constant (α)	Hardening Coefficient (n)
DB01	11.98	2.22	71.0	0.32	180.3	114.7	1808	9.02	0.28
DB02	11.96	2.22	70.6	0.33	134.5	116.3	1737	11.08	0.14
DB04	11.97	2.22	69.9	0.33	226.2	115.6	1828	9.25	0.24
DB06	12.00	2.25	72.1	0.37	169.6	115.6	1828	10.08	0.23
Average	11.98	2.23	70.9	0.34	177.6	115.6	1800	9.86	0.22
STDEV	0.02	0.01	0.9	0.03	37.8	0.7	43	0.93	0.06
COV (%)	0.1%	0.7%	1.3%	7.5%	21.3%	0.6%	2.4%	9.5%	26.7%

4.3.2 Large Scale CCT Specimen 5456-H116 Aluminum

Large scale marine grade 5456-H116 aluminum was not testing during this project. Raw data for a single 4 mm diameter ASTM E8 spool specimen was provided by the US Naval Academy, courtesy of Dr. Link along with available historical data, which are

listed in Table 2 [94, 96, 97] and the critical LEFM properties at the various grain orientations and material condition are listed in Table 3 [98, 99].

Table 2: Large Scale CCT Specimen 5456-H116 Aluminum Mechanical Properties

5456-H116 Aluminum Properties	
E (MPa)	72,500
G (MPa)	27,300
ν	0.33
0.2% Offset Yield (MPa)	210.3
Ultimate Strength (MPa)	356.2

Table 3: Large Scale CCT Specimen 5456-H116Aluminum Critical Stress Intensity (Brosi, Li et al. 2010)

Sample	Test Direction	Ksi-in$^{(1/2)}$
5456(H116)	Longitudinal	29.0
5456(H116) Sensitized	Longitudinal	24.5
5456(H116)	Transverse	26.3
5456(H116) Sensitized	Transverse	23.6

Test section elongation measured with an extensometer and machine load were used to measure engineering strain, that was converted to true strain. True stress strain data for 5456-H116 is presented in Figure 4-15. The true stress-strain data was fit to the Ramberg-Osgood material parameters are n and α of 5.47 and 1.42, respectively.

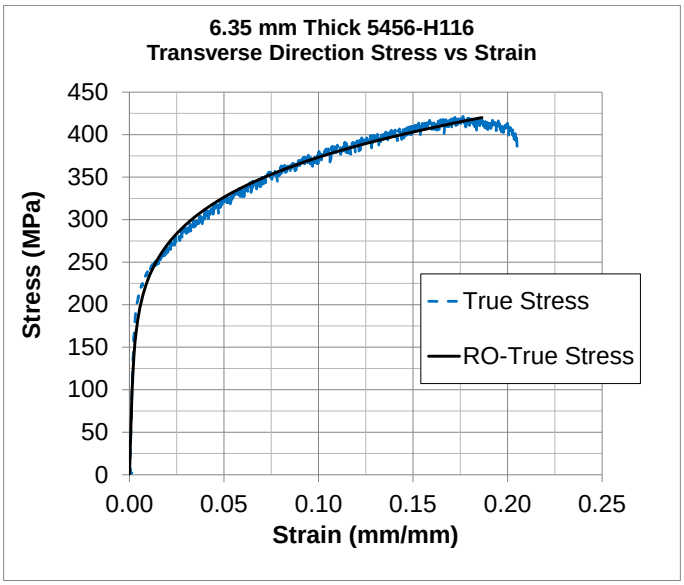

Figure 4-15 Aluminum 5456-H116 true stress-strain data from ASTM E8 tensile test.

4.3.3 Adhesive and Resin Tensile Properties

Both adhesive and resin specimens were cast in silicone forms. The M1002 resin specimens were then post cured after demolding. Specimens were fabricated according to the dimensions listed in ASTM D638. Resin was mixed by weight according to the M1002/M2046 technical data sheet (TDS). Molds were filled slightly proud of the top and then polished flat after material was fully cured. Each specimen had a 1/8 inch stacked 0/90 strain gauge applied to one side of the test section to measure axial and transverse strains. Strain data and specimen cross section dimensions were used to calculate the linear elastic Young's Modulus (E) and in-plane Poisson's ratio (ν).

4.3.3.1 West Six10 Adhesive Tension Test Results

Three batches of resin specimens were cast using unique resin cartridges, although all resin was from the same manufacturing lot number. Care was taken to eliminate air bubbles that formed in the gauge section. However, multiple voids were evident at the failure surfaces of tested specimens. Specimens were tested in a Bose 3300 Electroforce

test frame. Surface strain measurements were made using DIC with a FOV that encompassed the material from transition radius to transition radius with the speckle pattern consisting simply of flat black spray paint. This was found to produce enough contrast with the resin that no base coat of white was required. The test configuration and failed specimens are shown in Figure 4-16.

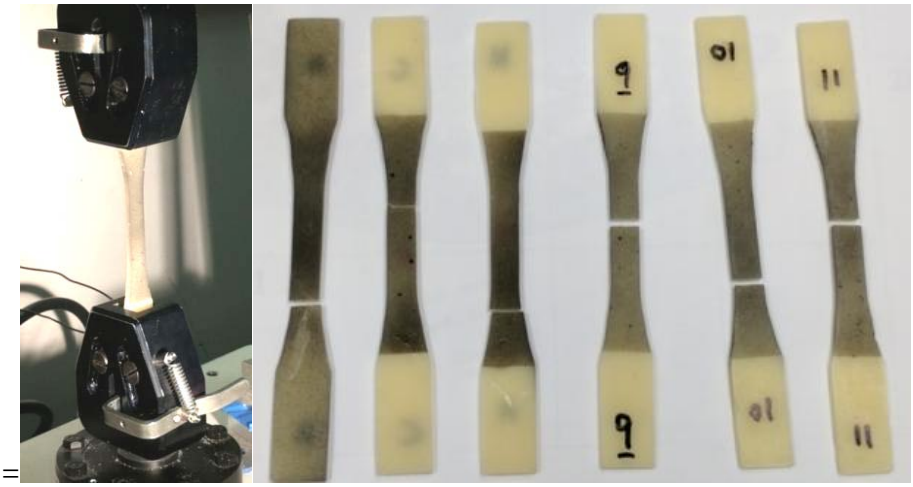

Figure 4-16 WestSix10 dog-bone tensile test configuration and failed specimens.

Typical stress-strain results for the dog-bone tensions testing of the adhesive are shown in Figure 4-17 with example full field DIC data beyond yielding and approaching ultimate failure showing strain concentrations due to imperfections in the resin. Mechanical properties determined are listed in Table 4.

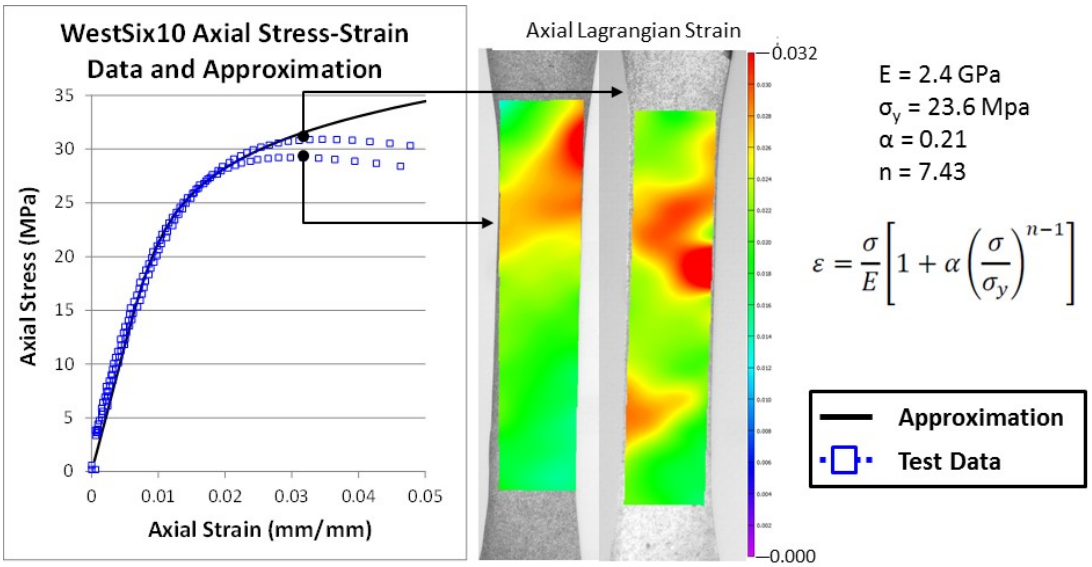

Figure 4-17 WestSix10 dog-bone tension stress-strain data.

Table 4 WestSix10 Dog-Bone Adhesive Tensile Test Results

WestSix10 Cast Adhesive Dog-Bone Testing						
Specimen ID	**Modulus (MPa)**	**Poisson's Ratio (ν_{12})**	**0.2% Yield Strain ($\mu\varepsilon$)**	**0.2% Yield Stress (MPa)**	**Ultimate Strength (MPa)**	**Plastic Strain Limit ($\mu\varepsilon$)**
C	2236	0.49	11138	20.4	26.8	197976
H	2314	0.53	12725	24.8	29.2	135470
7	2398	0.41	13550	27.4	37.9	30745
9	2513	0.55	11050	22.3	29.6	49939
10	2465	0.24	10567	21.1	28.5	86462
11	2261	0.31	13250	25.3	30.9	142892
Average	2365	0.42	12047	23.6	30.5	107247
STDEV	112	0.12	1279	2.7	3.9	63036
COV	4.8%	29.4%	10.6%	11.6%	12.7%	58.8%

4.3.3.2 M1002/M2046 Resin Tension Test Results

Cast dog-bone ASTM D638 specimens were manufactured in batches with 6 specimens per batch; each batch was poured and mixed separately. Statistical analysis of the data followed the reduced sample size procedures outlined by [76] to develop the B-Basis tensile properties for M1002-M2046.

Mean and B-Basis results along with the manufacturer's reported mean data are listed in Table 5. Mean elastic modulus was 4,275±414 MPa with a coefficient of variation (COV)

of 10.3% with a B-Basis value of 3,447 MPa. Modulus values are greater than reported by the manufacturer. Mean strength measured was 55.8±7.6 MPa with a COV of 14.1%, which was 19% lower than the manufacturers reported strength of 68.9 MPa. The peak measured strength value was 68.3 MPa. The B-Basis strength was 40.5 MPa. Strength and strain at failure are heavily dependent on cast resin quality. Although void content was low several failure surfaces included voids or surface imperfections.

Typical tensile stress-strain response is shown in Figure 4-18. The failure strain occurred at the peak measured load. The mean strain at failure was 2.1±0.6% with a COV of 27.9%. The mean failure strain was 60% lower than the manufacturer reported value. Strain was measured with a 0/90 stacked strain gauge on the surface of the specimen. This limited the ultimate strain value to the extension directly under the gauge. In retrospect the specimen extension should have been measured using an extensometer for the total gauge section extension. For all B-Basis values the tolerance factor from the analysis was reported, this value indicates how many standard deviations away from the reported value are required to represent 90% probability.

Table 5: Test and Manufacturer Tensile Data for M1002-M2046

	Mean	B-Basis	Tolerance Factor (K_b)	Manufacturer	Difference
Modulus (MPa)	4260	3426	1.90	2985	42.7%
Strength (MPa)	55.9	40.5	1.97	69.2	-19.2%
Poisson Ratio	0.38	0.37	1.92		
Failure Strain (%)	2.1%	1.0%	1.97	5.5%	-60.9%

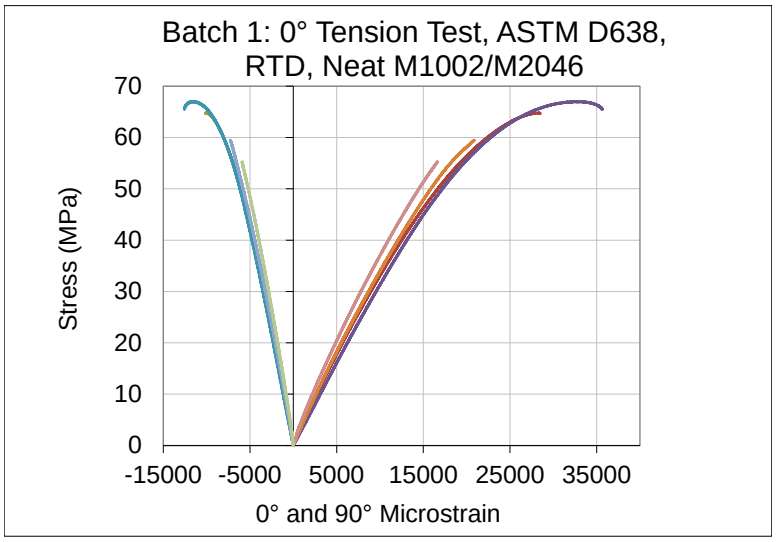

Figure 4-18: Typical tensile stress-strain response of M1002-M2046.

4.3.4 Adhesive and Resin Thick Adhesive Shear Properties

Thick adhesive shear testing was performed for WestSix10 adhesive and Pro-Set M1002-M2046 resin systems following ASTM, NASA, FAA, and DSTO guidance [79, 80, 81] using the Krieger test method (KGR). Standard ASTM D5656 parameters reported include elastic modulus (G_c), elastic stress limit (δ_{LL}), elastic strain limit (γ_{LL}), stress and strain at the plastic knee (δ_{KN}, γ_{KN}), the ultimate plastic stress (δ_{UL}), and the ultimate plastic strain (γ_{UL}).

The same machined 6061-T6 aluminum calibration sample was used for both the adhesive and resin testing. Loading was applied per ASTM D5656 guidance recording displacement at the 4000N load level and repeating that measurement six times. Data was then extrapolated to 4,448 N (1,000 lbs) and interpolated to 1,000 N to determine the

metal displacement factor (M). The average value for M was 0.001003 mm at 1000 N. This value was used to calculate the corrected displacement of the adherend.

Shear testing was performed with the goal of generating the Hart-Smith elastic-plastic bonded joint design parameters identified in [4]. Parameters required are the elastic modulus (G_e), elastic strain limit (γ_e), plastic shear stress limit (τ_p), the amount of plastic strain (γ_p), and the strain energy density (A_s), which is the area under the curve. Adhesive bondline A_s was identified as the critical parameter for determining the elastic limits and amount of plastic strain in processing methods outlined by Chalkley and van den Berg.

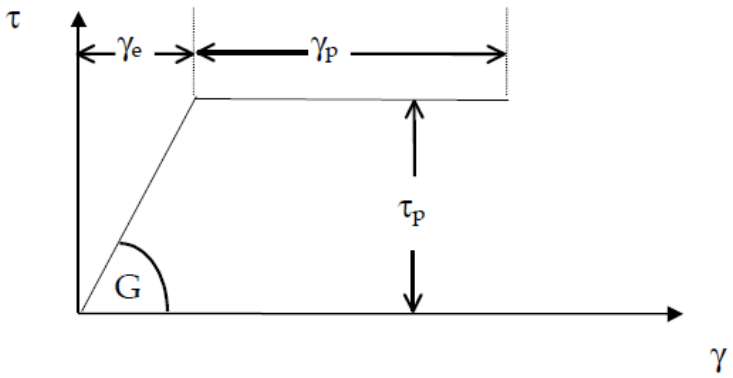

Figure 4-19: Hart-Smith elastic perfectly plastic approximation of adhesive stress strain behavior [4].

For each specimen the shear strain was offset with the assumption that at zero load the bondline had zero stress and strain. The maximum stress (τ_p) and offset strain(γ_{UL}) were tabulated. Then the trapezoid rule was used to calculate the strain energy density (A_s), or area under the stress-strain curve. Knowing A_s, and the following relationships defined by Hart-Smith defined several relationships between A_s, γ_e, τ_p, and γ_p. The elastic strain for Hart-Smith behavior is the calculated using Hooke's law, where τ_p, is the peak stress

measured. Iterate the elastic modulus (G_e) to match A_s and the area under the measured stress-strain response.

$$\gamma_e = {}^{\tau_p}/_{G_e} \quad \text{Equation 125}$$

The amount of plastic strain (γ_p) is simply the difference between the elastic-strain limit (γ_e) and the maximum measured strain (γ_{UL}).

$$\gamma_p = \gamma_{UL} - \gamma_e \quad \text{Equation 126}$$

Finally, the modulus is related to A_s through the following relationship:

$$A_s = \frac{1}{2}\tau_p\gamma_e + \tau_p\gamma_p = \tau_p\left(\frac{1}{2}\frac{\tau_p}{G_e} + \gamma_{UL}\right) \quad \text{Equation 127}$$

Solving for the equivalent modulus requires minimizing the RMS error between the measured and predicted strain energy density (A_s). With G_e known, the remaining parameters can be determined.

4.3.4.1 WestSix10 Thick Adhesive Shear Test Results

Basic ASTM D5656 shear stress-strain test data is presented in Figure 4-20 for the WestSix10 marine epoxy adhesive. Specimens had only adhesive at the bondline with an average bondline thickness of 0.88 mm determined by visual inspection. The basic shear response of the epoxy adhesive shows a plastic knee above the elastic stress-strain limit. Shear behavior parameters were determined following ASTM D5656 guidelines and are presented in Table 6 for 3 specimens. Adhesion failure at the adherend surface was the dominant failure mode with the ultimate failure surfaces being either clean adherend or resin as shown in Figure 4-21. This means the average ultimate strain is not the true strain

limit. Average elastic stress (δ_{LL}) limits were 27.6±1.5 MPa with a 5.4% COV and an average δ_{UL} of 29.1±1.8 MPa with a 6.1% COV. The average G_c was 1,434±127 MPa with a 8.9% COV. Variation of the elastic strain limit follows the modulus with an average γ_{LL} of 26,000 ±4,000 με and a 13.7% COV. Although invalid because of the adhesion failure mode, the average ultimate plastic strain level was 93,000±40,000 με and a 42.9% COV.

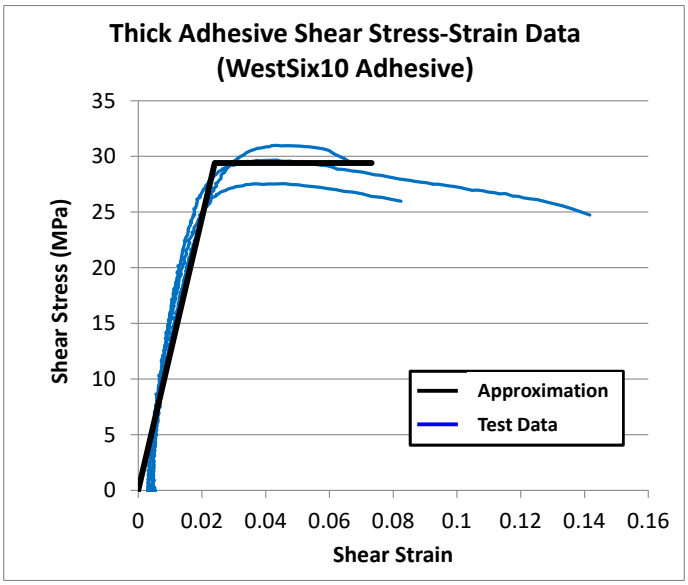

Figure 4-20 WestSix10 ASTM D5656 measured and predicted thick adhesive shear stress-strain response.

Table 6 WestSix10 ASTM D5656 Thick Adhesive Shear Properties

Specimen	G_c (MPa)	δ_{II} (MPa)	γ_{II}	δ_{kn} (MPa)	γ_{kn}	δ_{ul} (MPa)	γ_{ul}
610-01	1549	27.7	0.023	29.1	0.029	29.6	0.138
610-02	1298	29.0	0.030	30.2	0.036	30.5	0.063
610-03	1454	26.1	0.024	27.5	0.048	27.1	0.078
Average	1434	27.6	0.026	28.9	0.038	29.1	0.093
STDEV	127	1.5	0.004	1.3	0.009	1.8	0.040
COV%	8.9%	5.4%	13.7%	4.6%	25.0%	6.1%	42.9%

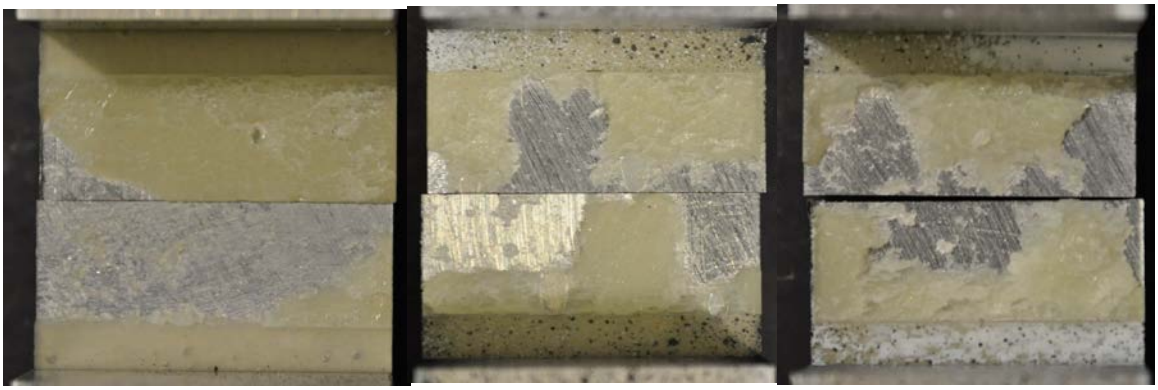

Figure 4-21 WestSix10 ASTM D5656 thick adhesive shear failure surfaces.

Hart-Smith parameters were calculated for each of the specimens with the average bi-linear representation shown in Figure 4-20 with specimen values listed in Table 7. To

represent the measured area under the stress-strain plot a perfectly plastic response is assumed at the ultimate shear stress and the shear modulus is iteratively solved for. The average shear modulus for bi-linear behavior is 1,230 MPa up to the plastic shear stress limit of 29.4 MPa, which is simply the maximum stress achieved and is higher than the reported ASTM D5656 ultimate stress limit on the plastic side of the stress-strain plot knee. This adhesive achieved peak plastic stress and then maintained a nonlinear behavior as shear stress capacity decreased with an increase in shear strain. The nonlinear response after the plastic knee is not ideal, however, the bilinear approximation should yield acceptable results.

Table 7 WestSix10 Hart-Smith Elastic-Plastic Parameters

	Hart-Smith Parameters				
Specimen	**G_e (MPa)**	**γ_e**	**γ_p**	**τ_p (MPa)**	**A_s (MPa)**
610-01	1300	0.023	0.119	29.7	3.9
610-02	1160	0.027	0.041	31.0	1.7
610-03	1227	0.022	0.060	27.5	2.0
Average	1229	0.024	0.073	29.4	2.5
Stdev	70	0.002	0.041	1.7	1.2
COV	5.7%	9.8%	55.5%	5.9%	47.5%

4.3.4.2 M1002-M2046 Resin Thick Adhesive Shear Test Results

Basic ASTM D5656 shear stress-strain test data is presented in Figure 4-22 for the M1002-M2046 resin. Specimens had only resin at the bondline with an average bondline thickness of 0.43 mm determined by visual inspection. The basic shear response of the rubber toughened epoxy system clearly shows a sharp plastic knee above the elastic stress-strain limit. Shear behavior parameters were determined following ASTM D5656 guidelines and are presented in Table 8 for 8 specimens. From the stress-strain response there is variation in the elastic limits as well as the ultimate plastic strain limit. Adhesion

failure at the adherend surface was the dominant failure mode with the ultimate failure surfaces being either clean adherend or resin as shown in Figure 4-23. This means the average ultimate strain is not the true strain limit. Stress limits were consistent, with an average δ_{LL} of 38.9±1.2 MPa with a 3.1% COV and an average δ_{UL} of 41.1±0.7 MPa with a 1.7% COV. The average G_c was 1,223±165 MPa with a 13.5% COV. Variation of the elastic strain limit follows the modulus with an average γ_{LL} of 48,000 ±9,000 με and a 19.6% COV. Although invalid because of the adhesion failure mode, the average ultimate plastic strain level was 153,000±40,000 με and a 26.4% COV.

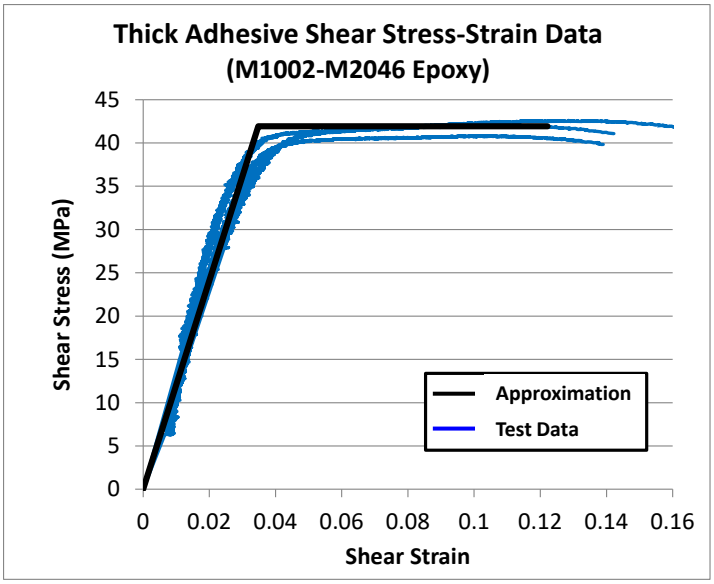

Figure 4-22. Typical shear stress-strain data for M1002-M2046 with the average Hart-Smith bi-linear approximation shown in black.

Table 8. M1002-M2046 Thick Adherend ASTM D5656 Results

Specimen	G_c (MPa)	δ_{II} (MPa)	γ_{II}	δ_{kn} (MPa)	γ_{kn}	δ_{ul} (MPa)	γ_{ul}
2	1611	37.5	0.033	39.2	0.039	40.2	0.102
3	1288	37.7	0.042	39.3	0.048	40.1	0.129
5	1122	38.8	0.063	40.3	0.069	41.2	0.148
6	1355	38.6	0.048	40.1	0.053	40.8	0.216
7	1512	38.6	0.050	40.3	0.056	41.0	0.167
10	1649	38.8	0.039	40.4	0.045	41.3	0.105
12	1397	41.0	0.055	41.4	0.057	42.2	0.195
13	1582	40.3	0.049	41.1	0.053	41.6	0.164
Average	1439	38.9	0.048	40.2	0.053	41.1	0.153
STDEV	182	1.2	0.009	0.8	0.009	0.7	0.040
COV%	12.6%	3.1%	19.6%	1.9%	16.9%	1.7%	26.4%

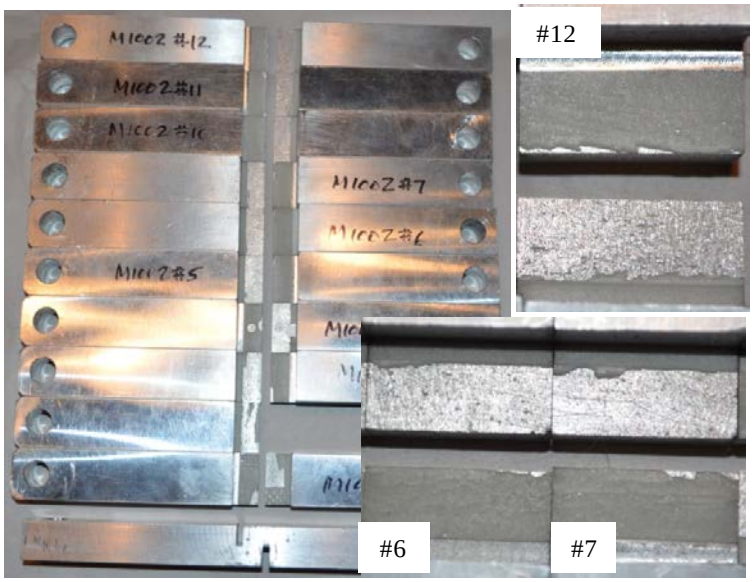

Figure 4-23. Typical failure surfaces for ASTM D5656 M1002-M2046 specimens showing adhesive failure between adherend and resin.

Hart-Smith parameters were calculated for each of the specimens with the average bilinear representation shown in Figure 4-22 with specimen values listed in Table 8. This material demonstrates perfectly plastic response beyond yield and can be reasonably represented with the bilinear stress-strain model. The average shear modulus for bilinear behavior is 1,220 MPa up to the plastic shear stress limit of 41.9 MPa.

Table 9. Thick Adherend Hart-Smith Parameters for M1002-M2046

	Hart-Smith Parameters				
Specimen	**G_e (MPa)**	**γ_e**	**γ_p**	**τ_p (MPa)**	**Area (MPa)**
2	1421	0.028	0.083	40.5	3.9
3	1108	0.037	0.102	40.8	4.9
5	1034	0.041	0.102	42.0	5.1
6	1084	0.039	0.179	42.5	8.5
7	1183	0.036	0.131	42.6	6.4
10	1492	0.028	0.084	41.8	4.1
12	1168	0.037	0.162	42.7	7.7
13	1293	0.033	0.134	42.4	6.4
Average	1223	0.035	0.122	41.9	5.9
STDEV	165	0.005	0.036	0.8	1.6
COV%	13.5%	13.4%	29.1%	2.0%	27.9%

4.3.5 Small Scale Laminate Tensile Test Results

Dog-bone laminate specimens were tested monotonically until failure in two load frames. Specimen numbers 01 through 04 were tested in an Instron 4202 axial bench top frame in NSWCCD's composites lab and specimens 09 and 10 were tested on a 22 kN Tinius-Olsen axial test frame in University of Maryland's Modern Engineering Materials Instructional Laboratory (MEMIL). Surface strain data was measured using DIC within the gauge section. Modulus was determined from axial strains averaged across three regions. The laminate thickness and testing without grip tabs made specimen ultimate properties vary significantly between test frames due to clamping conditions. Manual wedge grips of the Tinius-Olsen had to be carefully tightened to avoid applying torsion to the thin material while gripping the specimen surface sufficiently. Because specimens were designed for wider grips, careful specimen alignment in the Instron 4202 was required since specimens grip regions were wider than the wedge grip faces. Variation in clamping conditions resulted in varying Poisson's ratio and failure strengths. The Instron 4202 setup and typical DIC results are shown in Figure 4-24.

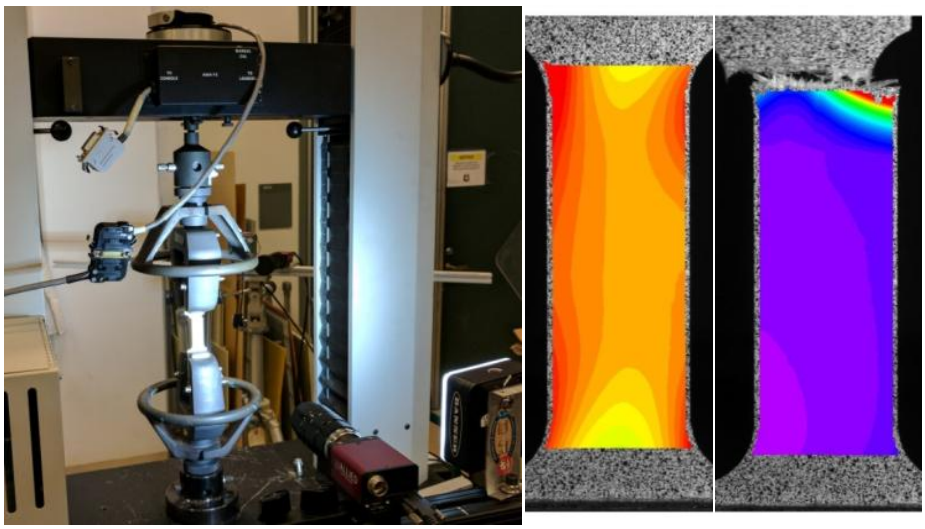

Figure 4-24 Prefabricated laminate test setup in the Instron 4202 and example DIC strain fields during loading and during failure.

Tensile behavior is shown in Figure 4-25 with average test results for all specimens listed in Table 10. Measured elastic modulus values averaged 22.2 GPa with a 5.3% COV. Local failure strain, measured using DIC at the location of failure initiation, averaged 15,144 με with a 2.7% COV. With the assumed addition of torsion, ultimate tensile strength of the laminate was significantly lower on the Tinius-Olsen frame and considered outliers. The average laminate strength is based on test data from the Instron 4202 and averaged 300 MPa with a 1.5% COV.

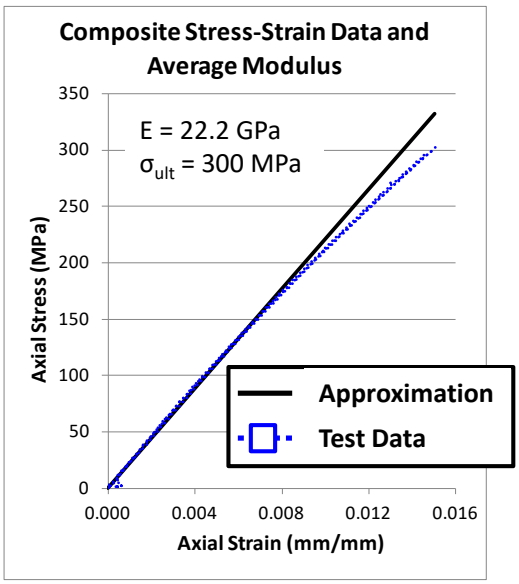

Figure 4-25 Small scale laminate axial tension behavior measured and approximated.

Table 10 Prefabricated 0/90 E-Glass Epoxy Laminate Tensile Mechanical Properties

G11 FR5 E-Glass Epoxy Composite Sheet						
Specimen ID	**Width (mm)**	**Thickness (mm)**	**Modulus (MPa)**	**Poisson's Ratio**	**Strength (MPa)**	**Failure Strain ($\mu\varepsilon$)**
GE-01	14.3	1.26	22856	0.08	302	14999
GE-02	16.0	1.30	21320	0.05	296	15811
GE-03	16.0	1.26	22130	0.07	306	15507
GE-04	16.0	1.29	23226	0.10	298	14849
GE-09	16.1	1.20	20270	0.09	198	14849
GE-10	16.0	1.29	23110	0.07	226	14849
Average	15.7	1.27	22152	0.08	300	15144
STDEV	0.7	0.03	1166	0.02	4	414
COV	4.5%	2.7%	5.3%	22.0%	1.5%	2.7%

4.3.6 Large Scale Laminate Tension and Compression Test Results

An abbreviated screening level set of tension and compression test results are reported together in this section for a laminate with the primary axis orientated in the 0 degree direction. Mechanical properties were measured for panels 8A, 14, and 18. Panels were selected to provide a performance envelope for the composite patch laminates and represent the as-built laminate, best FVF, and a laminate without vacuum consolidation.

Tension and compression testing were performed on 5 samples of each test type from each panel for a total of ten specimens per panel. Test result averages are listed in Table 11, strength and modulus results are shown in Figure 4-26, and the strain at failure and specimen thickness data are shown in Figure 4-27. Figure 4-28 shows the tensile test configuration on the left, and the combined loading compression configuration and fixture on the right. Typical failure modes observed are shown in Figure 4-29; Top image is a tabbed tensile specimen and the middle and bottom images are the bag side and edge of a failed compression specimen. Average strain to failure of this system was 2.06% for both compression and tension. Laminate stiffness varied with FVF. The average compression and tension moduli were 12.4 and 11.9 GPa, respectively. Moduli average 13.6 and 12.7 GPa for compression and tension when the FVF is greater than 30%. The lowest strengths and moduli occurred for panel 18, which closely represents a laminate with no vacuum consolidation. The compressive and tensile moduli are 10.3 GPa with 184.1 and 159.3 MPa strengths, respectively. Panel thickness, inversely related to ply consolidation and vacuum level, ranged from 3.3 to 5.1 mm as the level of vacuum and ply consolidation decreased. Material performance and physical characteristics listed show the minimum and maximum properties of currently installed composite patch laminates. Compression strength, dependent on resin content, decreases as the FVF decreases. Overall average compression strength was 214.4 MPa with a Coefficient of Variation (COV) of 13.4%. Peak compression strength of 246.1 MPa was achieved for the panel with 10 in-Hg of vacuum applied 1 hour after resin mix. Tensile strength for the group averaged 181.3 MPa with a COV of 9.4%. Peak tensile strength of 193.1 MPa was

achieved for the panel with 10 in-Hg of vacuum applied 1 hour after resin mix. Strength and modulus data show the variability possible for shipboard composite patch repairs.

Table 11. Large Scale Laminate Mechanical Testing Summary.

Sample ID	Thickness (mm)	Comp Strength (MPa)	Comp Modulus (GPa)	Comp Strain at Failure	Thickness (mm)	Tensile Strength (MPa)	Tensile Modulus (GPa)	Tensile Strain at Failure
#8A	3.4	245.9	14.0	2.14%	3.9	192.9	12.3	2.14%
#14	4.0	213.1	13.0	1.97%	3.8	192.4	13.0	2.01%
#18	5.1	184.3	10.3	2.10%	4.9	159.4	10.5	2.02%
Ave	4.1	214.4	12.4	2.07%	4.2	181.6	11.93	2.06%

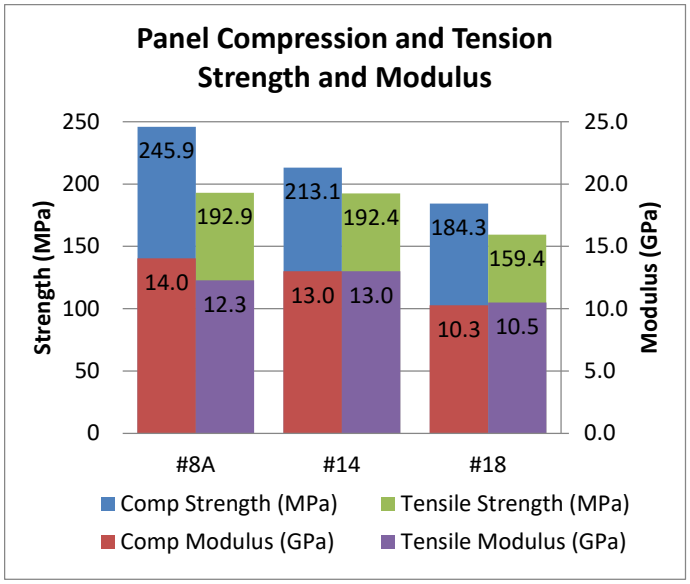

Figure 4-26. Compression and tension strength and modulus results.

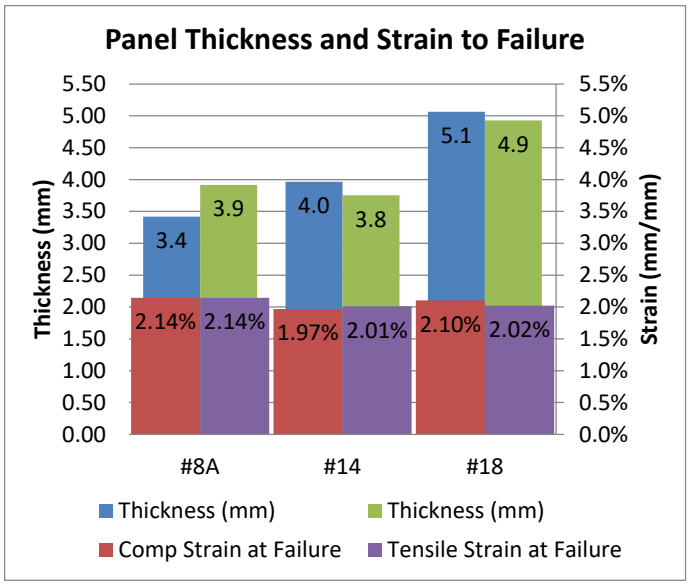

Figure 4-27. Strain to failure and panel thickness results.

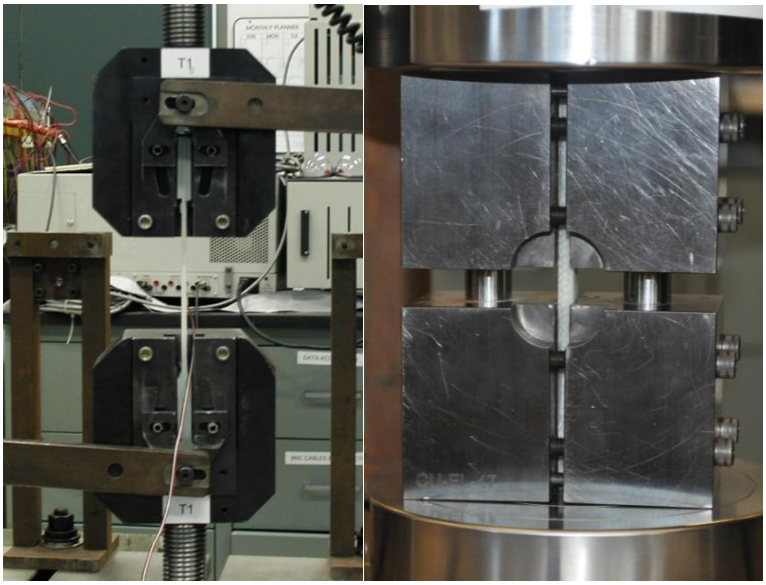

Figure 4-28. ASTM D3039 tension (L) and ASTM D6641 compression (R) specimens in test fixtures.

Figure 4-29. Typical failure modes observed for the tabbed tensile specimen (top) and compression specimen (middle and bottom).

5 Center Crack Tension Specimen Geometry and Manufacturing

Material testing and data supports the monotonic failure testing and analysis of the center crack tension (CCT) specimens. This section documents CCT test specimen geometry and manufacturing methods for both small and large scale specimens.

5.1 Small Scale CCT Test Specimen Geometry and Manufacturing Details

Two rounds of small scale testing were performed. The test section and initial notch machining remained constant for both rounds of testing. Each specimen configuration required the use of bonded grip tabs, which served two purposes: to provide sufficient thickness to use the hydraulic grip wedge faces available and to transition load from the grip faces to the test section.

5.1.1 Small Scale CCT Test Frame and Initial Specimen Geometry

Small scale CCT specimen geometry was selected for manufacturing and testing convenience as well as maintaining a configuration link to the large scale testing performed by Hart et. al. [16]. Aluminum selected for the small scale CCT specimens was based on readily available plate thickness that allowed a nominally 1/3rd scale from the large scale center crack tension specimens. Small scale CCT specimen blank plates, shown in Figure 5-1, were 24 mm wide (*2W*) and 114 mm long with electrical discharge machined (EDM) notches nominally 12 mm wide and 0.36 mm high. The geometry shown was designed for use with mechanical grips with a width of 24 mm. However, a larger load capacity was required for static testing. Both the fatigue crack growth and monotonic tensile loading was performed on a 20 kip 4-post hydraulic MTS frame with Instron hydraulic wedge grips and controls. Specimens were adapted to the wedge grips with temporarily bonded tabbing; the wedge grips had a minimum grip thickness of 7.8

mm and a 45 mm grip width. Tabbing was made using rough cut 45 mm x 45 mm pieces of 3 mm thick aluminum plates and spacer plates, each bonded to the end of the specimen using a cyanoacrylate adhesive (Gorilla Glue™). Cracks were then grown from the notch to develop sharp crack tips using high cycle low load tension-tension fatigue.

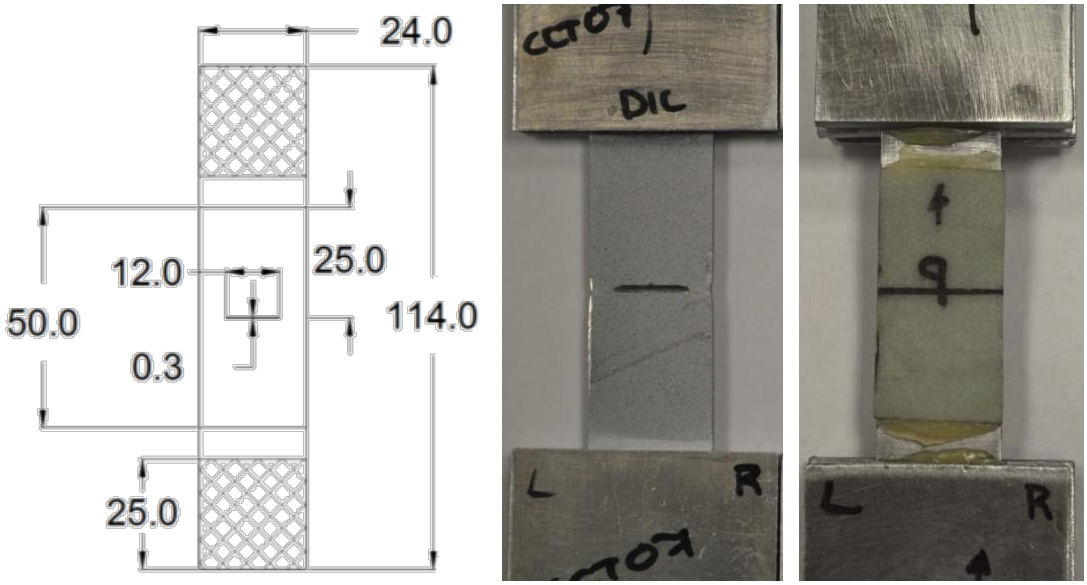

Figure 5-1 Round one small scale CCT specimen geometry.

5.1.2 Round Two Small Scale CCT Specimen Geometry

Lessons learned from setting up the initial round of testing were used to configure the second round of small scale specimens. To match the hydraulic grip faces the final specimens were based on the ASTM E466 test standards dog-bone type specimen with a rounded transition to the test section [88]. General specimen geometry is shown in Figure 5-2. The specimens have grip areas that are nominally 45 mm wide (G), 45 mm long (L3), with a transition radius of 49.2 mm (R), a transition length of 31.2 mm (L2), a test section length of 24 mm (L1), and a gauge section width of 24 mm (W). Note that the full width for the ASTM standard is represented with W, not the typical *2w* for LEFM.

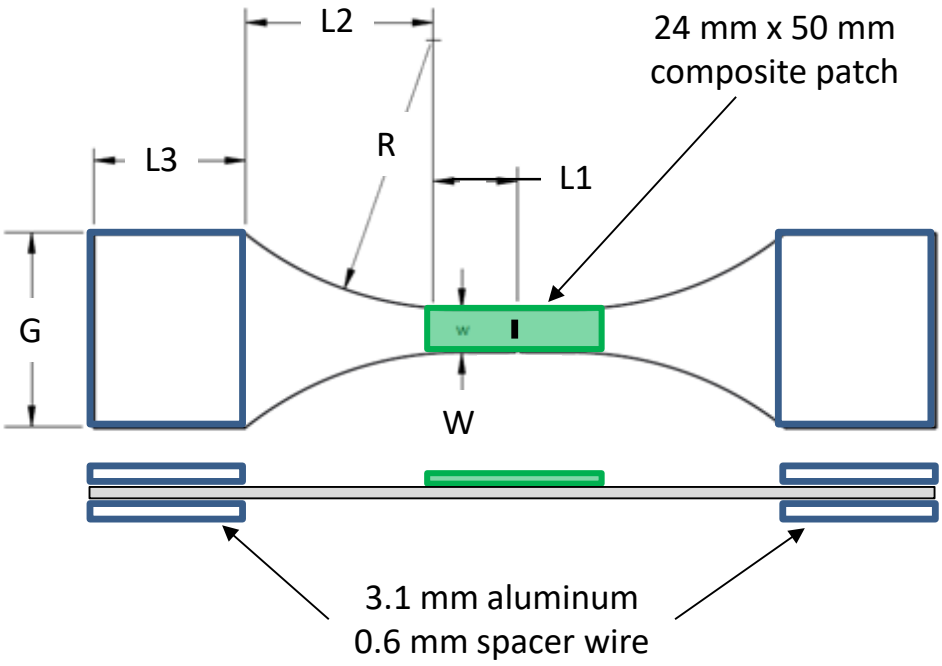

Figure 5-2 ASTM E466 dog-bone type specimen with rounded transitions to the test section.

5.1.3 Small Scale CCT Surface Preparation and Bonding

Surface preparation of the aluminum was consistent for both small scale specimen groups and involved an initial acetone wipe to clean the surface of contamination, followed by

surface abrasion with 80 grit aluminum oxide sandpaper for profile and removal of the oxide layer. After abrasion a final acetone wipe was performed, then application of 3M's AC-130-2 bonding agent. AC-130 is two part silane solution that is used as a dual purpose cleaner and bonding agent. The mixed solution cleans the surface and forms a thin organic/inorganic film on the surface through hydrolysis and oxygen. This thin film promotes adhesion between the aluminum substrate and the organic resin system and is the final surface preparation step prior to applying the epoxy adhesive. Preparing the prefabricated E-Glass laminate involved acetone wipe before and after light abrasion with 80 grit sandpaper.

After preparing both faying surfaces a commercially available marine adhesive, West Systems WestSix10, was selected for bonding the pre-fabricated 0/90 E-Glass epoxy laminate. The laminate had an average thickness of 1.27 mm and was cut to 50 mm long by 24 mm wide. The composite patch was centered on the machined notch and bonded to the cracked aluminum plate with a nominally 0.6 mm thick bondline that was controlled using 0.6 mm diameter steel welding wire. The clamping jig used is shown in Figure 5-3.

Figure 5-3 Small scale composite patch bonding jig configuration.

For the final small scale specimen group the adhesive and laminate were consistent with the initial specimens, however, both the patch and grip tabbing were bonded using the WestSix10 adhesive. Tabbing was bonded to the specimen ends and then high cycle low stress fatigue loading was used to grow cracks from the machined notches on all specimens. After crack growth the same surface preparation process was followed to bond composite patches to selected specimens. Final specimens both with and without the bonded laminate are shown in Figure 5-4.

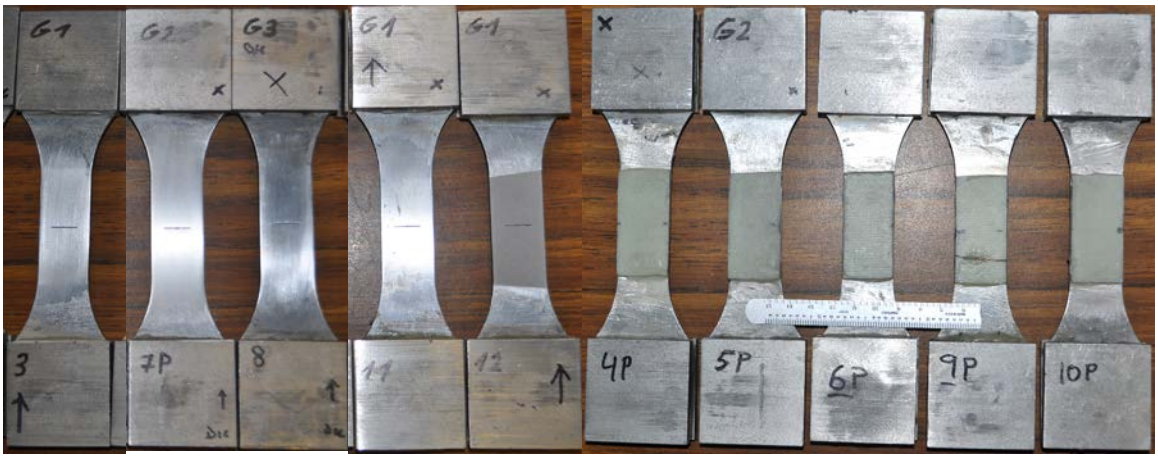

Figure 5-4 Final small scale CCT specimens.

5.1.4 Small Scale CCT Static Testing Procedures

Small scale CCT specimen testing, both round one and two, followed the same procedures for initial fatigue crack growth and static loading rates.

Prior to low cycle fatigue crack growth baseline load data was taken at 0, 200, and 2000 N. Then to generate sharp crack tips tensile-tensile fatigue loading was applied with a load ratio (R) of 0.1 and a peak load of 2000 N at a frequency of 10 Hz. For the initial geometry to the final crack length the nominal ΔK_I was between 5.0 and 6.4 MPa-$\sqrt{m}$. During crack growth fatigue loading was paused every 20k and 10k cycles to capture static DIC images for round one and two respectively. Images were captured at 0, 200, and 2000 N to process and compare with baseline images for each specimen. For each fatigue testing pause and each load level 20 static images were taken.

Quasi-static loading was performed under displacement control at a rate of 0.003 mm/sec. During loading DIC images were taken at varying frequencies. For each specimen a set of 20 images were taken at zero load to establish DIC processing parameters and the speckle pattern bias and error. During loading of unpatched aluminum specimens images were captured at rates of 1, 4, and 2 per second for load ranges of 0 to 2000 N, 2000 to

4000 N, and 4000 N to peak respectively. For patched specimens the image rates were the same for load ranges of 0 to 3000 N, 3000 to 6000 N, and 6000 N to failure respectively.

5.2 Large Scale CCT Test Specimen Geometry and Manufacturing Details

Test specimens are an aluminum panel cut to size with a machined notch that was fatigue precracked under stress intensity (*K*) control to develop a sharp crack tip. Precracked specimens are then prepared for the composite patch repair procedure, that consists of mechanical abrasion, acid etch, silane treatment of the surface, hand wet-out lamination, and vacuum consolidation of the composite patch. The test configuration and nominal specimen configuration are shown in Figure 5-5, with nominal specimen dimensions of 950 x 280 mm mounted in a 245 kN MTS 809 Axial/Torsion hydraulic test frame.

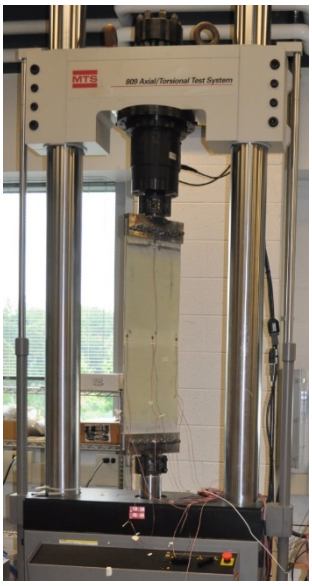

Figure 5-5: 245 kN MTS axial/torsion load frame with 950 x 280 mm large scale CCT test specimen.

5.2.1 Large Scale Aluminum Plate Geometry

Full thickness rectangular specimens were cut to nominal dimensions of 279.4 mm wide by 952.5 mm long. The aluminum alloy was 5456-H116 with assumed nominal yield and ultimate strengths of 227.5 MPa and 317.2 MPa [94]. Cracks were oriented in the transverse-longitudinal (T-L) material direction, as defined in ASTM E399 [84], with the load applied in the materials longitudinal-transverse (L-T) direction normal to the crack plane. Typical aluminum data for 5xxx alloys shows strength in the long-transverse direction as 10% lower than the longitudinal direction [96].

Aluminum panels were cut to size with a machined notch that was fatigue precracked under *K* control to develop a sharp crack tip. Precracked specimens are then prepared according to the composite patch repair procedure [100] that consists of mechanical abrasion, acid etch, silane treatment of the surface, hand wet-out lamination, and vacuum consolidation of the composite patch.

5.2.2 Large Scale CCT Surface Preparation

The procedure selected to manufacture the large scale specimens represents shipboard composite patch installations and laboratory data and experiences during process development. Galvanically compatible abrasives & media must be used since the residue remaining in abrasions can create a galvanic cell [101]. First, the surface was wiped with acetone to remove oils and contaminants. Then the aluminum surface was abraded with a 3M Strip and Clean XT purple disc to remove aluminum manufacturing scale. Final abrasion is performed with 60-grit aluminum oxide sandpaper on an orbital or dual action sander. Silica-based sandpaper should not be used for bond surface preparation.

Chemical etching of the surface is done using a DX-579 phosphoric acid and distilled water mix applied with an acid resistant scrub brush. Two scrubs are done keeping the surface wet for a minimum of 2 minutes then wiped dry with clean lint-free and dye-free paper towel or similar synthetic shop towel. The surface was rinsed with distilled water to remove reaction residue and neutralize any remaining phosphoric acid. Once rinsed, a flash break test was performed to verify a chemically active surface. Contaminants on the surface cause the water to bead, while water droplets flattening on the surface indicate a clean surface with surface energy required for quality adhesive bonding. The final process matches that of the small scale specimens, the surface was then treated with 3M's AC-130-2 bonding agent. Once cured the surface was ready for lamination.

5.2.3 Large Scale CCT Lamination Procedure

The lamination process consists of dry fabric for the laminate stack, mixing the M1002-M2046 resin and hardener, wet-out of the fabric, placement of the peel ply, P3 perforated film, bleeder cloth, and vacuum bag. Once the vacuum bag was sealed, vacuum was

applied to consolidate the laminate stack where excess resin flows through the perforations and is absorbed by the bleeder cloth as shown in Figure 5-6.

Figure 5-6 Large scale CCT lamination procedure. Clockwise from the upper left the plies are placed and wet-out with resin. Once fully impregnated with resin the laminate stack is applied and vacuum consolidates the stack.

Final nominal dimensions for the laminate are shown in Figure 5-7 and represent lamination consolidated at a vacuum level of 10 in-Hg applied approximately 1 hour after mixing with a single ply of bleeder cloth. The laminate was 760 mm long and 279.4 mm with 89 mm tapers on the top and bottom edges and full thickness on the cut edges. In this configuration the full thickness laminate extended 291 mm from the crack in both directions.

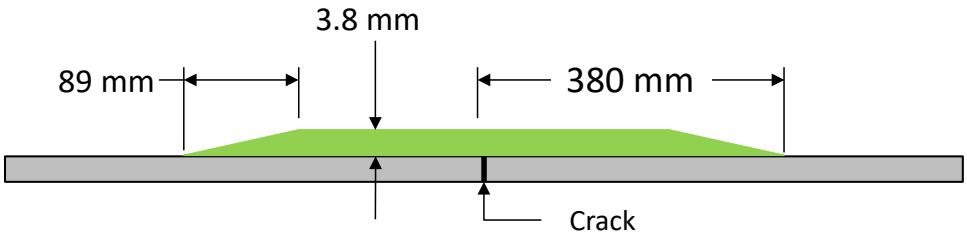

Figure 5-7 Typical composite patch repair configuration.

The test configuration and nominal specimen configuration are shown in Figure 5-8. Standard LEFM CCT specimen configuration and testing parameters were followed. Specimen bolted joint and composite reinforcement configuration are shown in Figure 5-9 with the bolt pattern, overall plate dimensions, patch details, and end connection details listed in Table 12 and shown in Figure 5-10.

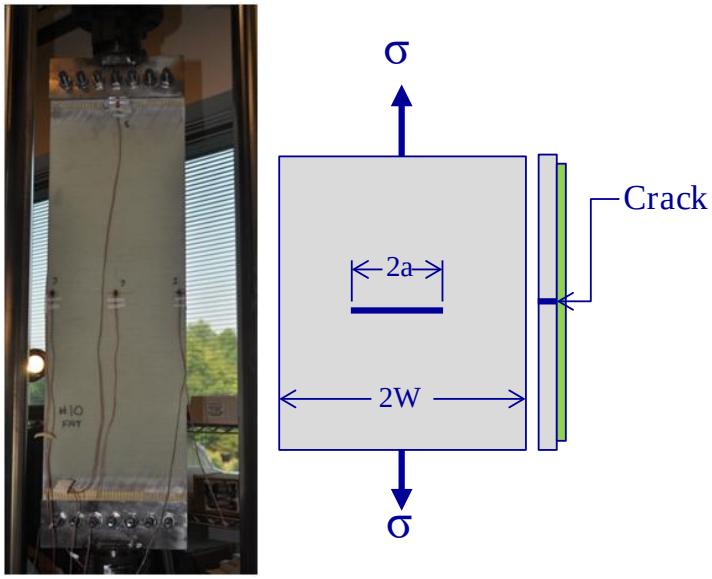

Figure 5-8: Large scale composite patched CCT specimen configuration.

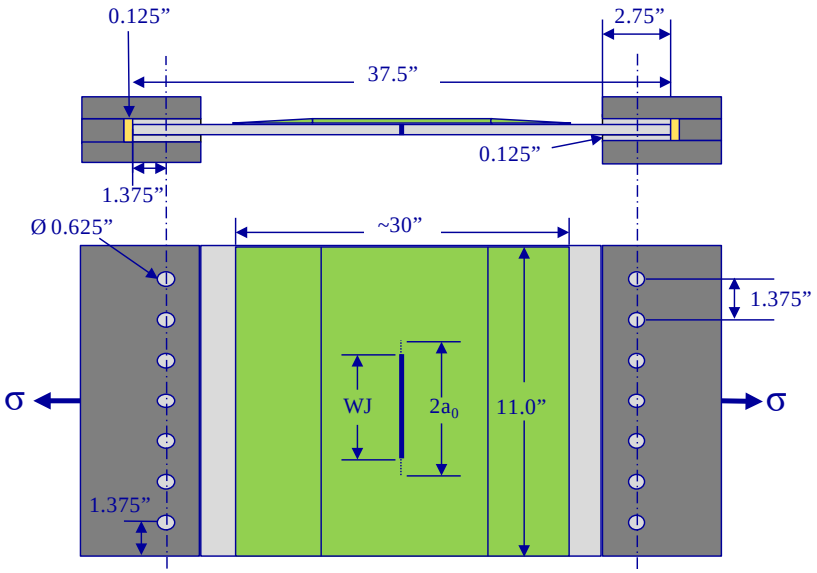

Figure 5-9: Large scale CCT test specimen geometry and dimensions.

Table 12: Nominal Large Scale CCT Test Specimen Dimensions.

Specimen Width [in]	11
Specimen Length [in]	37.5
Patch Length [in]	~30
Number of Bolts	7
Bolt Diameter [in]	0.625
Pitch [in]	1.375
Bolt Edge Distance [in]	1.375
Bolt Side Distance [in]	1.375
WaterJet Notch (WJ) [in]	4.9
Tab Thickness [in]	0.125
Tab Length [in]	2.75

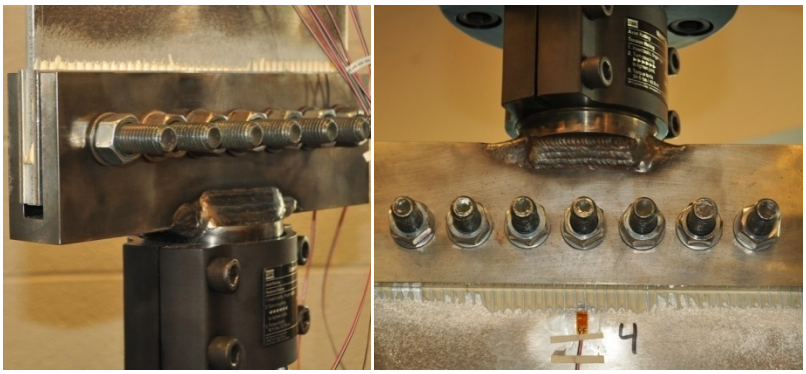

Figure 5-10: Threaded collar connections to the actuator (L) and load cell (R).

5.2.4 Large Scale Static Test Matrix and Procedures

Large scale CCT specimens were made to measure the performance of the composite patch repair technique and provide proof of concept for the original shipboard installed repairs. Table 13 lists the specimen, load, and instrumentation details for panels made for static testing to ultimate failure and to provide baseline comparison of cracked aluminum plate behavior and composite patch repaired plate behavior under a quasi-static tensile load with a 178 mm crack.

Table 13: Large Scale Static Test Specimen Matrix.

Configuration	Aluminum Condition	Initial Crack Length	Strain Gauges	Specimen ID
Unpatched	As-Delivered	177.8 mm	6	5
Unpatched	As-Delivered	177.8 mm	6	7
Unpatched	As-Delivered	177.8 mm	6	8
Patched	As-Delivered	177.8 mm	7	4
Patched	As-Delivered	177.8 mm	7	9
Patched	As-Delivered	177.8 mm	7	13
Patched	Oven Sensitized	177.8 mm	7	21

5.2.5 Large Scale CCT Specimen Instrumentation

Each specimen was fitted with axial strain gauges aligned with the load direction and a ring gauge to monitor the COD at the center of the panel. On patched specimens the ring gauge was fitted to the notch on the bare aluminum side because the notch was covered on the patched side. Along with the initial half crack length (a_0), the COD measurement is used to calculate specimen compliance, current crack length, and stress intensity for the control software commanding the test frame.

The axial strain gauge configuration is shown in Figure 5-11. Gauges are Micro Measurements CEA-06-250UW-350, which have a 0.25 inch long gauge length with 350

Ohm resistance. Aluminum specimens had 6 gauges, while composite patch repaired specimens had an additional axial gauge bridging the crack on the laminate at the center of the specimen.

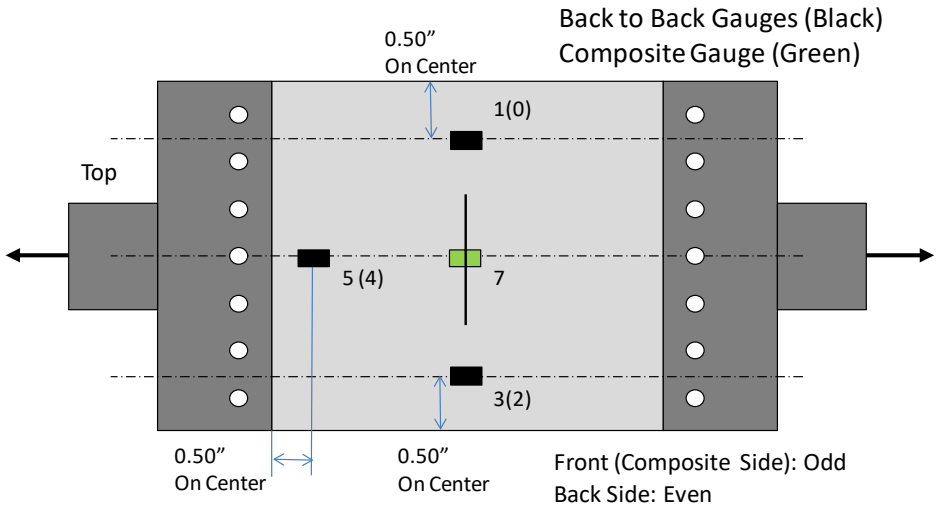

Figure 5-11: Large scale strain gauge configuration shown from the front side. Parenthesis indicate gauge is on the composite side.

The COD measurements were performed using a John A. Shepic Co. SFDG-30 ring gauge, as mounted in the specimen in Figure 5-12. The ring gauge has a maximum opening displacement of 0.3 inches with output from 0 to 10 volts. Gauge calibrations were performed from the minimum opening of 0.023 inches to the maximum 0.30 inches prior to each test.

Figure 5-12: Ring gauge mounted in machined notch of specimen.

5.2.6 As-Tested Large Scale Specimen Dimensions

Test specimens were measured prior to pre-cracking and testing according to Figure 5-13. Aluminum plate thickness and total thickness of composite patch repaired specimens were also measured. When possible, post-test fracture surface measurements were made for dimensions W1 and W2. The initial crack front shape was inspected and measured on each specimen after testing. Specimen measurements are listed in Table 14.

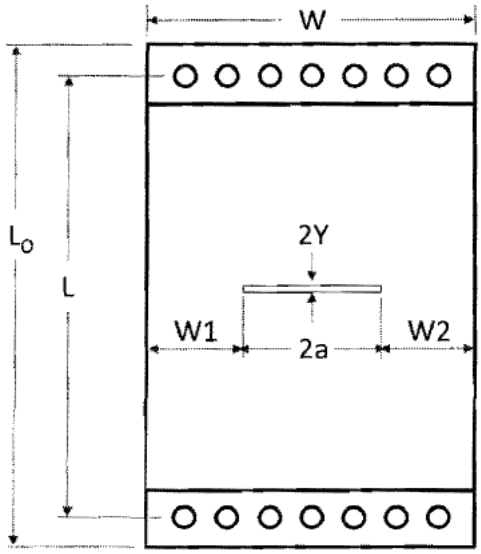

Figure 5-13: Large scale CCT test specimen dimensions.

Table 14 Large Scale Test Specimen Dimensions.

	Initial Geometry (in)						Post Test Inspection		
Specimen Label	B (thick)	B patch	W	LO	L	2Y	W1	W2	2a
4	0.250	0.380	11.008	37.5		0.034	1.957	1.965	7.086
5	0.249	na	10.974	37.5		0.023	2.112	2.143	6.719
7	0.255	na	11.018	37.5	34.50	0.023	2.300	2.163	6.555
8	0.255	na	10.993	37.5		0.036	2.136	2.109	6.748
9	0.255	0.389	10.980	37.5		0.033	na	na	na
13	0.250	0.405	11.003	37.5	34.75	0.034	na	na	na

5.2.7 Large Scale Static Testing Load Frames

Tests were conducted in Code 65's composite lab in Building 60 using a MTS Model 809.25 axial torsion hydraulic test system with 6 inches of travel and 55 kip axial capacity. Torsion capabilities of the machine were not employed in this study. The test system was run by the MTS FlexTest SE controller. Precracking was performed using input from the Fracture Technology Associates (FTA) control system, that allows the user to define the applied stress intensity profile [102]. COD and LEFM are used to

calculate the stress intensity at the crack tip for symmetric specimens without composite patch repairs.

Ultimate strength tests were conducted in Code 61's testing lab in Building 60 using the two post MTS axial hydraulic test system with a 75 kip axial capacity actuator. The test system was run by an MTS FlexTest controller and the FTA controller controlling ring gauge output.

5.2.8 Large Scale CCT Testing Procedures

Specimens and testing procedure were guided by standard composite material test procedures ASTM D3039, ASTM E647 [103], ASTM E561-08 [104], and US Air Force Damage Tolerant Design Handbook [105]. Instrumentation was calibrated for the initial load segment for each static test specimen. If static testing required multiple load segments, the initial calibration was retained and the testing restarted. Static specimens were loaded in tension until failure of the aluminum plate, composite patch repair, or the load limit of the test frame.

5.2.8.1 Large Scale Static Center Crack Tension Testing

Static testing was performed on the 245 kN MTS hydraulic test frame in Code 65's composite lab and the two post 330 kN MTS hydraulic test frame in Code 61's test lab. Specimens 5, 7, 8, and 4 were tested on the 245 kN machine with a load rate of 1.5 mm/min. Specimens 9 and 21 were testing on the 330 kN frame with a load rate that varied from 3.0 to 6.0 mm/min to accommodate the time required to perform multiple load sequences. All static specimens had an initial 127 mm machined notch which was grown to 178 mm under *K* controlled fatigue loading.

Aluminum only specimens achieved a peak load and failed with the crack propagating across the full width. Composite patched specimens did not fail under static loading (the crack did not propagate across the full width) because the load capacity of the test machine was reached before failure could occur. Specimen 4 was loaded once statically to 245 kN followed by 1,321 load cycles with an R of 0.1 and a peak load of 222 kN. Specimens 9 and 21 each saw two load cycles to 330 kN with 3.2 mm of crack growth on each side and approximately 17.8 mm of out-of-plane set after the first load cycle. Although elliptical laminate whitening occurred around the notch, laminate failure did not occur as confirmed by ultrasonic inspection.

6 Finite Element Model Details and Numerical Predictions Methods

This section covers the details of the small scale finite element model. Element selection, mesh refinement, ABAQUS output type and location, and the methods and limitations of the strain energy release rate predictions. Both small and large scale numerical predictions use ABAQUS finite element analysis (FEA) software. Standard ABAQUS outputs were used with both built-in and custom fracture mechanics methods used to predict SERR and J-integral values at the crack tips. Full results will be directly compared with test data in a later section.

6.1 Small Scale CCT Specimen Finite Element Model

Numerical predictions for the small scale specimen response were performed using a Finite Element Model (FEM) in the commercial software ABAQUS. The extended finite element method (XFEM) was used to define the crack and perform calculations of strain energy release rate at the crack tip and the J-integral around element defined paths ahead of the crack tip. Full integration linear brick elements (C3D8) elements were used for all materials and the crack plane was defined by the built-in XFEM method to split the solid elements [52]. The model was loaded in axial tension using nodal displacement control with only the surface nodes in the grip regions being displaced in the Y-direction. Displaced nodes were free to move in the X- and Z- directions to minimize nodal stress concentrations at the applied boundary conditions with mid-plane nodes constrained in the Z-direction. Large displacement formulation was used to account for nonlinear geometry due to bending from the asymmetric reinforcement when possible; limitations for J-integral calculation methods will be discussed later. Best practices were followed for the number of elements through the thickness and ahead of the crack tip while maintaining element

aspect ratios as close to one as possible. A minimum of five elements through the thickness was recommended to capture through thickness behavior and 0.5 mm elements were used to capture the strain gradient along the crack path [106, 15]. The resulting finite element model (FEM), shown in Figure 6-1, had ten elements through the thickness for the aluminum and five elements through the thickness for both the adhesive layer and the composite patch. Elements adjacent to the crack plane are 0.2 mm long (X) and 0.196 mm high (Y). Element thicknesses in the Z-direction vary; Aluminum elements are 0.226 mm thick, adhesive elements are 0.112 mm thick, and composite patch elements are 0.254 mm thick. The resulting element aspect ratios range from 0.56 to 1.30 in the region around the crack.

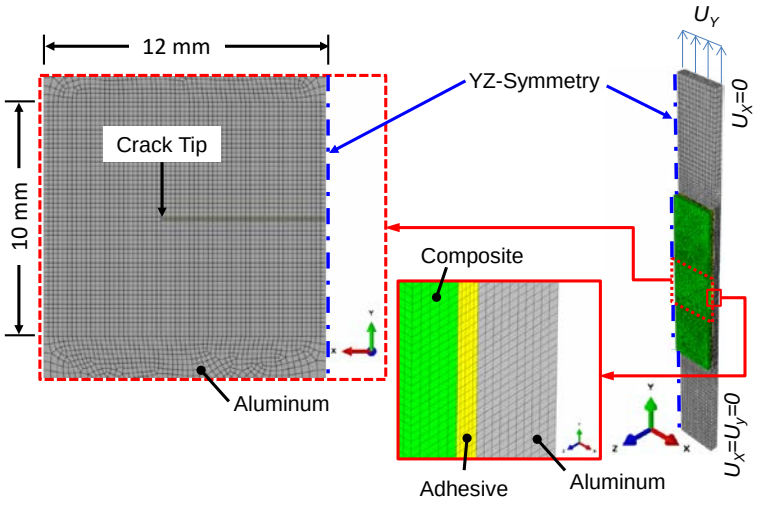

Figure 6-1 First round small scale specimen half symmetric finite element model and boundary conditions.

Modeling of the second round of small scale CCT specimens added two major details; Radius transition to the grip section and dummy hyper elastic plane stress shell elements in rectangular paths encompassing the crack tip. As shown in Figure 6-2, the test section element details and boundary conditions remain the same from round one with the addition of the transition regions and the grip areas. Dummy surface elements are plane

stress CPS4R elements with negligible stiffness and use surface nodes along the integral paths represented by the red line in Figure 6-2. Dummy elements are located on both the free surface and patched surface about the crack tip to match paths defined for DIC data processing shown in Figure 6-4. Elements use existing nodes and displace with the structural elements. The first order Ogden material parameters are orders of magnitude lower than typical rubber properties in ABAQUS example problems with the shear modulus (μ_1) of 0.1 MPa, principal stretch exponent (α_1) of 1.3, and the bulk modulus material parameter (D_1) of 0.2 MPa which is 2 divided by the bulk modulus (K_0). Negligible response contribution of the dummy elements was confirmed by running models with and without dummy elements and comparing the crack tip strain results.

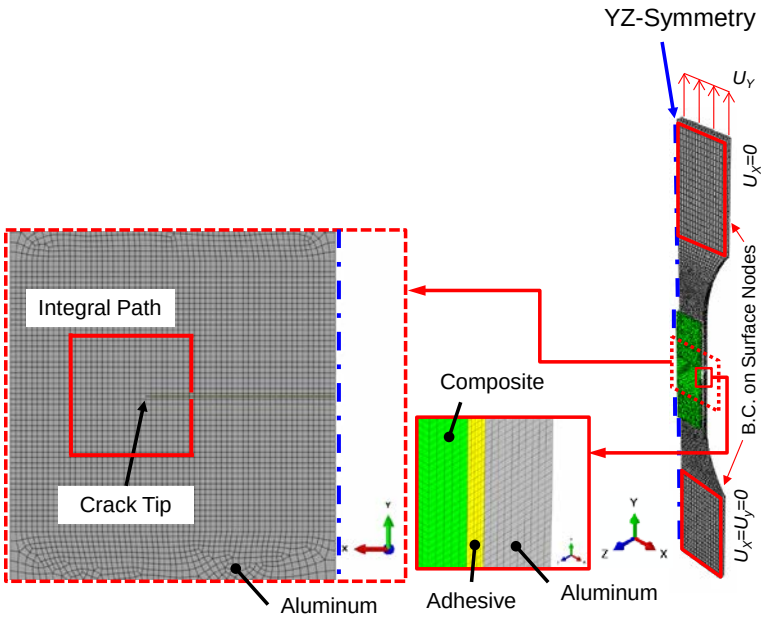

Figure 6-2 Second round small scale specimen half symmetric finite element model and boundary conditions.

6.1.1 Small Scale Numerical J-Integral Prediction Methods

Two methods were used to calculate the J-integral using built-in XFEM processing methods. The basic method uses the virtual crack closure technique (VCCT) that is based

on LEFM and uses crack geometry and nodal forces to calculate the strain energy release rates (G_i) for three modes (i = 1 to 3). Output from VCCT is the strain energy release rate (G), which for linear elastic material is equivalent to the J-integral ($G=J$). This method does not capture nonlinear behavior of the strain energy release rate as the material deforms plastically ahead of the crack tip.

Extension to EPFM theory is required to accurately capture the nonlinear behavior of the SERR at the crack tip using the J-integral, that can be calculated using the line integral as outlined in section 2.5 and a domain integral method. The domain integral method has been used for DIC data [63] as well as numerical prediction. The domain integral method built into ABAQUS uses procedures developed by Parks [107] and Shih, Moran, and Nakamura [108], who used virtual crack extension and the domain integral methods to calculate the value of the J-integral at the crack tip. This takes an area, or domain, defined by inner and outer contours, or paths. Implementation of this method is limited to the rings of elements defined mesh at the crack tip. The first contour is defined by the elements connected to the crack tip nodes and each successive contour is made of elements that boarder the previous contour. This method is limited to the small displacement solution, and although one can account for nonlinear material behavior the large displacements from combined bending and elastic-plastic material deformation are not adequately captured.

Predicting the out of plane bending and elastic-plastic material behavior at the crack tip requires the large displacement assumption. This requires a novel approach extracting the deformation gradient and subsequently the raw displacement gradients directly from rings of elements that enclose the crack tip. In ABAQUS, shell elements using hyper elastic

material behavior allow direct output of $\boldsymbol{F}$. Plane stress CPS4R elements with negligible stiffness were configured on both the free surface and patched surface about the crack tip to match paths defined for DIC data processing shown in Figure 6-4. Elements use existing nodes and displace with the structural elements. The first order Ogden material parameters are orders of magnitude lower than typical rubber properties in ABAQUS example problems with the shear modulus (μ_1) of 0.1 MPa, principal stretch exponent (α_1) of 1.3, and the bulk modulus material parameter (D_1) of 0.2 MPa that is 2 divided by the bulk modulus (K_0). To match DIC results for the J-integral, the raw displacement gradients must be determined from the deformation gradient tensor, $\boldsymbol{F}$, which defines a path between the reference and the deformed material state:

$$d\vec{x} = \boldsymbol{F} d\vec{X} \qquad \text{Equation 128}$$

Where the 2D tensor, $\boldsymbol{F}$, contains the partial derivatives along that path:

$$\boldsymbol{F} = \begin{bmatrix} {\partial x_1}/{\partial X_1} & {\partial x_1}/{\partial X_2} \\ {\partial x_2}/{\partial X_1} & {\partial x_2}/{\partial X_2} \end{bmatrix} \qquad \text{Equation 129}$$

An alternative definition for the current state uses the displacement tensor added to the reference state as shown in Equation 130. Taking partial derivatives of the reference state displacement tensor replaces the left side of Equation 128 and rearranging terms yields the relationship between the deformation and displacement gradients shown in Equation 130.

$$\vec{x} = \vec{X} + \vec{u} \rightarrow \boldsymbol{F} = I + \begin{bmatrix} {\partial u_1}/{\partial X_1} & {\partial u_1}/{\partial X_2} \\ {\partial u_2}/{\partial X_1} & {\partial u_2}/{\partial X_2} \end{bmatrix} \qquad \text{Equation 130}$$

The ***F*** tensor can be directly extracted from the output of hyper-elastic elements, then displacement gradients are determined from the predicted ***F*** tensor for each path element for each analysis increment. The results can then be post processed using simple trapezoidal quadrature to evaluate the integral in Equation 118.

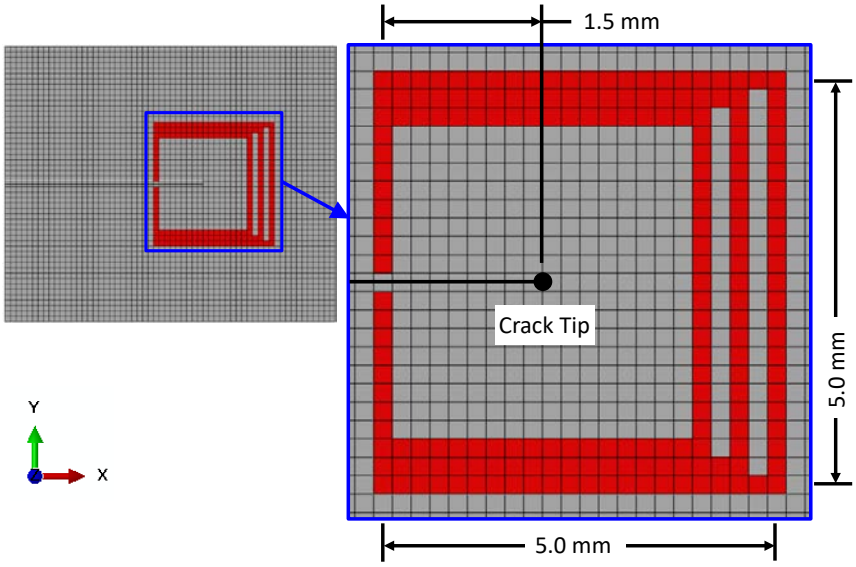

Figure 6-3 Configuration of dummy hyper elastic plane stress elements along the J-integral paths.

6.1.2 Large Strain Field and Volume Data and Results Extraction Details

General response correlation for this study is based on the axial load (*P*), COD, and an arbitrary 1 mm^2 area directly ahead of the crack tip, the locations of which are shown on the left side of Figure 6-4. Results for path and domain J-integrals are discussed later and use displacement gradients extracted along the rectangular paths shown on the right hand side of Figure 6-4. Rectangular paths simplify the numerical methods, encompass the crack tip, and are away from the initial plastic zone development at the crack tip.

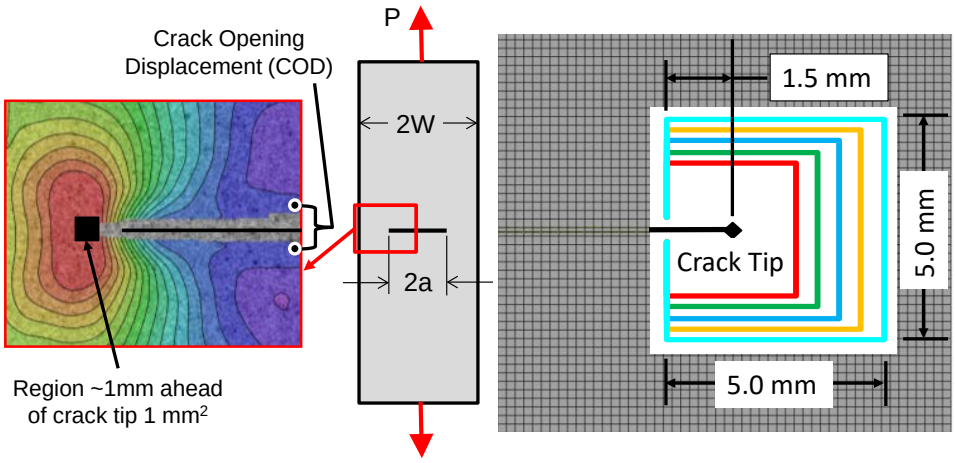

Figure 6-4 Results output locations for DIC and FEA. Average strain area ahead of the crack tip and COD locations (L) and J-integral paths for DIC and FEA (R).

Crack tip plastic zone evolution was studied using the displacement and strain fields for unpatched and patched CCT specimens. Comparison was performed by processing data extracted along radial crack tip paths, *r* and θ, from 0 to 90 degrees shown as the blue lines of the representative area in Figure 6-5. Results were extracted from the AOI centered about the crack plane, which were 15 and 10 mm tall (V and Y directions) for the DIC and FEA, respectively as shown in Figure 4-2 and Figure 6-1. Assumed symmetry of the FEM reduces that area to half the specimen width and one crack tip. The initial plastic zone radial positions and large strain boundary for both the free surface DIC and FEA are extracted along the radial paths for strain magnitudes unique to each COD level compared. That radial position, noted at the end of the blue lines, can then be used to approximate the area of large strain for direct comparison. Large strain volume comparison is done through the thickness using 2D surfaces at positions along the Z-axis (Z_{pos}) of the FEM to generate a representative volume. 2D surfaces can then be generated at segment midpoints by interpolating between surfaces using 3D vectors between large strain positions for each triangular region (highlighted yellow wedge). Midpoint areas are

integrated along the Cartesian Z-direction to estimate the volume of each wedge that were then summed for the representative volume estimate.

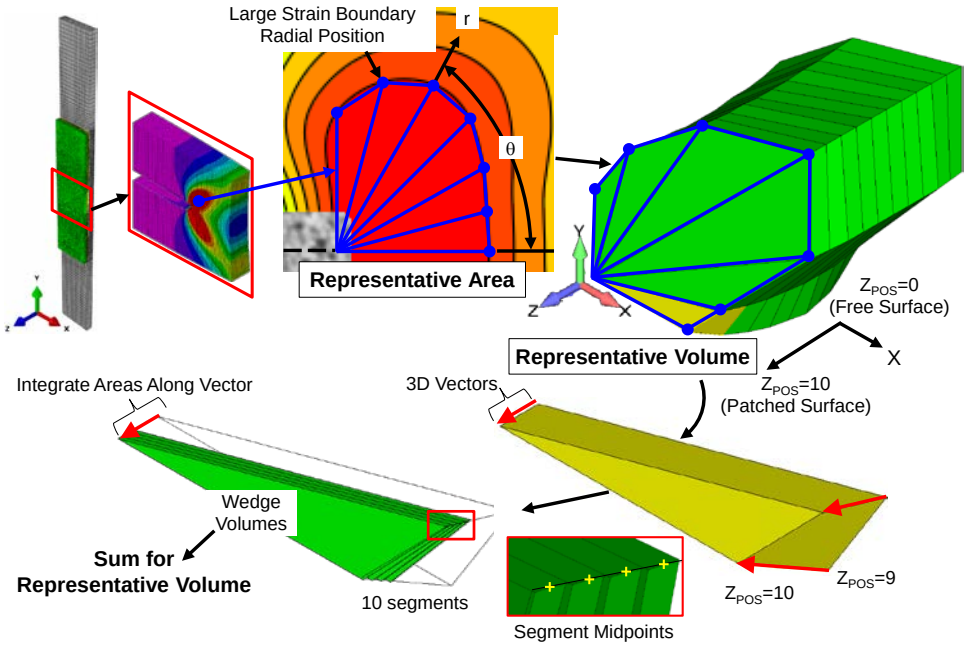

Figure 6-5 Process to measure large strain boundary radial positions relative to the crack tip, estimate the area, and integrate XY areas through the thickness to estimate volume.

Investigating the evolution of the plastic zone and later the large strain zone was done using von Mises strains on the free surface. Measured DIC von Mises strains are calculated from the directional strains using Equation 122. To compare FEA to DIC, predicted directional strain components were used to calculate the 2D von Mises strains at each integration point in the FEM using Equation 122. Quantitative comparison of the large strain boundaries and representative areas were performed along with presenting the qualitative comparison of the measured to predicted free surface regions for CODs of 0.024, 0.11, 0.20, 0.31, and 0.41 mm. These COD values correspond to the linear elastic response limit, initiation, middle, and end of crack blunting.

6.2 Large Scale CCT Specimen Finite Element Model

For the large scale specimens both analytical and numerical predictions were performed, however, only surface axial strain gauge data is available for comparison because no full field DIC data exists.

6.2.1 Large Scale CCT Specimen Finite Element Model

The Finite Element Model (FEM) used specimen geometry from the initial design and the average laminate and aluminum properties listed in Table 11 and Table 2, respectively. Linear elastic solid C3D8 brick elements were used to represent the aluminum plate and composite laminate, respectively. Analyses were run using ABAQUS and XFEM elements using the Virtual Crack Closure Technique (VCCT) method to calculated crack tip LEFM response [52]. The combination of nonlinear geometry with elastic-plastic Ramberg-Osgood aluminum behavior captured both out of plane bending due to the neutral axis being offset from the load line and aluminum yielding behavior close to the crack tip. Analyses were performed under displacement control with the forces output at the control node for each analysis increment. Loads were doubled to represent the full specimen. Loading was assumed to be uniform across the 6.35 mm thick unsupported aluminum plate. In the FEM this was done using rigid elements connecting the single control node to all nodes in the tabbing area. On the reaction side of the model all nodal displacements in the tabbing area were rigidly constrained. To reduce the degrees of freedom and LEFM calculations performed per step, symmetric Boundary Conditions (BC) were used along the load axis, forming a half-symmetry model. The left edge of the FEM shown in Figure 6-6 represents the loading axis. The crack plane is explicitly modeled using XFEM elements, shown in Figure 6-6, with surface contact and tied nodes

to define the interface between the aluminum and composite patch laminate. A total of 325,179 nodes and 279,960 C3D8 elements were used in the refined model. Elements adjacent to the crack plane are 0.60 mm long (X) and 0.59 mm high (Y). Element thicknesses in the Z-direction vary; Aluminum elements are 0.63 mm thick and composite patch elements are 0.69 mm thick.

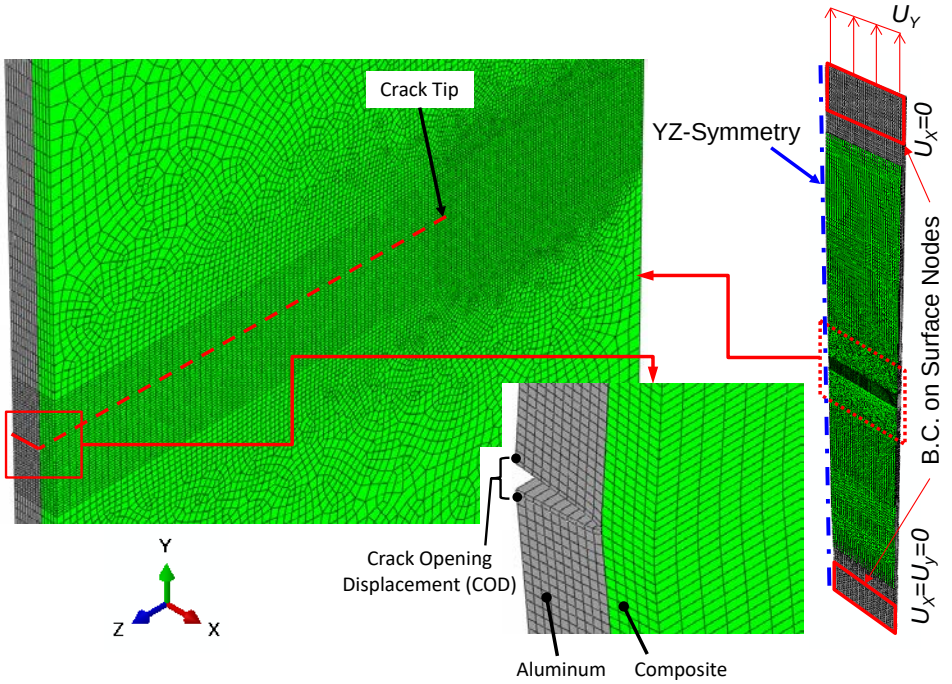

Figure 6-6: Finite element model and defined crack plane with the nodal extraction points to calculate COD and boundary conditions.

Post processing of FEA results was reduced to regions of interest. The COD was the vertical displacement difference between the surface nodes along the plane of symmetry, as shown in Figure 6-7. The crack tip stress singularity is represented within the XFEM element volumes that are intersected by the crack plane. LEFM results are output at the crack tip to get through thickness SERR values. Surface directional strains were extrapolated to the nodes and averaged to compare with existing strain gauge data at locations shown later in Figure 5-11. Analysis of the strain fields ahead of the crack tip

was performed using the same method described for the small scale specimen. The radial paths used for large strain results extraction are shown in Figure 6-7. Results are extracted at each element layer through the thickness for a total of eleven surfaces to calculate the representative large strain free surface area and through thickness volume.

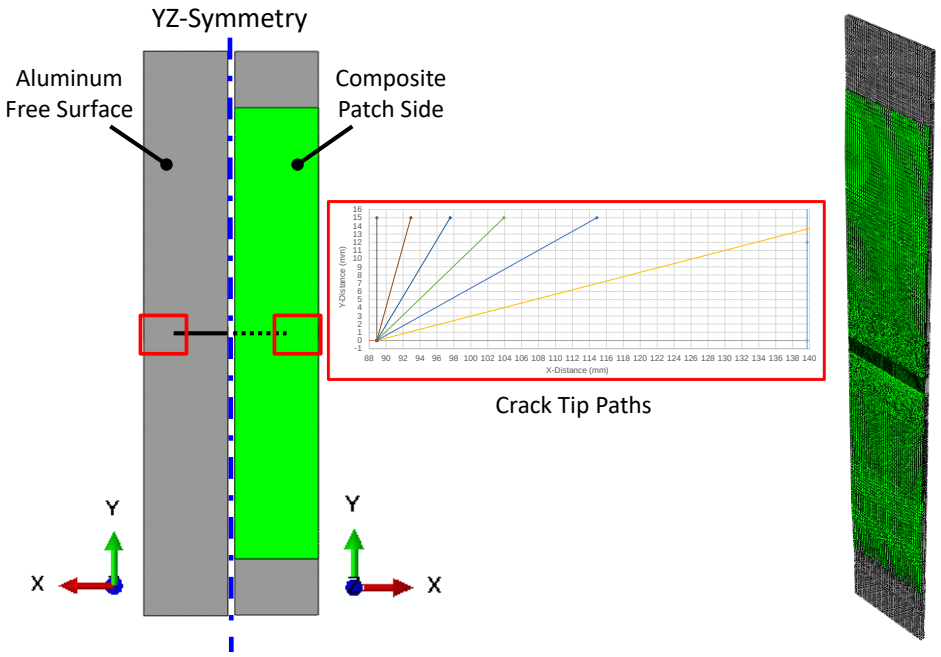

Figure 6-7: Large scale FEM crack tip extraction paths for directional strain components.

7 Center Crack Tension Testing and Analysis Correlation

Numerical predictions for both small and large scale CCT specimens were compared with test results. Specimens consisted of an aluminum plate with pre-fatigued crack grown from a machined notch, and if applied, a composite patch repair across the crack plane. All tests were performed monotonically until failure or test frame capacity was reached. Although large scale testing was performed first, the small scale results will be reported first.

7.1 Round One Small Scale CCT Testing and Analysis Correlation

Two rounds of small scale CCT testing will be covered in this section. Details of the data and prediction results are discussed in the round one small scale section. The same methods are then used for both round two small scale and large scale results.

7.1.1 Round One Small Scale CCT Sharp Crack Tip Development

Sharp crack tips were necessary to provide distance between any local residual effects from machining and to match assumed perfect crack tips in analytical and numerical models. Cracks were grown from the machined notch under low load and high cycle tension-tension fatigue. The load ratio was 0.1 for a tensile load that varied from 200 to 2000 N at a frequency of 10 Hz. The resulting effective ΔK was between 5.6 and 6.7 MPa-$\sqrt{m}$, that resulted in a nominal cycle count of 100K to achieve crack growth of approximately 1 mm. DIC was used to track crack tip displacement and strain fields from the initial baseline state. Fatigue loading was paused every 10-20k cycles to allow sets of static images to be taken for static loads of 0, 200, and 2000 N. Images and DIC data were used to track crack growth and quantify the final state of the sharp crack tip. With

sharp crack tips and a crack length (2a) of 14 mm the specimens were paired by crack length and one of each pair received an adhesively bonded composite patch.

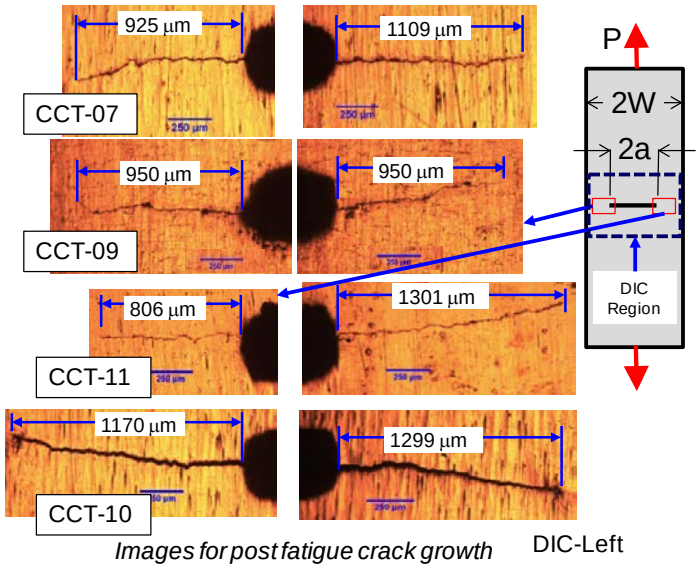

Figure 7-1 Round one post fatigue crack growth images

7.1.2 Round One Small scale Test DIC Processing Parameters

Images for DIC resulted in a nominally 28.2 mm x 14.9 mm overall field of view (FOV). With a little trial and error the initial depth of field (DoF) was set so that the free surface remained in focus for the range of out-of-plane deflection experienced minimizing bias error due to movement relative to the camera lens. Estimated out-of-plane displacement is the difference in the load line through the aluminum plate and the aluminum/composite centroid. The estimated out of plane displacement is maximum at the center of the notch on the free surface with a magnitude of 0.36 mm and is assumed to not warrant the use of 3D DIC. Images were processed using a subset size of 51x51 pixels (0.35 x 0.35 mm) and a step size of 10 pixels (0.069 mm). The strain filter was selected done using 20 initial images taken at zero load to minimize the bias and error associated with the speckle pattern and to determine filter selection on relative maximum of average von

Mises strain ahead of the crack. Across the specimens the nominal bias (offset) magnitude was 50 με with an error of 15 με (deviation) with strain filters that ranged from 31 to 41 data points. Arbitrary visual inspections of the contour patterns were used to confirm the strain filter selection with the goal of removing the wavy contour shapes without missing the local strain peaks. Once filtered the data points are smoothed using a center-weighted Gaussian filter across 15 data points.

7.1.3 Comparison of Round One Patched and Unpatched Specimen Response

The data reported in this section is limited to two unpatched and two patched specimens. Load versus crack opening displacement (COD) response due to monotonic tensile loading was consistent between like specimens. Static DIC images were processed for displacement and strain data and used to identify stages of failure progression from the linear elastic response through crack blunting and then finally crack growth until specimen failure. Load response with crack stage progression is shown in Figure 7-2 and the DIC measured average von Mises strain ahead of the crack tip versus COD is shown in Figure 7-3. The data indicates crack stage progression on the free surface for both patched and unpatched specimens occurs at the same COD magnitudes. In other words, crack blunting for both unpatched and patched specimens occurs from just beyond the elastic response limit at a COD of 0.11 mm until the end of crack blunting at a COD of 0.41 mm. Beyond crack blunting the voids coalesce into crack growth and peak load at a COD of 0.57 mm, the point at which the load required to achieve that COD is 160% greater for the patched specimen. Because the behavior of patched and unpatched specimens correlates as a function of COD, one can assume crack tip behavior plays a significant role in the failure progression. Evidence of patch disbonding occurs in

unprocessed static digital images used for DIC where adhesive was visible through the notch. When the patch adjacent to the notch is fully bonded, relative displacement between successive images was not detectable. During the crack growth, adhesive yielding response, and prior to the load drop sudden relative displacement between the notch and adhesive is visible. The sudden relative displacement coincides with initiation of the load drop and indicates disbonding of the patch. Based on observations made during testing and static images, adhesive yielding and failure continues until bond failure of half the patch, the point at which the crack growth behavior is only that of the aluminum. The disbond of the topside of the patch (a) is shown on the right side of Figure 7-2 along with the failed aluminum specimen (b). When comparing post peak load aluminum fracture at 3,500 N, the load level after patch failure, the COD is 20% greater for the patched specimen shown by the blue line in Figure 7-2. This additional 0.2 mm of COD on the free surface is related to the behavior of the crack tip plastic zone and tensile ligament ahead of the crack, which is partially constrained by the one-sided bonded patch reinforcement.

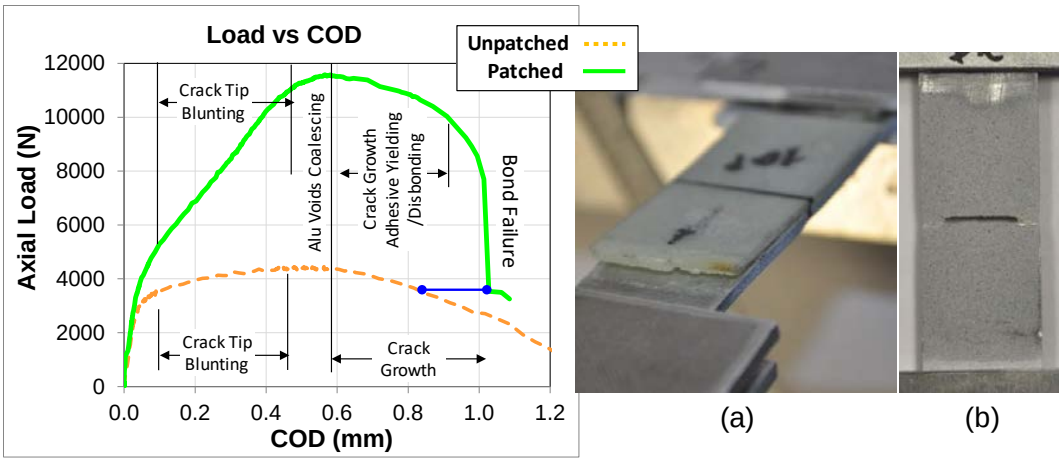

Figure 7-2 Consistent load response behavior as a function of COD with failure modes of a tested patched (a) and unpatched (b) specimen

Comparison of free surface von Mises strain behaviors of unpatched and patched specimens as a function of COD are shown in Figure 7-3. The strain values plotted are averaged over a 1 mm^2 region nominally 1 mm ahead of the crack tip. The strain behaviors ahead of the crack tip correlate into crack tip blunting at a COD of 0.3 mm, the point at which adhesive plasticity is assumed to play a role in the response. When the COD is greater than 0.3 the slope of the von Mises strain versus the COD of the patched specimen is lower than the unpatched specimen that is presumed to be related to an increase in the region of plastic shear stress in the adhesive layer. Near peak load, COD of 0.6 mm, the slope of the local strain response is the same for unpatched and patched specimens although there is a COD offset. Unpatched aluminum exhibits tearing and a gradual drop in load near failure. Composite patched specimen load decreases with a combination of crack growth and disbonding until full bondline failure resulting in a large load drop. As the composite patch bond fails, free surface strains level off and the patch reinforcement no longer constrains the aluminum on the patched side.

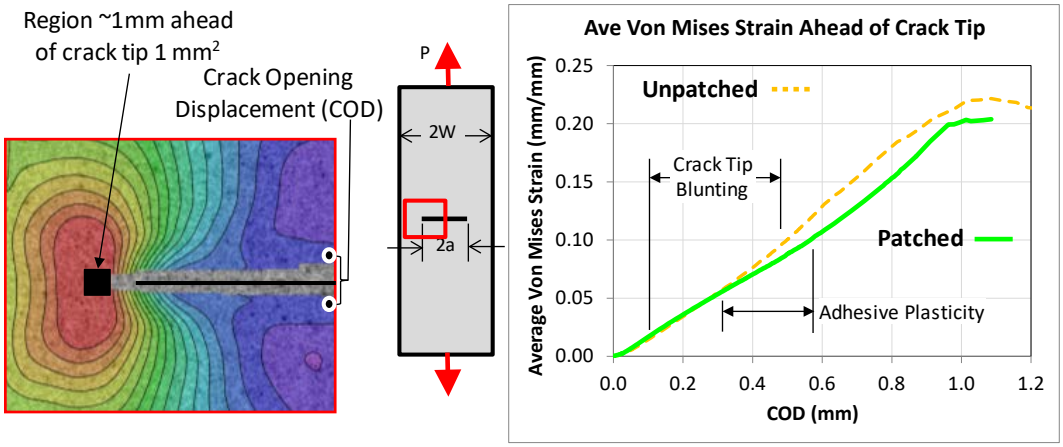

Figure 7-3 Total von Mises strain data ahead of the crack tip indicating adhesive plasticity and patch failure

At COD magnitudes below 0.02 mm the load versus COD response of the specimen is linear elastic. Von Mises strain contours in Figure 7-4 are showing greater strain magnitude and large strain region due to out-of-plane bending. In the linear elastic region, the out of plane bending increases until the load passes through the neutral axis of the patched specimen. During the bending response the surface strain of the composite patched specimen increases at a greater rate than the unpatched specimen, which only experiences an in-plane tensile material response.

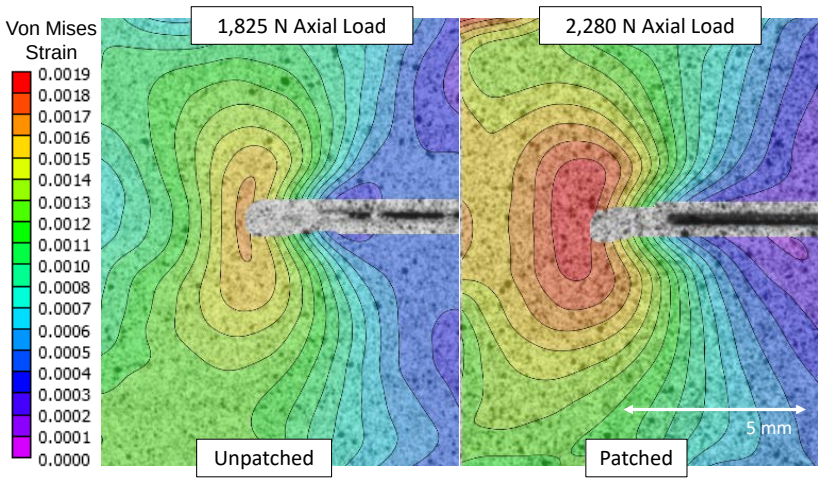

Figure 7-4 Von Mises strain contour comparison for a COD=0.02 mm in the linear elastic response range showing influence of bending on patched specimen surface strains.

Once the load axis aligns with the neutral axis of the specimen both the unpatched and patched strains increase at similar rates. Strain contours for a COD of 0.2 mm, early stage of crack blunting, are shown Figure 7-5. Strain contours for the patched specimen indicate a measurable effect of the surface reinforcement with a blunted region of large strain ahead of the crack tip with a greater area of large strain consistent with fiber reinforcement in both axial and transverse directions. The additional area of large strain increases the size of the plastic zone as load increases. That plastic deformation contributes to the 20% increase in COD when comparing specimen response at matching load levels after the patch fails. A quantification of the strain area is required to verify this result.

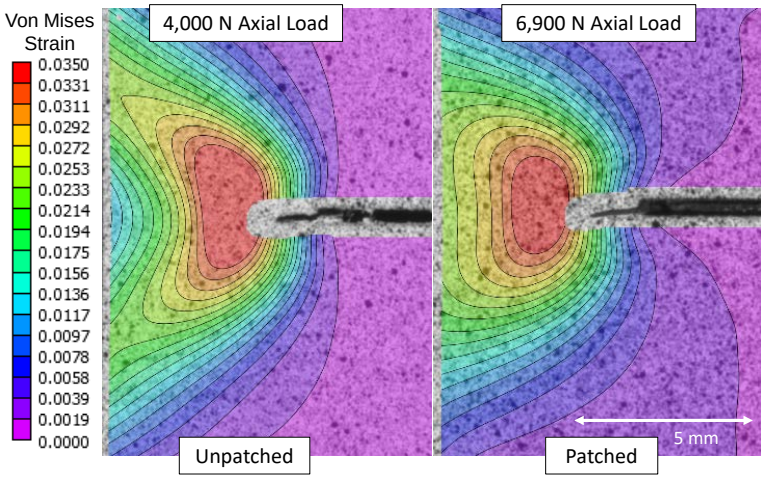

Figure 7-5 Von Mises strain comparison of unpatched (L) and patched (R) crack tips during the early stage of crack blunting (COD=0.2mm) showing increased area of large strain for the patched specimen.

Crack tip strain fields on the aluminum free surface show the effect of the one-sided patch reinforcement. Initially, the patched specimen developed plastic strains prior to the unpatched specimen primarily due to out of plane bending. Beyond initial development of the plastic zone as load and COD increase two trends emerged. The change in load and large-strain area with the addition of the composite patch are shown in Figure 7-6. First, as COD increases the additional patch material allowed the specimen to carry more load. That change in load capacity is linearly proportional to the COD. The second was a decreasing magnitude of the large strain area increase as a function of COD. For CODs less than 0.4 mm the patch reinforcement increases the region of large strain with the magnitude of area increase being inversely proportional to COD. Fitting of the data to a trend is not appropriate here, since the large strain magnitude studied changed for each COD and was arbitrarily selected to be within the AOI.

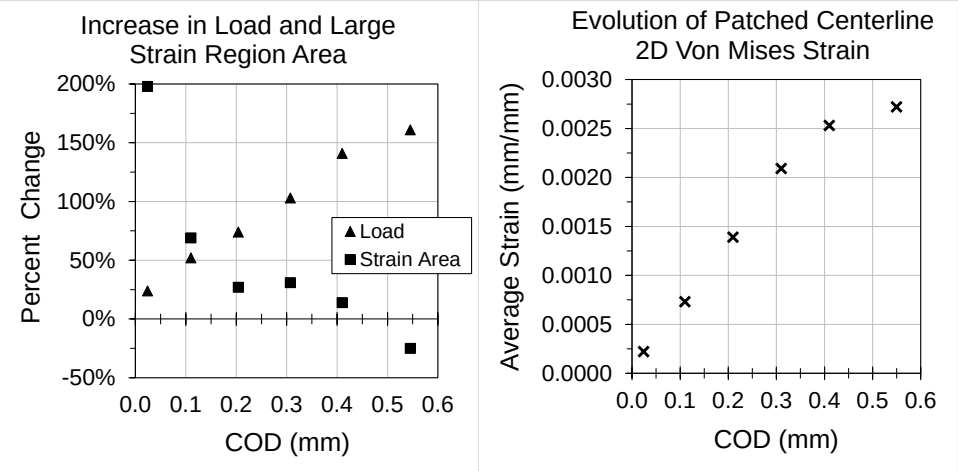

Figure 7-6 Load increase and change in large strain area as a function of COD showing linearly proportional load capacity benefit and decreasing large strain area increase for the patched specimen.

The unpatched specimen strain field at the crack tip is influenced by both the crack tip singularity and tensile ligament behavior and has an assumed symmetric through thickness response. Addition of the patch reinforces the transverse response of the aluminum ligament and offsets the neutral axis of the specimen introducing out of plane bending and an asymmetric response with through thickness behavior gradient at the crack tip where free surface stress intensity can nominally be 4x that of the patched surface, as shown by Wang and Rose [9]. With theoretical through thickness behavior and the global load and free surface strain responses as a function of COD, details about the specimen response can be infered. The COD at which the load goes through the patched specimen centroid is where the load as a function of COD slope is constant beyond the nonlinear region, which matches assumptions made by Baker to develop simplified equations to represent geometrically nonlinear response [8]. From this point, the bending contribution remains constant and the tensile behavior of the section advances with the free surface seeing more load than the patched surface and therefore

governing the failure response. Further investigation of the through thickness behavior requires detailed 3D FEA techniques.

7.1.4 Round One Qualitative Plastic Zone Evolution

Initial plastic zone size and shape were established using total von Mises strain contours shown in Figure 7-11 and Figure 7-12. As loading increases above initial yield, full-field strains for unpatched and patched specimens are compared ahead of the crack tip. In addition to the crack tip behavior the centerline strain near the notch was also compared to show the effect of load bridging for the patched specimen. Centerline von Mises strain is averaged over a 1 mm^2 area 4 mm above the center of the machined notch, as shown in Figure 7-7.

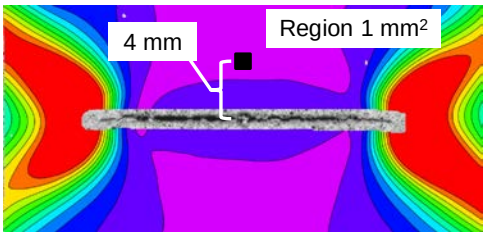

Figure 7-7 Centerline strain region definition to study the effect of load bridging for patched specimens.

In Figure 7-8, Figure 7-9, and Figure 7-10 the DIC area of interest (AOI) incorporates the entire width of the specimen with the exception of a half subset width (0.17 mm) at the left and right edges. The strain contours shown are consistent for images in that figure. The size of the AOI required an increase in the strain range to observe qualitative changes in the large strain region at the crack tip.

To observe initial plastic zone development, the strain contour was set to the measured tensile yield strains. For loading up to 3,000 N the total von Mises strain fields for the unpatched and patched specimens are shown in Figure 7-8 with the red contour indicating

total von Mises strain from 1,800 to 1,900 με. Initial plastic strains develop at approximately the same load, which was 2,040 N for the unpatched specimen versus 2,140 N for the patched specimen. The complete plastic zones do not develop and encompass the crack tip until 2,169 N and 2,399 N for the unpatched and patched specimen, respectively. At an axial load of 3,000 N the height of the unpatched plastic zone increases to the extent of the AOI while the patched specimen plastic zone increases in height but can still be distinguished within the AOI. The slower rate of plastic zone evolution for the patched specimen is due to the one-sided reinforcement that increases the width, but limits the height of the plastic zone by carrying a portion of the axial load across and around the crack.

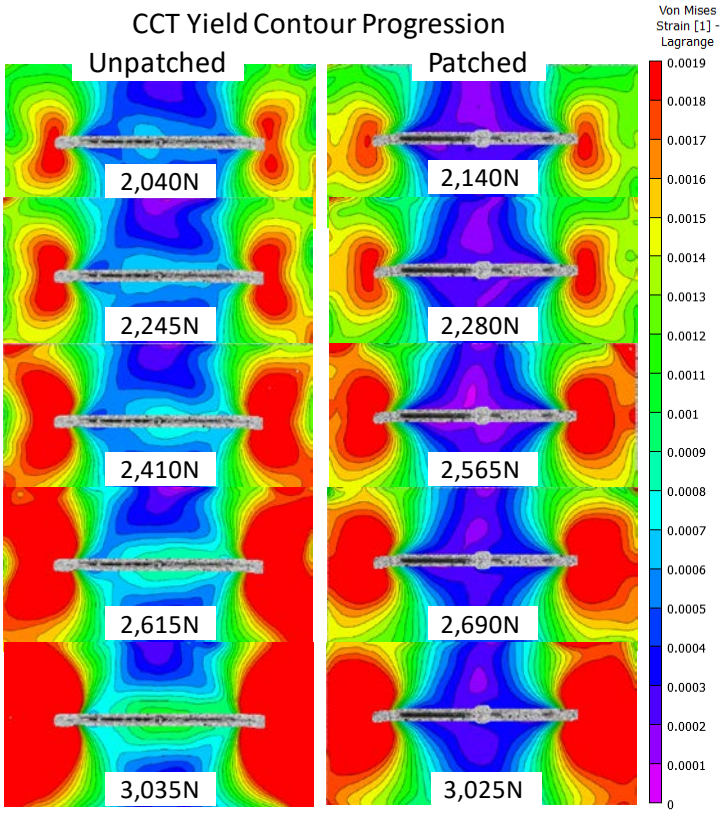

Figure 7-8 Direct comparison of unpatched (L) and patched (R) von Mises strain fields to 3,000 N showing qualitative progression of plastic strain region.

Above 3,000 N the total von Mises strain ahead of the crack tip increases above the yield strain and to observe the evolution of the large strain region the strain contour limits for images in Figure 7-9 were increased such that strains from 2,800 to 3,000 με are indicated by the red contour. As loading of the unpatched specimen increases from 3,500 N the shape of the large strain zone remains nominally the same but increases in area through 4,000 N. The boundary of the large strain contour in the wake of the crack tip, indicated by the dashed lines, moves 15-30% along the crack plane during increased loading and the COD increased 1.6x and 2.4x at 3,750 N and 4,020 N, respectively. Increasing COD with limited change in the strain field corresponds with the observed crack blunting behavior. Average unpatched centerline strain magnitudes are between 200 and 400 με from 3,000 to 4,000 N.

With a one-sided patch the large strain region increases in size with both the height and width proportional to the magnitude of the load. Crack blunting behavior is present above 5,000 N for the patched specimen and the distribution of the large strain contour continues to increase with load. Centerline average strain magnitude increases from 400 με at 3,000 N to 1,400 με at 6,890 N indicating an increasing amount of load being transferred across the notch through the patch. Patch reinforcement with fibers in both the 0- and 90-degree directions facilitates distribution of strain across the specimen as bending and aluminum plastic deformation occurs.

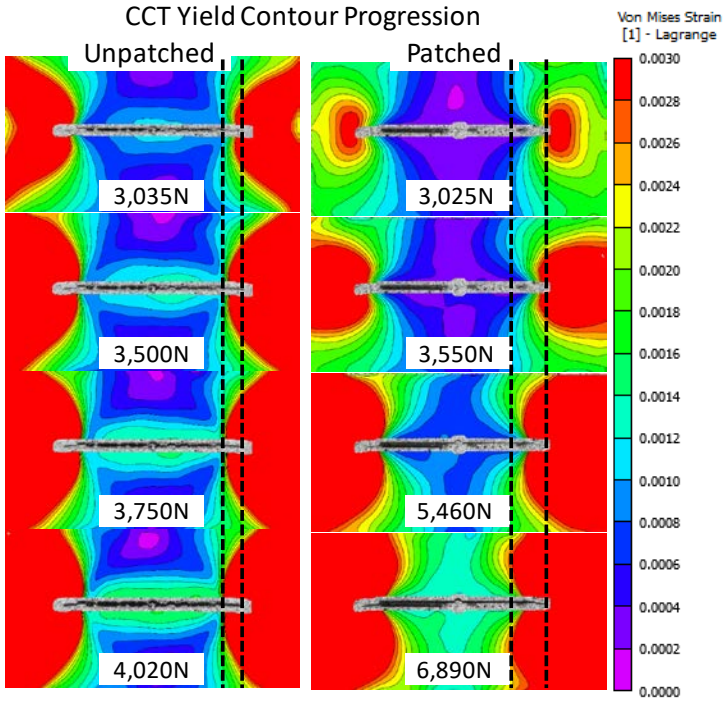

Figure 7-9 Direct comparison of unpatched (L) and patched (R) contour progression from 3,000 N showing larger strain region in the crack wake for the patched specimen.

As loading increases and crack blunting transitions to initial stages of crack growth the similarity in the shape of the unpatched and patched large strain region increases. Measured DIC strains approaching crack growth are shown in Figure 7-10 with a dashed line marking the crack tip prior to crack growth. The unpatched specimen maintains

centerline average von Mises strains in the 200-400 με range. As COD continues to increase the crack stops blunting and transitions to crack growth and failure after 4,400 N. The patched specimen region of large strain continues to grow with patch reinforcement distributing strains across the test section. The centerline strains increase beyond the plastic limit due to the patch reinforcement redistributing strain.

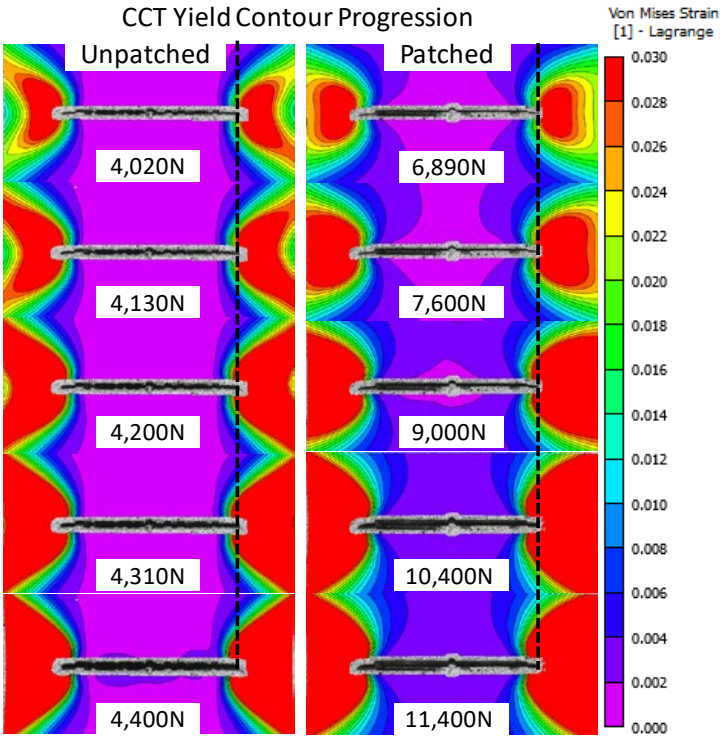

Figure 7-10 Direct comparison of unpatched (L) and patched (R) contour progression showing a decrease in patch effects approaching peak load and crack growth.

7.1.5 Round One Crack Tip Plastic Zone Estimate

Irwin's approach can be used to estimate the plastic zone radius ahead of the crack tip assuming plane stress conditions. Elastic material yield occurs when the normal stress is equal to the yield stress from the uni-axial tension test. Under plane stress conditions this yields a second order estimate of the plastic zone diameter, r_p, in Equation 100 that is

derived by performing a force balance near the crack tip that includes elastic and plastic stresses.

Irwin provided a 1-D estimate of the plastic zone size on the plane of the crack. For elastic isotropic material the plastic zone shape can be estimated relative to the crack tip by setting the von Mises equivalent stress equal to the uniaxial tensile yield stress. The equivalent stress is a function of the principle stresses, which for Mode-I loading can be approximated with singular stress fields based on the stress intensity. Setting the equivalent stress equal to the yield stress results in an expression for the plastic zone as a function of the angle from the crack plane. For plane stress the cylindrical coordinates of the plastic zone boundary at a prescribed level of mode-I stress intensity, K_I, are related using Equation 101 and under plane strain conditions are related using Equation 102.

Initial plastic zone development was compared to the LEFM plastic zone estimates and an effective free surface K_I value at initiation of yield was iteratively determined that qualitatively matched the measured shape. The measured plastic zone shape was determined by comparing the total Lagrangian 2D von Mises strain contours to the 0.2% offset strain level from tensile material tests. DIC data from the unpatched aluminum CCT specimens was processed with upper strain contour between 0.0018-0.0019 mm/mm for the plastic strain level, as shown in Figure 7-11. The plastic zone shape appears to be dominated by plane stress behavior with the influence of edge effects. These DIC results were used to measure the radial position of the plastic zone boundary for angles of 0-, 15-, 30-, 45-, 60-, 75-, and 90-degrees. At a COD of 0.024 mm and a load of 2,169 N the 0.2% yield strain was exceeded forming a complete plastic zone encompassing the crack tip, which was located using a parabolic least squares fit of the vertical displacements (V)

parallel to the crack plane [51]. Measured radial positions of the yield strain are listed in Table 15.

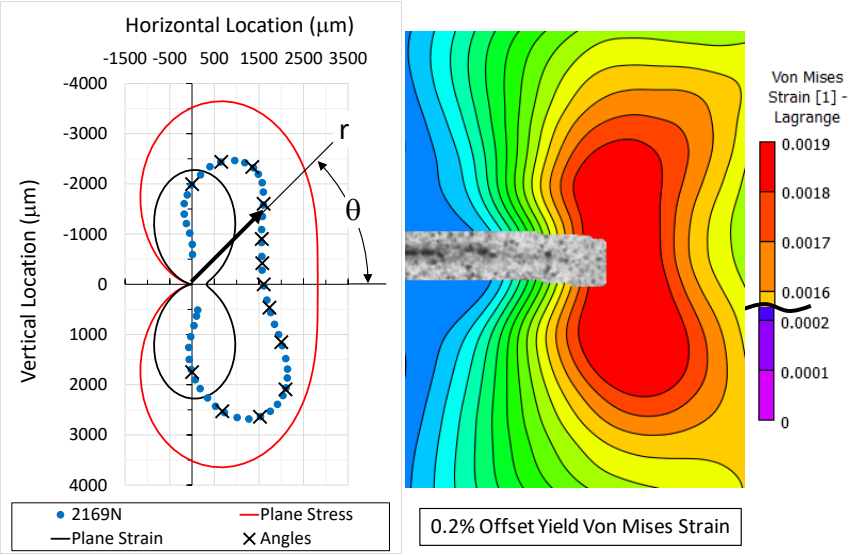

Figure 7-11 Unpatched 0.2% offset initial LEFM yield prediction and DIC measurement showing crack tip behavior dominated by plane stress.

Table 15. Points on Fully Developed Unpatched Plastic Zone Boundary

Points on Unpatched Plastic Zone			
Angle (deg)	**DIC Radial Position (µm)**	**Plane Stress Radial Position (µm)**	**Plane Strain Radial Position (µm)**
0	1537	2756	319
15	1624	2848	452
30	1919	3088	814
45	2510	3386	1306
60	2771	3617	1789
75	2408	3663	2129
90	1646	3445	2226

The initial plastic zone measured from DIC data was again used to iteratively solve for effective stress intensity resulting in a predicted radial position value at 0-degrees that was half way between plane stress and strain, or the plastic zone waist. The resulting K_I is 15.3 MPa√m, which is 30% lower than critical and 80% greater than estimated effective K_I using standard finite geometry solutions at the measured load [50].

DIC data for a patched specimen is shown in Figure 7-12 at a load of 2,399N. Composite patch surface reinforcement causes the qualitative strain behavior to match LEFM plane stress behavior. Although not strictly applicable due to the patch, plane stress LEFM predictions were made using Equation 101. K_I was iteratively changed to match measured DIC radial positions at both 0- and 60-degrees, the later prediction is shown in Figure 7-12 (left, red line). Measured radial positions are listed in Table 16. The resulting effective K_I values are 12.1 and 11.7 MPa$\sqrt{m}$ when matching radial position at 0- and 60-degrees, respectively.

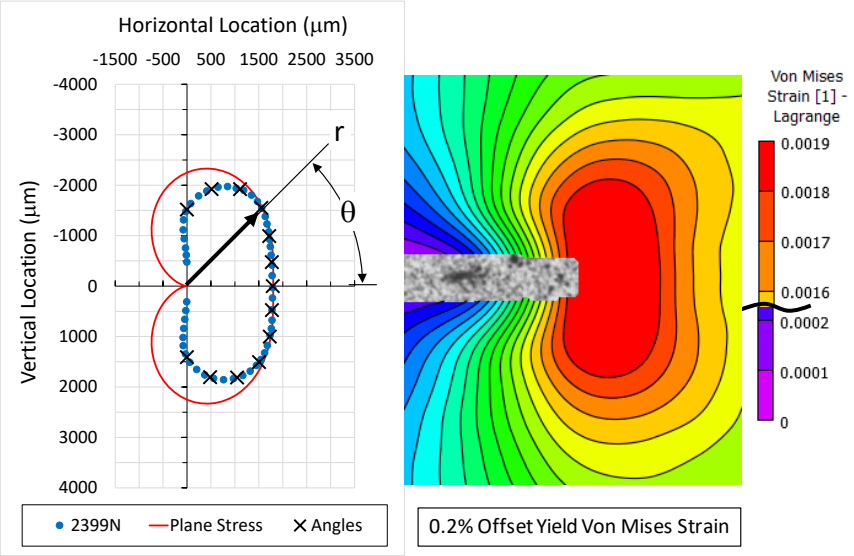

Figure 7-12 Patched CCT specimen 0.2% offset initial LEFM yield prediction and DIC measurement showing patched crack tip behavior similar to plane stress.

Table 16. Points on Fully Developed Patched Plastic Zone Boundary

Points on Patched Plastic Zone			
Angle (deg)	DIC Radial Position (μm)	K_I=11.7 MPa-√m Plane Stress Radial Position (μm)	K_I=12.1 MPa-√m Plane Stress Radial Position (μm)
0	1722	1628	1722
15	1766	1682	1779
30	1919	1824	1929
45	2105	2000	2116
60	2136	2136	2260
75	1955	2163	2289
90	1573	2034	2152

The region of plastic strains for both unpatched and patched plastic zones are 3 orders of magnitude larger than the measured grain size that ranged from 5.4 to 18.1 μm, supporting the assumption that the aluminum ahead of the crack tip behaves as a homogenous material during the evolution of the plastic zone.

7.1.6 Comparison of Round One Measured and Predicted Response

Load and average vertical strain response was presented up to peak load in Figure 7-13, since the interest was to advance the prediction past the LEFM limit to include EPFM but not progressive damage. From the measured and predicted response progressive damage appears to begin near a COD of 0.4 mm, which is within the crack blunting region of crack evolution. The predicted load versus COD response for both unpatched and patched specimens correlates well with test data when elastic-plastic material behavior is included and the numerical solution uses the large displacement formulation, which is the nonlinear geometry option in ABAQUS. Predicted loads for unpatched and patched specimens as a function of COD are within 15% of the test data. Unpatched response prediction is typically within 3% to 8% of measured, while the patched predictions are within 2-12% of test data. Small versus large displacement solutions were studied only

for the patched specimen as a built in option to perform the domain integral method to predict the J-integral value. The implementation is limited to the small displacement solution method. Use of the small displacement solution does not adequately capture the bending and elastic-plastic material behavior observed during loading of the patched specimen.

Vertical strains were extracted for comparison for simplicity as both DIC and FEA output these values directly. Average vertical strain magnitude was extracted from a 1 mm^2 area approximately 1 mm directly ahead of the crack and correlated well as a function of COD for unpatched and patched response for COD less than 0.11 mm. Previous observations by Hart and Bruck indicated that crack blunting initiates at a COD of 0.11 mm and ends at 0.45 mm where behavior transitions to crack growth and peak loads at 0.56 mm along with connecting crack tip fracture behavior to the COD independent of the composite patch [18]. The predicted strain responses correlate well, although for COD greater than 0.11 predictions do diverge slightly from test data with the predicted strain levels being 15% and 12% lower than measured for unpatched and patched specimens, respectively.

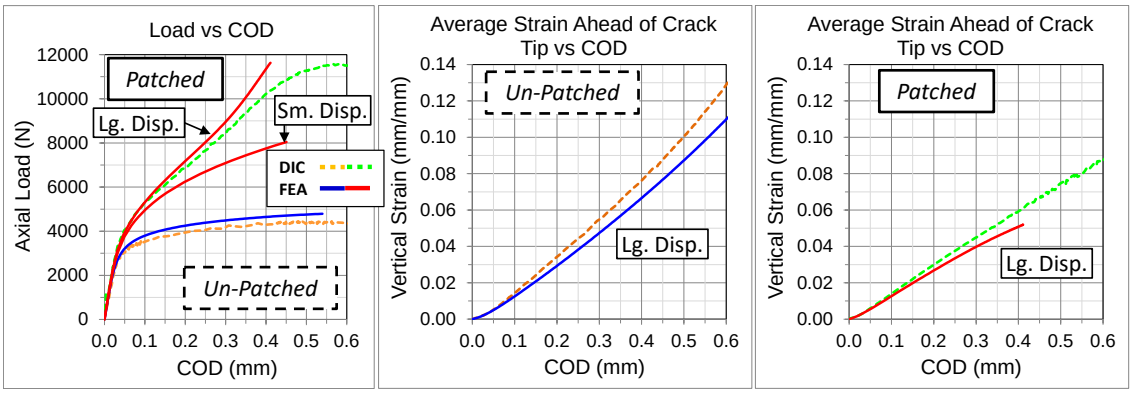

Figure 7-13 Measured and predicted load versus COD with small and large displacement assumptions for finite element analysis predictions.

7.1.7 Round One Quantitative Plastic Zone Evolution

A quantitative comparison of the large strain regions as a function of COD is required to support the observed improvement in the patched load versus COD behavior. From Figure 7-2 the crack tip behavior and failure of unpatched and patched specimens appear to correlate with the COD; crack blunting begins and ends at the same CODs, peak load occurs at the same COD, and crack growth starts at the same COD. Initial plastic zone size and shape were established using total 2D free surface von Mises strain contours and a quantitative comparison of the large strain regions as a function of COD to support the observed improvement in the patched load versus COD behavior. In the vicinity of the crack tip, the large strain area was estimated, not directly measured, using the triangles created between the radial large strain positions as illustrated in Figure 7-14. For the 0- to 90-degree quarter, the summation of all the triangles provides an area for comparison assuming the change in this area is representative of the total change in area defined by the selected large strain magnitude. The initial comparison was performed at the plastic strain limit, however, as load increases the plastic strain region extends beyond the DIC area of interest (AOI) and that requires measuring the radial positions at large strain magnitudes unique to each COD. The large strain magnitudes were selected such that

each radial path had a distinguishable large strain radial position. The load and COD magnitudes studied are indicated by the "+" marks on the load versus COD plot in Figure 7-14 and fall within the linear elastic response range, the crack blunting stage and initiation of crack growth before the peak load is achieved.

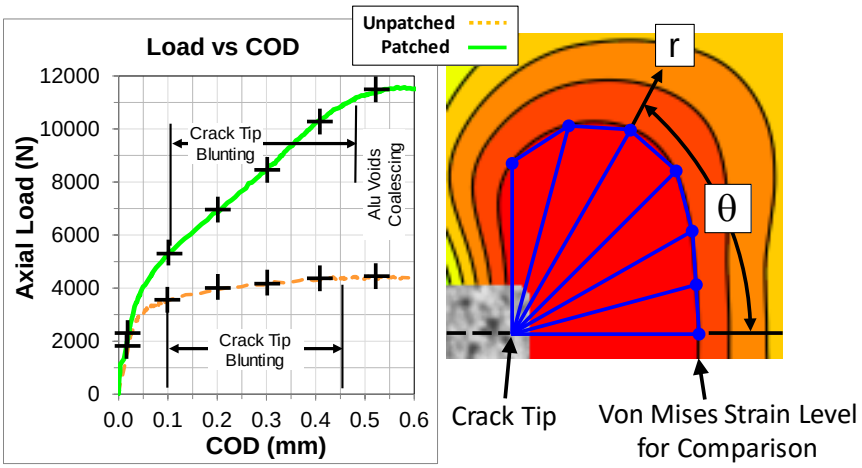

Figure 7-14 Load and COD magnitudes studied (L) and the large strain area definition (R) for unpatched to patched response comparison.

Large strain volume comparison is done through the thickness utilizing 2D surfaces at positions along the Z-axis (Z_{pos}) of the FEM to generate a representative volume. The process for generating the large strain volume is outlined in Figure 7-15. 2D surfaces are generated at segment midpoints by interpolating between surfaces using 3D vectors between large strain positions for each triangular region (highlighted yellow wedge). Midpoint areas are integrated along the Cartesian Z-direction to estimate the volume of each wedge, which were then summed for the representative volume estimate.

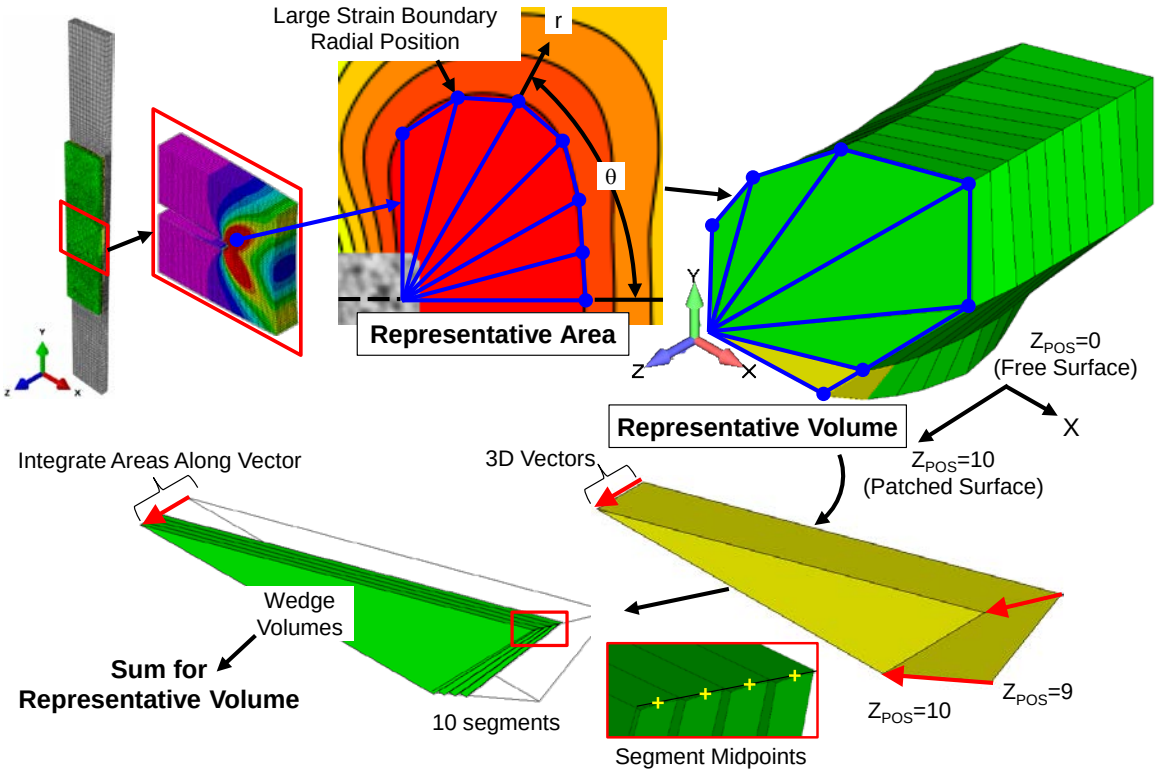

Figure 7-15 Process to measure large strain boundary radial positions relative to the crack tip, estimate the area, and integrate XY areas through the thickness to estimate volume.

7.1.7.1 Round One Crack Tip Free-Surface Large Strain Area Study

From the previous discussion, the fully formed plastic zone occurs at a load of 2,170 N for the unpatched and 2,400 N for the patched specimen. Studying the evolution as a function of COD demonstrates that the additional bending present in the patched specimen leads to development of plastic strains at a COD of 0.021 mm (Left of Figure 7-16), the point before plastic strains develop on the unpatched specimen surface. Increasing the load, at a COD of 0.024 mm, both the unpatched and patched specimens exhibit fully developed plastic strains (Right of Figure 7-16). Here the load carried by the patched specimen is 24% greater with a plastic zone area that is three times greater. The plastic strain radial positions are listed and compared in Table 17. Composite patch reinforcement increases the radial position of the plastic zone boundary 28-166%.

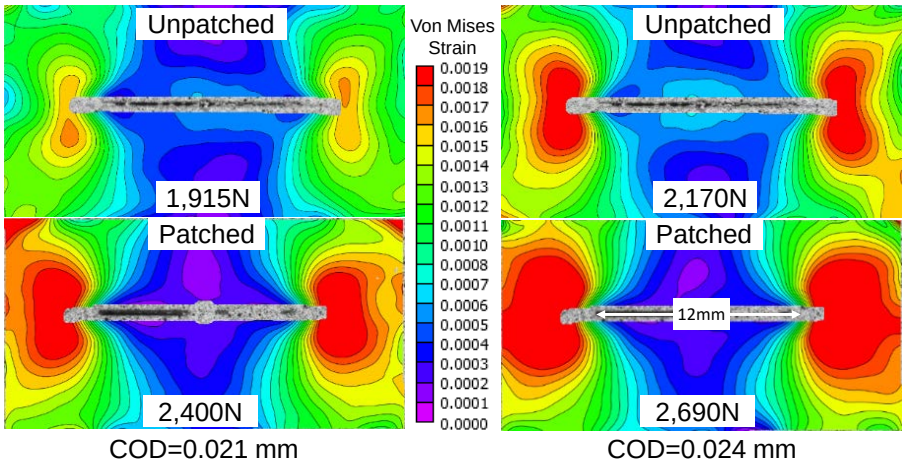

Figure 7-16 Comparison of plastic strain at COD=0.021 mm (L) and 0.024 mm (R). Patched surface plastic strain occurs first, then the patched specimen maintains a greater area of plastic strain.

Von Mises strain fields compared at the linear elastic response limit, or a COD of 0.024 mm, is shown in Figure 7-17 with the load versus COD response on the left and strain fields on the right. The increase in load due to the patch is 24% and 14 % greater than the measured and predicted unpatched response, respectively. The large strain boundary is measured at the plastic strain limit of 1,800 με with results listed in Table 17. Qualitatively strain field correlation is good for nominal shape. Quantitatively, the predicted yield strain area is 11% greater and 19% smaller for the unpatched and patched specimens respectively. At this strain level the DIC resolution with subset size and strain filter selection do not correlate with the sharp crack tip FEA predictions. Yield strain boundary radial position correlation varies significantly; 61% smaller to 37% larger for the unpatched predictions and 35% smaller to 1% larger for the patched. Using the radial positions to calculate a representative area, both the measured and predicted plastic strain area with the patch increases 183% and 110% respectively.

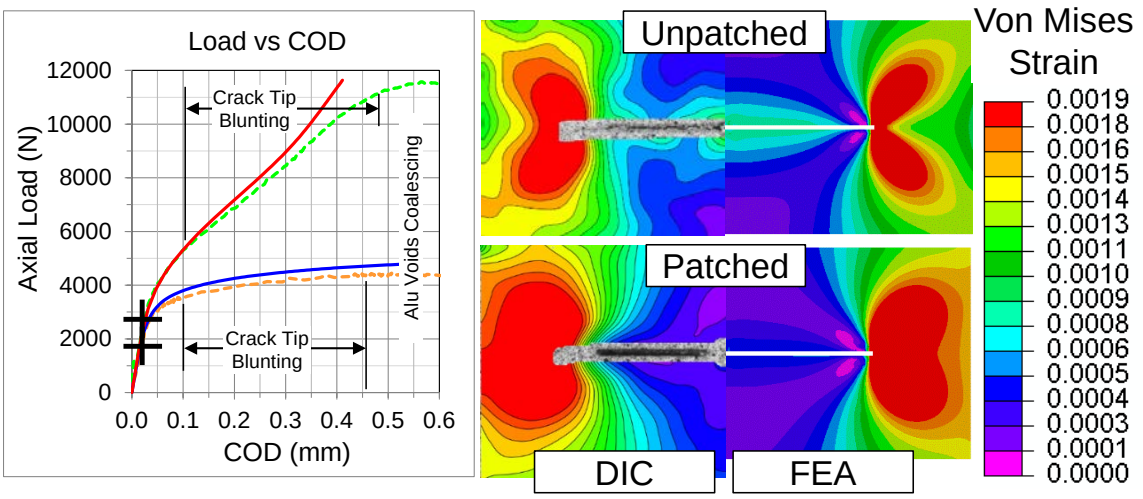

Figure 7-17 Load versus COD position with unpatched and patched comparison for both DIC and FEA results on the free surface at COD=0.024 mm.

Table 17. Measured and Predicted Large Strain Radial Positions for Yield Boundary of Fully Developed Plastic Zone at COD=0.024 mm (DIC/FEA)

Angle (deg)	Unpatched	Patched	% Diff
0	1.41/0.55	3.81/2.75	170%/400%
15	1.43/0.72	3.72/3.25	161%/350%
30	1.71/2.02	4.42/3.93	158%/94%
45	2.43/3.32	4.05/4.10	67%/23%
60	2.76/3.29	3.59/3.64	30%/11%
75	2.72/2.58	3.20/2.74	18%/6%
90	2.36/1.65	2.61/1.70	11%/3%

Note: Results listed as DIC/FEA

Von Mises strain fields compared at the initiation of crack blunting, or a COD of 0.11 mm, is shown in Figure 7-18. Change in load due to the patch 52% and 44% greater for the measured and predicted responses, respectively. The large strain boundary is measured at a strain level of 11,500 με with results listed in Table 18. Qualitatively the composite patch reinforces the ligament ahead of the crack tip in both the axial and transverse directions, while the unpatched specimen shows the influence of edge effects in the form of a plastic zone shape that does not match theoretical plane stress predictions. From the linear elastic response limit to the initiation of crack blunting the

large strain field height is constrained while the width increases due to transverse patch stiffness. Quantitatively, the predicted large strain area matches exactly and is 9% smaller for the unpatched and patched specimens, respectively. Large strain boundary radial position correlation is reasonable and varies from matching to a 30% difference. The unpatched predictions are 29% smaller at 0- and 90-degrees and correlate within 12% from 15 degrees to 75 degrees. Patched predictions match from 30 degrees to 60 degrees, are within 14% for 0 degrees and 75 degrees, and then 35% smaller for 90-degrees. Using the radial positions to calculate a representative area, both the measured and predicted large strain area due to the patch increases 62% and 47%, respectively. The axial and transverse patch reinforcement increases the large strain area width 75% and the overall height 5-10%

Centerline strain for the patched specimen exhibited load bridging with a von Mises strain increasing to 700 με, which exceeds the 300 με for the unpatched specimen.

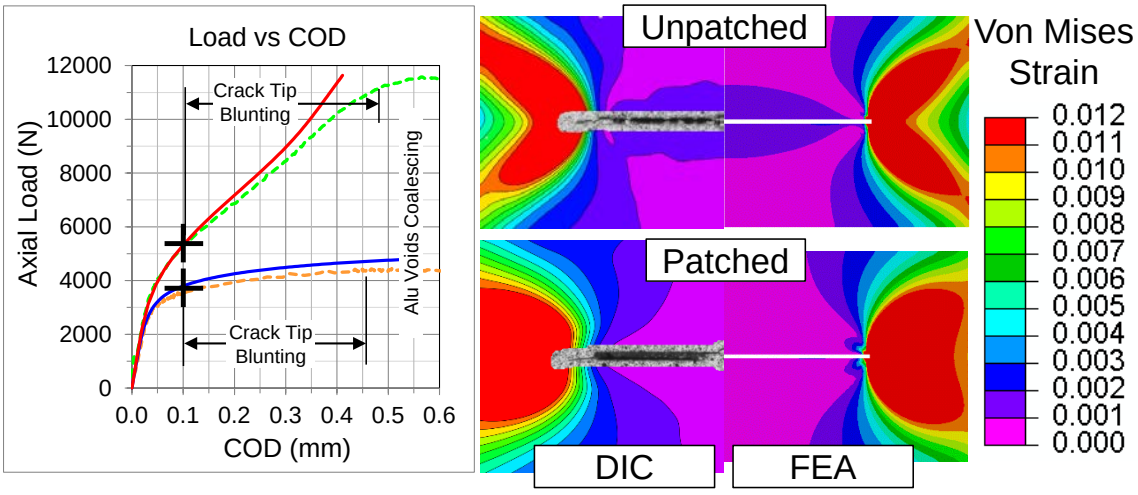

Figure 7-18 Comparison of large strain fields at COD=0.11 mm (L) and the large strain boundary radial positions at 11,500 με (R) showing increased large strain area on the free surface with a bonded patch.

Table 18. Measured and Predicted Large Strain Radial Positions for Yield Boundary of Fully Developed Plastic Zone at COD=0.024 mm (DIC/FEA)

Angle (deg)	Unpatched	Patched	% Diff
0	1.97/1.40	4.11/3.55	108%/154%
15	2.06/1.96	4.29/3.87	108%/97%
30	3.32/3.76	4.55/4.68	37%/25%
45	4.40/4.60	4.32/4.31	-2%/-6%
60	3.28/3.24	3.24/3.24	-1%/0%
75	2.28/2.01	2.38/2.07	4%/3%
90	1.62/1.15	1.76/1.15	9%/0%

Note: Results listed as DIC/FEA

Further along the load versus COD response at a COD of 0.20 mm the crack tip region is progressing through the crack blunting region with von Mises strain fields shown in Figure 7-19. Load increase due to the patch is 74% and 69 % greater for the measured and predicted responses, respectively. The large strain boundary was measured at a strain level of 23,000 με with results listed in Table 19. Qualitatively strain field correlation is good for nominal shape and size, however, measured strains for the patched specimen indicate more blunting ahead of the crack than predicted by the sharp crack represented by the FEA. Quantitatively, the predicted large strain areas are 2% and 7% smaller for the unpatched and patched specimens, respectively. Large strain boundary radial position correlation was reasonable and again varies from matching to a 30% difference. The unpatched predictions are typically within 15% with higher divergence at the extreme angles. Patched predictions also match within 14% from 15 degrees to 75 degrees with correlation between 22% and 33% for 0 degrees and 90 degrees. Using the radial positions to calculate a representative area, both the measured and predicted large strain area due to the patch increases 27% and 20%, respectively. Although the area of plastic strain is increasing for the unpatched specimen, the amount of load bridging for the

patched specimen continues to increase with a von Mises strain increasing to 1,300 με while the unpatched centerline strain remains consistent at 300 με.

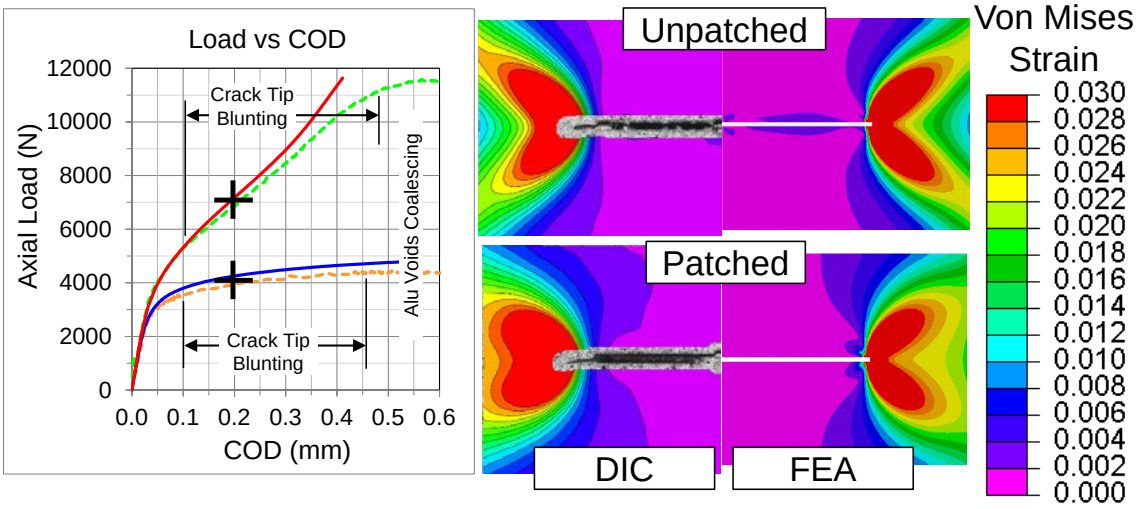

Figure 7-19 Comparison of large strain fields at COD=0.20 mm (L) and large strain boundary radial positions at 11,500 με (R) showing increased large strain area on the free surface with a bonded patch.

Table 19. Measured and Predicted Large Strain Radial Positions for Yield Boundary of Fully Developed Plastic Zone at COD=0.024 mm (DIC/FEA)

Angle (deg)	Unpatched	Patched	% Diff
0	2.32/1.70	3.77/2.95	62%/74%
15	2.47/2.27	3.96/3.56	60%/57%
30	3.62/4.16	4.44/4.57	22%/10%
45	4.50/4.74	3.94/4.24	-13%/-10%
60	3.30/3.18	3.10/3.12	-6%/-2%
75	2.32/1.91	2.29/1.96	-1%/3%
90	1.67/1.10	1.65/1.10	-1%/0%

Note: Results listed as DIC/FEA

Increasing the COD to 0.31 mm the crack tip region is progressing through the crack blunting region with von Mises strain fields shown in Figure 7-20. Load increase due to the patch is 100% for both the measured and predicted responses. The large strain boundary was measured at a strain level of 37,000 με with results listed in Table 20. Again, qualitatively strain field correlation is good, however, data for the patched

specimen indicates more blunting ahead of the crack than predicted by the FEA. Quantitatively, the predicted large strain area is 9% larger and 11% smaller for the unpatched and patched specimens respectively. Large strain boundary radial position correlation is reasonable and again varies from matching to a 30-45% difference at the extreme angles. The unpatched predictions are typically within 20%, while patched predictions are within 10% from 15 to 75 degrees. Using the radial positions to calculate a representative area, the measured and predicted large strain area due to the patch increases 22% and is nominally unchanged, respectively.

The amount of load bridging for the patched specimen continues to increase with a von Mises strain increasing to 2,000 με while the unpatched centerline strain remains at 380 με.

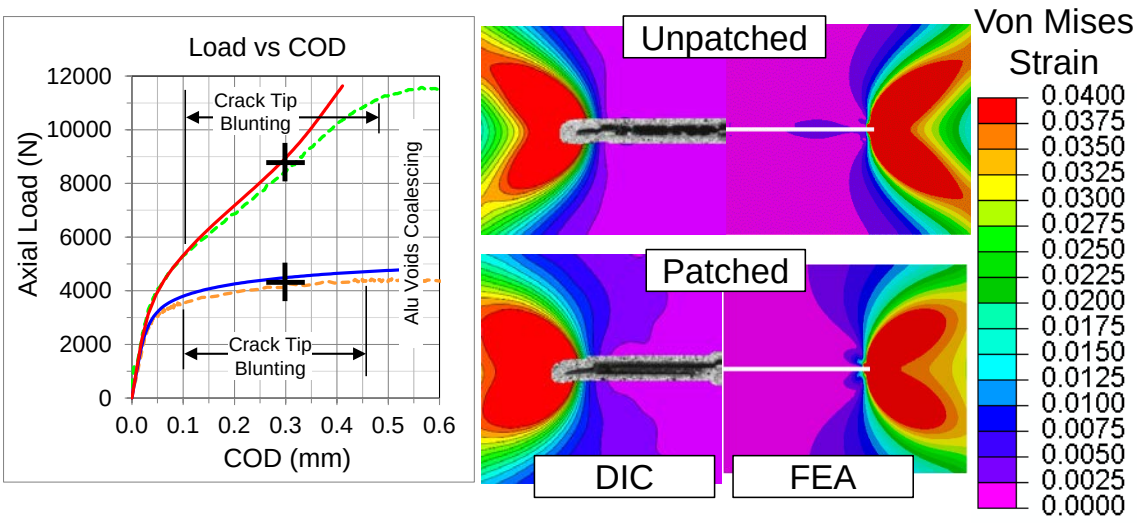

Figure 7-20 Comparison of large strain fields at COD=0.31 mm (L) and large strain boundary radial positions at 34,000 με (R) showing increased large strain area on the free surface with a bonded.

Table 20. Measured and Predicted Large Strain Radial Positions for Yield Boundary of Fully Developed Plastic Zone at COD=0.024 mm (DIC/FEA)

Angle (deg)	Unpatched	Patched	% Diff
0	2.36/1.75	2.99/1.65	27%/-6%
15	2.49/2.32	3.14/2.79	26%/20%
30	3.52/4.22	4.19/4.34	19%/3%
45	3.99/4.67	3.96/4.10	-1%/-12%
60	3.02/3.06	3.15/3.06	4%/0%
75	2.15/1.81	2.10/1.91	-2%/6%
90	1.58/1.05	1.61/1.05	2%/0%

Note: Results listed as DIC/FEA

Near the end of crack blunting, at a COD of 0.41 mm the crack tip region was near the transition to crack growth with von Mises strain fields shown in Figure 7-21. Load increase due to the patch is 160% and 150% for the measured and predicted responses, respectively. The large strain boundary was measured at a strain level of 51,000 με with results listed in Table 21. Qualitatively strain field correlation was good, however data for the patched specimen indicates more blunting ahead of the crack than predicted by the FEA. Quantitatively, the predicted large strain area is 5% larger and 14% smaller for the unpatched and patched specimens respectively. Large strain boundary radial position correlation is reasonable and again varies from matching to a 30-60% difference at the extreme angles. The unpatched predictions are typically within 15%, while patched predictions are within 10% from 15 degrees to 75 degrees. Using the radial positions to calculate a representative area, the measured and predicted large strain area due to the patch remains nominally unchanged and decreases 17%, respectively.

The amount of load bridging for the patched specimen continues to increase with the von Mises strain increasing to 2,700 με while the unpatched centerline strain is 450 με.

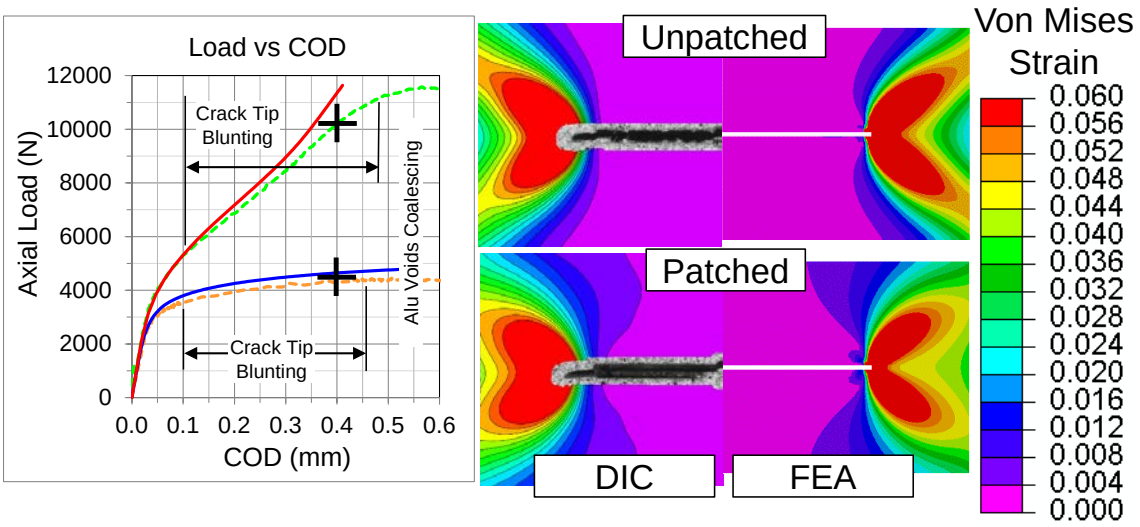

Figure 7-21 Comparison of large strain fields at COD=0.41 mm (L) and large strain boundary radial positions at 44,000 με (R) showing increased large strain area on the free surface with a bonded patch.

Table 21. Measured and Predicted Large Strain Radial Positions for Yield Boundary of Fully Developed Plastic Zone at COD=0.024 mm (DIC/FEA)

Angle (deg)	Unpatched	Patched	% Diff
0	2.51/1.80	2.54/1.00	1%/-44%
15	2.68/2.38	2.63/1.70	-2%/-28%
30	3.69/4.22	3.78/3.87	2%/-8%
45	3.88/4.53	3.78/4.03	-3%/-11%
60	2.87/2.95	3.03/3.06	6%/4%
75	2.06/1.76	2.04/1.91	-1%/9%
90	1.51/1.00	1.56/1.10	3%/10%

Note: Results listed as DIC/FEA

Beyond the crack blunting stage crack growth initiates prior to the peak load. At a COD of 0.55 mm the comparison of the large strain region boundaries was performed at a von Mises magnitude of 65,000 με for the test data only, since the patched FEA predictions did not include a COD greater than 0.50 mm. The strain fields and the measured large strain boundary radial positions are shown and compared for a COD OF 0.55 mm in Figure 7-22. Local crack tip strain contours show specimen edge effects evident in the patched strain contours. This indicates dominance of tensile behavior ahead of the crack tip compared to bending and a reduced influence of the patch on the free surface. As

COD increases the magnitude of load increases proportionally with the load now 160% greater. The patched large strain area is 25% smaller than that of the unpatched specimen. The measured radial positions for the patched specimen are consistent with the lower area and are 5-17% smaller. The effect of the composite patch has diminished with the centerline strain stagnating at 2,700 με, although still carrying load, while the unpatched centerline strain remains consistent at 450 με. Composite patch reinforcement transfers enough load across the notch for the centerline aluminum to achieve plastic von Mises strain on the surface. Note here that the von Mises strains are not zero along the centerline of the unpatched specimen because of transverse strain contributions. Axial strain (ε_{yy}) magnitudes are nominally zero within the static image bias and error for the range of CODs studied and the patched specimen axial strains are 35-50% smaller than the 2D von Mises strains above a COD of 0.20 mm due to transverse strain contributions.

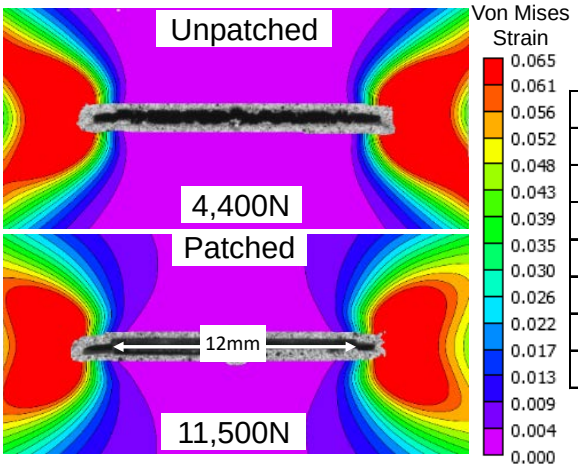

Large Strain Radial Position (mm)

Angle	Unpatched	Patched	% Diff
0	3.24	2.69	-17%
15	3.38	2.87	-15%
30	4.16	3.41	-18%
45	3.90	3.41	-13%
60	2.76	2.62	-5%
75	1.95	1.78	-9%
90	1.38	1.18	-14%

Figure 7-22 Comparison of large strain fields at COD=0.55 mm (L) and large strain boundary radial positions at 65,000 με (R) showing large strain areas indicating decreased influence of the patch on the free surface with edge effects and qualitatively similar shapes.

7.1.7.2 Round One Crack Tip Large Strain Volume Study

Evaluation of the large strain volume through the thickness of the specimen must be done using FEA results. An additional study of the strain field development at the crack tip will be discussed in terms of the 2D XY Surface and the XZ Cross Section of the high mesh density region of the FEM at the crack tip as shown in Figure 7-23, although the patched specimen model is shown, the location and orientation of the crack tip results are independent of the patch. As a function of COD the 2D XY Surfaces are extracted at various Z_{pos} and the XZ Cross Section ahead of the crack tip is helping describe the through thickness behavior.

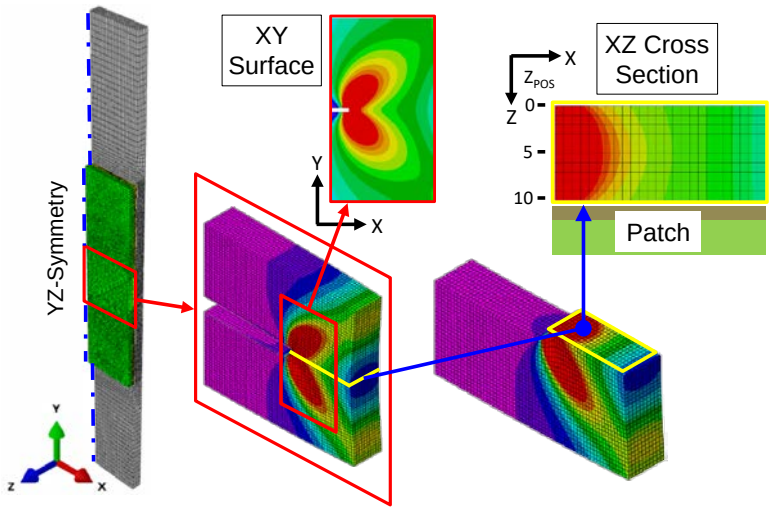

Figure 7-23 FEM location and orientation of prediction results presented for discussion. 2D XY-surface results presented for various Z-positions at the crack tip and XZ-cross sections presented for the crack plane at θ=0°

Comparison of the through thickness behavior at a COD of 0.024 mm at the end of the linear elastic response is shown in Figure 7-24. The unpatched specimen has a symmetric strain behavior along the z-axis, with the peak plastic strain radial position at θ=0 degrees occurring at, Z_{pos}=5, the mid thickness of the specimen. The thumbnail pattern is similar

to mode I composite fracture patterns. Behavior just beyond classical plastic zone patterns was also predicted by both Besel & Breitbart and Fernandez-Zuniga with first order and second order elements, respectively [109, 66]. Besel and Breitbart studied 2024 aluminum and documented variation of plastic zone shape from classical theory at specimen thickness between plane strain and stress conditions with 0.02 mm first order elements. Fernandez-Zuniga analyzed 7075 aluminum with 0.05 mm second order elements show 3D plane stress and strain fields.

Adding composite patch reinforcement to one side results in an elliptical through thickness strain gradient with the through thickness profile and 2D surface of the 3D maximum principal strains shows the overall height of the unpatched plastic zone decrease while the radial position at θ=0 degrees increases. Plastic radial strain on the patched surface is 84% smaller than the free surface. The patched specimen initially has a predicted surface strain area 100% greater than unpatched, however, the volume of plastic strain is 39% smaller.

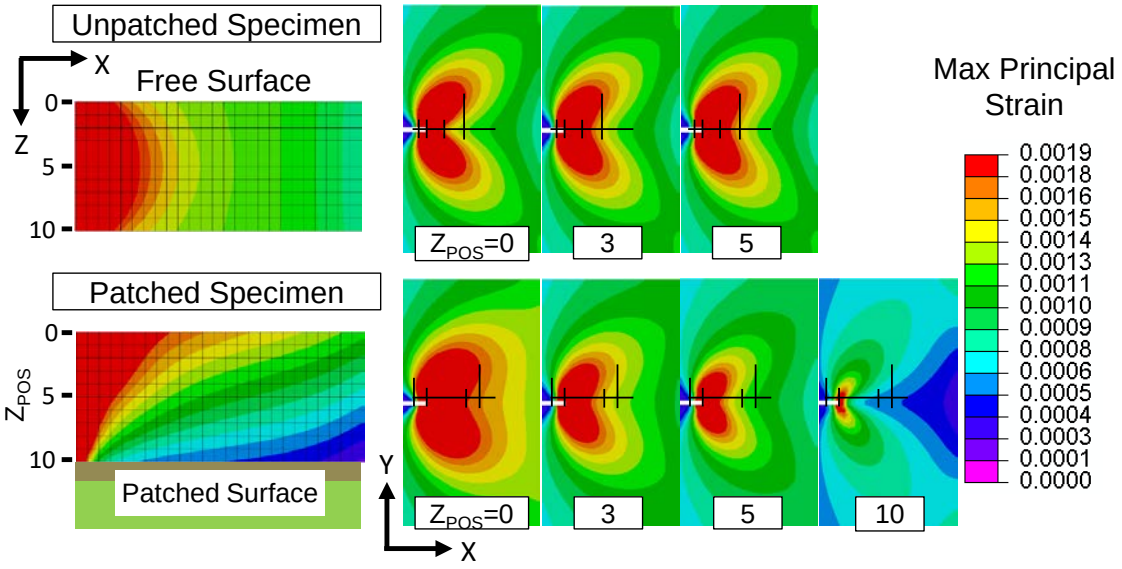

Figure 7-24 FEA results for COD=0.024 mm. Maximum principal strain contours shown for the XZ-cross section (L) and the XY-surface at various Z-positions (R).

At the initiation of crack blunting, a COD=0.11 mm shown in Figure 7-25, the XZ-plane profile has a finger nail profile with the peak radial position occuring at the midplane. The height of the large strain zone remains the same and the radial position at 0 degrees increases. The patched strain profile is transitioning from parabolic to a sinusoidal distribution with the free surface, Z_{pos}=0, being 47% greater and the total large strain volume being 54% smaller. The patched XY profile blunts slightly at the mid thickness and remains a hybrid of plane stress and plane strain classical shapes with the patched surface large strain radial position 83% smaller than the free surface.

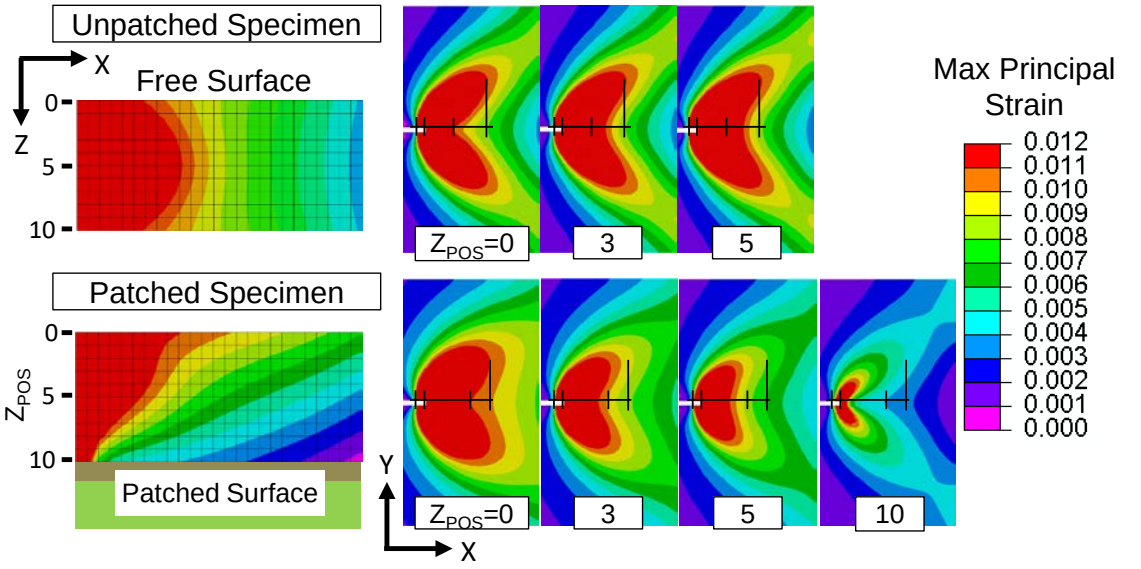

Figure 7-25 FEA results for COD=0.11 mm. Maximum principal strain contours shown for the XZ-cross section (L) and the XY-surface at various Z-positions (R).

During crack blunting at a COD=0.20 mm shown in Figure 7-26 the XZ-plane profile has a finger nail profile with the peak radial position occuring at the midplane 61% greater than the free surface. The patched strain profile is a sinusoidal distribution with the peak radial position occuring at Z_{pos}=3 and the patched surface radial position being 78% smaller. At this COD the free surface area of the patched specimen is 20% greater and the total large strain volume is 61% smaller. The patched XY profile blunts slightly at the mid thickness with the patched surface large strain radial position 75% smaller than the free surface. Based on subsequent patched XZ-profiles not changing shape, by a COD of 0.20 mm out-of-plane bending has reached a maximum with the load line passing through the neutral axis of the specimen.

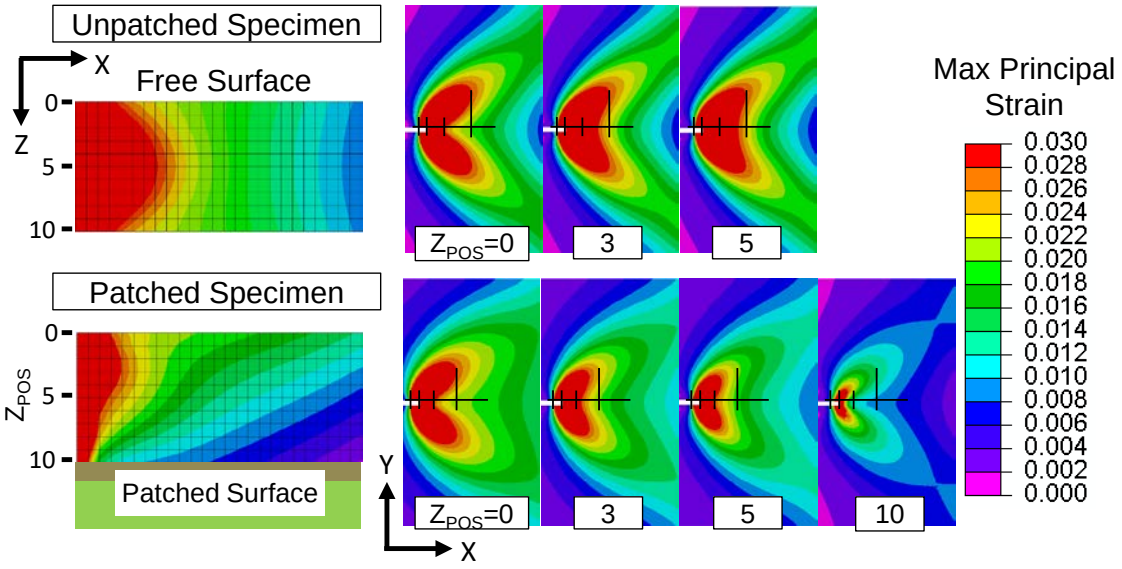

Figure 7-26 FEA results for COD=0.20 mm. Maximum principal strain contours shown for the XZ-cross section (L) and the XY-surface at various Z-positions (R).

The large strain fields for a COD=0.31 mm area shown in Figure 7-27. General large strain contours are similar to those at a COD of 0.20 mm. The unpatched XZ-plane profile has a finger nail profile with the peak radial position occuring at the midplane 54% greater than the free surface. The patched strain profile is a sinusoidal distribution with the peak radial position occuring at Z_{pos}=3 and the patched surface radial position being 75% smaller. At this COD the predicted free surface area of the patched specimen is 1% smaller and the total large strain volume is 64% smaller.

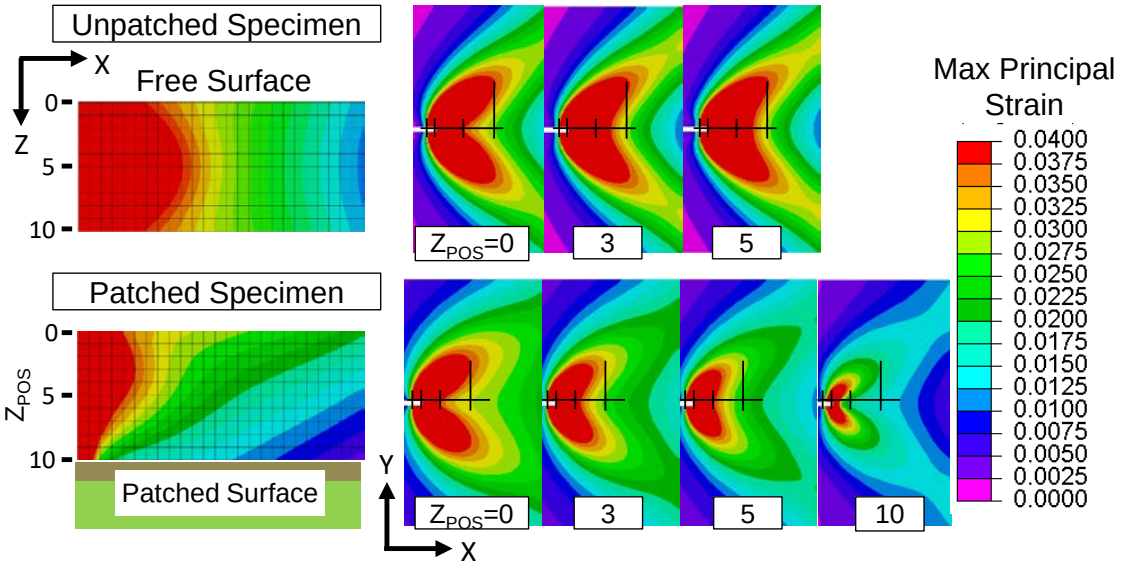

Figure 7-27 FEA results for COD=0.31 mm. Maximum principal strain contours shown for the XZ-cross section (L) and the XY-surface at various Z-positions (R).

The large strain fields near the end of crack blunting at a COD=0.41 mm are shown in Figure 7-28. General large strain contours are similar to those at CODs of 0.20 and 0.31 mm during crack blunting. The unpatched XZ-plane profile has a finger nail profile with the peak radial position happening at the midplane 54% greater than the free surface. The patched strain profile is a sinusoidal distribution with the peak radial position occuring at Z_{pos}=3 and the patched surface radial position being 72% smaller. At this COD the predicted free surface area of the patched specimen is 18% smaller and the total large strain volume is 66% smaller.

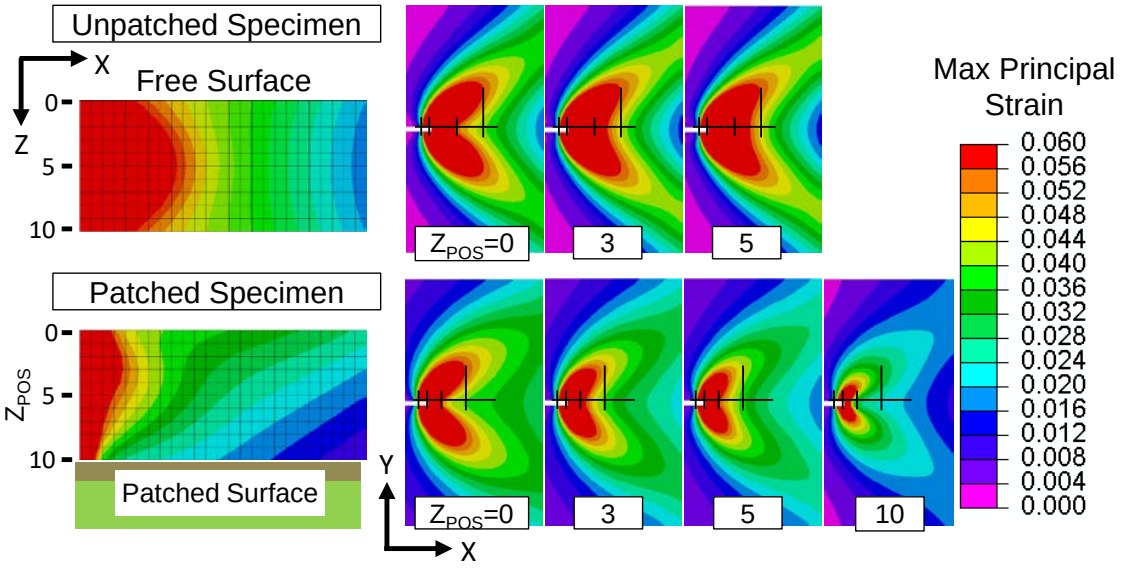

Figure 7-28 FEA results for COD=0.41 mm. Maximum principal strain contours shown for the XZ-cross section (L) and the XY-surface at various Z-positions (R).

7.1.8 Comparison of Round One Unpatched versus Patched Strain Field Evolution

A summary of the measured and predicted change in the crack tip response due to the composite patch reinforcement as a function of COD is shown in Figure 7-29. The increase in load, change in free surface von Mises strain area, and the predicted crack tip large strain volume based on maximum principal strains are summarized. Change in load and surface strain area correlation was good with the measured and predicted response showing the same trends. Both predicted and measured load response change was linearly proportional to the COD with the predicted increased load response consistent with the test response. The predicted load response for COD less than 0.4 mm, which is near the end of crack blunting, matches the measured response within 15% for both unpatched and patched specimens. Large strain area increase is inversely proportional to COD.

Crack tip large strain volume change was investigated using FEA results has an inverse relationship with COD that is consistently smaller with the addition of composite patch. The decrease in total large strain volume ahead of the crack tip is a measure of the load

sharing being done by the composite reinforcement. At higher loads the tensile behavior of the ligament begins to dominate the bending caused by the patch and the large strain begins to distribute more evenly through the thickness with less disparity between the free and patched surfaces, as seen in Figure 7-24 through Figure 7-28. The change in large strain volume correlates with an apparent minimum in the behavior as a function of COD.

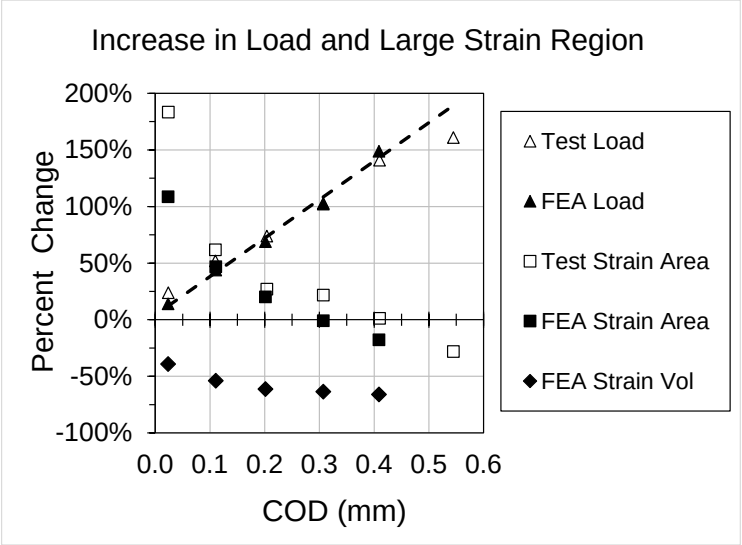

Figure 7-29 Percent change of load, free surface large strain area, and large strain volume at the crack tip as a function of COD. Results show proportional load change and inversely proportional strain area and volume changes.

The change in response provides insight into the response not readily discernable from the individual responses. In the early stages of loading the increased area of plastic strain with the consistently smaller large strain volume indicates the dominance of bending, which correlates with the through thickness strain cross sections. As COD increases the magnitude of large strain area change decreases indicating that the neutral axis of the patched specimen aligns with the load axis and the specimen response begins to be dominated by tensile response that can be seen in the difference of the through thickness large strain cross section contours in section 7.1.7.2. Under continued loading, the region

of free surface large strain for the unpatched specimen becomes larger than that of the patched specimen and the change in large strain volume reaches a minimum. Beyond predicted COD for the patched specimen the tensile response was assumed to dominate the response and the effect of the patch reinforcement continues to decrease. Both unpatched and patched displacement field behavior indicated an undersized ligament ahead of the crack tip resulting in a combination of singularity dominant and ligament tensile displacement behavior.

In summary, two primary factors contribute to the improved load response and the similarity in the fracture response as a function of COD. First, the additional load capacity can be attributed to the increase in large strain area, and presumably plastic zone size, measured to the end of crack blunting with more plastic area ahead of the crack tip and larger strain at the specimen centerline due to the bonded composite patch. Second, an increased magnitude of the large strain area of the patched specimen for CODs less than 0.40 mm. As COD increases beyond 0.40 mm the strain fields at the crack tip are similar to the strain fields of the patched specimen. Near peak load the free surface strain response is similar and the aluminum voids coalesce into crack growth and specimen failure of both specimen types.

One can assume that as COD increases and the in-plane tensile response begins to dominate, the crack tip response of both unpatched and patched specimens transitions from SSY to LSY and initiation of dislocations within the crack blunting response at the start of crack growth and failure. The COD where the minimum occurs for volume change is taken to be a critical crack tip behavior transition and can be used to determine

a critical patched failure load within the elastic-plastic response where failure transitions from SSY to LSY.

7.1.9 Round One Measured and Predicted HRR Field Correlation

Comparison of numerical predictions and the DIC data for fundamental displacement fields and calculated J-integral values will be discussed in this section. Good correlation of the global specimen response was shown for general load versus COD behavior as well as the average surface von Mises stress for an arbitrary area ahead of the crack tip.

7.1.9.1 Unpatched Crack Tip Displacement Fields

Axial displacement fields, *V,* of the unpatched specimen are shown in Figure 7-30 with the fields for CODs of 0.024, 0.11, and 0.41 mm corresponding to the load, COD, and crack tip behavior identified in the upper right of the figure. Measured displacement field data is shown for radii from an inner position of 0.5-0.7 mm to an outer position of 4.2-5.0 mm, limited by DIC correlation near the crack plane and subset size. At a COD of 0.024 mm, edge of the linear elastic response limit, where the yellow circles indicate the yield strain boundary (1,800 με). The measured and predicted yield strain boundary correlates reasonably well, although the predicted crack plane plastic zone size correlates with the first order Irwin plastic size (r_y) and the measured response indicates a larger plastic zone. Correlation to HRR fields does not occur consistently. From 15 to 45 degrees both measured and predicted displacement fields demonstrate HRR field behaviors at radial positions less than the plastic zone boundary transitioning to K field behavior approaching and going beyond the plastic boundary. Above 45 degrees the behavior remains K dominated and transitions to large strain approaching the crack tip. As COD increases the plastic strain radial position increases beyond the displacement

fields shown and edge effects are both measured and predicted for the 30 degrees and lower. Approaching the crack tip and the large strain region the displacement fields at path angles greater than 45° begin to diverge from HRR and K fields due to the initiation of crack blunting. At 45° and below, measured and predicted displacements correlate well with HRR fields and transition to K fields, although at different radial positions due to the difference in local crack tip geometry. For all CODs both DIC and FEA indicate crack tip behavior includes the influence of ligament plasticity and edge effects rather than being dominated by the crack tip singularity. The region ahead of the crack tip is considered to be in a state of SSY when the response correlates with HRR fields and transitions to K fields inside the plastic zone with the predictions indicating finite strain between the crack tip and HRR behavior.

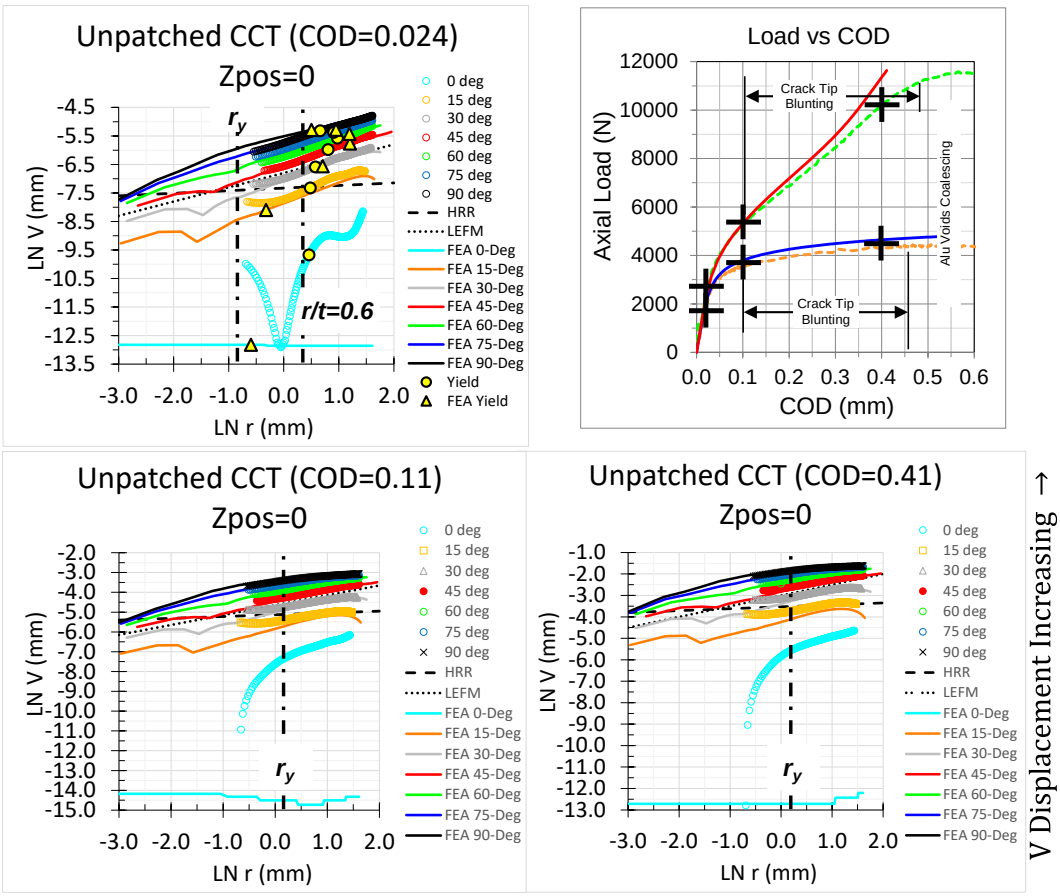

Figure 7-30 Unpatched axial displacement fields at the linear elastic limit, initiation of crack blunting, and the end of crack blunting. Yield boundary, first order Irwin plastic zone (ry), and nominal HRR and K fields are shown for comparison. Results show the region ahead of the crack tip in a state of SSY and K field dominance for lower angles outside r_y.

Horizontal, or *U*, displacement fields are reported for the crack tip and orientation shown in the 2D large strain boundary definition of Figure 7-14, where under tension the true displacements are negative as both the specimen and the ligament contract. To plot the logarithmic *U* versus *r* the absolute value of displacement is plotted in Figure 7-31. Note that for low angles the $\tilde{u}_{ij}$ can be negative [58, 59], and therefore $D(\theta,n)$ in Equation 115, to represent contraction. Measured and predicted *U* behavior correlates well qualitatively with deviation in radial position and *U* magnitude related to local crack geometry and crack tip direction. No measured displacement fields display true correlation with either

HRR or K fields, although for angles of 0 and 15 degrees in the crack blunting range of COD the fields appear to correlate with HRR for LN(r) > 0. FEA results appear to correlate with HRR fields close to the crack tip for LN(r) < -2.2. The combined influence of the crack tip singularity, ligament plasticity, and edge effects are evident in both measurements and predictions. Predicted correlation does exists near the crack tip, overall correlation to either HRR or K fields is not possible because U-displacements change sign along the same radial path due to the combination of crack tip singularity and edge effect influences. One would expect more displacement near the crack tip, however, with this specimen geometry free edge effects are dominating the horizontal displacements ahead of the crack tip. At higher angles the influence of the combination of crack tip singularity and edge effects is significantly reduced with the horizontal displacements decreasing rapidly for r >1.8 mm (LN(r)>0.6). At a COD of 0.11 mm, inside the plastic strain region, *U*-displacements correlate with HRR fields beyond the large strain region close to the crack tip. Closer to failure the measured displacements are between HRR and K fields. This response differs from the response measured by Dadkhah et. al. for cruciform type specimens [68, 69], where *U*-displacements showed K field dominance approaching the crack tip, but showed similar *V*-displacement response shown in Figure 7-30.

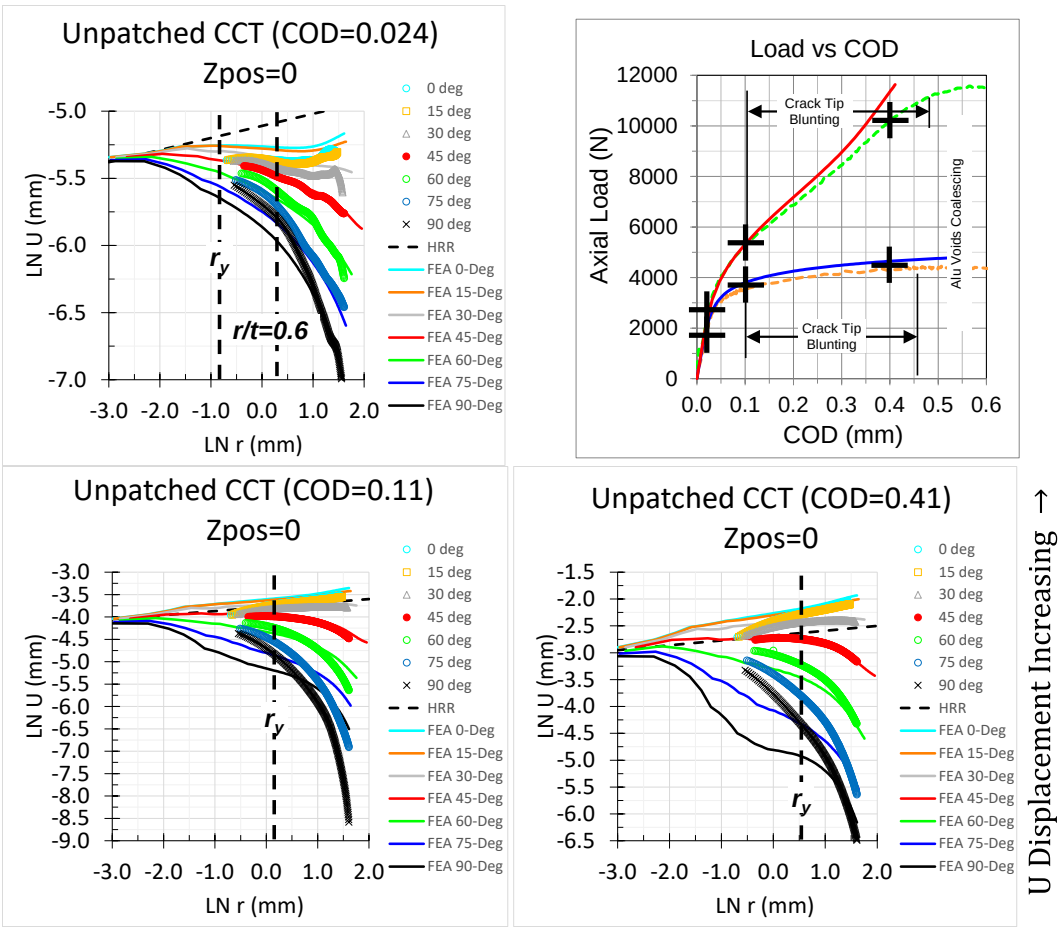

Figure 7-31 Unpatched horizontal displacement fields at the linear elastic limit, initiation of crack blunting, and the end of crack blunting. First order Irwin plastic zone (ry) and HRR fields are shown. Results show good correlation between FEA and DIC.

7.1.9.2 Patched Crack Tip Displacement Fields

Adding composite patch surface reinforcement across the notch changes the behavior on the free aluminum surface at the crack tip. Axial displacement, or *V*-displacement, fields in Figure 7-32 indicate that the surface reinforcement provides enough transverse constraint to eliminate free edge effects. For patched specimens, displacement field data is shown for inner radii of 0.5-0.6 mm to outer radii of 4.2-5.0 mm, which again are limited by DIC correlation near the crack plane and subset size. At the linear elastic response limit all displacement fields indicate K field dominance beyond LN(r) of 0.3, however, angles of 45° and less both measured and predicted response is close to

correlating with HRR fields for LN(r) < 0. As load increases HRR fields begin to appear closer to the crack tip for angles of 45° and lower. The transition from HRR to K field dominance for the lower angles appears constant at r=0.7 mm (LN(r) = -0.3) during crack blunting. For angles above 45° data indicates that crack tip blunting contributes to the divergence of displacement fields from either HRR or K dominance.

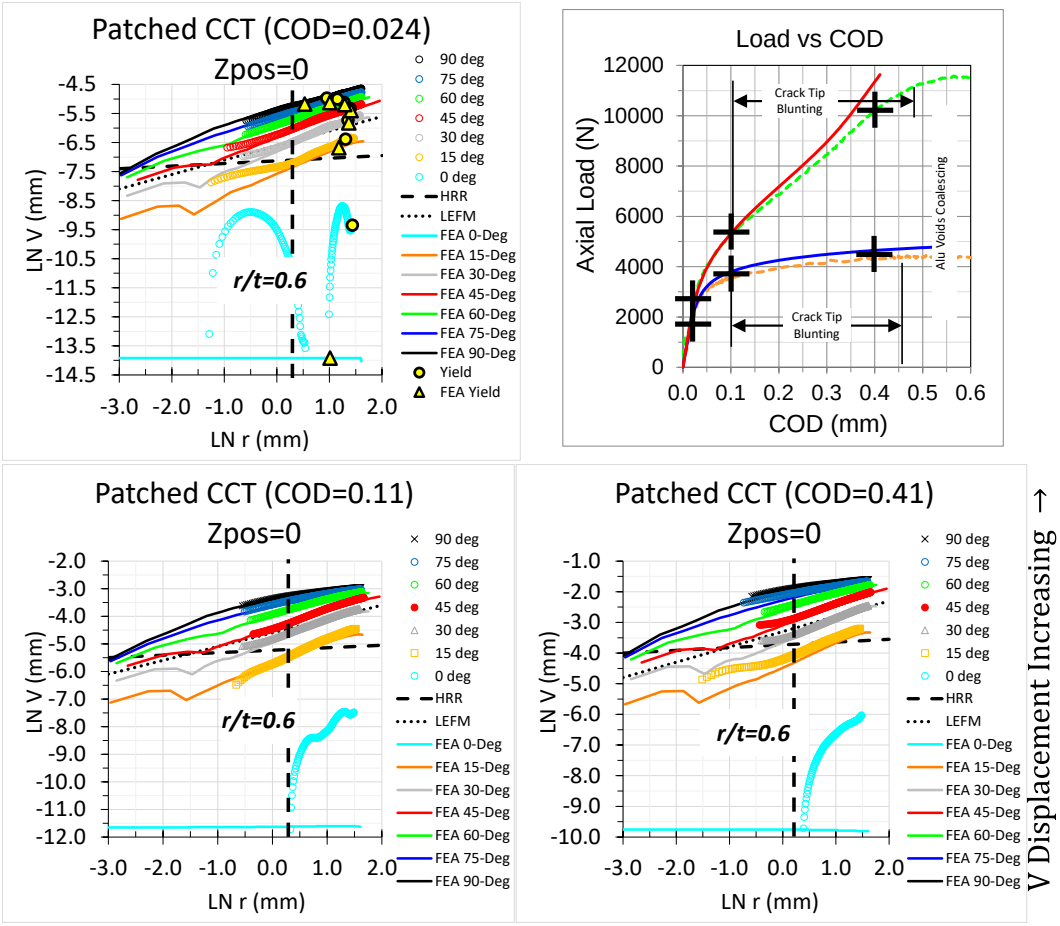

Figure 7-32 Patched axial displacement fields showing measured and predicted HRR field correlation approaching the crack tip and K field dominance outside r/t=0.6 for all CODs .

Patched *U*-displacements are plotted in Figure 7-33 for loads in the linear elastic response, crack blunting, and prefailure regions of the specimen response as noted on the load versus COD plot. Qualitatively, the patched specimen displacements show partial behavior correlation at the linear elastic response limit through crack blunting for path

angles of 45 degrees and less. However there is a displacement offset of nominally 0.085 mm with predicted displacement being greater than measured. At higher angles *U*-displacement fields did not respond proportionally with loading as required to meet HRR and K field assumptions; displacements along constant angle paths reverse sign that cannot be accounted for with HRR fields alone. At the linear elastic response limit a combination of bending and material nonlinearity creates a response with slopes between HRR and K Fields for angles of 0°, 15°, and 30°. As COD increases the displacement fields show correlation to K fields for the angles closer to the crack plane (0°, 15°, and 30°) for r > r/t=0.6. With correlation to HRR or K fields the behavior is assumed to be SSY.

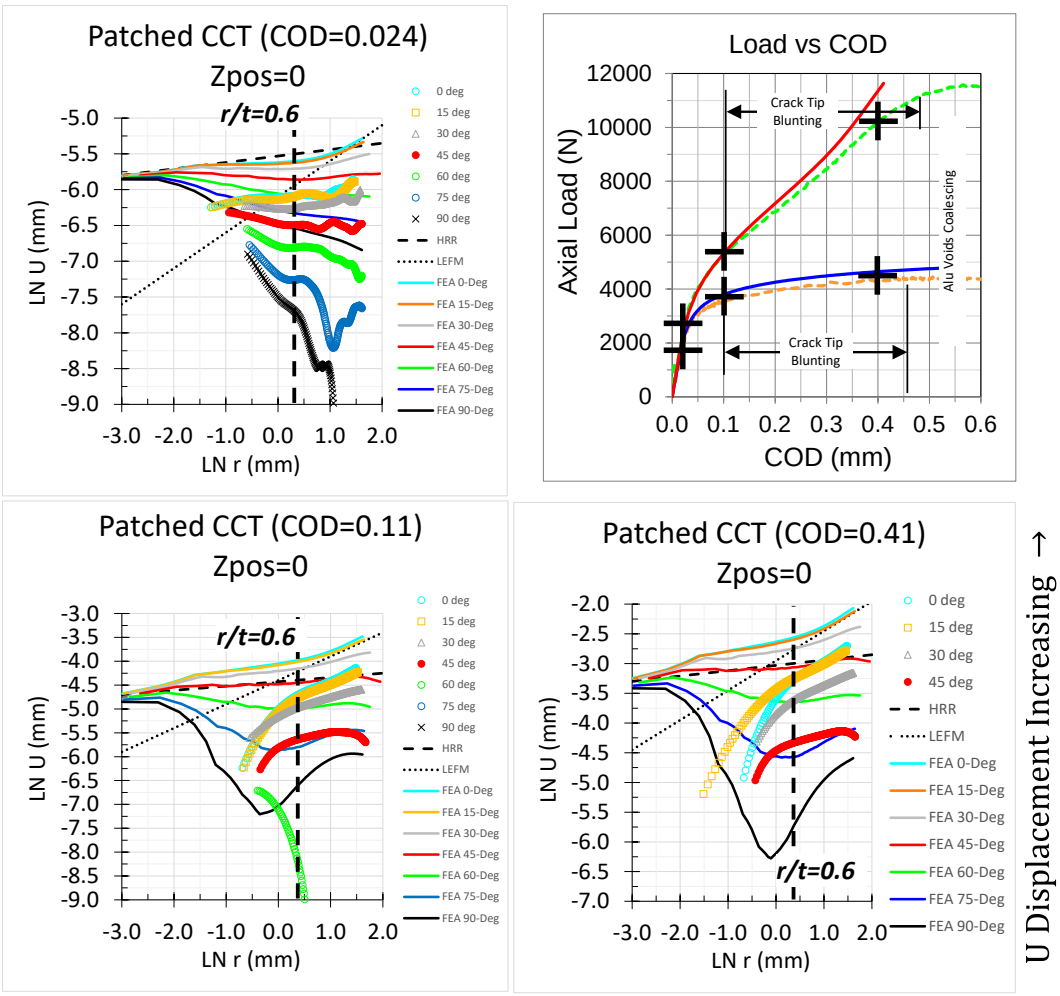

Figure 7-33 Patched horizontal displacement fields versus radial distance from the crack tip that show qualitative correlation and greater predicted displacement.

7.1.9.3 Summary and Comparison of Displacement Fields

Comparison of the *V*-displacements for mode-I loaded unpatched (Figure 7-30) and patched (Figure 7-32) specimens demonstrates measurable effects of one-sided surface reinforcements. Both specimen types exhibit SSY behavior near the crack tip with HRR and K fields within the plastic zone. Baseline unpatched specimens exhibited free edge effects evident at lower angles with the effects of crack blunting and full ligament plasticity shown in the higher angle displacement fields. The transition of *V*-fields from HRR to K dominant fields occurs within the plastic zone at a radius that increases with

load until crack blunting initiates. Addition of patch surface reinforcement does not change the general correlation with HRR and K fields within the plastic zone. The HRR to K transition occurs at a radius that does not change with load until the crack tip behavior changes from crack blunting to crack growth near the failure load. Qualitatively the patch reduces free edge effects from the displacement fields and quantitatively maintains K dominance for a wider range of angles and radius.

Comparison of the *U*-displacements for mode-I loaded un-patched (Figure 7-31) and patched (Figure 7-33) specimen show consistently lower displacement magnitudes for the patched specimen. The patch reduces the displacement magnitude and isolates the behavior of the ligament such that *U*-displacements change sign. The material displaces left due to global specimen contraction as well as right from ligament contraction. The displacement fields are similar between unpatched and patched with angles 30° and below exhibiting behavior somewhere between HRR and K fields. Both specimen types show near tip HRR field correlation at the linear elastic response limit loads. As loads increase a large strain field occurs near the crack tip where measured displacements diverge from HRR fields. For unpatched specimens K field dominance does not occur, likely due to free edge effects and general ligament plasticity instead of crack tip singularity dominated plastic zone. The patched specimen displacements from 0° to 30° have a narrow radius range of HRR field correlation that eventually transitions to an apparent K field dominance inside the plastic zone. This is opposite of theory predicting HRR field dominance within the entire elastic-plastic region depicted in Figure 2-4. In both cases the higher angle (60-90°) displacement fields do not correlate with either theory. For the unpatched specimen *U*-displacements logarithmically approach zero as

the radius increases. There is no transverse displacement outside the effect of the crack plane. The undersized ligament changes the local material behavior from crack tip singularity dominant to a combination of crack tip and overall ligament tensile behavior. Patched specimen *U*-displacement behavior for higher angles is not proportional to loading and as loading increases changes sign along the same radial path that cannot be accounted for with HRR or K fields.

The 0/90 directional surface reinforcement of the patched specimen provides a bridge across the plastic zone that distributes high strains. The directional reinforcement also resists the horizontal contraction of the full width material approaching the crack plane resulting in the ligament ahead of the crack responding more like an isolated tensile specimen centered near the crack tip. The raw displacements shown in Figure 7-34 are for a nominal COD of 0.05 mm (Unpatched 3 kN, Patched 4 kN) with the arrows indicating displacement direction; white for negative (to the left) and black for positive (to the right). The baseline unpatched specimen shows typical tensile behavior with horizontal contraction for full width and ligament material near the crack plane. Ahead of the crack tip *U*-displacement magnitudes are on the order of 0.010 mm, which decrease to zero at the center of the specimen. Patched specimen response shows material contraction centered nominally about the crack tip, with positive *U*-displacement magnitudes from the free edge to the crack tip of 0.006 to 0.002 mm, respectively, then from the crack tip to specimen centerline displacements are negative to zero.

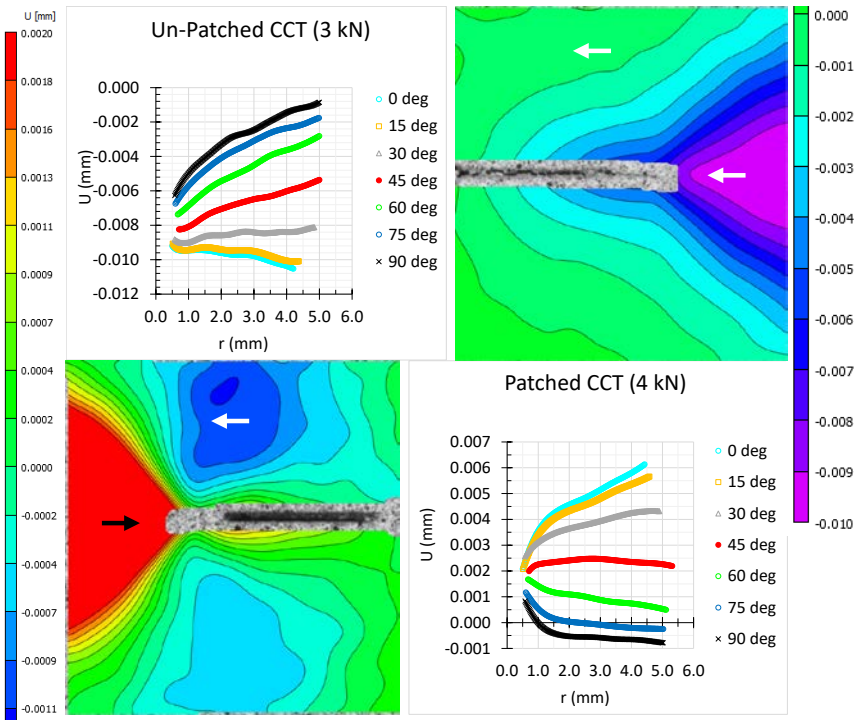

Figure 7-34 Unpatched and patched displacement fields at COD=0.05 mm showing the local crack tip response being similar to a tensile specimen centered at the crack tip with the addition of the composite patch.

7.1.10 Round One Measured and Predicted J-Integral Behavior

For both DIC and FEA results the J-integral was performed using Equation 118 with the assumptions that the free surface is under plane stress conditions and that linear elastic material properties are sufficient for the unpatched to patched comparison, although not appropriate for a true J-integral value. To perform the integral calculation, raw displacement gradients, du/dx, du/dy, dv/dx, and dv/dy, are output directly from the DIC software as a 2D tensor. Tensor values are used directly in Equation 118.

The measured COD as a function of J-integral response is shown in Figure 7-35, where the J value was averaged over the five paths, shown in Figure 6-4, and the left and right crack tips. DIC data shows little change for the free surface strain energy release rate with the addition of the composite patch. At the linear elastic response limit, COD=0.024 mm,

the load for the patched specimen is 25% greater and the J value is 25% greater. As load increases the change in J decreases, with J being 15% greater at a COD of 0.2 mm and equivalent to the unpatched specimen at a COD of 0.45mm, which is beyond crack blunting and into the initiation of crack growth. Beyond a COD of 0.45 mm the unpatched specimen SERR is greater than the patched specimen.

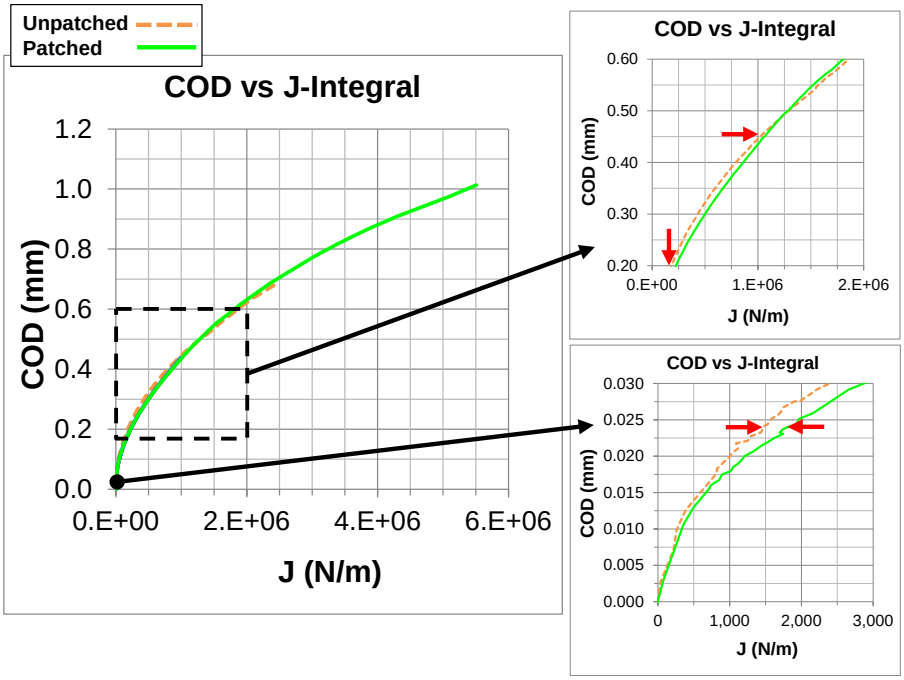

Figure 7-35 DIC COD as a function of J-Integral showing little difference between unpatched and patched response.

Numerically predicted response for load and J-integral value are shown in Figure 7-36. The measured and predicted load response for unpatched and patched responses assuming both small and large displacement solutions for the patched specimen show the global response prediction correlates when using the large displacement solution. The unpatched specimen solution diverges from measured with the limitation of assuming small displacements that is a limitation of the ABAQUS built in domain integral method. The center and right side of Figure 7-36 show the COD as a function of J-integral value. The difference between LEFM and EPFM predictions are evident as well as the

importance of capturing the out of plane bending and material nonlinearity with the large displacement assumption. The LEFM prediction cannot capture the nonlinear behavior of the SERR and the small displacement assumption over predicts the SERR as a function of COD. Using the large displacement assumption the measured and predicted J-integral values correlate into crack blunting (COD=0.2). For the unpatched specimen the correlation continues beyond a COD of 0.5 mm, while the patched specimen FEA predicts less SERR as a function of COD beyond a COD of 0.2 mm. Predictions for the patched specimen free and patched surface J-integral value are shown on the right of Figure 7-36 and show similar nonlinear behavior with a lower magnitude because of the reinforcement of the aluminum on the patched surface. No DIC data is available under the patch and therefore no comparison can be made.

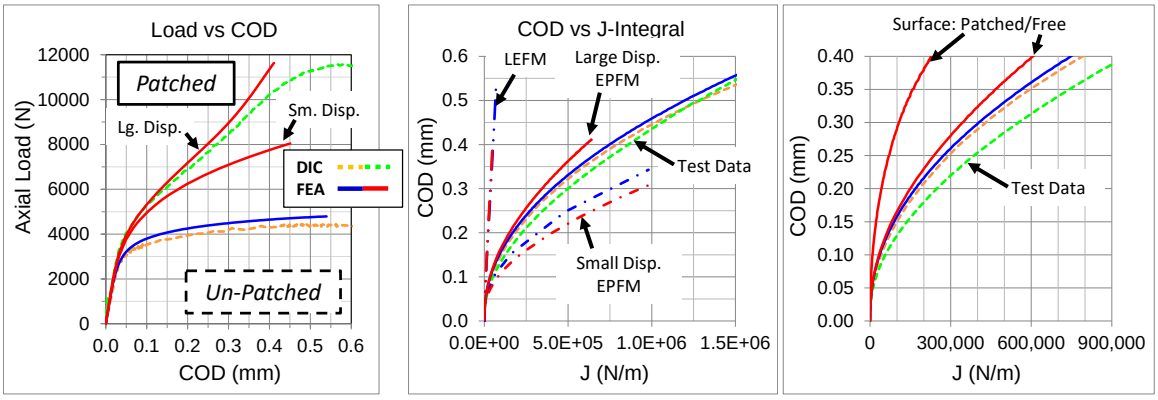

Figure 7-36 Round One measured and predicted load and J-integral response full range and below 9e5 N/m showing the need for large displacement assumption and EPFM.

7.2 Round Two Small Scale CCT Testing and Analysis Correlation

Two rounds of small scale CCT testing will be covered in this section. The intention of the second round was to corroborate observations from the first round of testing and analysis, therefore, the depth of reported results will be limited to general behavior and the change in behavior due to application of the composite patch.

7.2.1 Round Two Small Scale CCT Sharp Crack Tip Development

Fatigue cracks were again grown from the EDM notch using the same fatigue procedures as defined for round one small scale CCT specimens. A deviation from the round one was that fatigue loading was paused every 10k cycles so sets of static images could be taken for static loads of 0, 200, and 2000 N. Images and DIC data were used to track crack growth. Final quantification of the crack tip locations was performed using a Zeiss PrimoStar microscope in the Modern Engineering Materials Instructional Laboratory (MEMIL). Images of the cracks were magnified 5x and 10x and calibrated using images of a Westward metric scale that resulted in image calibration factors of 0.000791 and 0.000391 mm/pixel.

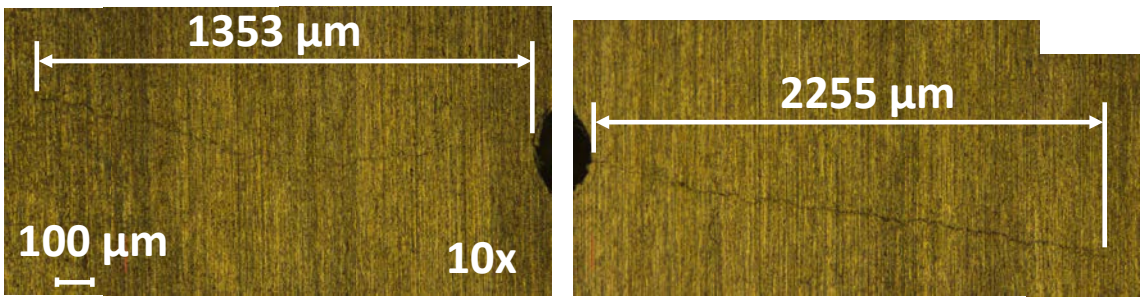

Figure 7-37 Round two example post fatigue crack growth image for CCT 2-02.

Final crack growth lengths for each aluminum blank along with total crack length and whether or not the specimen received a patch are listed in Table 22. Although the example image shows a significant crack growth missmatch, the left and right crack growth lengths used to compare with predictions matched within 10%. All specimens were tested, but only data from unpatched specimens 3 and 7 and patched specimens 4, 5, 6, 9, and 10 were fully processed.

Table 22 Round Two Small Scale CCT Specimen Fatigue Crack Growth Lengths

Spec ID	Notch Width (mm)	Crack Length (mm)	Left Crack (mm)	Right Crack (mm)	diff	Notes
CCT2-02	11.96	15.57	1.35	2.25	40%	tested
CCT2-03	11.96	14.22	1.07	1.18	10%	baseline
CCT2-04P	11.96	14.09	1.07	1.06	-1%	patched
CCT2-05P	11.99	13.97	1.02	0.96	-7%	patched
CCT2-06P	11.99	14.95	1.46	1.50	2%	patched
CCT2-07	11.99	14.31	1.13	1.19	6%	baseline
CCT2-08	11.99	14.23	1.19	1.06	-13%	baseline
CCT2-09P	11.99	13.97	1.04	0.94	-11%	patched
CCT2-10P	11.99	13.92	0.91	1.02	11%	patched
CCT2-11	11.96	14.49	1.46	1.06	-37%	tested
CCT2-12	11.99	13.72	0.92	0.81	-13%	baseline
Ave	11.98	14.31	1.15	1.19	-1.06%	
Stdev	0.01	0.53	0.20	0.40	19.31%	
COV	0.1%	3.7%	17.2%	33.4%	-1816%	

7.2.2 Round Two Small Scale Test DIC Processing Parameters

In round two DIC images of both the free surface (Side_0) and patched surface (Side_1) were taken during testing. Images on the patched surface were lower resolution and were not used for detailed crack tip study, however, they did yield information about disbonding of the patch at the notch. The DoF for both cameras were focused so that the surface remained in focus for the range of out of plane deflection experienced minimizing bias and error due to movement relative to the camera lens.

Processing parameters for both surfaces are listed in Table 23 and Table 24 for the free and patched surfaces, respectively. Free surface images for DIC resulted in a nominal FOV 26.7 mm x 14.1 mm and an AOI 23.3 mm x 13.4 mm. Free surface images were processed using a nominal subset size of 45x45 pixels (0.29x0.29 mm) and a step size of 9 pixels (0.059 mm). Patched surface images for DIC resulted in a nominal FOV 23.0

mm x 18.2 mm and an AOI 21.5 mm x 16.8 mm. Patched surface images were processed using a nominal subset size of 51x51 pixels (0.90x0.90 mm) and a step size of 10 pixels (0.17 mm).

Strain filter selection was based on the error and bias calculated for 20 images taken at zero load. A general setting of 41 data points was selected at first and then refined when studying specimens CCT2-07 and CCT2-04P in detail. Across the specimens the nominal bias (offset) magnitude was 10-40 με with an error of 20-40 με (deviation) with strain filters that ranged from 15 to 41 data points.

Table 23 Round Two Small Scale Free Surface DIC Processing Parameters

	DIC Information _0 (Free Surface)								
Specimen ID	Subset (pixels)	Step (pixels)	Strain Filter (data points)	Smoothing Filter (data points)	calibration (mm/pixel)	FOV Width (mm)	FOV Height (mm)	AOI Width (mm)	AOI Height (mm)
CCT2-03	45	9	41	15	0.00652	26.7	14.1	23.0	13.5
CCT2-04P	51	10	21	15	0.00652	26.7	14.1	23.6	13.3
CCT2-05P	45	9	41	15	0.00651	26.7	14.1	23.3	13.5
CCT2-06P	45	9	41	15	0.00651	26.7	14.1	23.1	13.4
CCT2-07	45	9	15	15	0.00650	26.6	14.0	23.3	13.5
CCT2-09P	45	9	41	15	0.00648	26.6	14.0	23.2	13.1
CCT2-10P	41	8	41	15	0.00653	26.7	14.1	23.7	13.5
Average					0.006513	26.7	14.1	23.3	13.4
STDEV					0.000019	0.1	0.0	0.2	0.1
COV (%)					0.3%	0.3%	0.3%	1.0%	1.1%

Table 24 Round Two Small Scale Patched Surface DIC Processing Parameters

	DIC Information _1 (Patched Surface)								
Specimen ID	Subset (pixels)	Step (pixels)	Strain Filter (data points)	Smoothing Filter (data points)	calibration (mm/pixel)	FOV Width (mm)	FOV Height (mm)	AOI Width (mm)	AOI Height (mm)
CCT2-03	51	10	51	15	0.01772	23.5	18.6	21.3	16.8
CCT2-04P	51	10	25	15	0.01714	22.8	18.0	21.4	16.8
CCT2-05P	51	10	51	15	0.01708	22.7	17.9	21.5	16.7
CCT2-06P	61	10	51	15	0.01705	22.6	17.9	21.3	16.7
CCT2-07	51	10	51	15	0.01788	23.7	18.7	21.5	16.8
CCT2-09P	51	10	51	15	0.01722	22.9	18.0	21.5	16.8
CCT2-10P	51	10	51	15	0.01712	22.7	17.9	21.4	16.8
Average					0.01733	23.0	18.2	21.5	16.8
STDEV					0.0003	0.4	0.3	0.2	0.0
COV (%)					1.7%	1.7%	1.7%	0.8%	0.2%

7.2.3 Comparison of Round Two Patched and Unpatched Specimen Response

Round two included two unpatched and five patched small scale CCT specimens. Load versus COD response due to monotonic tensile loading was consistent between like specimens and correlated well with round one test data for both unpatched and patched specimens prior to disbonding of the adhesively bonded patch adjacent to the notch, as shown in Figure 7-38. The load versus COD response of the unpatched specimens correlated with round one data through ultimate failure.

Peak load occurs prior to aluminum crack growth for all round two patched specimens, as seen in the patched load versus COD response that correlates well with the unpatched response after patch disbonding. Although an optimum peak load was not achieved, the data acquired allows continued investigation of the plastic zone evolution prior to failure.

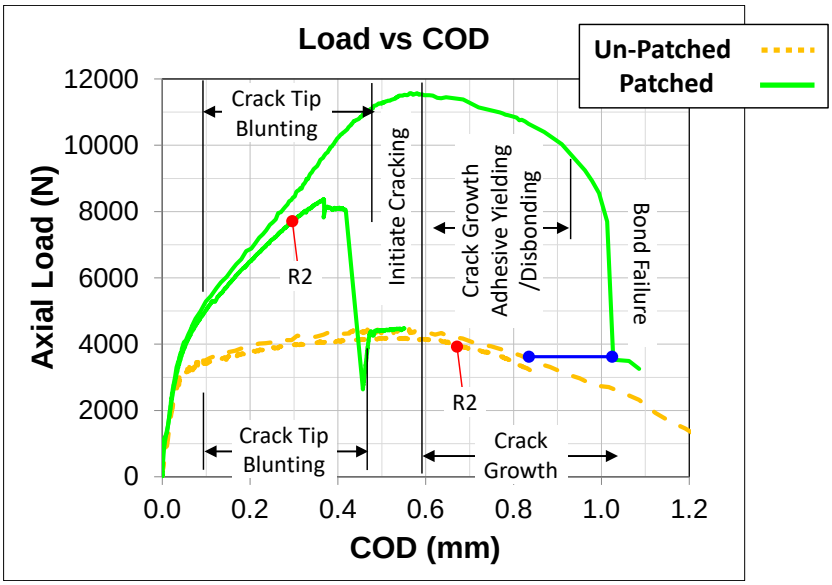

Figure 7-38 General round two small scale load vs COD compared with round one behavior.

Full comparison of both round one and two load versus COD responses are shown in Figure 7-39. The average peak load of the round two unpatched specimens was 4,280N at an average COD of 0.54 mm, which is statistically equivalent to round one average peak load of 4,500 N and COD of 0.54 mm. Patched specimen achieve an average peak load of 8,580 N, which is 25% lower than the round one peak of 11,574 N, although the peak load is still 100% greater than the unpatched round two specimens. Again, the initial stages of crack behavior correlate as a function of COD, although premature failure prevents comparison of the later stages of crack blunting and failure.

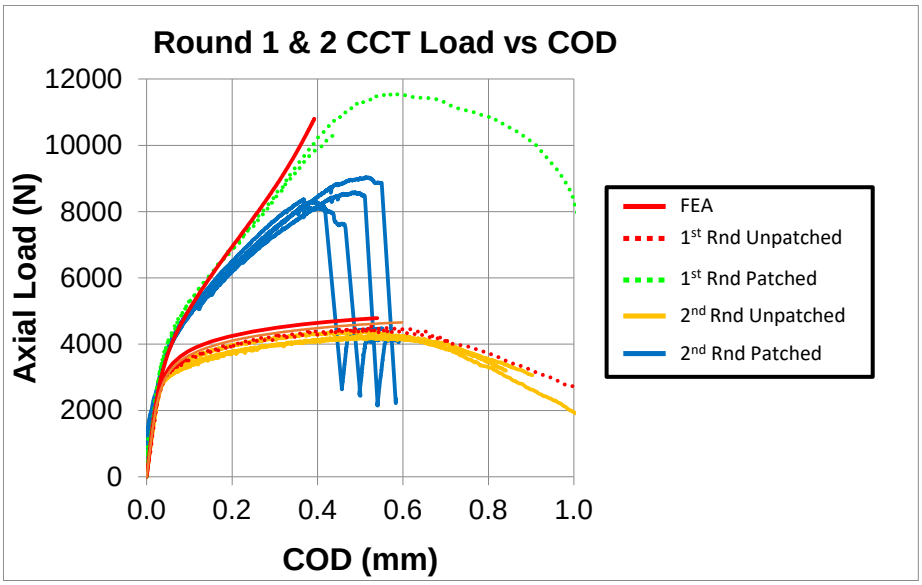

Figure 7-39 Round one and two small scale load vs COD with FEA predictions.

Round one and two free surface average von Mises strain behaviors of unpatched and patched specimens as a function of COD are shown in Figure 7-40. The strain values plotted are averaged over a 1 mm^2 region nominally 1 mm ahead of the crack tip. The strain behaviors ahead of the crack tip correlate into crack tip blunting. For round two the COD of 0.2 mm was the point at which the patch appears to disbond locally at one crack tip as shown in Figure 7-41.

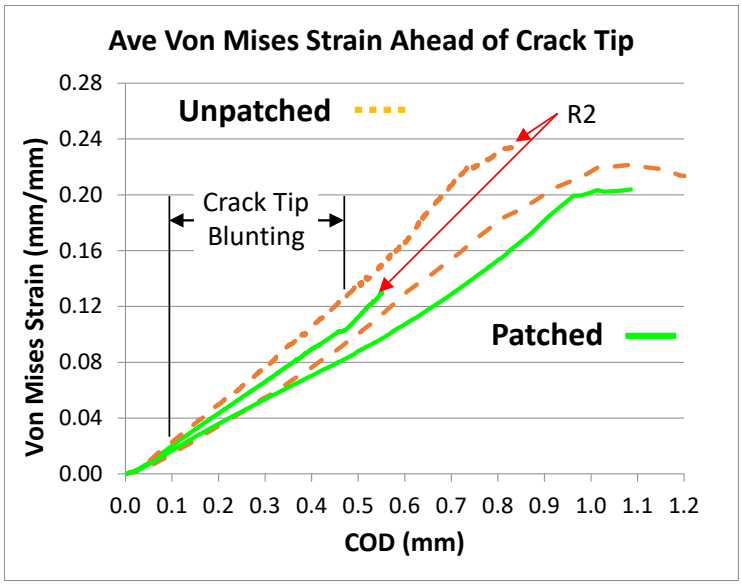

Figure 7-40 Small scale CCT average von Mises strain ahead of the crack tip for both round one and two.

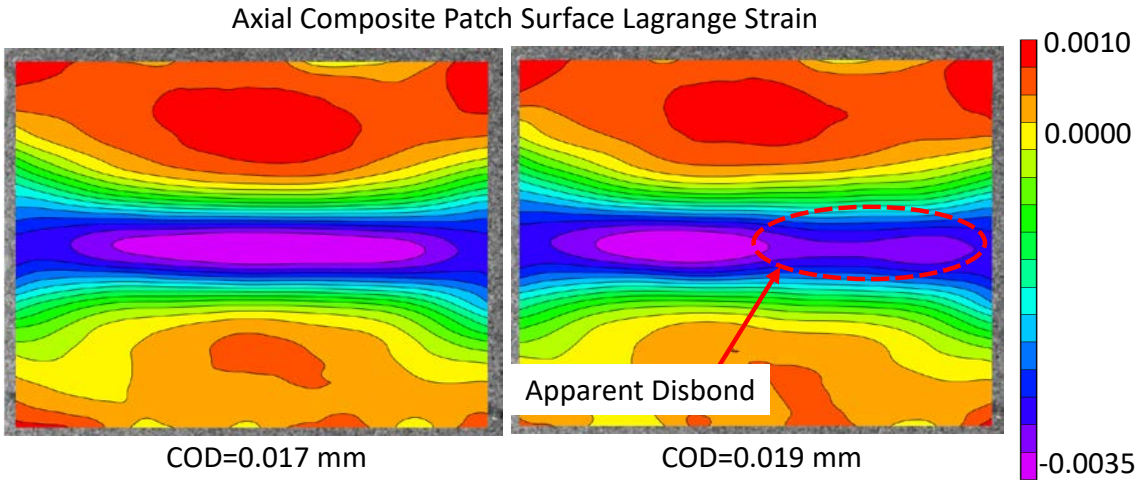

Figure 7-41 Small scale CCT patched surface axial strain showing apparent disbond on left crack tip.

Similar von Mises strain behavior occurs at the crack tip for round one and two specimens. For comparison contours for a COD of 0.2 mm, early stage of crack blunting, are shown in Figure 7-42. Strain contours for the patched specimen indicate a measurable effect of the surface reinforcement with a blunted region of large strain ahead of the crack tip and a greater area of large strain consistent with fiber reinforcement in both axial and transverse directions.

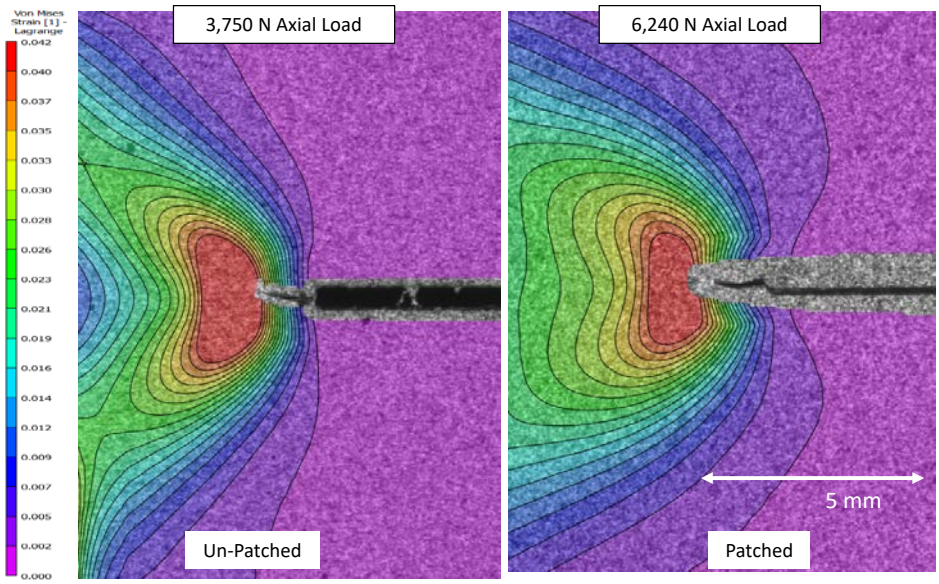

Figure 7-42 Von Mises strain comparison of unpatched (L) and patched (R) crack tips during the early stage of crack blunting (COD=0.2mm) showing increased area of large strain for the patched specimen.

7.2.4 Comparison of Round Two Measured and Predicted Response

Load and average vertical strain responses are presented up to peak load in Figure 7-43 with the load response for both round one and two. Only the round two unpatched and patched average axial strain ahead of the crack tip are presented. Correlation of the predicted and measured unpatched response was good with the behavior matching for both load and average axial strain. Evidence of patched specimen disbonding near the crack tip, as shown in Figure 7-41, is further highlighted in the comparison of the predicted and measured load response. Correlation of the response is good until a COD of 0.19 mm, where the measured load versus COD stiffness decreases with average failure occurring at 8,580 N and an average COD of 0.54 mm. Despite the initial disbond further progressive damage leading to full patch disbond begins near a COD of 0.4 mm, which is within the crack blunting region of crack evolution. Predicted loads for unpatched and patched specimens as a function of COD are again within 15% of the test data to a COD of 0.3 mm, where patch disbond results in the patched prediction deviating up to 30%.

Unpatched response prediction is consistently within 8% to 12% of measured up to peak load, while the patched predictions are within 5-13% of test data until the initial disbond.

Using the same process as round one, axial strains were extracted for comparison of DIC and FEA responses. Both unpatched and patched average axial strain magnitude correlated well as a function of COD for COD less than 0.19 mm, where unpatched predicted strains match measured and predicted patched strains at 18% lower than measured. At a COD of 0.3 mm unpatched predictions continue to match and patched strains continue to diverge and are 23% lower than measured.

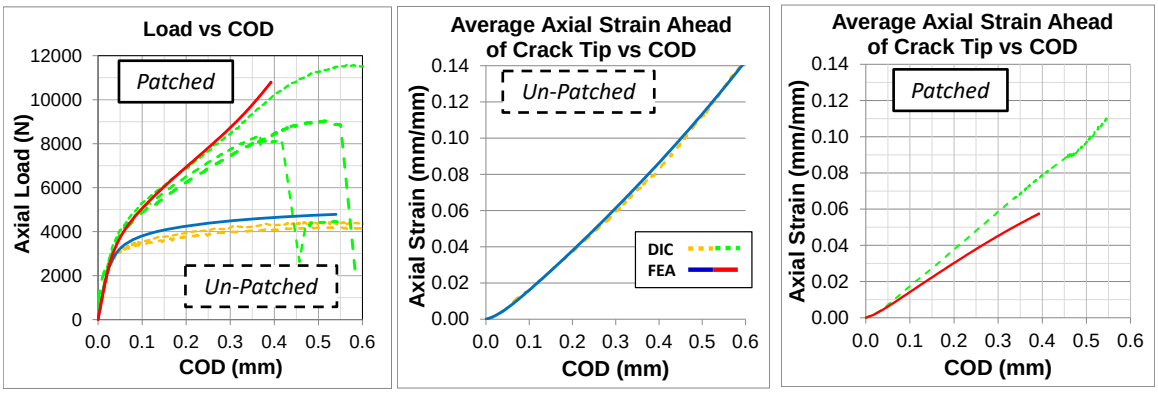

Figure 7-43 Round two measured and predicted load versus COD with small and large displacement assumptions for finite element analysis predictions.

7.2.5 Round Two Quantitative Change with Application of a Composite Patch

Quantitative comparison of the load and large strain regions as a function of COD supports the observed improvement in the patched load versus COD behavior. As previously discussed for round one test response and shown in Figure 7-2 and Figure 7-38, the crack tip behavior and failure of unpatched and patched specimens appear to correlate with the COD. The change in response for round two test specimens due to application of a composite patch will be quantitatively studied with reference back to round one results.

Similar to the round one response as COD increases the additional patch material allowed the specimen to carry more load. That change in load capacity is again linearly proportional to the COD as shown in Figure 7-44. The measured trend correlates well with round one data until CODs greater than 0.3 mm and the predicted trends match.

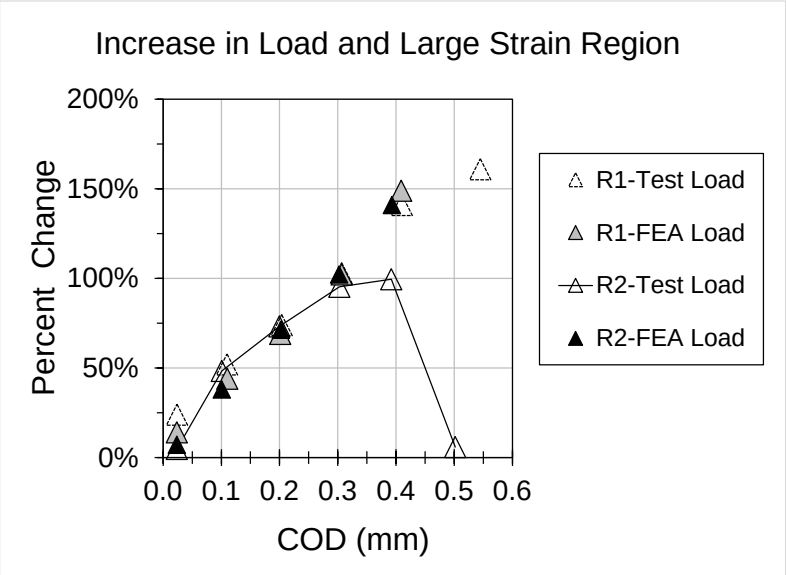

Figure 7-44 Round one and two load increase as a function of COD showing linearly proportional load capacity benefit until disbond.

Large strain area and volume are approximated using the process defined in round one and shown in Figure 7-14 and Figure 7-15. The round two change in large strain area and volume, along with round one results for reference, are shown in Figure 7-45. Again, the free surface large strain area decreases as a function of COD. For CODs less than 0.4 mm the patch reinforcement increases the region of large strain with the magnitude of area increase being inversely proportional to COD.

Large strain volume change has an inverse relationship with COD and the patched volume is consistently smaller with the addition of surface reinforcement. The decrease in total large strain volume ahead of the crack tip is a measure of the load sharing being done by the composite reinforcement. The change in large strain volume appears to

approach a local minimum where the unpatched large strain area exceeds that of the patched specimen.

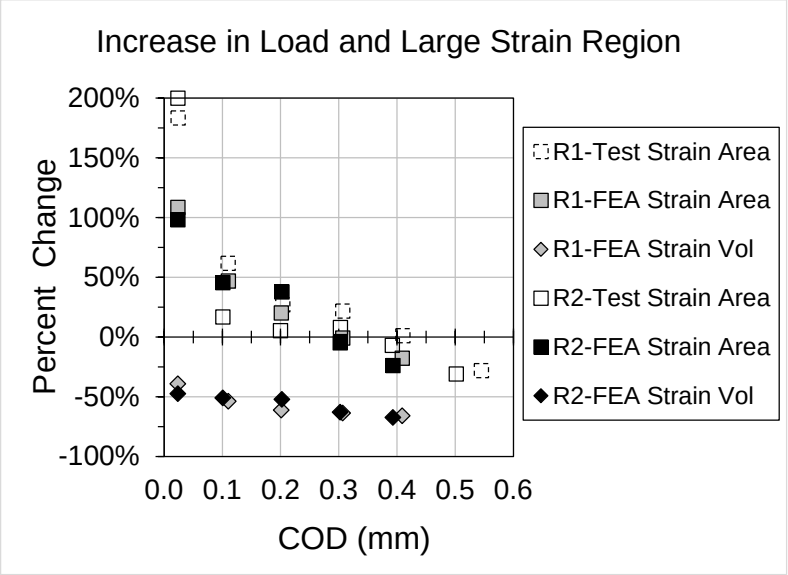

Figure 7-45 Round one and two percent change of free surface large strain area, and large strain volume at the crack tip as a function of COD. Results show inversely proportional strain area and volume changes.

7.2.6 Round Two Measured and Predicted HRR Field Correlation

Comparison of numerical predictions and the DIC data for fundamental displacement fields and calculated J-integral values will be discussed in this section for round two specimens.

7.2.6.1 Unpatched Crack Tip Displacement Fields

Axial displacement fields, *V*, of the round two unpatched specimen are shown in Figure 7-46 with the fields for CODs of 0.024, 0.11, and 0.39 mm corresponding to the load, COD, and crack tip behavior identified in the upper right of the figure. Better speckle patterns allowed data to be captured closer to the crack tip. At the crack tip the data and predictions indicate a region of LSY from the crack tip to a radial position of 0.37 mm. As the COD increases test data indicates the same LSY zone, however, DIC data is not

available that close to the crack tip. Beyond LSY DIC data indicates SSY and correlation with HRR fields until a radial position of 1.0 mm. Round two test data and FEA does not correlate as well as round one predicted behavior. General displacement magnitude correlates approaching the specimen edge and beyond LSY indicates K dominated displacement fields. Edge effects and element integration order may play a role in the correlation.

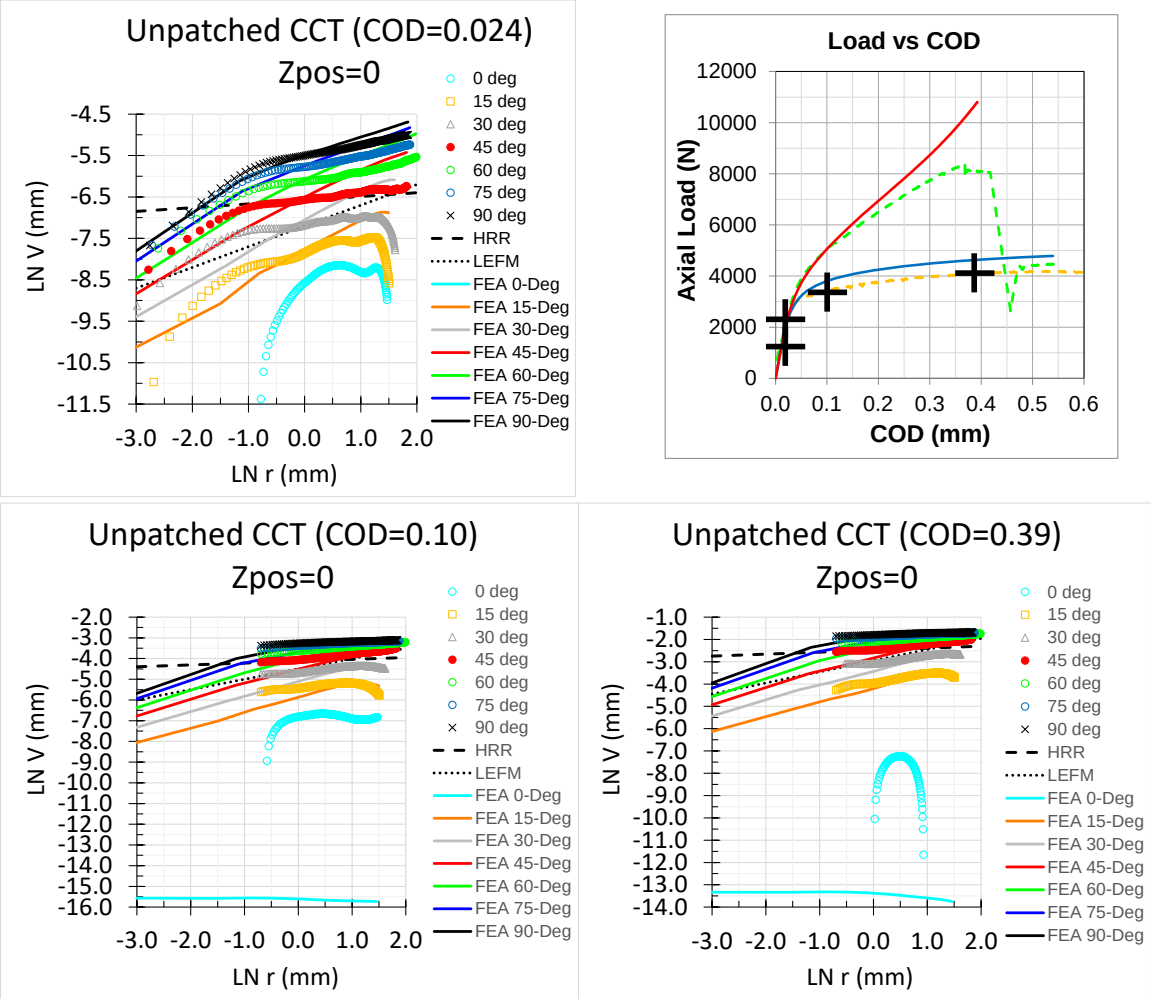

Figure 7-46 Unpatched axial displacement fields at the linear elastic limit, initiation of crack blunting, and the end of crack blunting. Nominal HRR and K fields are shown for the 45 degree path. Results show the region close to the crack tip in a state of LSY.

Horizontal, or *U*, round two displacement fields are reported in Figure 7-47. Again, displacements are negative, therefore, absolute displacements are plotted. Although there

is a consistent offset between the measured and predicted displacements, the overall behavior correlates well. Path angles less than 30-deg show correlation with HRR fields close to the crack tip. HRR field correlation increases as COD increases, although edge effects are evident beyond a radial position greater than 1.65 mm.

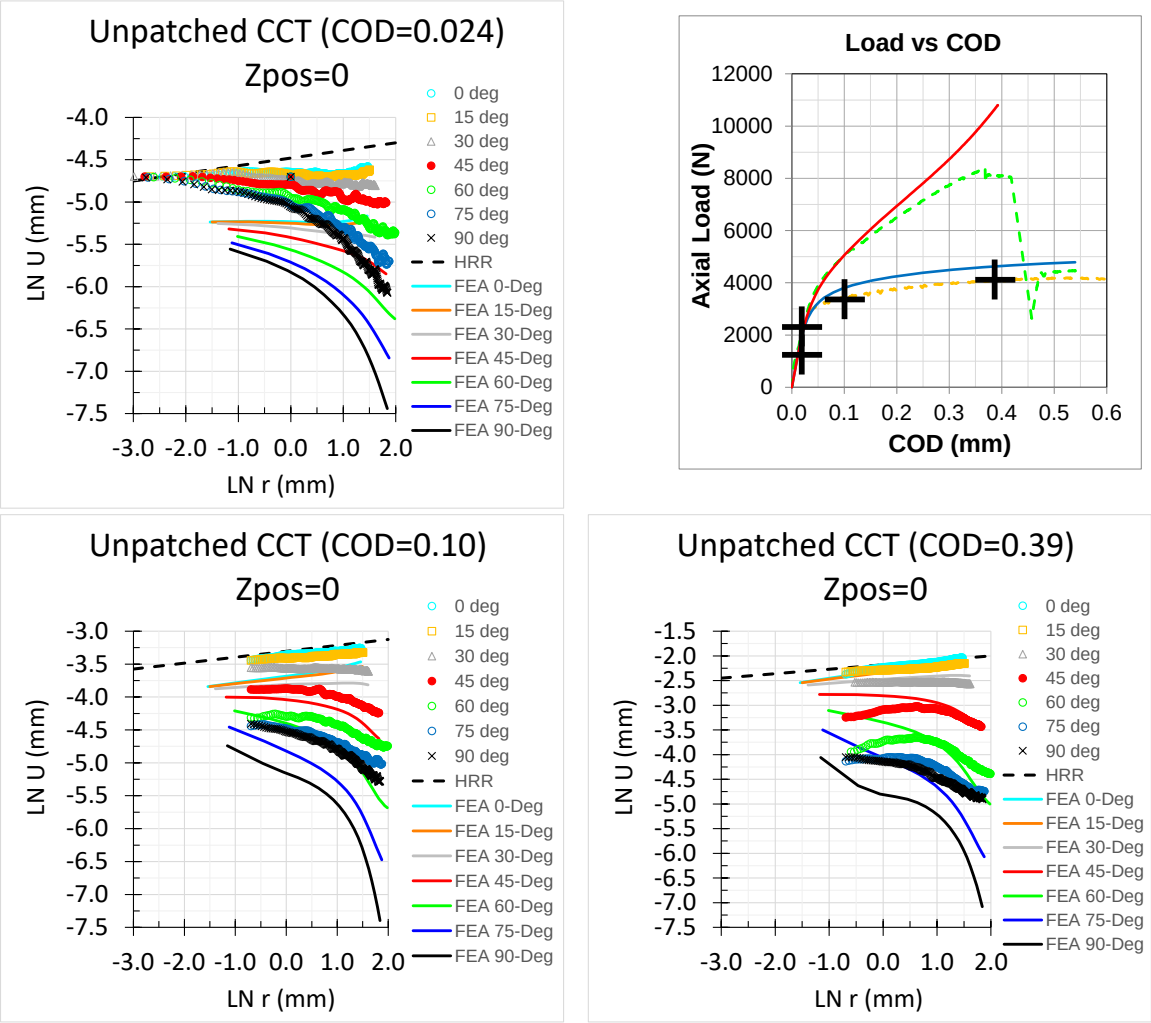

Figure 7-47 Unpatched horizontal displacement fields at the linear elastic limit, initiation of crack blunting, and the end of crack blunting. HRR fields are shown. Results show good correlation between FEA and DIC behavior with an offset.

7.2.6.2 Patched Crack Tip Displacement Fields

Round two patched free aluminum surface axial displacement, or *V-displacement*, fields are shown in Figure 7-48 at the same CODs studied for the unpatched specimens. Surface

reinforcement provides enough transverse constraint to reduce free edge effects until a radial position of 4.48 mm for angles of 30-deg or less. HRR field correlation for DIC data shifts to radial positions between 0.47 and 0.78 mm. FEA results do not correlate with HRR fields, but they do approach K fields as radial position increases.

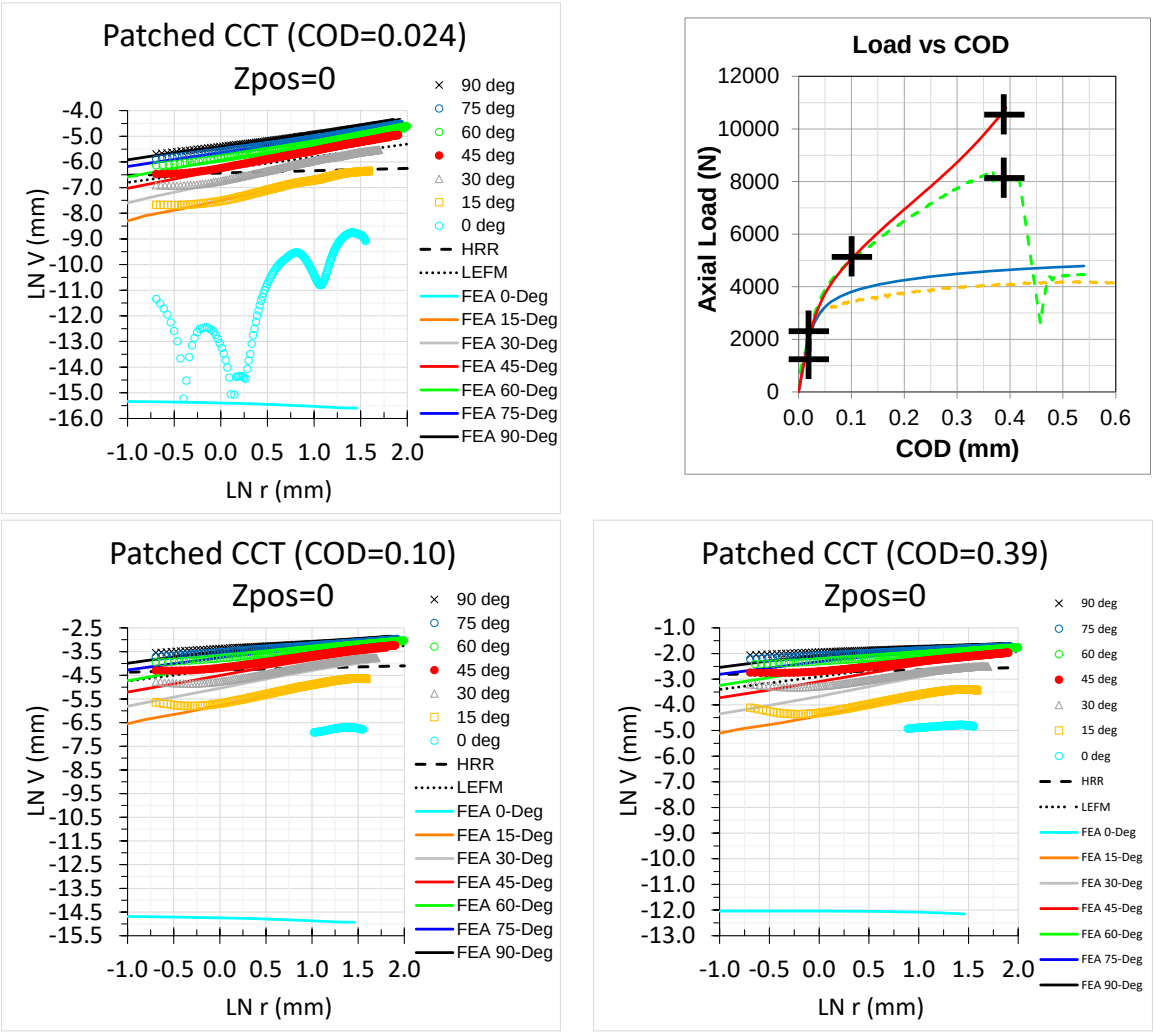

Figure 7-48 Patched axial displacement fields showing measured and predicted HRR field correlation approaching the crack tip and K field dominance as COD increases.

Patched *U*-displacements are plotted in Figure 7-49. Similar to round one, predicted patched specimen displacements show qualitative behavior correlation for path angles of 45 degrees and less. There is a displacement offset of nominally 0.010 to 0.035 mm with

predicted displacement being greater than measured. At lower angles predicted *U*-displacement fields correlate with HRR and K fields.

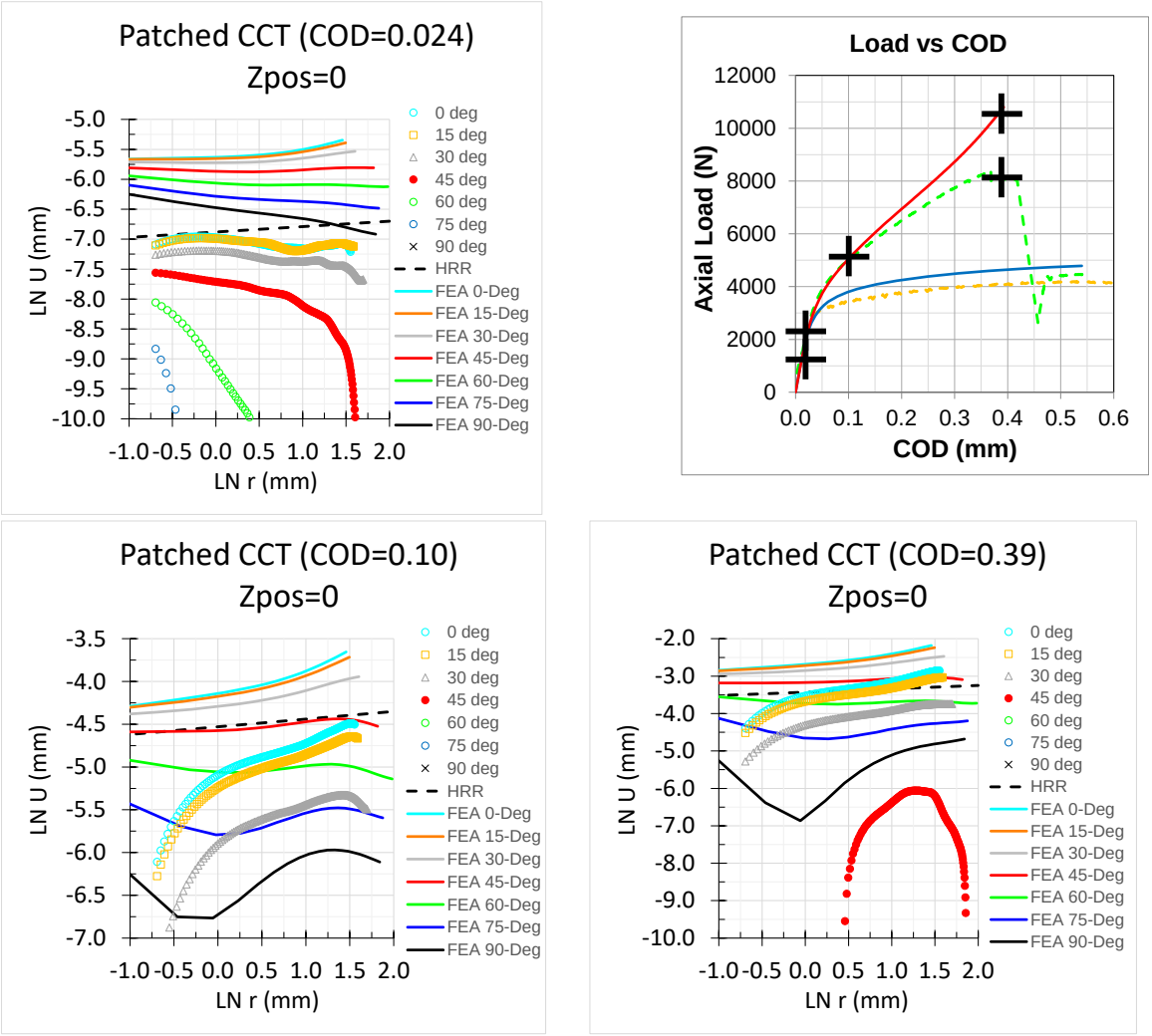

Figure 7-49 Patched horizontal displacement fields versus radial distance from the crack tip that show qualitative correlation and greater predicted displacement.

7.2.7 Round Two J-Integral Prediction Correlation

Round two J-integrals were performed using Equation 118 with the assumptions that the free surface is under plane stress conditions and that linear elastic material properties are sufficient for the unpatched to patched comparison. The measured COD as a function of J-integral response is shown in Figure 7-50, where the J value was averaged over the five paths, shown in Figure 6-4, and the left and right crack tips. DIC data shows little change

for the free surface strain energy release rate with the addition of the composite patch. The predicted response shows a patched free-surface J-integral magnitude that correlates well to a COD of 0.2 mm and is then lower than the unpatched specimen. No DIC data is available under the patch, and therefore no comparison can be made for the patched surface J-integral value.

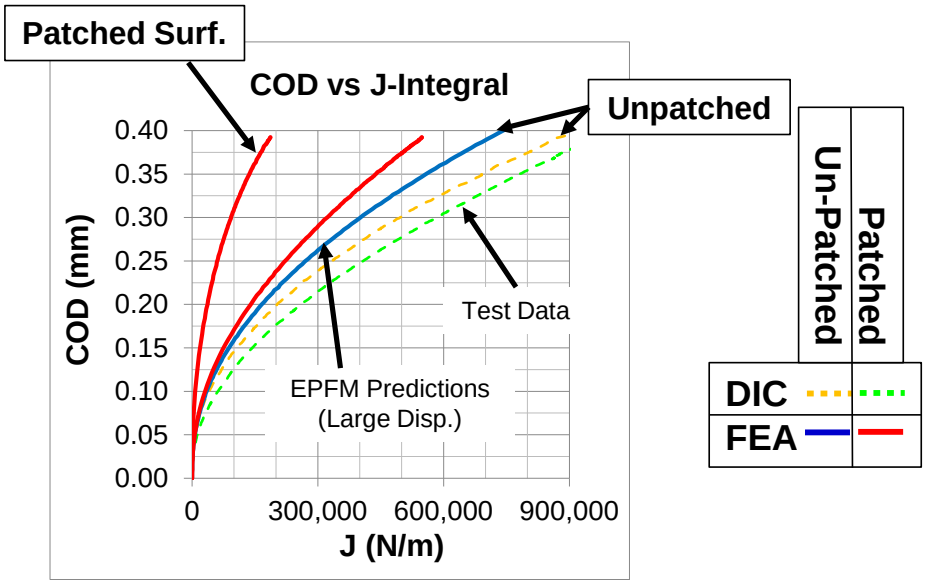

Figure 7-50 Measured and predicted load and J-integral response below 9e5 N/m showing the need for large displacement assumption and EPFM.

7.3 Summary and Discussion of Small Scale Correlation Results

For both round one and two simple FEA predicted response correlated with the measured load and free aluminum surface test data for both unpatched and patched CCT specimens through the initiation of crack blunting to a COD of 0.19 mm. Unpatched predictions correlate well until a COD of 0.5 mm prior to the initiation of crack growth. Round one and two predicted loads as a function of COD were within 0% to 13% of test data for both unpatched and patched specimens. Predicted free surface large strain fields and measured areas correlate well with DIC with representative areas within 0% to 44%, with round one predictions within 0% and 11% and typically larger while round two

predictions are typically smaller with magnitudes within 2% and 44% for the unpatched specimens. Round one predictions were within 0% to 11%, while round two predictions were typically within 19% with the exception of the lower CODs. Predicted patched representative large strain areas are within 6% to 20% typically smaller than measured. Quantitative and qualitative correlation of the free surface large strain fields in section along with correlation of the displacement fields give confidence that FEA is producing a reasonable approximation of the specimen response for the unpatched specimen through crack blunting and for the patched specimen to a COD of 0.4 mm when patch disbonding does not occur. Increased load capacity of the patched specimen is linearly proportional to COD while the increase in large strain area is inversely proportional to COD. Additional patched load and displacement capacity correlates with the accumulation of increased large strain area and plastic deformation on the free surface of the aluminum. The through thickness plastic aluminum behavior and centerline free surface axial strain indicate effective transfer of load across the adhesive layer to the composite patch until patch disbond. The overall volume of large strain (predicted) is always lower with the addition of the composite patch due to the load sharing between the patch and the aluminum. Because of out of plane bending, increased contribution of in-plane tension and yielding, the resulting magnitude of change in large strain volume due to the patch begins to be equal.

For EPFM the predicted free surface displacements fields correlate well with DIC data for the vertical direction parallel to the load axis. Predicted horizontal displacement fields ahead of the crack tip quantitatively correlate well for the unpatched specimens. The patched displacement fields only correlate qualitatively at the linear elastic response limit

but diverge in both response characteristics and magnitude as COD increases. Correlation with HRR fields occurs for vertical displacements along angle paths between 15 and 45 degrees, both predicted and measured. Horizontal correlation is predicted close to the crack tip, but the influence of edge effects is evident in U-displacement data for both unpatched and patched responses. With correlation in the primary, vertical displacement, direction the predicted and measured J-integral are a valid measure of the nonlinear strain energy release rate response [50].

Studying the free surface J-integral behavior shown in Figure 7-36 and Figure 7-50, predictions using a large displacement assumption and EPFM correlates well with the unpatched specimen response. Round one and two predictions correlate with each other and indicate that the addition of the patch reduces the magnitude of SERR available at the crack tip. Test data indicates greater SERR with the patch as a function of COD. Both measured and predicted values are inversely proportional to COD. Compared to round two data, the prediction deviates after the initial patch disbond at a COD of 0.19 mm. The predicted J-integral values for unpatched specimens are within 12% of round one test data but within 19% for round two. Predicted patch response was within 20% to 30% and 36% to 50% for round one and two comparisons respectively. A possible explanation for the discrepancy in measured and predicted J-integral values is a difference in bending due to the boundary conditions. FEM has perfect nodal displacement at the end of the repaired plate, while the test specimens had grip plates adhesively bonded to the repaired plate that could have allowed additional flexibility at the grips.

7.4 Large Scale CCT Testing and Analysis Correlation

Comparison of measured and predicted results for the large scale CCT specimens does not include the free surface large strain areas or displacement fields since DIC was not used. Basic axial load and axial strain gauge data as a function of COD will be compared with the FEA predictions to establish correlation. Then analytical and numerical predictions of failure loads will be presented.

7.4.1 Unpatched Large Scale CCT Results

Static responses of the aluminum only CCT specimens were consistent. Initial load versus COD was linear response transitioning to nonlinear. Nonlinearity of the load versus COD was assumed to indicate crack extension. Load versus COD data for specimens 5, 7, and 8 are shown in Figure 7-51. The peak loads were 174.4, 182.4, and 181.6 kN for specimens 5, 7, and 8, respectively, for an average peak load of 179.8 kN with a coefficient of variance of 2.5%. Initiation of nonlinear behavior occurred at 85.4, 78.3, and 95.7 kN for specimens 5, 7, and 8 respectively. The average load for nonlinear behavior was 86.5 kN or far field stress level of 49 MPa. The average initial compliance of the aluminum specimens, change in COD versus change in load, from 22.3 to 66.8 kN was 0.004 mm/kN. Figure 7-52 shows the aluminum ligament failure mode for both specimens 5 and 7, on the left and right, respectively. In both cases, the center notch is bound by smooth, straight fatigue precracks. Crack extension in specimen 5 angled downward on both sides of the notch and exhibited stable ductile tearing until about the last 3.2 mm in each ligament. The crack extension in specimen 7 remained relatively straight as it progressed through the remaining ligament on the strain gauge 0/2 side of the notch, however, the crack extension angled upward on the S1/3 side of the notch.

Both sides became unstable with 6.4 mm of ligament left. Specimen 8 crack extension angled upward under stable ductile tearing and became unstable with about 6.4 mm left in each ligament.

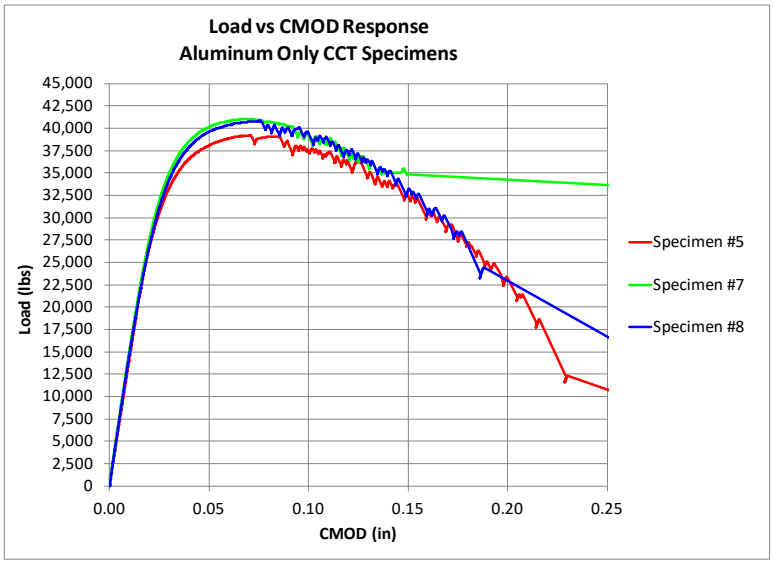

Figure 7-51: Large scale unpatched static specimen load versus COD response.

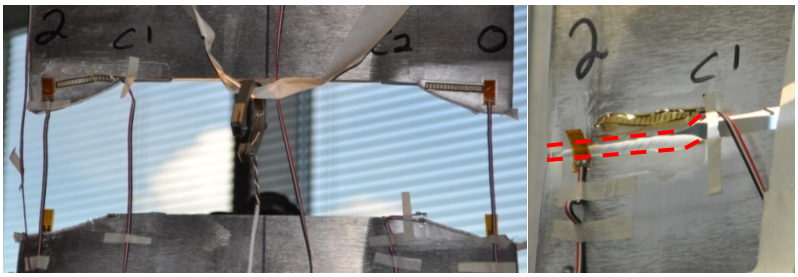

Figure 7-52: Large scale unpatched aluminum failure modes for specimens 5 (L) and 7 (R). The ring gauge hangs from tape in the left photo.

7.4.2 Patched Large Scale CCT Results

Linear elastic static responses of the composite patched CCT specimens were consistent. Initial load versus COD response was linear transitioning to nonlinear. Nonlinearity of the load versus COD was assumed to indicate aluminum plate crack extension. Load versus COD data for specimens 4, 9, and 21 are shown in Figure 7-53. The peak loads were governed by the load limits of the test frames. Specimen 21 follows the same load

versus COD curve as specimen 4, suggesting that the sensitization of specimen 21 has no significant effect on the response. The difference in load versus COD response between specimen 9 and the shared response of specimens 4 and 21 could potentially be attributed to actual initial crack lengths, differences in the composite patch thickness, or other variability in the underlying constituents.

Specimen 4 had laminate whitening around the crack shown in Figure 7-54, however, with no disbond or laminate failure detected during the UT inspection and no visible crack growth observed. The crack extension and plastic zone at the crack tips of specimen 9 are 3.2 mm long as shown in Figure 7-55. Figure 7-56 shows the post loading 17.8 mm out of plane permanent set of specimen 9 resulting from the plastic deformation and crack extension of the aluminum constrained by the elastic patch still bonded to the aluminum. The crack extends 6.4 mm from the crack tip into the plastic zone at the crack tip of specimen 21 shown in Figure 7-57. Figure 7-58 shows the laminate whitening zone around the crack of specimen 21, which had the largest area of whitening, extending approximately 25 mm perpendicular to the crack plane at the center. Laminate damage along the specimen 21 crack was limited to the location of the crack tip. Initiation of nonlinear behavior occurred at 477, 536, and 531 kN for specimens 4, 9, and 21 respectively. The average load for nonlinear behavior was 115.7 kN or far field stress level of 64.8 MPa. Measured strain included a moment, centroid off the load axis, and 3D panel displacements making derivation of the far-field stress difficult without more strain data across the width. Average initial compliance of the specimens, change in COD versus change in load, from 22.3 to 66.8 kN was 0.0027 mm/kN.

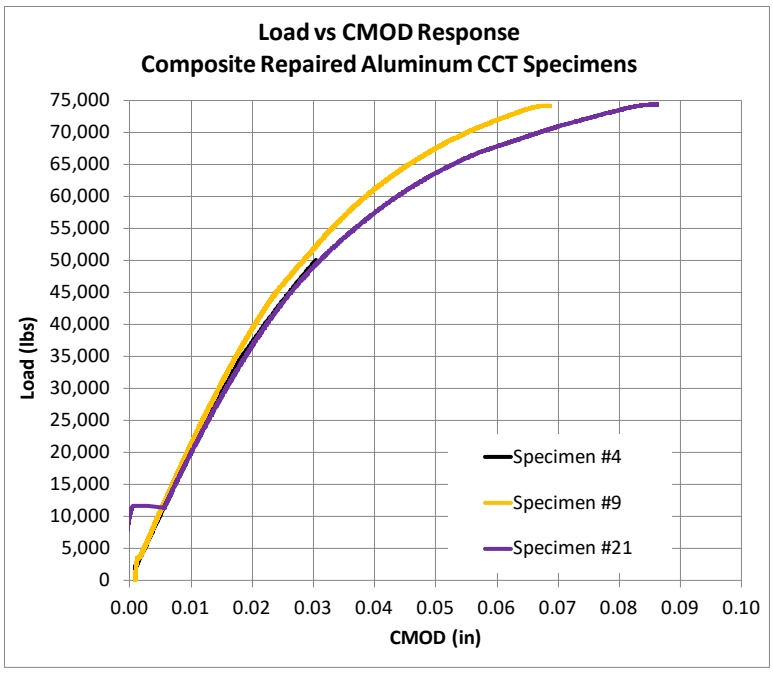

Figure 7-53: Large scale composite patch repaired specimen load vs. COD data.

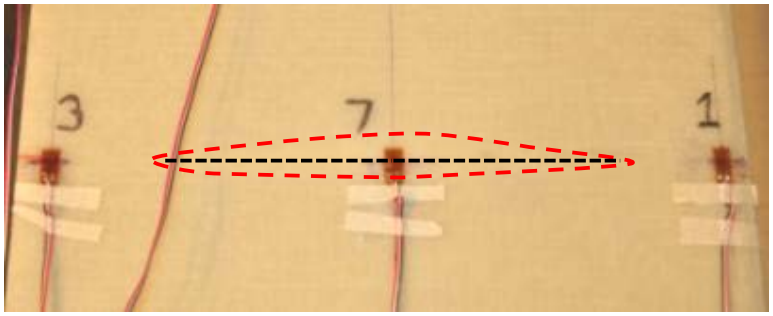

Figure 7-54: Specimen 4 laminate whitening across crack, detected by UT inspection. Red dashed lines indicate extent of damage and black line indicates underlying aluminum crack location.

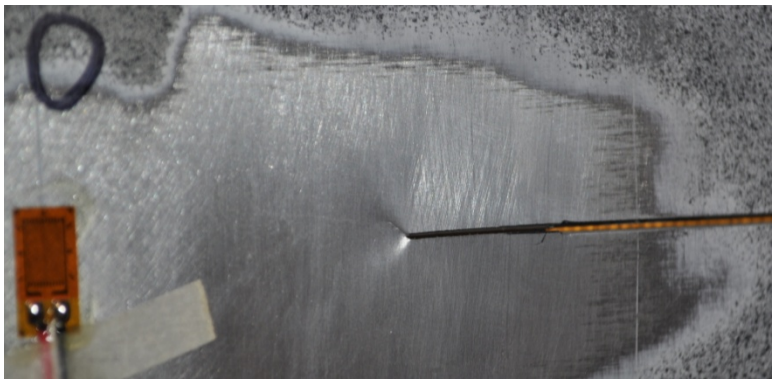

Figure 7-55: Specimen 9 plastic deformation at crack tip, 31.8 mm from strain gauge 0.

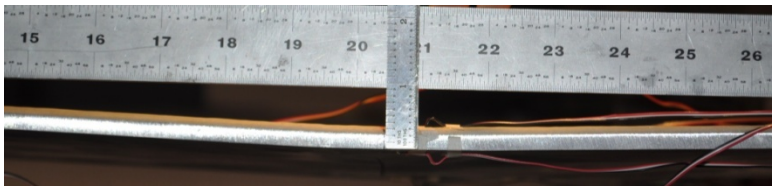

Figure 7-56: Permanent set measured after tensile loading of specimen 9. Measured 17.8 mm of out of plane deflection at zero load.

Figure 7-57: Specimen 21 plastic deformation at crack tip, 28.6 mm from strain gauge 0.

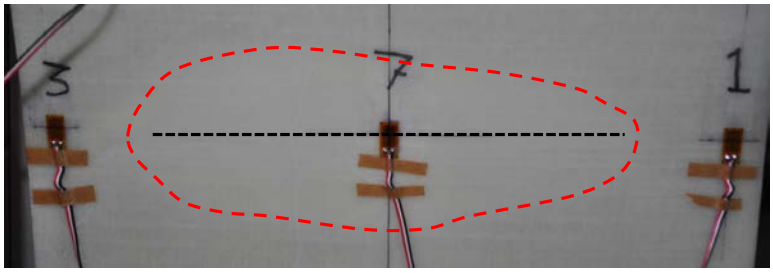

Figure 7-58: Specimen 21 laminate whitening across crack tip.

7.4.3 Large Scale CCT Static Testing Summary

Aluminum only specimens had an average peak load of 179.8 kN. Nonlinear behavior initiated at an average load of 86.3 kN or far field stress level of 49 MPa. Initial compliance of the specimen, change in COD versus change in load, from 22.3 to 66.8 kN was 0.0040 mm/kN.

Composite patch repaired aluminum panels were not tested until ultimate failure because of test machine capacity limitations. Specimen 4 was statically tested to 245 kN with only limited matrix whitening occurring around the crack with no laminate failure. Specimens

9 and 21 were loaded to 330 kN statically without laminate failure and similar matrix whitening around the crack. Nonlinear behavior initiated at an average load of 115.7 kN or far field stress level of 64.8 kN. Initial compliance of the patched specimens was 0.0027 mm/kN.

Direct comparison of the composite patch repaired versus unrepaired is shown in Figure 7-59. Under static tensile loading, the compliance of the panel decreased by 30.3%, which corresponds to a 43.5% increase in stiffness. The load at which crack propagation initiated increased by 33.7%, as indicated by nonlinear load vs. COD behavior. Ultimate failure of the patched panels is at least 80% greater than the un-patched panels. The load based far-field stress level increased from 100.0 to 185.5 MPa.

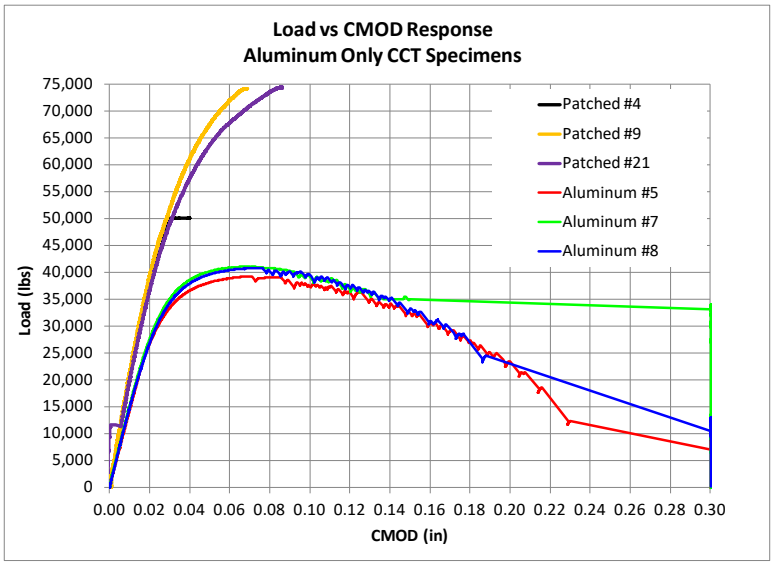

Figure 7-59: Combined large scale unpatched and patched static testing load vs. COD responses.

7.4.4 Unpatched Large Scale CCT Test and Prediction Correlation

Correlation of the numerical predictions and the test results provides the required confidence in the FEM necessary to make more complex predictions. The initial load versus COD numerical predictions for both the aluminum and composite patch repaired

aluminum specimens are shown with the experimental results in Figure 7-60. Initial stiffness of aluminum solid elements and the test data correlate well. From 20 to 100 kN, the average initial stiffness measured in the specimens was 253.9 kN/mm and the predicted stiffness was 0.6% higher at 255.5 kN/mm. Average initial stiffness of the composite patch repaired specimens was measured as 364.6 kN/mm and the predicted stiffness was 17.0% higher at 426.3 kN/mm. The over-estimated stiffness is due to the as-built properties of the composite patch being lower than measured or the use of smeared orthotropic laminate properties. Unpatched specimen predicted loads correlate within 0% to 10%, with correlation greater than 8% occurring at later CODs. Patched prediction correlation is within 20% for CODs of 0.6 mm or less. For CODs greater than 0.6 mm possible patch disbonding about the notch causes the prediction to diverge from the data with loads between 30% and 57% greater than measured.

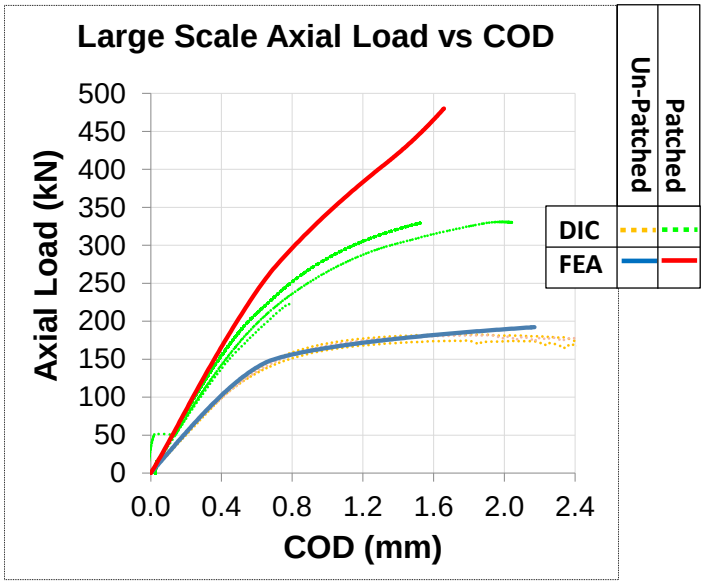

Figure 7-60: Comparison of large scale FEA and test data Load vs. COD response.

Both the ligament strains ahead of the crack tip and the far-field strains near the fixtures are shown in Figure 7-61 as a function of COD. The predicted axial strains correlated

well, although the far-field strains ahead of the crack tip are under predicted. Under prediction is likely due to variations in the actual gauge placement and true crack length.

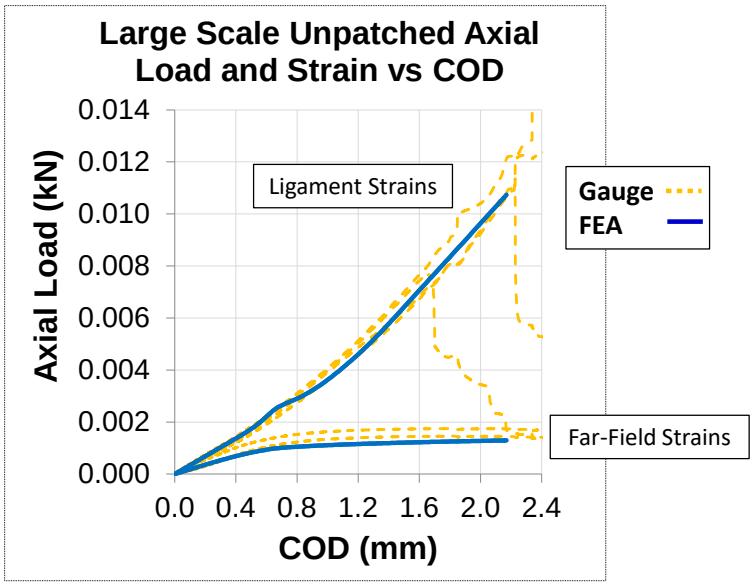

Figure 7-61: Large scale unpatched CCT measured and predicted axial strain response comparison.

Overall predictions for the unpatched specimens correlated well with test data. Both the load and strain versus COD responses were within 1% of the test response. This indicates the aluminum material behavior and geometry are correctly represented in the FEM.

7.4.5 Patched Large Scale CCT Test and Prediction Correlation

Simple in-plane composite stress levels can be compared with laminate properties. For the patch across the notch the bottom ply of the patch sees tensile stresses whereas the top surface of the patch sees compressive stresses due to the bending. From the load versus COD response in Figure 7-60 the patched nonlinear response begins at approximately 60 kN, which from the numerical predictions is where the bottom ply predicted tensile stress exceeds the smeared laminate strength. The peak tensile stresses are confined to the bottom surface of the patch and the span across the notch. Using the tensile strength of the bottom Hexcel 7500 plain weave, the predicted initiation of laminate failure increases

to 96 kN. Observations made during testing indicates that exceeding the tensile strength does not lead to catastrophic failure, but may initiate delamination and relaxation of the tensile and compressive stresses across the notch due to increasing the crack bridging length. Behavior corresponding to increased crack bridging length is shown in the patch surface strain data.

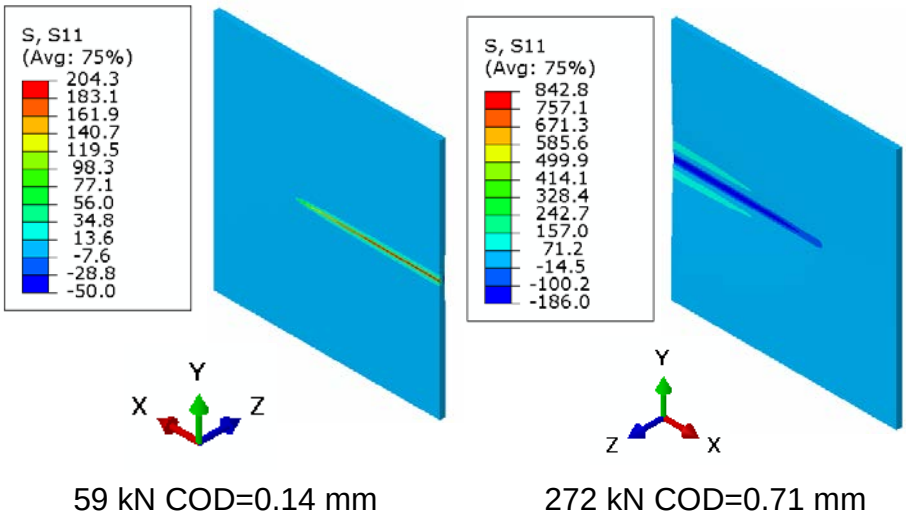

Figure 7-62 Large scale numerically predicted composite patch axial stress across the notch at tensile and compressive failure stresses load and COD levels.

Patched specimen axial strain correlation is shown in Figure 7-63. Although the overall stiffness of the patched specimen is over-predicted, axial strain gauge correlation is reasonable for the far-field and ligament strains. The local notch behavior is not adequately captured by the FEM, since magnitude of compressive axial strains across the notch on the composite surface being over-predicted. Patch surface strain predictions over-predict local bending with greater strain magnitudes predicted as loading increases, because the FEM does not capture patch delamination adjacent to the notch. Local delamination increases the length bridged by the patch and decreases the magnitude of local bending due to the offset section centroid.

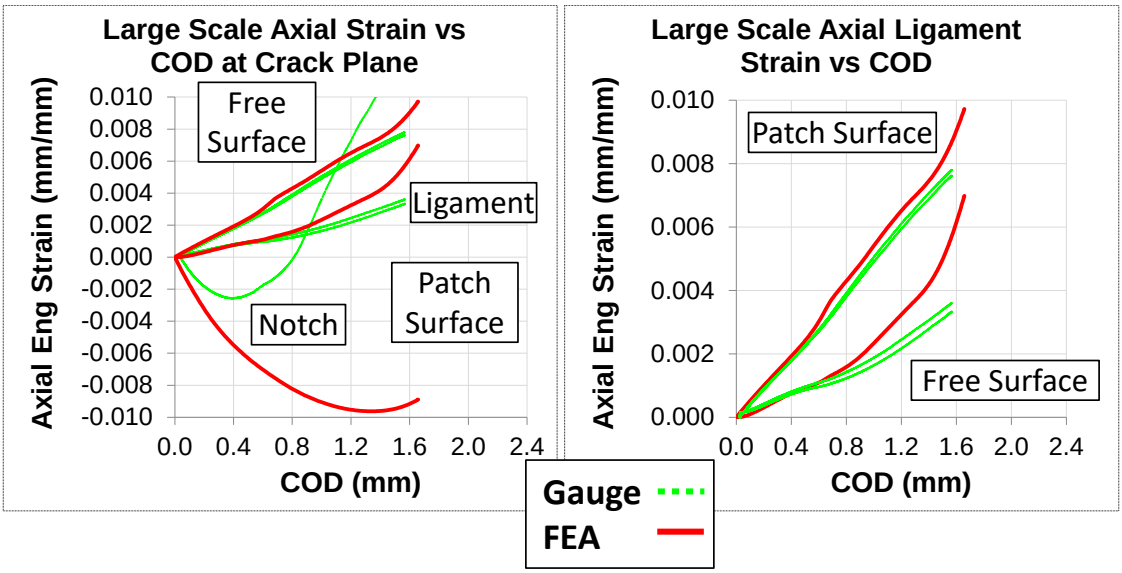

Figure 7-63 Measured and predicted large scale patched CCT axial strains as a function of COD showing reasonable correlation.

7.4.6 Large Scale Quantitative Change with Application of a Composite Patch

Quantitative comparison of the load and large strain regions as a function of COD for the large scale CCT is reported in this section and shown in Figure 7-64. The numerical predictions correlate well with measured response with the exception of strain gauge 7 where the delamination across the notch is not captured. Similar to the small scale responses, the increase in load due to the composite patch is linearly proportional with COD.

Large strain area and volume are approximated using the process defined in round one of the small scale analysis processing as shown in Figure 7-14 and Figure 7-15. Free surface large strain area decreases as a function of COD. For CODs less than 1.0 mm the patch reinforcement increases the region of large strain with the magnitude of area increase being inversely proportional to COD. For CODs greater than 1.0 mm the unpatched large strain area is greater than the patched large strain area.

The large strain volume change has an inverse relationship with COD and the patched volume is consistently smaller with the addition of surface reinforcement. The decrease in total large strain volume ahead of the crack tip is a measure of the load sharing being done by the composite reinforcement. The change in large strain volume does not approach a local minimum as with the small scale specimens.

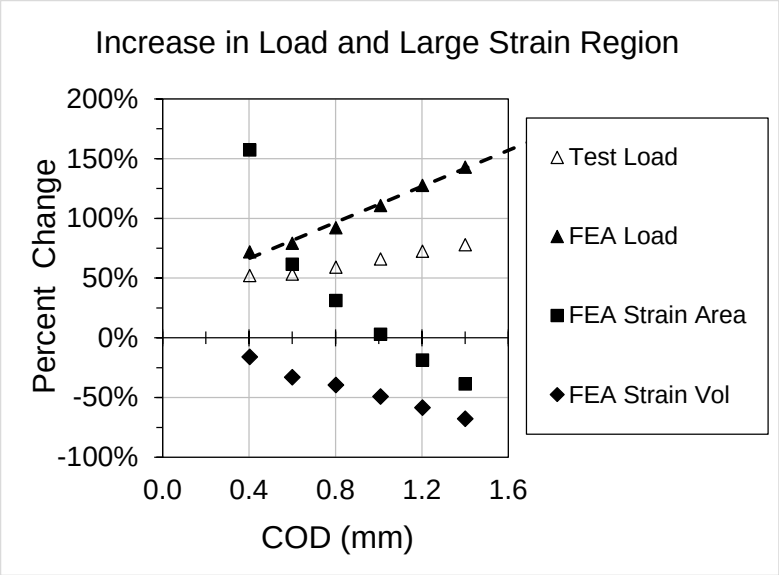

Figure 7-64 Large scale change in load and large strain region with application of a composite patch.

8 Predicted Failure of CCT Specimens

Specimen failure predictions using analytical and numerical methods to approximate the material behavior at the crack tip of both unpatched and patched specimens will be discussed in this section. Prediction methods will be discussed and the basic LEFM methods will be compared with the proposed method using the change in crack tip large strain due to the application of the composite patch.

8.1 Small Scale CCT Failure Predictions

Two small scale specimen geometries were tested and analyzed with a variation in grip section geometry and manufacturing methods. However, the test section geometry for both patched and unpatched specimens remained constant.

8.1.1 Small Scale CCT LEFM Failure Prediction

Two analytical methods were used to predict failure of the unpatched and patched specimens. For the unpatched specimen basic LEFM equations for finite geometry CCT specimens was used. The patched specimen required the use of Rose's model to predict the variation in SERR through the thickness of the aluminum. In addition to the analytical methods, first order element based FEA using the XFEM framework was used to calculate crack tip SERR behavior with the VCCT built into ABAQUS. Both methods will be compared with the proposed change in large strain region method.

8.1.1.1 Basic Unpatched LEFM Analytical Predictions

Basic LEFM predictions can be compared to a critical stress intensity value; K=21.5 MPa$\sqrt{m}$. Assuming in the linear elastic response region that the relationship between J, G, and K in Equation 107 holds, and using the plane stress and strain relationships in

Equation 108, the critical K can be converted to critical SERRs of 6,544 and 5,831 N/m, respectively.

The analytical prediction approach is only applicable to the unpatched specimens. Definitions of the parameters used for the LEFM calculations are illustrated in Figure 2-2 and Figure 8-1. Using the stress concentration method for finite specimen dimensions the effective K_I can be calculated starting the general form in Equation 105. The empirical data based CCT specific finite crack length concentration factor is then calculated using Equation 106. To account for crack tip plasticity the effective crack length is used. For for plane stress the estimated first order Irwin plastic zone size ($r_y = {r_p}/{2}$), illustrated in Figure 2-2, is added to the half crack length a, shown in Figure 2-2. Irwin's second order plastic zone size (r_p) is estimated using Equation 100. The effective crack length must then be solved for iteratively. Using the original K_I estimate based on the load and half crack length r_y is calculated and added to the half crack length to get an effective crack length (a_{eff}). Use a_{eff} to calculate an effective stress intensity (K_{Ieff}). Repeat the cycle until a_{eff} and K_{Ieff} converge on a solution. The LEFM effective SERR at 2,000N, linear elastic response region, is shown in Figure 8-2 for comparison with measured post fatigue free surface DIC and numerical predictions. When solving for the load at which the critical K_I is exceeded requires the use of the original K_I, as the a_{eff} exceeds the width of the specimen at the LEFM predicted failure load of 6,160 N.

8.1.1.2 Small Scale Unpatched Specimen XFEM LEFM Model Predictions

Numerically predicted SERR are based on the XFEM method assuming LEFM and the VCCT to calculate G_I, which for LEFM G=J. The unpatched specimen has a symmetric distribution of SERR through the thickness, as shown in Figure 8-1 for a load of 2,000N

for comparison purposes. Using the large displacement formulation and elastic-plastic aluminum behavior the predicted critical SERR is exceeded on the free surface at loads of 3,670 N and 3,560 N for round one and two specimens respectively. Corresponding critical COD values are 0.084 and 0.086 mm. From Figure 8-2, the peak SERR occurs at the mid-thickness of the aluminum that results in failure loads at 3,330 N and 3,200 N for round one and two, respectively. Corresponding COD values are 0.056 and 0.055 mm. Note that the critical COD values are consistent between round one and two specimen geometries because crack geometry is consistent and crack tip fracture behavior can be directly linked to the COD regardless of global geometry.

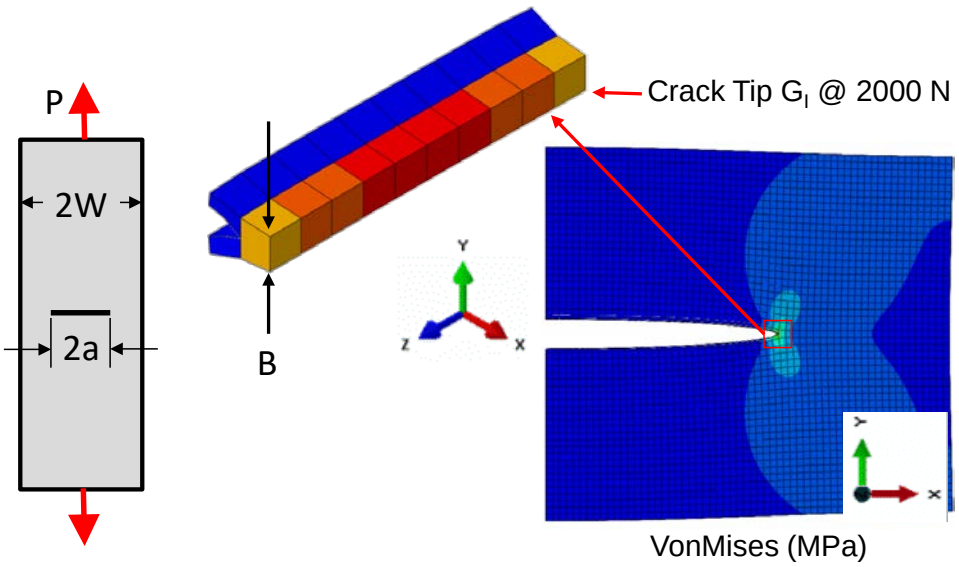

Figure 8-1 Small scale unpatched crack tip SERR through thickness distribution and parameter definitions for LEFM calculations.

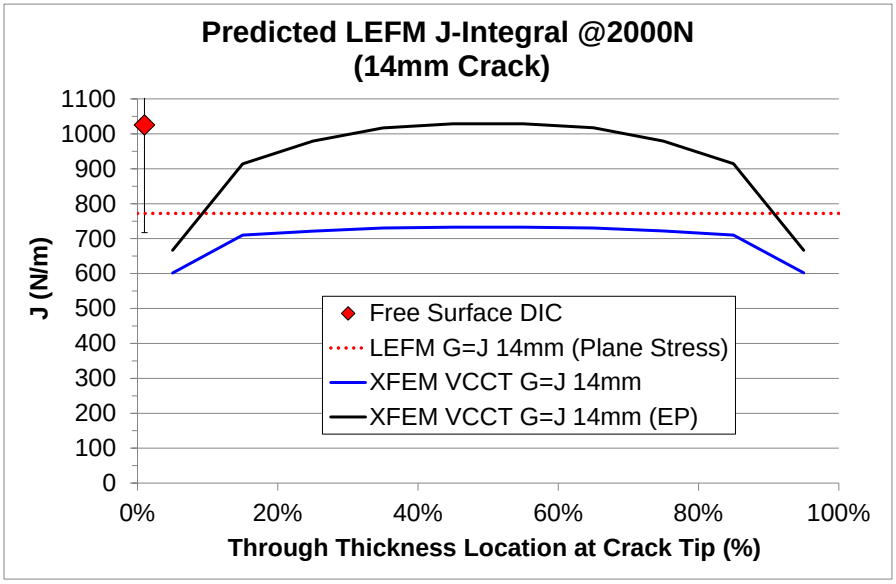

Figure 8-2 Small scale LEFM predicted SERR magnitudes through the thickness for a 14 mm total crack length at a load of 2,000 N.

8.1.1.3 Small Scale Patched Specimen Rose's Model Predictions

No standard LEFM method is available for a simple hand calculation of the SERR at the crack tip of a patched crack, therefore the Rose's model to approximate the SERR distribution is used.

First, for a one-sided composite patch repair Rose and Wang define a simplified process to approximate the root mean square stress intensity for a finite crack length ($K_{rms}(a)$), as discussed in section 2.3.3. The parameters need for this equation are determined in Equation 10 (β), Equation 13 (S), Equation 18 (k), and Equation 25 (z_{bar}) then the total second area moment of inertia terms for the total repair in Equation 26 (I_t), aluminum plate in Equation 27 (I_P), and the patch in Equation 28 (I_R). Information combined with far-field stress state for the centroid force and moment at the crack calculated using Equation 29 (N_0) and Equation 30 (M_0), respectively. Bending stiffness for the aluminum plate and composite patch are calculated using Equation 39 (D_p and D_R) and the stiffness factor in Equation 40 (κ). A simplified bending factor is calculated using Equation 42 (ω) to then calculate $K_{rms}(a)$ for a finite half crack length (a) using Equation 44. This formulation assumes the out of plane displacement is negligible, which is not the case for the large scale CCT specimens. Setting the $K_{rms}(a)$ equal to the critical K value of 21.5 MPa√m results in a failure load of 3,400 N, which is in the linear elastic response region.

To separate the membrane and bending components of the $K_{rms}(a)$ term above requires the crack bridging model developed by Wang and Rose [9]. Both Kirchoff-Poisson's and Reissner's plate theories are used in the crack bridging model. However, the numerical solutions for Reissner's theory were not successfully solved, since simple Gauss-Legendre quadrature was not able to be implemented to correctly solve the logarithmic singularity in Equation 80 as detailed in Equation 81. Numerical methods to solve the Kirchoff-Poisson's plate theory are detailed in section 2.3.3. Normalized stress intensity as a function of crack length compared with those reported by Wang and Rose are shown in Figure 8-3 with 64 summation terms (n=64).

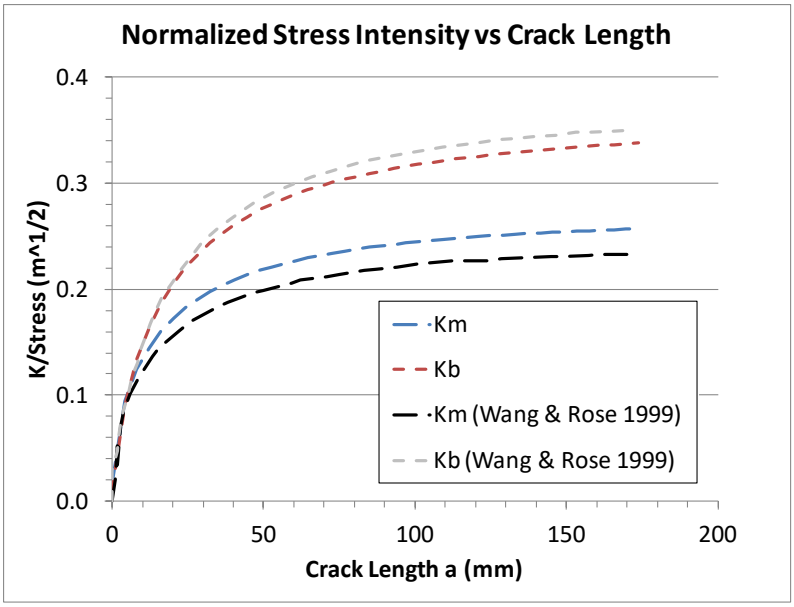

Figure 8-3 Normalized Stress Intensity as a Function of Crack Length using Kirchoff Plate Theory Prediction Compared with Wang & Rose Reported Results [9].

The failure prediction using small scale patched specimen properties and comparing the free surface stress intensity results to the critical value, shown in Figure 8-4, in a failure load of 1,180 N. This load is comparatively low due to the over prediction of the bending contribution. This is a known issue with the Kirchoff-Poisson plate theory due to the coupling of the membrane and bending springs and the integral used to derive the bending relationship [8] [9] [38].

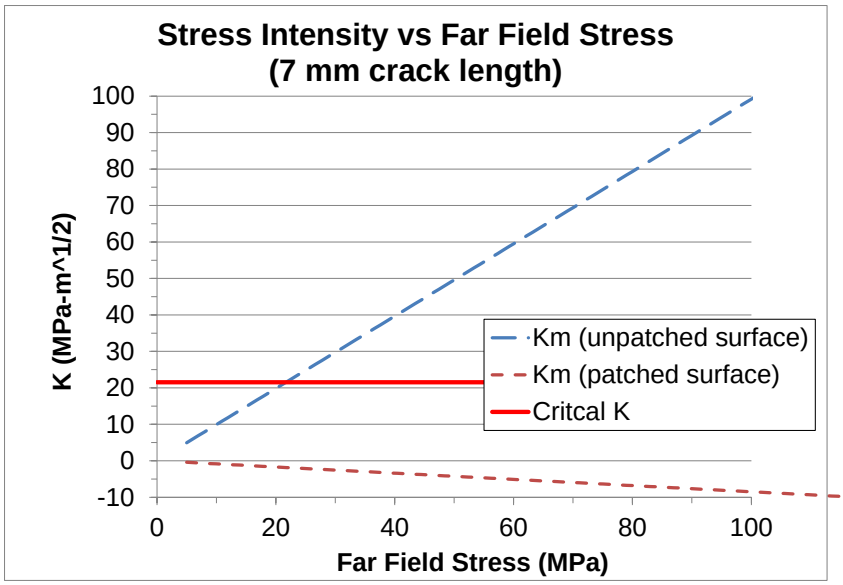

Figure 8-4 Roses's model using Kirchoff-Poisson plate theory to predict small scale patched specimen free surface stress intensity.

8.1.1.4 Small Scale Patched Specimen XFEM LEFM Model Predictions

Relying on numerical predictions, the estimated through thickness distribution of SERR at a load of 2,000 N are shown in Figure 8-5 and Figure 8-6, with the post fatigue crack growth measured DIC free surface SERR included for comparison. The asymmetric distribution of SERR shows the peak value occurring at nominally 15% of the thickness from the free surface. Again, the patched FEA results use the large displacement formulation and elastic-plastic aluminum and adhesive behavior. The predicted critical SERR is exceeded on the free surface at loads of 5,020 N and 4,750 N for round one and two specimens respectively. Corresponding critical COD values are 0.087 and 0.086 mm. Peak SERR based failure loads are 4,590 N and 4,200 N for round one and two, respectively. Corresponding COD values are 0.070 and 0.065 mm.

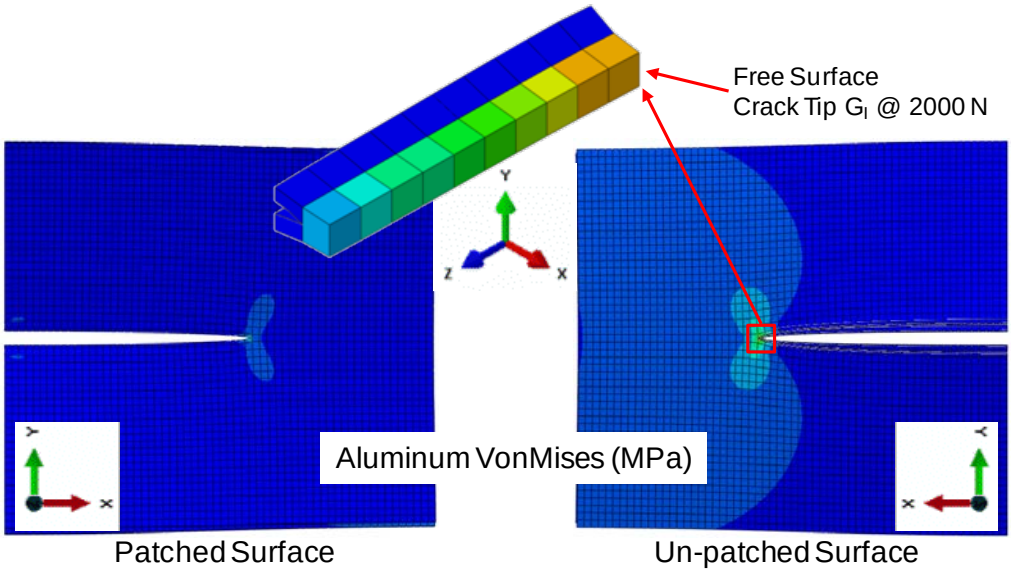

Figure 8-5 FEA SERR Predictions for small scale patched specimen in the linear elastic response region.

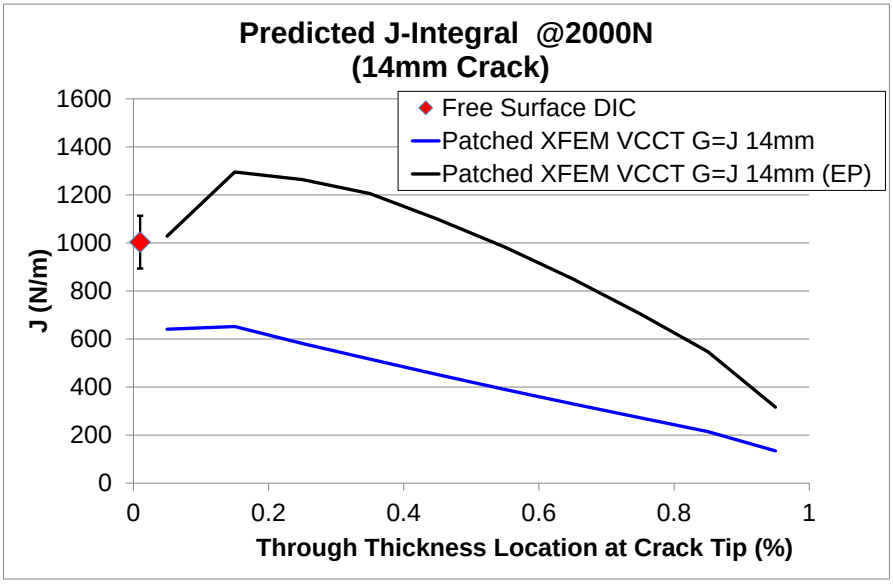

Figure 8-6 Small scale LEFM predicted SERR magnitudes through the thickness for a patched 14 mm total crack length at a load of 2,000 N.

8.1.2 Small Scale Patched CCT Change in Large Strain Area Prediction

The proposed patched specimen failure prediction method uses the numerically predicted change in local free surface crack tip large strain region area due to application of the composite patch to identify a critical COD prior to the initiation of aluminum crack growth. The critical COD is assumed to be where the free surface strain area of the

unpatched specimen is equal to or greater than that of the patched large strain area. One must also assume that this occurs before patch disbond or laminate failure that results in significant load drop. This method does not require fracture data that can be costly and time consuming to acquire and specific to the plate thickness and alloy used for the patched configuration.

Numerically predicted specimen response correlated with the measured load and free aluminum surface test data for both unpatched and patched small scale CCT specimens. Predicted loads as a function of COD were within 0% to 13% of test data. Predicted free surface large strain fields correlate well with DIC with free surface representative areas 0 to 11% larger for round one and within 2% to 19% smaller for round two for the unpatched specimen and 7% to 19% smaller for patched specimens. Quantitative correlation, qualitative correlation of the free surface large strain fields and correlation of the displacement and HRR fields give confidence that FEA produced reasonable approximations of the small scale specimen response for both round one and two.

A summary of the measured and predicted change in the crack tip response due to the composite patch reinforcement for both free surface von Mises strain area and predicted crack tip principal large strain volume as a function of COD is shown in Figure 8-7. Large strain area increase is inversely proportional to COD for the 2D von Mises strain prediction. From both the round one and two FEA results, the unpatched free surface large strain area equals that of the patched specimen at a COD of 0.30 mm, which is assumed to be the critical COD.

Using FEA results the crack tip large strain volume change has an inverse relationship with COD that is consistently smaller with the addition of composite patch. The decrease

in total large strain volume ahead of the crack tip is a measure of the load sharing being done by the composite reinforcement. At higher loads the tensile behavior of the ligament begins to dominate the bending caused by the patch and the large strain begins to distribute more evenly through the thickness with less disparity between the free and patched surfaces, as seen previously in the FEA study. Although the overall volume of large strain is always lower with the addition of the composite patch, due to the load sharing between the patch and the aluminum, out of plane bending plays a decreasing role and in-plane tension contributions increase with COD. From the small scale results as COD increases and the in-plane tensile response begins to dominate, the crack tip response transitions from SSY to LSY and initiation of crack growth. The transition from SSY to LSY is assumed to be the same point at which the unpatched free surface von Mises large strain area is equal to or greater than that of the patched specimen and where the large strain region of the unpatched aluminum specimen begins to increase at a faster rate than the patched specimen.

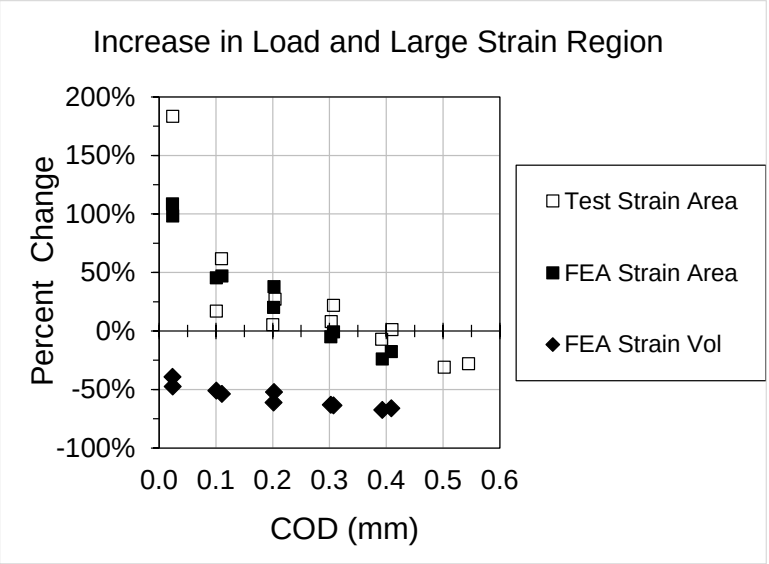

Figure 8-7 Round one and two small scale change in large-strain region summary.

The method for translating the critical COD of 0.30 mm to a failure load is shown in Figure 8-8, where both round one and two free surface large strain areas show no change at the critical COD. Using the critical COD results in a predicted patched failure load of 8,700 N. This is a significant improvement from the numerically predicted LEFM critical stress intensity predictions that predict patched specimen failure loads from 4,200 to 4,590 N when using a critical stress intensity of 21.5 MPa$\sqrt{m}$. Using elastic-plastic material behavior and the change in free surface large strain area behavior increases the predicted failure load more than 90% with a critical COD more than three times that predicted by LEFM. Assigning a critical COD value produces a conservative estimate of the predicted patched failure load that occurs at the end of the crack blunting stage and before the COD associated with ultimate specimen load.

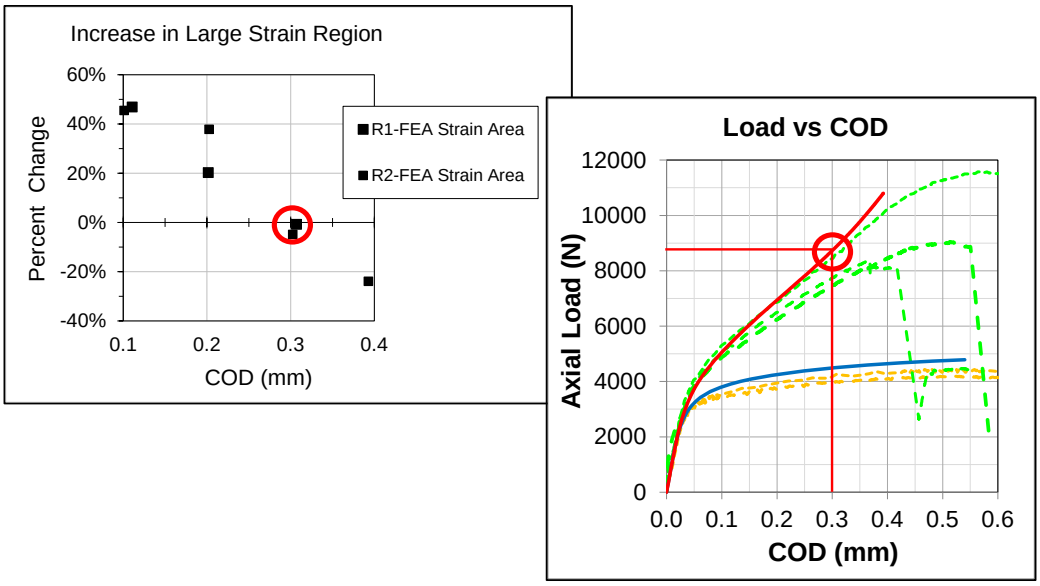

Figure 8-8 Round one and two small scale failure prediction method.

8.2 Large Scale CCT Failure Predictions

This section discusses the initial LEFM based and updated large strain area methods to predict a failure load for unpatched and patched CCT specimens, both small and large scale. Although attempts to use Rose's one-sided method were unsuccessful, the simplified method was used for comparison.

8.2.1 Large Scale CCT LEFM Failure Prediction

Following the methods used for the small scale LEFM predictions. Analytical solutions for the unpatched specimen basic LEFM equations for finite geometry CCT specimens was used. The patched specimen required the use of Rose's model to predict the variation in SERR through the thickness of the aluminum. Numerical predictions using LEFM methods to calculate crack tip SERRs and the proposed change in large strain region method will be used and compared.

8.2.1.1 Basic Unpatched LEFM Analytical Predictions

Basic LEFM predictions can be compared to a critical stress intensity value for the 5456-H116 of 28.9 MPa√m and converted to critical SERRs of 10,265 and 11,520 N/m for plane strain and stress, respectively.

Following the analytical prediction approach described for small scale unpatched specimens, the load at which the critical K_I is exceeded is 68,246 N and uses a_{eff}, as the large scale specimen geometry kept the plastic zone size estimate at 3 mm, less than half the plate thickness.

8.2.1.2 Large Scale Unpatched Specimen XFEM LEFM Model Predictions

Numerically predicted SERR are based on the XFEM method assuming LEFM and the VCCT to calculate G_I, which for LEFM G=J. The unpatched specimen has a symmetric distribution of SERR through the thickness, as shown in Figure 8-9 for a load of 60,154N for comparison purposes. Using the large displacement formulation and elastic-plastic aluminum behavior the predicted critical SERR is exceeded on the free surface at a load of 83,410 N. Corresponding critical COD value is 0.32 mm. The peak SERR occurs at the mid-thickness of the aluminum that results in a failure load of 60,150 N corresponding to a COD of 0.23 mm.

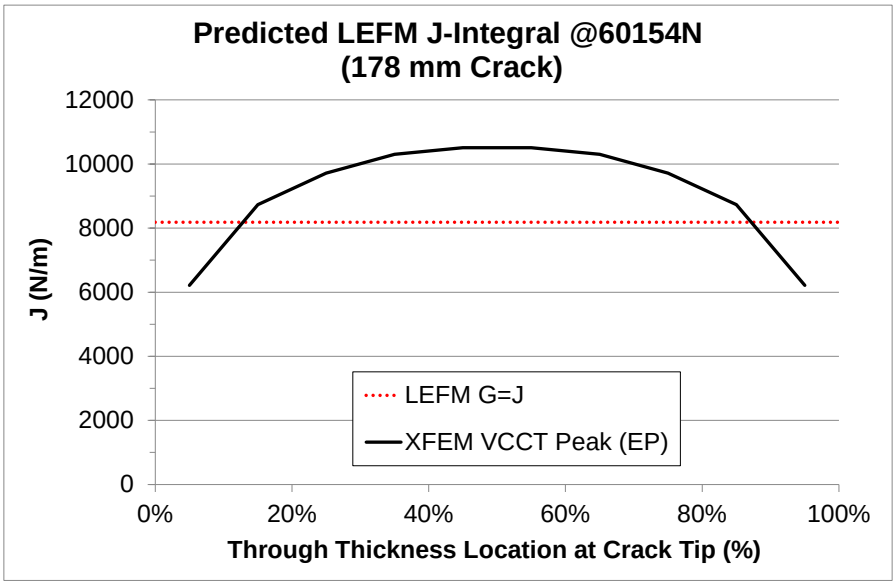

Figure 8-9 Large scale LEFM predicted SERR magnitudes through the thickness for a 178 mm total crack length at a load of 60.2 kN.

8.2.1.3 Simplified Rose's Model Predictions for Large Scale CCT Specimens

Rose's models require an explicit adhesive layer, which does not exist for the cocured large scale composite patch laminates. For the calculations in this section an adhesive layer thickness of 0.05 mm was assumed based on the fiber volume fraction, weight, and cured thickness of the Hexcel 7500 interface ply. For the woven interface ply the assumed cured ply thickness is 0.33 mm with a fiber volume fraction of 37.5% with 62.5% of the cross section being resin. The cross section of fibers and resin is shown in Figure 8-10, where only 25% of the section reacts in shear resulting in an assumed resin layer that is 0.33 mm thick.

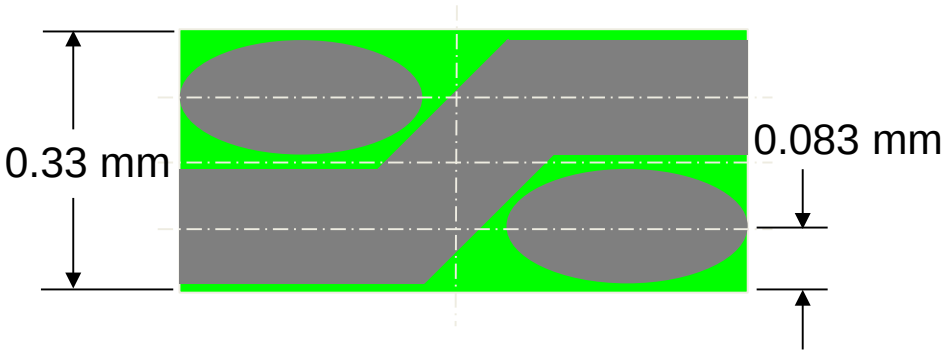

Figure 8-10 Cross section of large scale Hexcel 7500 woven fabric bondline layer unit cell geometry used to approximate an adhesive bondline thickness.

Using the same simplified one-sided composite patch repair equations to approximate the root mean square stress intensity for a finite crack length ($K_{rms}(a)$), as discussed in section 2.3.3 and 8.1.1.3 are followed here. Setting the $K_{rms}(a)$ equal to the critical K value of 28.9 MPa$\sqrt{m}$ results in a failure load of 144.5 kN, which is within the linear elastic response range.

Using the same procedure outlined in sections 2.3.3 and 8.1.1.3 Rose's one-sided repair predictions based on Kirchoff-Poissons plate theory were used to predict failure of the large scale patched specimen. Comparing the unpatched surface stress intensity to the critical value, shown in Figure 8-11, results in a failure load of 97.0 kN, which is conservative due to the over prediction of the bending contribution.

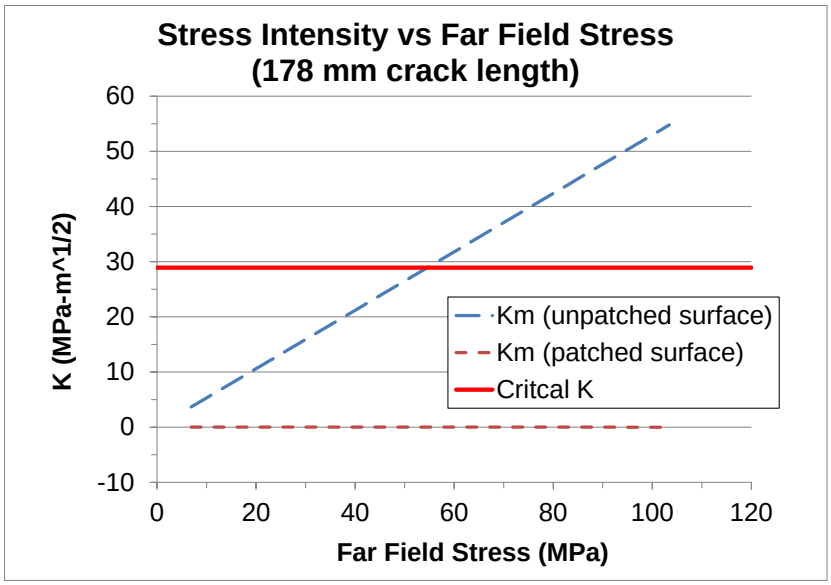

Figure 8-11 Rose's model using Kirchoff-Poisson plate theory predictions for large scale patched CCT specimen.

8.2.1.4 Large Scale Patched Specimen XFEM LEFM Model Predictions

Patched specimen numerical predictions for the estimated through thickness distribution of SERR at the crack tip a load of 123.2 kN are shown in Figure 8-12 for the free surface and peak SERR values. The asymmetric distribution of SERR shows the peak value occurring at nominally 15% of the thickness from the free surface. The patched FEA results use the large displacement formulation and elastic-plastic aluminum behavior; no adhesive layer is modeled. The predicted critical SERR is exceeded on the free surface at a load of 123,200 N and a COD of 0.29 mm, and using the peak SERR, the failure load is 104,840 N and a COD of 0.25 mm.

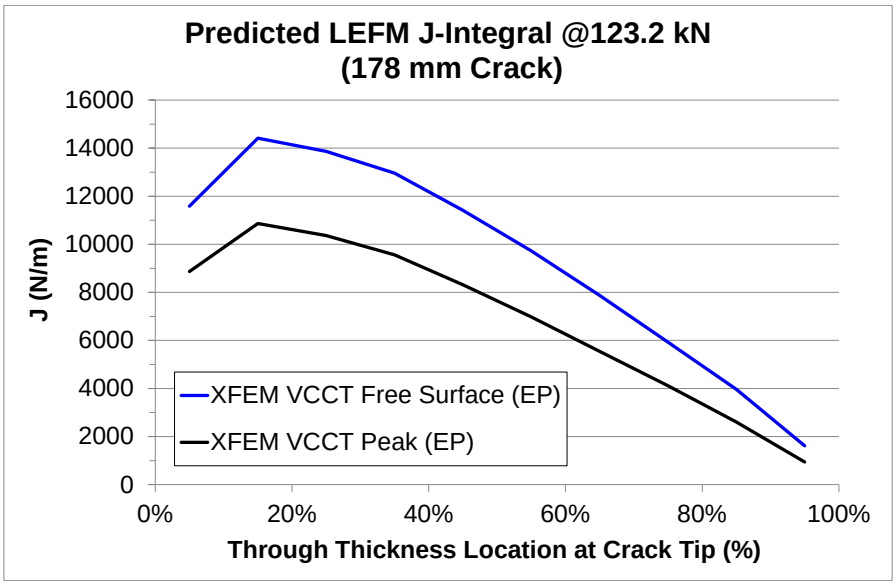

Figure 8-12 Large scale CCT XFEM SERR predictions at a load of 123.2 kN.

8.2.2 Large Scale CCT Change in Large Strain Area Prediction

Numerically predicted large scale specimen response correlated with the measured load and strain gauge data for both unpatched and patched large scale CCT specimens. Predicted loads as a function of COD were within 0% to 10% of test data for the unpatched specimen and 13% to 57% for the patched specimen. Predicted axial strains correlate well with measured strains for both unpatched and patched specimens.

A summary of the predicted change in the crack tip response due to the composite patch reinforcement for both free surface von Mises strain area and predicted crack tip principal large strain volume as a function of COD were initially shown in Figure 7-64. The unpatched free surface large strain area equals that of the patched specimen at a COD of 1.06 mm, which is assumed to be the critical COD.

The method for translating the critical COD to a failure load is shown in Figure 8-13. Using the critical COD results in a predicted patched failure load of 350 kN. This is a failure load prediction increase more than 200% with a critical COD more than four times

that predicted by LEFM. No true conclusion can be made about the nature of the prediction because early disbonding occurred and specimen failure was not achieved due to exceeding the capacity of the load frame. However, one can assume the actual failure load of the specimen is greater than 350 kN.

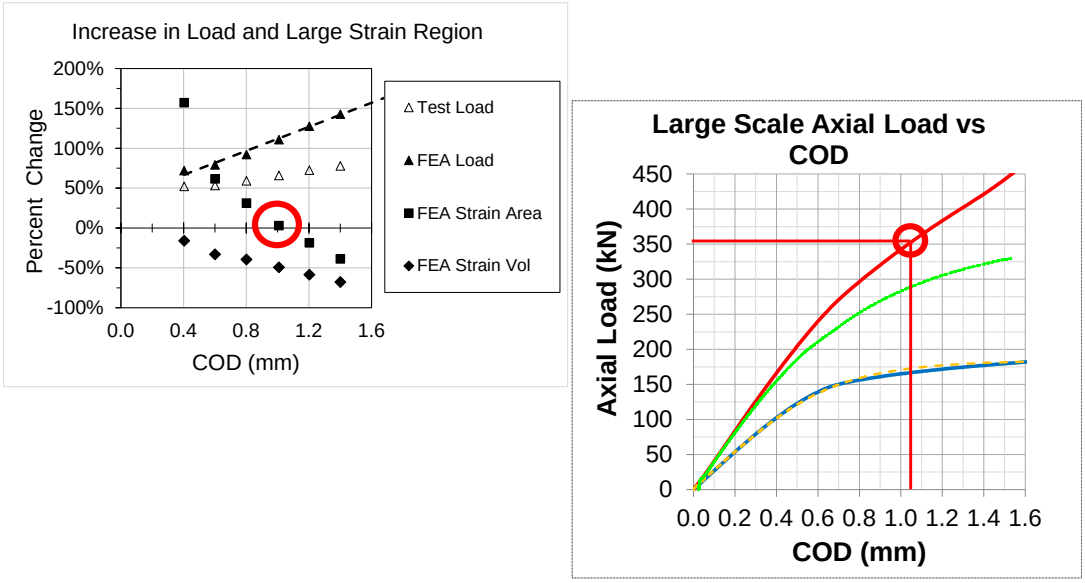

Figure 8-13 Large scale change in large strain area based failure prediction method.

9 Conclusion

The novel findings presented in this research used three sets of unique data to study the effects application of a one-sided low-modulus composite patch has on local crack tip behavior. Small scale free surface full field DIC data was used to measure the evolution of the initial plastic zone and then the comparative large strain areas. Numerically predicted specimen response allowed the investigation of the large-strain volume evolution. Two small scale data sets demonstrated that failure behavior for both unpatched and patched specimens was governed by the aluminum COD and therefore aluminum failure progression was governed by COD independent of the composite patch. A simplified method to predict ultimate failure of a composite patched CCT specimen was proposed that uses the change in large-strain area due to the patch as a function of COD to determine failure by identifying the point at which SSY transitions to LSY and the initiation of crack growth. This method was demonstrated on both small and large scale test data for a different specimen geometry and different materials.

9.1 Scientific and Technical Contributions

Composite patch repairs of aluminum structures are designed using linear elastic fracture mechanics (LEFM), which is reasonable for linear elastic behavior but not for predicting ultimate capacity of the repair since the prediction methods do not account for the elastic-plastic behavior observed at the crack tip of ductile patched materials. As a result of this research, several unique scientific contributions have been made elucidating the plastic behavior of a one-sided composite patch repaired crack tip. First, full field elastic-plastic crack tip response change due to the application of a one-sided low-modulus composite patch was presented. The second novel contribution was studying the evolution of the

crack tip response change due to the patch by comparing the displacement fields to HRR and K fields and the large-strain region at increasing CODs. The third and final contribution was a proposed methodology to determine ultimate tensile load of a cracked ductile panel repaired with a one-sided composite patch.

9.1.1 Full Field Free Surface Elastic-Plastic Crack Tip Behavior Change

As a result of this research the change in free surface crack tip response was documented. Two details make this a novel contribution. First, the E-Glass/Epoxy composite patch modulus was less than one third of the repaired aluminum. Typical strength related repairs target a cracked plate to composite patch stiffness ratio of one, although from the data presented full stiffness match is not required to influence crack tip behavior. Second, free surface full field DIC investigation of the change in crack tip behavior due to a one-sided patch has not been found in the literature. Data was limited to free surface DIC data and required assumptions about the link between measured changes in behavior due to the composite patch. Results, observations, and conclusions were presented at the June 2018 Society for Experimental Mechanics conference and proceedings [17] and were accepted for publication in the peer reviewed Experimental Mechanics journal [18].

Free surface 2D DIC full field displacements and strains ahead of the crack tip for small scale unpatched and patched center crack tension specimens showed measurable effects of surface reinforcement on crack tip behavior. Free surface fracture response was observed to be an intrinsic property of the aluminum from the initial development of the plastic strain zone through crack blunting and peak load with all stages occurring at crack opening displacements independent of the one-sided composite patch reinforcement. The result of this observation is the foundation for a simplified composite patch repaired

cracked ductile panel failure prediction criteria based on the COD where unpatched and patched large strain area are equivalent.

The increase in load capacity was linearly proportional to COD due to the application of the patch reinforcement that increased the ultimate tensile load 160% and total achieved crack opening displacement by 20% over the unpatched behavior for round one and increased average tensile capacity more than 100% for round two without an increase in COD capacity due to early disbonding of the composite patch. Increased capacity was assumed to be related to an increase in accumulated large strain area and distributed plasticity measured on the free surface.

Although not novel, the grain structure of 5052-H32 was characterized using a LOM with gamma filtered polarized light to measure grain size of this alloy. Grains of this alloy have an approximate 2D surface major diameter of 10.8±4.5 μm with the maximum and minimum measurements being 18.1 and 5.4 μm, respectively. When compared to the measured plastic zone size for both unpatched and patched specimens, radial positions between 1,500 and 2,800 μm, the difference between the region of interest and the grain size is greater than two orders of magnitude, therefore, the material responds as a homogenous material during evolution of the plastic zone.

9.1.2 Numerically Predicted Free Surface and Through Thickness Crack Tip Large Strain Evolution

A finite element model for two- and three-dimensional plastic zone evolution ahead of cracks in ductile panels with one-sided patches was developed. The effect of a one-sided adhesively bonded low modulus E-Glass/Epoxy composite patch on development of the through thickness crack tip plastic zone, free surface displacement fields, and free surface

nonlinear SERR was studied using experimental data and numerical predictions with first order elements. Evolution of the plastic zone was studied both quantitatively and qualitatively by correlating full field DIC data and FEA predictions. Free surface displacements, both measured and predicted, were compared to theoretical HRR fields and large strain fields. Also studied were numerically predicted through thickness large strain volume evolution. Although these behaviors have been previously investigated, the effects one-sided composite patch reinforcement has on measured and predicted behaviors have not been documented.

As a result of numerically predicted unpatched and patched responses, the observed connection between a critical COD correlates with through thickness crack tip and ligament behavior. Numerically predicted response correlation was established for both small and large scale unpatched and patched load as well as average strain versus COD. Unpatched responses correlate well until the initiation of crack growth. The patched specimens correlated well into the crack blunting stage but did not capture partial disbonding that occurred during round two small scale and large scale testing. Predicted large strain volume supported the assumed alignment of the load line with the neutral axis of the patched specimen between CODs of 0.10 and 0.20 mm, which corresponds to the initiation of crack blunting and the end of the first nonlinear load versus COD transition. Consistent through thickness qualitative behavior also supports the transition from combined tension and bending behavior to behavior dominated by tension that makes behavior similar between unpatched and patched specimens.

The assumption that the crack tip is in a state of SSY prior to failure was supported by the small scale crack tip displacement fields. Predicted displacements correlated reasonably

well with test data for axial displacements, although first order elements do not capture the HRR field behavior seen in both round one and two test data. Measured displacements correlate with HRR fields and transition to K fields as the radial position increases, confirming that general crack tip behavior is typical of SSY.

With the crack tip region being in a state of SSY during initial loading, the transition to LSY must occur just prior to crack growth. Because crack tip fracture behavior is an intrinsic property related to the COD, when tensile behavior dominates the patched response and the free surface large strain area of the unpatched specimen increases at an equal or greater rate than the patched specimen the crack tip behavior is approaching the end of crack blunting and the initiation of crack growth. The COD at which the free surface large strain of the unpatched and patched are equal can be considered critical.

Objective evidence was provided for the necessary use of elastic-plastic material behavior and large displacement formulation in the numerical solution procedure to adequately predict nonlinear SERR and the J-integral. Good correlation was found when using direct extraction of the deformation gradient from ABAQUS hyper elastic elements and determining the displacement gradients along the rectangular J-integral path. Although the J-integral calculation assumed linear elastic material relationship, this was assumed sufficient for direct comparison of the change in response due to the composite patch and did not warrant the additional computation of Ramberg-Osgood stresses at each calculation point along the integral path.

9.1.3 Improved Prediction for Ultimate Load Bearing Capacity for Patched Ductile Specimens

As a result of studying crack tip large strain region evolution, a novel methodology for predicting the ultimate capacity of a cracked ductile panel repaired with a one-sided composite patch was developed. The simplified method uses the numerically predicted change in large strain free surface area due to the application of a composite patch as a function of COD. When the unpatched large strain area is equal to or greater than the patched specimen large strain area, the dominant plastic response at the crack tip transitions from combined tension and bending to tension as the crack tip and ligament yield and behavior transitions from SSY to LSY and crack growth. Even though cracking initiates, the ultimate load capacity occurs at a later COD. Therefore, identifying a critical COD at which SSY transitions to LSY results in a conservative estimate of the ultimate tensile load for both the small scale and large scale patched aluminum CCT specimens.

When compared with the analytical Rose's method and LEFM based numerical predictions, the predicted ultimate capacity of patched CCT specimens increased more than 90% for the small scale specimens and more than 200% for the large scale specimens. Predicted ultimate load capacity was below measured for small scale specimens. For large scale specimens predicted ultimate load capacity was when crack growth initiated and was assumed to be below ultimate capacity, which was not achieved during testing.

The numerical prediction work demonstrating the through thickness large strain field evolution will be compiled and submitted to the International Journal of Fracture Mechanics.

10 Future Research

Future research will focus on investigating the application of this simplified method that uses the predicted change in behavior for other specimen scales and geometry. Numerical prediction efforts can investigate further mesh and geometry refinement and use of higher order elements to improve predictions of local crack tip displacement and strain fields along with the inclusion of adhesive and composite failure.

Investigate the use of a critical J-integral value for failure criteria of the aluminum. This requires the redesign of the small scale specimen to eliminate edge effects and the inclusion of elastic-plastic material behavior to determine stress for the J-integral calculation.

Further investigation of HRR crack tip fields and understanding of how those fields change due to the composite patch is likely necessary to further understand load bearing capacity beyond ultimate load.

Research and development of analytical methods to capture failure modes associated with the marine structures will produce the design guidance required to extend current composite patch repair from low stress applications to structural repairs and class wide alterations. Future efforts are required to advance naval use of composite patches beyond low stress planar applications. These should include testing and analysis such that analytical methods and design guidance can be developed for non-structural to structural alterations or applications.

Current needs for composite patches include both aluminum and steel structures. Applications include plate wastage, plate cracking, structural damage, and structural

reinforcement. Plate wastage affects decks, hulls, and tanks and often requires costly crop out and replace repair methods. Cracking due to sensitization, fatigue and overload can be reduced with the use of composite patches, or bonded repair, and significantly reduce the cost of maintenance and increase service life.

Further investigation of crack tip and composite patch interaction can be simplified by removing significant contributions from out of plane bending. This can be done with roller bearing support of the patched surface.

Ultimate effectiveness, reinforcement limit, or plastic zone effect limit of bonded reinforcement should be investigated. Identifying the limit of load transfer through plastic shear and the presence of a stress shadow through the thickness of the adherend is an important aspect to consider when designing bonded reinforcement of a structure.

Through thickness behavior study was limited to the use of numerical predictions. The use of advanced 3D imaging methods to investigate full plastic zone development would provide objective evidence to correlate FEA with.

11 References

[1] O. Volkerson, "Die Niektraft in Zugbeanspruchten mit Kontanten Laschenquerschritten," *Luftfahrtforschung,* vol. 5, pp. 41-47, 1938.

[2] M. Goland and E. Reissner, "The Stress in Cemented Joints," *Journal of Applied Mechanics,* vol. 77, 1944.

[3] L. J. Hart-Smith, "Adhesive-Bonded Double-Lap Joints," CR-112235, NASA, 1973.

[4] L. J. Hart-Smith, "Adhesive-Bonded Single-Lap Joints," CR-112236, NASA, 1973.

[5] G. C. Tsai and S. B. Shen, "Fatigue Analysis of Cracked Thick Aluminum Plate Bonded with Composite Patches," *Composite Structures,* vol. 64, pp. 79-90, 2004.

[6] R. Jones and W. K. Chiu, "Composite Repairs to Cracks in Thick Metallic Components," *Composite Structures,* vol. 44, pp. 17-29, 1999.

[7] C. N. Duong, "Design and Validation of Composite Patch Repairs to Cracked Metallic Structures," *Composites Part A,* vol. 40, pp. 1320-1330, 2009.

[8] A. A. Baker, L. R. Rose and R. Jones, Advances in the Bonded Composite Repair of Metallic Aircraft Structures, vol. 1, Elsevier, 2002.

[9] C. H. Wang and L. R. F. Rose, "A Crack Bridging Model for Bonded Plates Subjected to Tension and Bending," *International Journal of Solids and Structures,* vol. 36, pp. 1985-2014, 1999.

[10] J. M. Noland, D. C. Hart, E. P. Udinski and R. A. Sielski, "Initiatives in Bonded Ship Structural Repairs," in *ASNE Fleet Maintenance and Modernization Symposium,* San Diego, CA, 2013.

[11] A. A. Baker, L. R. Rose, K. E. Walker and E. S. Wilson, "Repair Substantiation for a Bonded Composite Repair to F111 Lower Wing Skin," *Applied Composite Materials,* vol. 6, pp. 251-267, 1999.

[12] R. Muller and R. Fredell, "Analysis of Multiple Bonded Patch Interaction Simple Design Guidelines for Multiple Bonded Repairs in Close Proximity," *Applied Composite Materials,* vol. 6, pp. 217-237, 1999.

[13] D. C. Hart, "Aluminum Sensitization and Application of Laminated Composite Patch Repairs," in *Proceedings of the Society for Experimental Mechanics XIII International Congress and Exposition on Experimental Applied Mechanics, Experimental Dynamic Behavior: Integrating Experimental Mechanics,* Orlando, FL, 2016.

[14] K. Nahshon, W. A. Hoffman and C. B. Ullagaddi, "Characterization of Structural Scale Ductile Fracture of Aluminum Panels Using Digital Image Correlation," in *Proceedigs of the 214 Annual Conference on Experimental and Applied Mechanics,* 2014.

[15] D. C. Hart, E. P. Udinski, M. J. Hayden and X. Liu, "Fatigue Performance and Analysis of Composite Patch Repaired Cracked Aluminum Plates," in *Sustainability and Stewardship, Vessel Safety and Longevity Through Research*, Linthicum Heights, MD, 2014.

[16] J. M. Noland, D. C. Hart, D. C. Loup, E. P. Udinski and R. A. Sielski, "Initiatives in Bonded Ship Structural Repairs," in *ASNE Fleet Maintenance and Modernization Symposium*, San Diego, CA, 2013.

[17] D. C. Hart and H. A. Bruck, "Low Modulus Composite Patched Aluminum Center Crack Tension Specimen DIC Surface Displacements Compared with Predictions," in *Society for Experimental Mechanics Annual Conference and Exposition on Experimental Applied Mechanics*, Greenville, SC, 2018.

[18] D. C. Hart and H. A. Bruck, "Effects of Plasticity on Patched and Unpatched Center Crack Tension Specimens," *Experimental Mechanics,* Accepted Oct. 2019.

[19] D. C. Hart, "Design and Analysis of the CG-47 Ticonderoga Class Composite Patch Repair," NSWCCD-65-TR-2011/54, Naval Surface Warfare Center Carderock Division, 2011.

[20] ASTM-D3878, Standard Terminology for Composite Materials, Conshohocken, PA, 2007.

[21] T. F. J. Christian, D. O. Hammond and J. B. Cochran, "Composite Material Repairs to Metallic Airframe Components," *Journal of Aircraft,* vol. 29, no. 3, May-June 1992.

[22] R. C. Allan and J. D. Clark, "Use of Adhesives in Repair of Cracks in Ship Structures," *Materials Science and Technology,* vol. 4, p. 853, 1988.

[23] I. Grabovac, P. J. Pearce, A. Camilleri, K. Challis and J. Lingard, "Are Composites Suitable for Reinforcement of Ship Structures?," in *12th International Conference on Composite Materials*, Paris, 1999.

[24] I. Grabovac and D. Whittaker, "Application of Bonded Composites in the Repair of Ships Structures - A 15-year Service Experience," *Composites: Part A,* vol. 40, pp. 1381-1398, 2009.

[25] I. Grabovac, R. A. Bartholomeusz and A. A. Baker, "Composite Reinforcement of a Ship Superstructure - Project Overview," *Composites,* vol. 24, no. 6, p. 501, 1993.

[26] T. J. Turton and F. Livingstone, "Oil Platforms, Destroyers, and Frigates-Case Studies in QinetiQ's Marine Composite Patch Repairs," *Composite: Part A,* vol. 36, pp. 1066-1072, 2005.

[27] D. C. Hart and E. P. Udinski, "Testing and Analysis of Center Crack Tension Aluminum Plates with Composite Patch Repair," NSWCCD-65-TR-2013/1, Naval Surface Warfare Center Carderock Division, 2013.

[28] W. J. Golumbfskie, "Aluminum Sensitization and the Navy," in *The Minerals, Metals, and Materials Society 143rd Annual Meeting and Exhibition*, San Diego, CA, 2014.

[29] W. J. Golumbfskie, K. T. Tran, J. M. Noland, R. Park, D. J. Stiles, G. Grogan and C. Wong, "Survey of Detection, Mitigation, and Repair Technologies to Address Problems Caused by Sensitization of Al-Mg Alloys on Navy Ships," *Corrosion,* vol. 72, no. 2, 2016.

[30] A. J. Kinlock, Adhesion and Adhesives: Science and Technology, New York, New York: Chapman and Hall, 1987.

[31] M. J. Davis and D. A. Bond, "The Importance of Failure Mode Identification in Ahdesive Bonded Aircraft Structures and Repairs," in *12th International Conference on Composite Materials*, Palais Des Congres, Paris, 1999.

[32] M. J. Davis and J. S. Tomblin, "Best Practice in Adhesive-Bonded Structures and Repairs," DOT/FAA/AR-TN06/57, U.S. Department of Transportation, Federal Aviation Administration, 2007.

[33] M. J. Davis and A. McGregor, "Assessing Adhesive Bond Failures: Mided Mode Bond Failures Explained," in *ISASI Australian Safety Seminar, Adhesion Associates, Prosolve Ltd.*, Canberra, Australia, 2010.

[34] M. Y. Tsai and D. W. Oplinger, "Improved Theoretical Solutions for Adhesive Lap Joints," *International Journal of Solids and Structures,* vol. 35, no. 12, pp. 1137-1312, 1998.

[35] C. N. Duong, "A Unified Approach to Geometrically Nonlinear Analysis of Tapered Bonded Joints and Doublers," *International Journal of Solids and Structures,* vol. 42, pp. 3498-3526, 2006.

[36] C. N. Duong, "A General Approach to Fracture Analysis of Tapered Bonded Joints and Doublers," *Engineering Fracture Mechanics,* vol. 96, pp. 355-379, 2012.

[37] J. Wang and C. Zhang, "Energy Release Rate and Phase Angle of Delamination in Sandwich Beams and Symmertric Adhesively Bonded Joints," *International Journal of Solids and Structures,* vol. 46, pp. 4409-4418, 2009.

[38] C. H. Wang, L. R. F. Rose and R. Callinan, "Analysis of Out-of-Plane Bending In One-Sided Bonded Repair," *International Journal of Solids and Structures,* vol. 35, no. 14, pp. 1653-1675, 1998.

[39] P. F. Joseph and F. Erdogan, "Plates and Shells Containing a Surface Crack Under General Loading Conditions," CR-178328, NASA Langley Research Center, 1987.

[40] C. B. Guyt, "Design and Installation of Bonded Repairs to Cracked Fuselage Skins on a C-5A," T/N 69-021, USAF European Office of Aerospace Research and Development and the Fatigue and Fracture Group, Flight Dynamics Directorate, 1995.

[41] Boeing, "Composite Repair of Aircraft (CRAS) Software Users Manual v1.0.1," Boeing, 2003.

[42] C. Yan, Y.-W. Mai, Q. Yuan, L. Ye and J. Sun, "Effects of Substrate Materials on Fracture Toughness Measurement in Adhesive Joints," *International Journal of Mechanical Sciences,* vol. 43, pp. 2091-2102, 2001.

[43] S. W. Johnson, L. M. Butkus and R. V. Valentin, "Applications of Fracture Mechanics to the Durability of Bonded Composite Joints," DOT/FAA/AR-97/56, U.S. Department of Transportation, Federal Aviation Administration, 1998.

[44] H. Osnes, D. McGeorge, J. R. Weitzenbock and G. O. Guthu, "Predicting Failure of Bonded Patches Using a Fracture Mechanics Approach," *International Journal of Adhesion and Adhesives,* vol. 37, pp. 102-111, 2012.

[45] H. Osnes and D. McGeorge, "Analysis of Overlaminated Double-Lap Joints," *Composites: Part B,* vol. 36, pp. 544-558, 2005.

[46] H. Osnes and D. McGeorge, "Experimental and Analytical Strength Analysis of Double-Lap Joints for Marine Applications," *Composites: Part B,* vol. 40, pp. 29-40, 2009.

[47] D. McGeorge, "Inelastic Fracture of Adhesively Bonded Overlap Joints," *Engineering Fracture Mechanics,* vol. 77, pp. 1-21, 2010.

[48] Q. Luo and L. Tong, "Closed-Form Solutions for Nonlinear Analysis of Single-Sided Bonded Composite Patch Repairs," *American Institute of Aeronautics and Astronautics,* vol. 45, no. 12, pp. 2957-2965, 2007.

[49] D. Ouinas, B. B. Bouiadjra and B. Serier, "The Effects of Disbonds on the Stress Intensity Factor of Aluminum Panels Repaired Using Composite Materials," *Composite Structures,* vol. 78, pp. 278-284, 2007.

[50] T. L. Anderson, Fracture Mechanics Fundamentals and Applications, Second ed., CRC Press LLC., 1995.

[51] H. A. Bruck, "Analysis of 3-D Effects Near the Crack Tip on Rice's 2-D J-Integral Using Digital Image Correlation and Smoothing Techniques," Department of Mechanical Engineering University of South Carolina, 1989.

[52] ABAQUS, "Version 2016 Software Users Manuals," 2016.

[53] M. J. L. Van Tooren and L. A. Krakers, "A Generalized Stress Singularity Approach for Material Failure Prediction and its Application to Adhesive Joint Strength Analysis," *Journal of Adhesion Science Technology,* vol. 20, no. 9, pp. 981-995, 2006.

[54] J. W. Hutchinson, "Singular Behaviour at the End of a Tensile Crack in a Hardening Material," *Journal of Mechanics and Physics of Solids,* vol. 16, pp. 13-31, 1968.

[55] J. R. Rice and G. F. Rosengren, "Plane Strain Deformation near a Crack Tip in a Power-Law Hardening Material," *Journal of Mechanics and Physics of Solids,* vol. 16, pp. 1-12, 1968.

[56] Y. J. Chao, S. Yang and M. A. Sutton, "On the Fracture of Solids Characterized by One or Two Parameters: Theory and Practice," *Journal of Mechanics and Physics of Solids,* vol. 42, no. 4, pp. 629-647, 1994.

[57] G. B. May, F. X. Wang and A. S. Kobayashi, "Two-Parameter Crack Tip Field Associated with Stable Crack Growth in a Thin Plate - A Hybrid Analysis," 1993.

[58] S. Yang, Y. J. Chao and M. A. Sutton, "Higher Order Asymptotic Crack Crack Tip Fields in a Power-Law Hardening Material," *Engineering Fracture Mechanics,* vol. 45, no. 1, pp. 1-20, 1993.

[59] S. Yang, Y. J. Chao and M. A. Sutton, "Complete Theoretical Analysis for Higher Order Asymptotic Terms and the HRR Zone at a Crack Tip for Mode I and Mode II Loading of a Hardening Material," *Acta Mechanica,* vol. 98, pp. 79-98, 1993.

[60] M. A. Sutton, J. J. Orteu and H. W. Schreier, Image Correlation for Shape, Motion, and Deformation Measurements, Springer LLC., 2009.

[61] H. A. Bruck, "Analysis of 3-D Effects Near the Crack Tip on Rice's 2-D J-Integral Using Digital Image Correlation and Smoothing Techniques," 1989.

[62] M. A. Sutton, J. L. Turner, Y. J. Chao, H. A. Bruck and T. L. Chae, "Experimental Investigations of Three Dimensional Effects Near a Crack Tip Using Computer Vision," *International Journal of Fracture,* vol. 53, pp. 201-228, 1992.

[63] S. Yoneyama, S. Arikawa, S. Kusayanagi and K. Hazumi, "Evaluating J-Integral From Displacement Fields Measured by Digital Image Correlation," *Strain,* vol. 50, pp. 147-160, 2014.

[64] W. F. Hickey, "An Investigation into the Failure of Aluminum Alloys," Masters Thesis in Material Science and Engineering, University of Texas at Austin, Austin, TX, 2011.

[65] T. H. Becker, M. Mostafavi, R. B. Tait and T. J. Marrow, "An Approach to Calculate the J-Integral by Digital Image Correlation Displacement Field Measurement," *Fatigue and Fracture of Engineering Materials and Structures,* vol. 35, pp. 971-984, 2012.

[66] D. Fernandez-Zuniga, J. F. Kalthoff, A. Fernandez-Canteli, J. Grasa and M. Doblare, "Three Dimensional Finite Element Calculations of Crack Tip Plastic Zones and KIC Specimen Size Requirements," in *European Conference on Fracture,* Stockholm, Sweden, 2004.

[67] R. Hamam, F. Hild and S. Roux, "Stress Intensity Factor Gauging by Digital Image Correlation: Application in Cyclic Fatigue," *Strain,* vol. 43, pp. 181-192, 2007.

[68] M. S. Dadkhah, A. S. Kobayashi and W. L. Morris, "Crack-Tip Displacement Fields and JR-Curves of Four Aluminum Alloys," in *Fracture Mechanics: Twenty-Second Symposium (Volume 11), ASTM STP 1131*, Philadelphia, 1992.

[69] M. S. Dadkaha and A. S. Kobayashi, "Further Studies on the HRR Field of a Moving Crack, An Experimental Analysis," *International Journal of Plasticity,* vol. 6, pp. 635-650, 1990.

[70] M. S. Dadkhah and A. S. Kobayashi, "HRR Field of a Moving Crack, An Experimental Analysis," *Engineering Fracture Mechanics,* vol. 34, no. 1, pp. 253-262, 1989.

[71] M.-L. Lu, C.-B. Lee and F.-C. Chang, "Fracture Toughness of Acrylonitril-Butadiene-Styrene by J-Integral Methods," *Polymer Engineering and Science,* vol. 35, no. 18, pp. 1433-1439, 1995.

[72] A. Acciaioli, G. Lionello and M. Baleani, "Experimentally Achievable Accuracy Using a Digital Image Correlation Technique in measuring Small-Magnitude (<0.1%) Homogeneous Strain Fields," *Materials,* vol. 11, no. 5, p. 751, 2018.

[73] R. Balcaen, P. L. Reu, P. Lava and D. Debruyne, "Stereo-DIC Uncertainty Quantification Based on Simulated Images," *Experimental Mechanics,* vol. 57, pp. 939-951, 2017.

[74] International Digital Image Correlation Society, "A Good Practices Guide for Digital Image Correlation," (Eds) Jones, E. M. C.; Iadicola, M. A., https://doi.org/10.32720/idics/gpg.ed1/print.format, 2018.

[75] D. C. Hart, E. P. Udinski and J. M. Noland, "CG Task Force Composite Patch Material Testing," NSWCCD-65-TR-2015/15, Naval Surface Warfare Center Carderock Division, 2016.

[76] J. S. Tomblin, Y. C. Ng and K. S. Raju, "Material Qualification and Equivalency for Polymer Matrix Composite Material Systems," DOT/FAA/AR-00/47, US Department of Transportation Federal Aviation Adminsitration Office and Aviation Research, April 2001.

[77] DoD, "Composite Materials Handbook, Volume 1 Polymer Matrix Composites Guidelines for Characterization of Structural Materials," MIL-HDBK-17-1F, Department of Defense, 2002.

[78] Correlated Solutions Inc., "Vic-2D v6 Reference Manual," Correlated Solutions Inc., Irmo, SC 29063, 2018. [Online]. Available: https://www.correlatedsolutions.com. [Accessed March 2018].

[79] R. B. Krieger, "Adhesive Bonding Design and Analysis," in *Engineered Materials Handbook*, 1990.

[80] J. Tomblin, W. Seneviratne, P. Escobar and Y. Yoon-Khian, "Shear Stress-Strain Data for Structural Adhesives," DOT/FAA/AR-02/97, U.S. Department of Transportation Federal Aviation Administration Office of Aviation Research, Washington D.C., 2002.

[81] P. Chalkley and J. van den Berg, "On Obtaining Design Allowables for Adhesives Used in the Bonded-Composite Repair of Aircraft," DSTO-TR-0608, Defence, Science, and Technology Ogranisation, Airframes and Engines Division, Aeronautical and Maritime Research Laboratory, Australia, 1998.

[82] ASTM D5656, "Standard Test Method for Thick-Adherend Metal Lap-Shear Joints for Determination of the Stress-Strain Behavior of Adhesives in Shear by Tension Loading," ASTM International, Conshohocken, PA, 2004.

[83] Mathworks, "MATLAB R2017a Documentation," 2017.

[84] ASTM E399-08, "Standard Test Method for Linear-Elastic Plane-Strain Fracture Toughness KIC of Metallic Materials," American Society for Testing and Materials International, Conshohoken, PA, 2008.

[85] ASTM E407-07, "Standard Practice for Microetching Metals and Alloys," American Society for Testing and Materials International, Conshohoken, PA, 2015.

[86] ASTM E112-13, "Standard Test Methods for Determining Average Grain Size," American Society for Testing and Materials International, Conshohoken, PA, 2013.

[87] ASTM E8M-08, "Standard Test Methods for Tension Testing of Metallic Materials," American Society for Testing and Materials International, Conshohocken, PA, 2008.

[88] ASTM E466-07, "Standard Practice for Conducting Force Controlled Constant Amplitude Axial Fatigue Tests of Metallic Materials," American Society for Testing and Materials International, Conshohocken, PA, 2007.

[89] ASTM D638, "Standard Test Method for Tensile Properties of Plastics," American Society for Testing and Materials International, Conshohocken, PA, 2003.

[90] ASTM D3039, "Standard Test Method for Tensile Properties of Polymer Matrix Composites," American Society for Testing and Materials International, Conshohocken, PA, 2000.

[91] ASTM D6641, "Standard Test Method for Determining the Compressive Properties of Polymer Matrix Composite Laminates Using a Combined Loading Compression (CLC) Test Fixture," American Society for Testing and Materials International, Conshohocken, PA, 2001.

[92] ASTM D3846, "Standard Test Method for In-Plane Shear Strength of Reinforced Plastics," American Society for Testing and Materials International, Conshohocken, PA, 2002.

[93] T. G. O'Shaughnessy, "ALCOA 5000-Series Alloys Suitable for Welded Structural Applications," Aluminum Company of America Applications Engineering Division, Green Letter No. 143 Second Revision, Pennsylvania, 1985.

[94] ASM International, Aluminum Properties and Physical Metallurgy, J. E. Hatch, Ed., ASM International, 1984.

[95] F. Ozturk, S. Totos and S. Kilic, "Evaluation of Tensile Properties of 5052 Type Aluminum-Magnesium Alloy at Warm Temperatures," *Archives of Materials Science and Engineering,* vol. 34, no. 2, pp. 95-98, 2008.

[96] A. N. Whitfield and D. J. Stiles, "Literature Survey of Historical Data Relating to Marine Grade Aluminum Alloys: Part I - 5xxx Alloys," NSWCCD-61-TR-2008/10, Naval Surface Warfare Center Carderock Division, 2008.

[97] ACM, "Section 3, Engineering Data for Aluminum Structures 4th Edition," in *Aluminum Construction Manual*, The Aluminum Association Technical Committee on Engineering and Design, 1981.

[98] J. K. Brosi and J. J. Lewandowski, "Delamination of Sensitized Commercial Al-Mg Alloy During Fatigue Crack Growth," *Scripta Materialia,* vol. 62, pp. 799-802, 2010.

[99] D. Li, H. Hassan, A. El-Shabasy and J. J. Lewandowski, *Effect of Sensitization on the Microstructure and the Mechanical Properties of 5xxx Aluminum Alloys,* Clevelend, OH: Case Western Reserve University, 2010.

[100] D. C. Hart and J. M. Noland, "Composite Patch Repair Installation Procedure for 5xxx Aluminum Alloy Effected by Stress Corrosion Cracking," NSWCCD-TR-65-2012/30, Naval Surface Warfare Center Carderock Division, 2012.

[101] J. D. Minford, "Durability Evaluation of Adhesive Bonded Structures," in *Adhesive Bonding*, L. H. In Lee, Ed., New York, Plenum Press, 1991, pp. 239-290.

[102] D. K. Blair, "Automated Fatigue Crack Growth Testing and Analysis - Series 2001 Version 3.09 Users' Steady State Reference Manual," Fracture Technology Associates, Bethlehem, PA, 2009.

[103] ASTM E647-08, "Standard Test Method for Measurement of Fatigue Crack Growth Rates," ASTM International, Conshohocken, PA, 2008.

[104] ASTM E561-08, "Standard Test Method for K-R Curve Determination," ASTM International, Conshohocken, PA, 2008.

[105] J. P. Gallagher, F. J. Giessler, A. P. Berens and R. M. J. Engle, "USAF Damage Tolerant Design Handbook: Guidelines for the Analysis and Design of Damage Tolerant Aircraft Structures," AFWAL-TR-82-3073, U.S. Air Force, 1984.

[106] E. Fang, M. Stuebner and J. Lua, "XFEM Co-Simulation of Delamination and Matrix Cracking in Fiber Metal Laminated Structures Under Fatigue Loading," in *54th AIAA/ASME/ASCE/AHS/ASC Structures, Structural Dynamics, and Materials Conference*, Boston, Massachusetts, 2013.

[107] D. M. Parks, "The Virtual Crack Extension Method for Nonlinear Material Behavior," *Computer Methods in Applied Mechanics and Engineering*, vol. 12, pp. 353-364, 1977.

[108] C. F. Shih, B. Moran and T. Nakamura, "Energy Release Rate Along a Three-Dimensional Crack Front in a Thermally Stressed Body," *International Journal of Fracture*, vol. 30, pp. 79-102, 1986.

[109] M. Besel and E. Breitbarth, "Advanced analysis of crack tip plastic zone under cyclic loading," *International Journal of Fatigue*, vol. 93, pp. 92-108, 2016.